UNIVERSITY OF CATANIA

Department of Chemical Sciences
International PhD in Chemical Sciences – XXXIV Cycle
Marie Curie Fellowship ─ MSCA-ITN-2017 'AiPBAND'

PhD Thesis

ORGANIC ELECTRONIC TRANSISTORS AND MICROFLUIDICS FOR CANCER BIOMARKER SENSING

MEENU SELVARAJ

Tutor: Prof. Dr. Giuseppe Spoto

Co-Tutor: Prof. Dr. Fabio Biscarini

Dr. Pierpaolo Greco

PhD Coordinator:

Prof. Dr. Salvatore Sortino

This project has received funding from the European Union's Horizon 2020 research and innovation programme under the Marie Skłodowska-Curie grant agreement 764281.

SUPERVISOR: PROF. DR. GIUSEPPE SPOTO

Department of Chemical Sciences

University of Catania

Viale Andrea Doria 6, 95125, Catania, Italy

Tel: +39 095 7385141

Fax: +39 095 580138

e-mail: spotog@unict.it

CO-SUPERVISOR: PROF. DR. FABIO BISCARINI

Life Science Department

University of Modena and Reggio Emilia

Via Campi, 103 I-1125 Modena, Italy

Tel: +39 059 205 8587

Fax: +39 059 205 5410

e-mail: fabio.biscarini@unimore.it

CO-SUPERVISOR: DR. PIERPAOLO GRECO

Life Science Department

University of Modena and Reggio Emilia

Via Campi, 103 I-1125 Modena, Italy

e-mail: ppgreco@unimore.it

To my mom and dad

"BE THE CHANGE YOU WANT TO SEE IN THIS WORLD"

MAHATMA GANDHI

ABSTRACT

MicroRNAs (miRNA) are a class of biomarkers whose relevance in oncology is increasing enormously, especially for cancers with high degree of invasiveness such as glioblastoma and lung cancer. Detection of miRNA circulating in blood appears a potential strategy for early diagnosis and patient monitoring, besides providing insights into the cellular path of disease. In the present PhD thesis, a biosensor based on Electrolyte-Gated Organic Field-Effect Transistor (EGOFET) is presented. A dual Gate/common Channel architecture was designed and prototyped for quantifying the concentration of one of the strands of miRNA-21 in saline buffer. The organic electronic device allows one to measure the differential response of the gate functionalized with oligonucleotide probe, with respect to a reference electrode functionalized with thiol based self-assembled monolayer. Both electrodes were immersed in the electrolyte above the transistor Channel. Hybridization with oligonucleotide in the picomolar regime induces a sizable reduction of the current flowing through the transistor Channel. The device signal is reported at various Gate voltages, showing maximum sensitivity at low Gate voltages, with a limit of detection as low as 35 pM. I modeled the dose curves with an analytical function derived from a thermodynamic model of the reaction equilibria relevant in the experiment and for the device configuration. I have also shown that the experimental dependence on analyte concentration emerges from the interplay of the different equilibria of reactions occurring on the surface of the Gate electrode and in solution. The binding free energy characteristic of the hybridization on the device surface is found to be approximately 20% lower with respect to the reaction in solution, hinting to partially inhibiting effect of the surface and presence of competing reactions. Impedance spectroscopy and surface plasmon resonance (SPR) performed on the same oligonucleotide pair were correlated to the electronic current transduced by the EGOFET

and confirmed the selectivity of the biorecognition probe covalently bound on the gold surface.

The aggregation of α-synuclein is a critical event in the pathogenesis of neurological diseases, such as Parkinson or Alzheimer. An EGOFET device was integrated with a microfluidics fabricated with 3D printing and replica molding allowing to detect amounts of α-synuclein in the range from 2.5 pM to 250 nM. The lower limit of detection (LOD) measures the attainable performance of the integrated device as a tool for prognostics and diagnostics. In the prototype device, the Gate electrode is the effective sensing element as it is functionalized with anti-(α-synuclein) antibodies using two alternative strategies: i) an amino-terminated self-assembled monolayer activated by glutaraldehyde, and ii) the His-tagged recombinant protein G. In both approaches, comparable sensitivity values were achieved, featuring very low LOD values at the pM level. The microfluidics engineering is central to achieve a controlled functionalization of the gate electrode and avoid contamination or physisorption in the transistor Channel where the organic semiconductor is patterned. The demonstrated sensing architecture, being a disposable stand-alone chip, can be operated as a label-free tool to explore *in-vitro* protein aggregation that takes place during the progression of neurodegenerative illnesses.

Keywords: Organic electronics, miRNA-21, α-synuclein, Electrolyte-gated organic field effect transistors (EGOFETs), Surface plasmon resonance (SPR), Impedance spectroscopy (IS), Hybridization kinetic modeling, Microfluidic devices

TABLE OF CONTENTS

CHAPTER 1

NOVEL ORGANIC ELECTRONICS-BASED DETECTION

1.1 Introduction

In the following chapter, I will briefly introduce the framework and the longstanding research aim in which my doctorate work can be placed. The development of biosensors for glioblastoma research was the topic of the Marie Sklodowska Curie project where I was involved as an early stage researcher, and so I explain the basic aspects and terminology of this type of cancer in Chapter 1.3 after giving few key milestones on biosensors development and role in Health Care in Chapter 1.2. Biopsy techniques in glioblastoma have been summarized at the end of Chapter 1.3, to introduce the new frontier of diagnostics which is Liquid Biopsy. A Crucial role in the achievement of cancer detection in serum or cerebrospinal fluid is the selection of robust biomarkers, as explained in the subchapter. of miRNA-21. In Chapter 1.5, I introduce Organic Bioelectronics. In Chapter 1.6, I describe the fundamental parameter equations of organic transistors. In Chapter 1.7, I present electrolyte gated organic transistors which represented my tool for prototyping a biosensor for either miRNA-21 and α-synuclein detection. At the end of the chapter, I make a brief excursus on the results reported in the literature on different schemes of biosensors based on organic transistors with biorecognition units interacting with one or more terminals of the device.

1.2 Role of Biosensors in Health Care

Biosensors are one of the most challenging and enabling technologies at service of the mankind. Biological sensors are short termed as Bio sensors. A biosensor is defined as a biochemical, analytical, sensing device which transduces signals when the analyte interacts with biorecognition moieties connected with the transducing components [1]. Research in the field of biosensors dated back in history to early 19^{th} century where electrodes were used for pH measurement [2]. One of the greatest discoveries in the field of biosensors is the discovery of Clark electrode by Leland C. Clark, Jr in 1956. It is a sensing device used to measure oxygen level in blood and in various tissue cells of body parts. Clark's device was inserted into the blood vessels for continuous measurement and recording of oxygen level [3].

By demonstrating extensive research with enzyme-based electrodes, Clark Jr was able to develop a device to detect level of glucose content in blood in 1962, which eventually led him to be referred

as the father of biosensors [4]. It has become a multidisciplinary source of research and development, leading to extraordinary contribution to the well-being of humans.

It has a major role in biomedical diagnosis and is also well suited for a wide range of applications including disease detection, monitoring, following its progression and treatment, drug discovery, food safety, fermentation processes, plant metabolism and also other applications [5]. Technology and research related with biosensors are the key factors leading to the advancement in early detection and therapy discovery of certain diseases, i.e. glioblastoma (chapter 1.3).

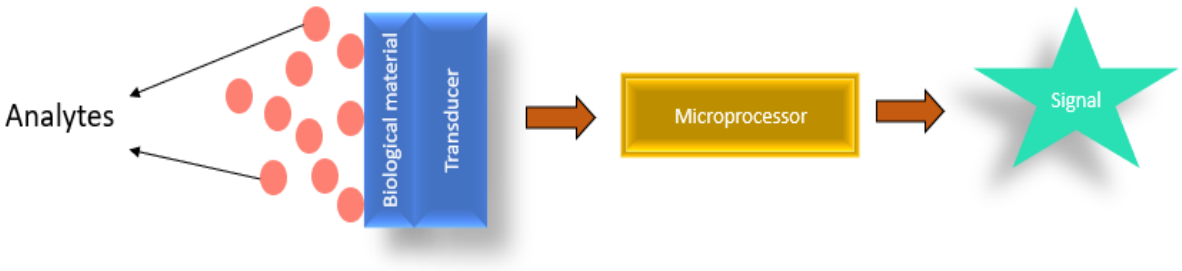

Figure 1.1: Biosensor components and Principle

The main components of a classic biosensor are the Bioreceptor, Transducer, Microprocessor and Display [1]. A fully developed biosensor will detect analyte concentration, although also devices providing "yes or no" response (qualitative) are valuable in the specific research fields. The biological material used in the biosensor could be blood, saliva, tissue, enzymes, DNA, antibodies and selection of a particular material is based on different factors such as application, accuracy, signal transmission. A signal is generated when the biomaterial interacts with the analyte leading to the detection and quantification of that particular analyte. Transducer helps in the detection of physical parameter change or chemical reaction output, by means of a measurable electrical signal which can be voltage or current, or also optical signal. In Biosensor, the transducer helps to convert the energy generated during analyte interaction to quantifiable electrical energy. Transducer can be active or passive based on the power source for its functioning. An active transducer requires power for its functioning, whereas a passive does not need an additional source to operate. Signal generated in the transducer is sent to the controlling unit of the biosensor. It amplifies the

physicochemical signal from the transducer to a measurable electric signal. The output from the microprocessor is routed to the Display portion of the biosensor. It displays the output based on the user specific interpretation which could be numeric, graphic, alphanumeric, binary or any user defined forms [6].

Currently, also due to pandemics affecting the health system worldwide, early detection of disease, with monitoring of involved therapies or progression, have become priorities. It is very crucial in the case of older people and children, where significant care and attention need to be provided. Survival and recovery from the disease are significantly higher if the abnormal condition is recognized in advance. Mankind has suffered and is suffering from an extensive range of diseases causing impacts ranging from mild complications to life threatening events.

Research and development in the field of science and technology have led to the discovery of user friendly, fast responsive, efficient and environmentally friendly devices that can be applied in various fields of health care. Extensive research in biomedical engineering, nanotechnology, medicine, clinical physics, electrical engineering, electronics engineering, has resulted in the worldwide development of sensing devices for healthcare management. Cancer and diabetics are the most relevant diseases to consider for research, based on the prevalence in the population, mortality, recovery rate, disease detection and treatment [7].

1.3 Glioblastoma Multiforme (GBM)

1.3.1 Glioma

Glioma is a type of cancer where glial cells of organs such as the brain and bone marrow are affected. Glial cells don't transmit electrical impulses unlike neuronal cells. They are part of the peripheral and central nervous systems of the human body. The name glial is coined from the Greek word, which translates to glue. This type of cell is attached to the nerve and works as a supportive medium for its functionality. They contribute a major portion of brain mass estimated between 30% and 60%. It was first discovered by neurological researchers and scientists named Virchow, Cajal and Río-Hortega during the 19th century [8].

Glioblastoma (GBM) are one of the most widespread and dangerous type of brain cancer in current period. It is predominant in malignant nature and estimated to have minimal chance of survival

rate of average 1.25 years. The reoccurrence rate is extremely high, which is around 90% of patients. It is more common in men than in women and affects more adults than young people. The chances of glioma cancer are relatively proportional with increase in age [9].

In the US it is roughly estimated to have around 0.7 million brain tumors patients and around 90,000 people were diagnosed in 2020. It is also estimated that around 95% of patients won't survive within 5 years of diagnosis. About occurrence in the general population, current statistics report a prevalence of 0.0002% in 2015, affecting the people in rage between 45 and 70 years. The median age of death affected by Glioblastoma is around 64 years [10]. Brain cancer is the tenth leading causes of death in mankind. Bladder, brain and lung are some of primary cancer sites that can spread metastases to the glial cells compartment leading to brain cancer.

1.3.2 Types of Glioma

Depending on the type of glial cell affected and its behaviour, glioma can be classified into three different types as Astrocytoma, Ependymomas and Oligodendrogliomas.

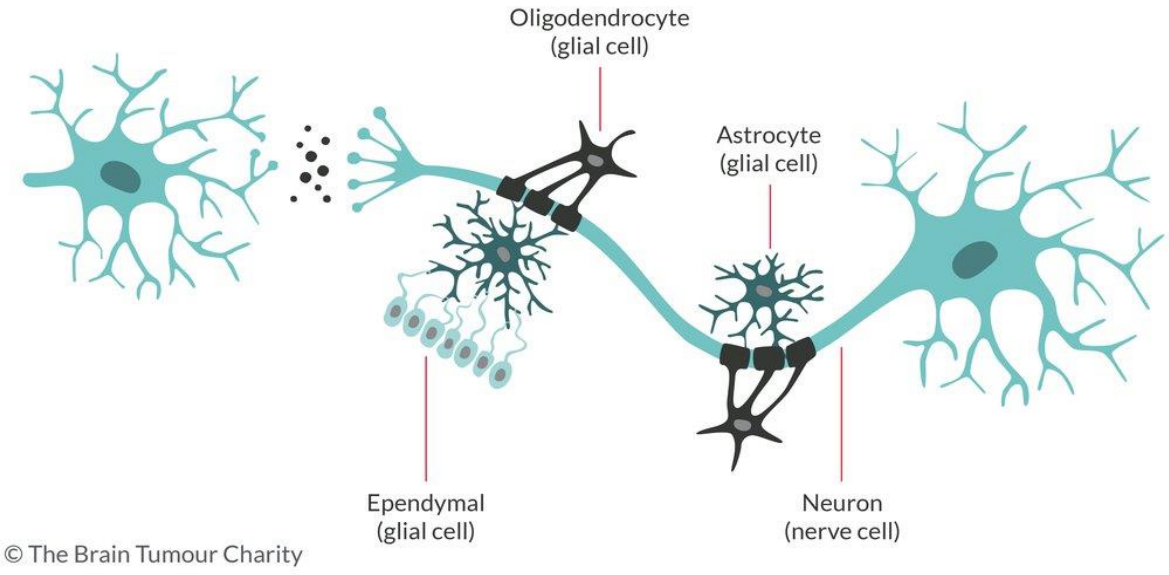

Figure 1.2: Pictographic representation of Brain cells and Brain tumors [11]

The type of diagnosis and treatment depends on the type of glial cells affected. Astrocytes, the name is derived from ancient Greek meaning ‘star’, have a star like structure. Astrocytoma is tumor involving directly astrocytes. During the progression of the disease, patients are subject to disability, loss of appetite and weakness, reduction of the overall metabolism and spinal cord related incidents. The rate of aggressive progression of cancer determines the nature of treatment and correlated diagnostics.

The Ependymomas glioma occurs when the ependymal cells of the brain and spinal cord is affected. These cells are the important structures to produce cerebral spinal fluid (CSF) and establish connection between brain and spinal cord. Ependymomas predominantly affect the younger generation [12]. In adults, Ependymomas occur mainly on the spinal cord causing disability and restrict movement. Oligodendrocyte cells aid in myelinate axons of the central nervous system and protect them. Oligodendrogliomas are less common gliomas (3-5% of intracranial tumors) and they affect adults more than children [13]. There is increasing interests in diagnostic tools for oligodendrogliomas, because they are more likely to respond to chemotherapy and do not evolve quickly to higher grade tumors [14].

1.3.3 General diagnosis methods of Glioma in Health care

In most scenarios, the general physician starts the neurological exam, analyse patient symptoms and evaluate the patients past medical history. The neurological exam assesses the central nervous system and it doesn’t cause any pain to the patient. Vision, hearing, balance, sense, memory, reflexes and body reactions will be reviewed by the physician.

In addition to that, eyes optic nerves will be checked for swelling. They are connected to the brain and if there is any blockage, the optic nerve starts to swell. In such cases the physician will look for immediate action. If the tumor is suspected, the physician generally asks to carry out further tests such as Magnetic resonance imaging (MRI) and computerized tomography (CT). After tumor detection, it is important to do a biopsy to identify the nature of tumor.

1.4 Biopsy

Traditional biopsy is the process of removing samples of tissues from the affected region to perform analysis. The sample is often analyzed by the neuropathologist to identify whether the tumor is cancerous or non-cancerous. This almost provides complete information associated with the tumors like its invasive nature, progression stage, treatment methods and recovery chances of a patient. Depending on the biopsy instruments, the source of sample tissues and affected organ biopsy can be classified as bone marrow biopsy, endoscopic biopsy, needle biopsy, skin biopsy and surgical biopsy. A surgical biopsy is performed when the sample tissue is inaccessible with other methods and is left with the surgical option to collect samples from tumor region [15].

1.4.1 Brain tissue Biopsy

In order to collect tumor samples from the brain for biopsy, there are two standard procedures. They are needle biopsy, open biopsy. A needle biopsy is equipped with a stereotactic device that helps to spot the desired and optimal location to collect the sample tissue from affected tissue. It is usually performed when the tumor is located deeper in the brain. A needle is inserted through the skull and reaches the desired part and will be controlled by the physician operating it. It can also be controlled with remote navigation, by connecting it with MRI scan or CT scan devices [16].

In an open biopsy, a small portion of the skull needs to be removed to generate access to the tumor region. It is generally performed if a large portion of the sample needs to be collected for analysis. It avoids a high risk of bleeding.

Neuroendoscopy is a minimally invasive type of biopsy where an endoscopy will be inserted into the patient's body through the nose or mouth to collect sample tissue from tumor. It consists of a high-resolution camera at one end for the physician's view and an eyepiece which helps in navigation and to access tumor spots. It is often used when surgical biopsy or open biopsy is not possible [17].

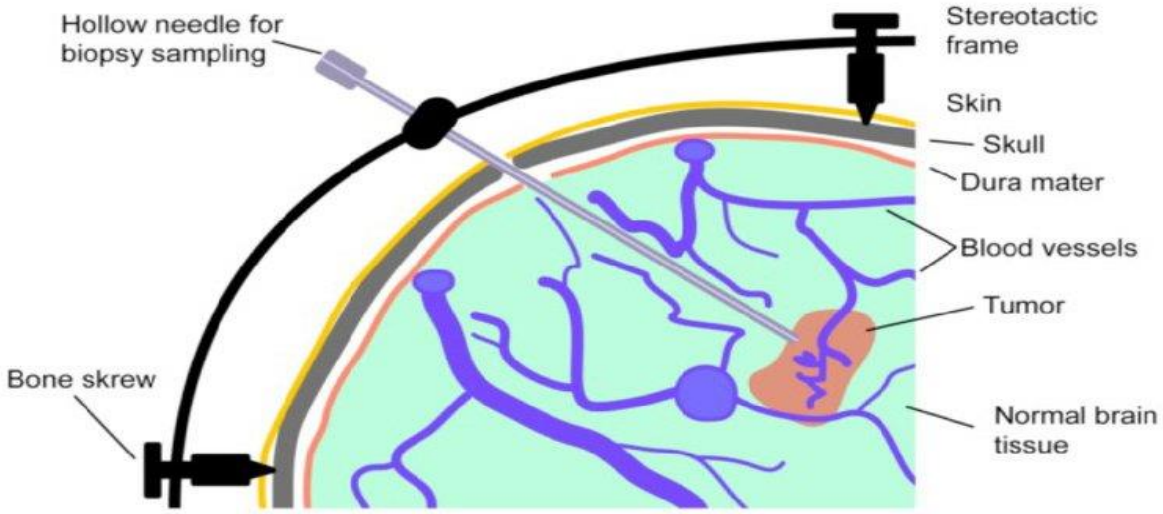

Figure 1.3: Schematic representation of Brain tissue biopsy [18]

1.4.2 Liquid Biopsy

In order to overcome invasive procedures and difficulties related to a patient's pain in a tissue biopsy, Liquid biopsy is emerging as a new tool for diagnostics and therapy evaluation. It is a type of biopsy where a liquid sample is taken to check the presence of cancer biomarkers, by evaluating DNA fragments, peptides and antigens released by cancer.

Sometimes it may be necessary to collect multiple samples to undertake different types of tests. Cell free DNA (cfDNA), Cell free tumor RNA (cfRNA), Cell free Tumor DNA (ctDNA), Micro RNA (miRNA), Circulating tumor cells (CTC), Tumor-educated platelets (TEP), Tumor proteins (TP) and Exosomes are the cell products found in blood, in cerebrospinal fluid or in the lymphatic system [19].

CTC in blood cells was first observed by R.T. Ashworth in 1869, while a metastatic cancer patient's blood was analyzed under a microscope. Even though it is first observed during 18th century, only during the middle of the 19th century it was discovered that CTCs are the main source of metastatic cancer when cancer has spread from the primary cancer location to other parts through blood and body fluids [20].

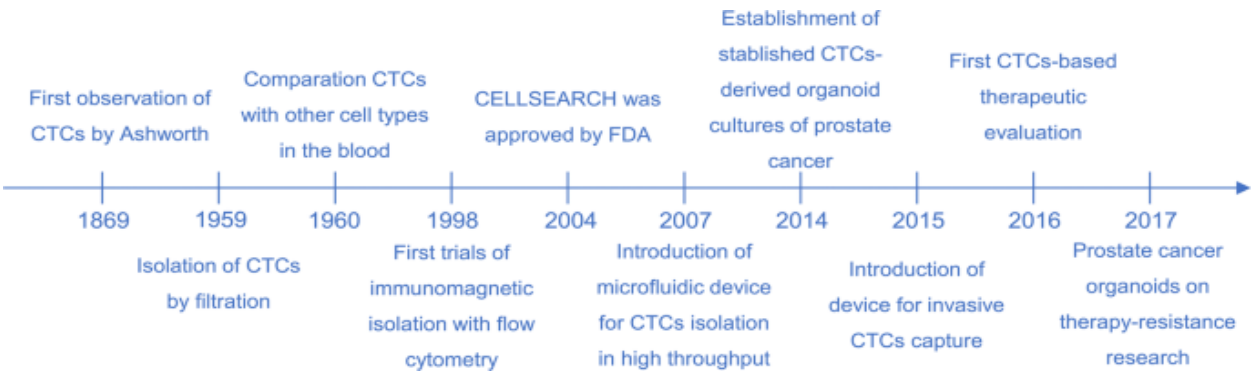

Figure 1.4: Discovery and therapeutic evaluation of Circulating tumor cells (CTCs) [21]

During 1960, CTC related research has gained significance, where its metabolism, structure, properties, biological movements were identified. This helped to generate an idea of isolation of CTC to understand the complexity of tumor. One of the major breakthroughs in the implementation of CTC related tumor biopsy is the approval of device to capture CTC isolation by US Federal food and drug Administration (FDA) [21].

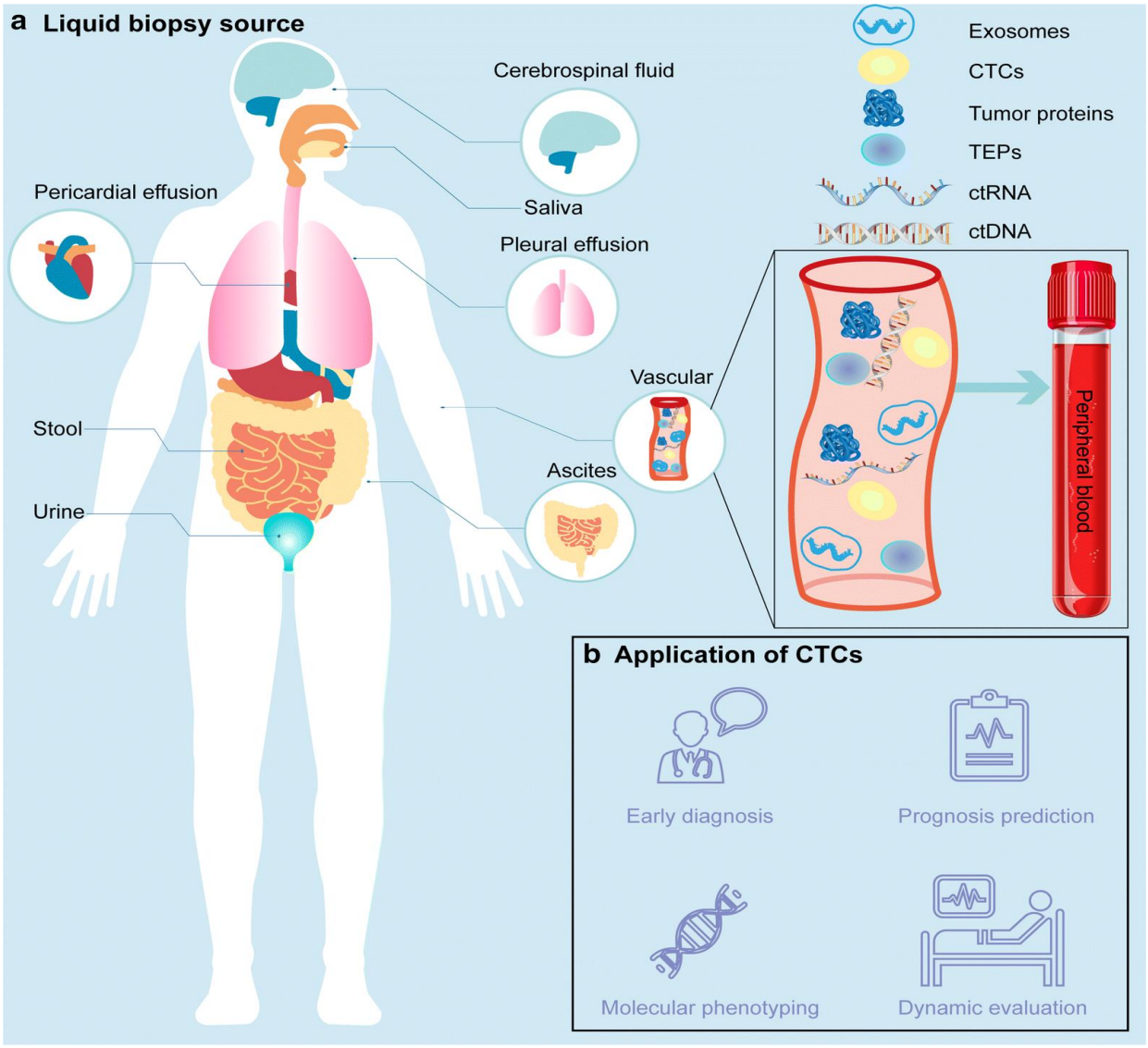

Figure 1.5: a) Body fluid sources which can be collected for liquid biopsy b) Application of Circulating tumor cells (CTCs) [21]

In August 2020 FDA approved a combined cancer diagnostics device that applies Liquid biopsy and next generation sequencing technology (NGS). The blood sample is collected non-invasively for biopsy and NGC technology is used to analyze the genetic mutations of epidermal growth factor receptor (EGFR). This analysis helps to diagnose one of the most critical types of lung cancer, which is non-small cell lung cancer (NSCLC). It is a metastatic type of cancer and contributes around 85% of cases. Guardant360 is the diagnostic assay that is approved by FDA to

diagnose metastatic lung cancer. It is capable of testing 55 genetic mutations of a tumor at a time, where conventionally only one testing was possible before.

After the patient's sample blood is collected from liquid biopsy, it needs to be further processed to separate serum or plasma.

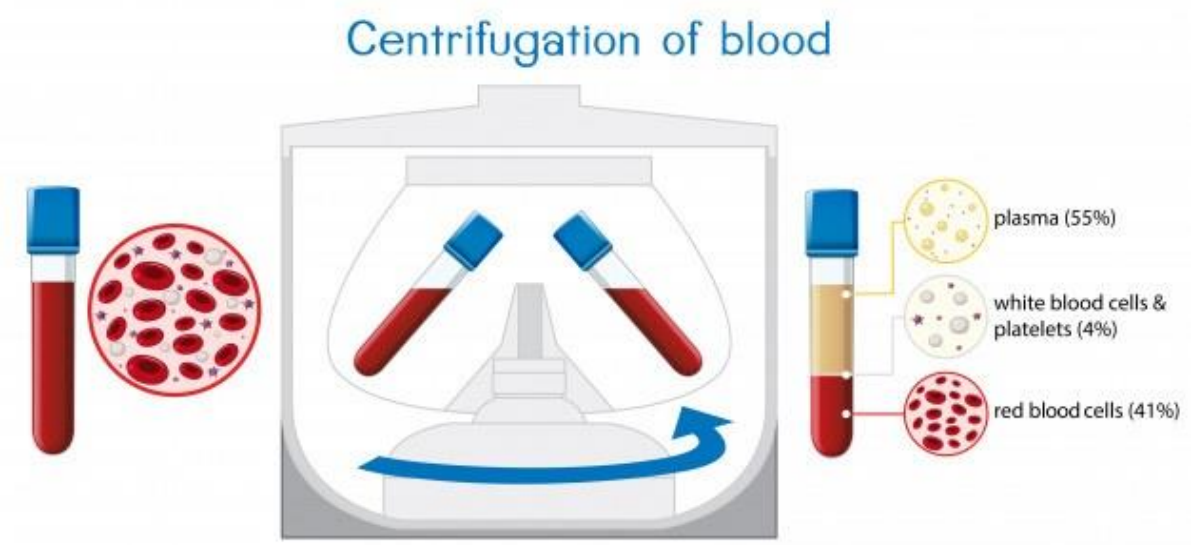

Figure 1.6: Centrifugation process of the blood, in order to separate serum and plasma [22]

To separate plasma in blood sample, the coagulation step is not performed. Blood is kept in centrifuge device for predefined settings to separate components of blood. Once centrifuging process is completed, plasma can be extracted.

The blood contains red blood corpuscles, white blood corpuscles and platelets. Red blood cells (41%) have high density and will get deposited at the bottom of the tube, followed by platelets and white blood cells (4%) and plasma is found on the top of the tube [23]. After the collection of serum or plasma, it can be further purified by High Performance Liquid Chromatography (HPLC).

HPLC is widely used to purify amino acid chains, small and medium sized organic elements. Normal phase HPLC and Reverse phase HPLC are the two common types of HPLC. Depending on the nature of liquid used, characteristics of components and properties, the right choice of HPLC method is chosen [24].

Upon interaction between the mobile and stationary phase, the components of the sample will elute from the packaging column of HPLC. Components having higher degree of interaction with packaging column will elute faster and with slower degree of interaction components elute in a slower rate [25]. It is then passed further to a detector which helps to identify, detect components from the sample and send the information to the computer connected with it.

1.4.3 Glioblastoma biomarkers detected in serum or CSF

ctDNA may provide sufficient evidence of the glioblastoma genome at the moment of the analysis.[26] Time constrained validity of the analysis on ctDNA reflects the largely reported instability of the genetic features of GBM, with several mutations appearing only in time. The factors affecting the persistence of mutations are matter of research in cancer molecular biology and represent a large obstacle also in the development of personalized therapies.

miRNA-21 (refer subchapter 1.4.4) has been reported in several studies to be positively correlated with the gravity of the disease, although not specifically to just glioblastoma. miR-128 and miR-342 instead are less present in high-grade glioblastoma patients, but their level is restored after surgery, showing the specificity of these miRNAs to gliomas and their potential use as therapy biomarkers.

Although very promising, diagnosis and prognosis based on miRNAs in GBM is still under high debate. There are reported also contradictory results on the same biomarkers with respect to disease correlation, and a robust model describing the concentration in serum is still not available. Biosensors based on miRNA and statistical analysis methods should be validated before accepting miRNAs as biomarkers in clinics.

Another interesting biomarker potentially useful for GBM is extracellular vesicles (EVs), EVs have been found in several compartments of the human body, such as blood, CSF or urine, therefore are good candidate for selective separation and analysis. EVs are small spheres enclosed by a lipid membrane (diam. in range 40 to 1000 nm) by many different cell types through complex molecular mechanisms. The different types of EVs can be classified into exosomes (40–200 nm), membrane-derived vesicles (40 to >1000 nm) and apoptotic bodies (100–5000 nm). EVs contain

biomolecules coming from viable tumor cells, such as nucleic acids, proteins, lipids. These components can be transferred to nearby or distant cells or tissues with processes of internalization or contact. EVs are reported to influence greatly the interaction between glioblastoma and its microenvironment. The signals contained in the EVs might affect the behaviour of surrounding brain cells and lead to tumor growth.

Proteins involved in the serum or CSF based diagnostics of GBM are still in validation phase for diagnostic purposes. In particular, out of 27 identified candidates, with different grade of expression, only 5 have been demonstrated to be linked with the tumor progression. Haptoglobin alpha-2 is one of the most expressed protein biomarker in glioma patients, however therapies do not seem to affect the serum levels of the protein [27].

Tumor-educated platelets (TEPs) constitute an innovative frontier in early diagnosis, since it has been demonstrated that somehow their partial reprogramming induced by tumor cells through EV is effective since initial stages of tumor, before the lesion reaches sizes which can be detected by other MR scan techniques. Also, TEPs profiling seems to provide a specific fingerprint for GBM, by looking at the capability to intake EGFRvIII from EVs. This capability is completely absent in platelets from healthy donors [28].

1.4.4 miRNA-21 as a potential biomarker in GBM

Micro RNA are small, single stranded, non-coding RNA molecules with around 21-25 nucleotides. They play a vital role in gene regulation, RNA silencing and gene translation repression in plants, animals and human beings. RNA helps to perform different functions such as maintaining cell metabolism, proliferation, immunity management, patterning of neurons and aiding hematopoiesis [29].

An abnormal and uncontrollable presence of miRNA leads to a variety of malfunctions, diseases and disorders. They include neurological disorders, cerebral disorders, Lung diseases, immune related disorders and brain diseases especially cancers. These factors make miRNAs a class of powerful biomarkers as they are able to identify the onset of the diseases at an earlier stage.

Though miRNA is considered to be an effective biomarker, it has its own limitations and challenges. It is difficult to detect a micro RNA when its amount constitutes roughly around 0.01% of the total RNA available in a sample. It is smaller in size than the messenger RNA (mRNA), challenging the analysis and making it difficult to detect. Time taken for incubation, temperature defined for the hybridization process and composition of the buffer play a role in the detection of miRNA in samples [30].

About 2000 human miRNAs have been found through cloning and /or sequence analysis.Whereas, miR-21 is a highly expressed miRNA in mammalian cells. The upregulation is associated with numerous types of cancer. It has been proved that miR-21 acts as an oncogene with its overexpression, for example in malignant B-cell lymphoma, when the conditional miR-21- knock-in mouse was made. [31] High levels of miR-21 are also associated with the activation of immune cell response. The location of gene encoding miR-21 differs, for rats and mice on the chromosomes 10 and 21 respectively. Whereas for humans, the location of miR-21 is located on the chromosome 17q23.2 [31].

To describe the cycle involved in the miRNA-21 generation from glioma cell types, I comment in the following Figure 1.7 which is taken from [32]

I) Precursor miRNAs (pre-miRNA) was generated by primary microRNAs (pri-miRNA), when pri-miRNA was transcribed in the nucleus by DNA polymerase and cleaved

II) Generated Precursor-miRNA (pre-miRNA) from primary microRNA (pri-miRNA), which was present in the nucleus

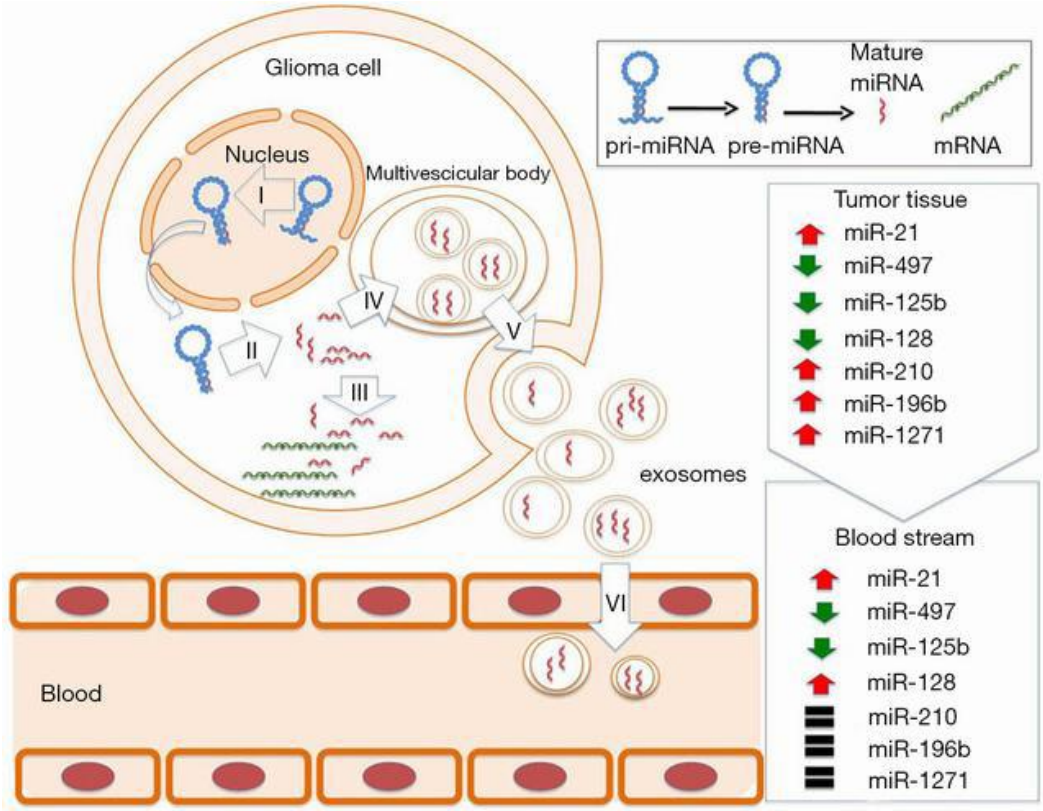

Figure 1.7: Mechanism of secretion of microRNAs from tumor cells to bloodstream [32].

III). Pre-miRNA is processed by dicer to produce mature miRNAs. These are binding target messenger RNAs to down-regulate their stability or for protein translation

IV) miRNA is entering Multivesicular Bodies

V) generated exosomes containing nucleic acids (DNA, RNA and miRNAs) and proteins are secreted in the tumor microenvironment

VI). After secretion, exosomes can be taken up by the tumor cells or normal cells, where miRNAs can regulate the expression of other target genes.

VII) Part of the exosomes secreted by tumor cells are disseminated in the blood stream. Right side of the figure, the red arrows symbolizes the overexpressed biomarkers as an oncogenic effect, whereas the green arrows are less expressed [32].

In many human cancers, the microRNA (miR-21) is overexpressed and it promotes glioblastoma tumorigenesis by down-regulating insulin-like growth factor-binding protein-3 (IGFBP3), which acts as a tumor suppressor in human glioblastoma [33].

1.5 Bioelectronics

As the name indicates, Bioelectronics is the combination of biological matter and electronics. In engineering terms, it is referred to as the application of principles of electronics to different fields such as botany, zoology, medicine, physiotherapy, health care, well-being and disease management. It effectively helps in disease early detection, controlling of disease progression, diagnosis, rehabilitation treatment and most importantly improves the health of an individual. Instrumentation and control engineering, biomedical engineering, microbiology, environmental engineering, genetic engineering and molecular engineering are some of the interdisciplinary sectors that are closely associated with bioelectronics [34].

1.5.1 Evolution of bioelectronics

The very first application of bioelectronics will date back to the 18th century of prominent scientist Luigi Galvani, where he experimented his research on frog corpses with electricity. In his science experiment, he connected the legs of a frog corpse on a lightning rod and he waited until lighting to strike.

He observed that lighting energy was observed by the lightning rod which in turn transmitted to the frog through a wire [35]. The frog legs twitched, which is one of the most important fundamentals for the science and development in the field of bioelectronics.

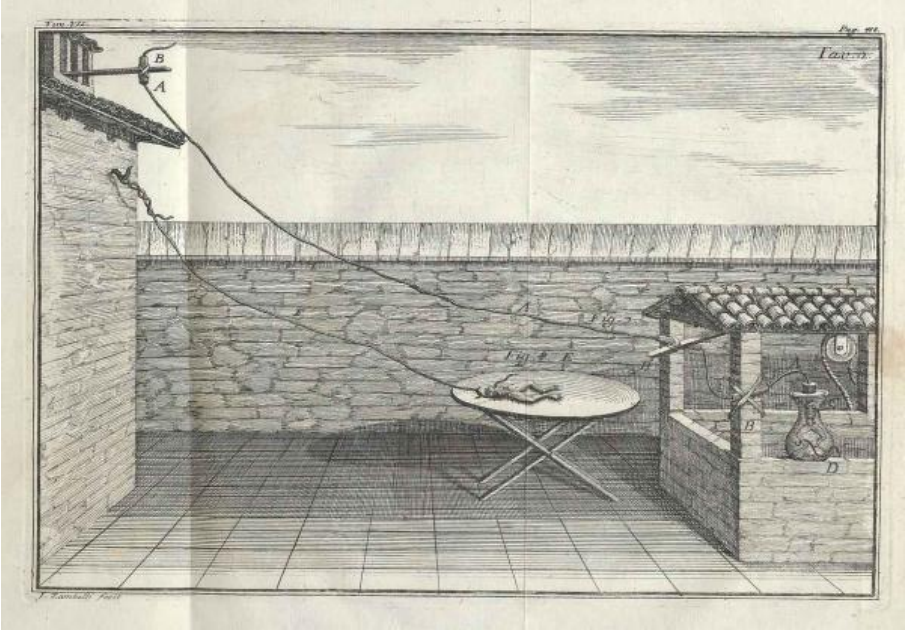

Figure 1.8: Galvani's setup from his publication [35].

A similar experiment is done under laboratory conditions with the help of a static electric generator, where electricity was supplied to the frog corpse. It caused movement in frog legs and it was evident that biological matter reacted when current passed through the tissues. This became a sensational discovery and it was widely discussed by scientists during that era [36].

Later he did an experiment by connecting the leg and spinal cord of a dead frog with two pieces of conducting metals. When the metals come in contact, current caused frog legs to twitch.

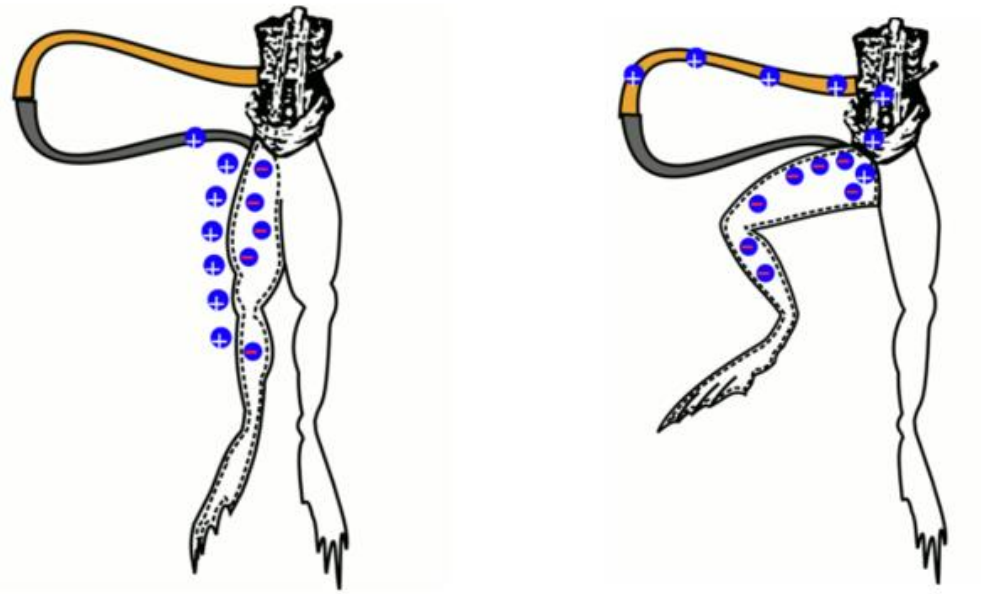

Figure 1.9: The bronze (yellow wire) is connected to iron (silver wire), charges flow between the frog's positively-charged outside and the frog's negatively-charged inside. This circuit completion causes the frog's muscles to contract [37]

These research and experiments have led to the emergence of numerous devices, technologies to aid mankind. One of the benchmark devices in the field of bioelectronics is the invention of the pacemaker, a device that is used to control the working of the human heart [38]. The first successful implementation of the pacemaker was done in 1958. It controls the hearth rate and rhythm by sending electrical impulses to the respective muscles surrounded to the heart [39].

Figure 1.10: Picture of the first pacemaker implanted in USA 1960, the electrode has two small holes to be sutured to the epicardium (left) and Current development to 'The Nanostim leadless pacemaker' which is less than a 10% of the size of a conventional pacemaker (right) [40]

Modern day markets offer a wide range of bioelectronics devices for human health care. It supports and elevates human health unanimously. The factors that influence the performance of devices include signal generation, processing, transmission and its digitalization from the electronics perspective. Signal transmission efficiency, signal strength and type of material used are the sources of limitation for the widespread of bioelectronic devices [41].

1.5.2 History of Electrochemical based Glucose Biosensor

Increased sugar level over an extended period of time affecting the body metabolism is the root cause of Diabetes mellitus (DM), generally cited as Diabetes. Pancreas secretes the enzyme Insulin, which is the main hormone controlling the glucose level in blood. Insulin secretion is related with the food consumption. Insufficient insulin secretion, high blood pressure, obesity, unbalanced lifestyle and food malnutrition are some of the common causes for diabetes [42].

World health organization declared that about 9.3% of the world population is affected by diabetics in 2019. By 2045, it is estimated to reach 650 million people worldwide. Even though the research and development with respect to advancements in sensing techniques emerge, it is also evident to note that the trend of diabetes is on a steady rising phase unfortunately. One of the greatest

breakthroughs in biosensor development is the invention of an amperometric glucose sensor, a device that can output the blood sugar level. Soon after its invention, it was commercialized for home usage for its immense importance in diabetes monitoring and prevention of further complications.

Glucose oxidase (GOD) is the commonly used enzyme based biological material in the glucose sensor. Glucose in blood is the analyte, which needs to be detected by the device. Glucose oxidase enzyme starts to catalyse the oxidation reaction of glucose with oxygen. It produces gluconolactone and hydrogen peroxide (H_2O_2) as a result [43].

This oxidation reaction causes boost of a H_2O_2 concentration and subsequently reduces the oxygen concentration. This reaction is directly proportional to the glucose concentration where quantifiable reading can be derived on the output.

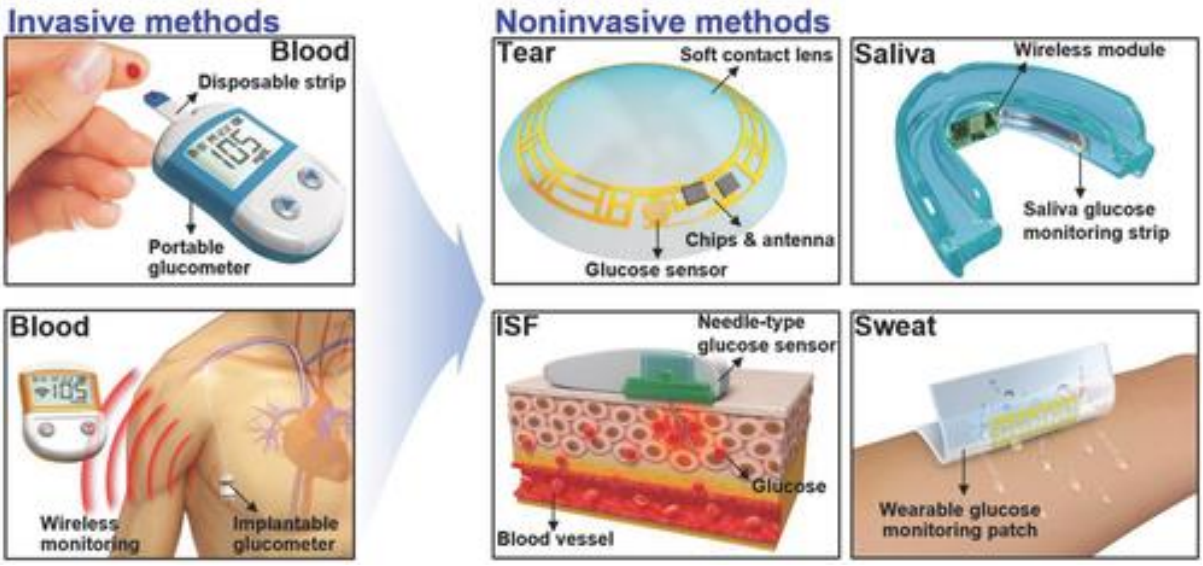

Figure 1.11: Evolution of glucose sensors from invasive to noninvasive electrochemical glucose monitoring system. [43]

Glucose biosensor market is growing day to day and is estimated to reach around 31 billion USD by 2022. Growing population, increased number of incidents, easy usage and several other factors

contribute to the market expansion of glucose biosensors [44]. The requirement of self-monitoring instrument in current generation with inbuilt modern technologies have made glucose biosensor one of the greatest lifesavers.

1.5.3 Development of Multisensing Biosensor

In our routine life it is quite essential to monitor our body to measure performance, efficiency, stamina, nutrition and other well-being factors regularly. Flexibility, user friendly profile, less complexity, high performance, the economic range is the factors that should be considered for selecting a biosensing device. It is quite important to evaluate its multi functionality where it can be suitable to measure, detect different analytes or use the analyte to perform multiple indicative analysis and derive output as signals. The common approach is to measure biomarkers, in the sports industry, for example, it is often used to measure the status of hydration levels, heartbeat and other performance characteristics. It helps to effectively manage and control one's physical and psychological health [45].

One of the most used body fluids containing biomarkers is sweat, where the sample is analyzed to output useful diagnostic information. It is proved that sweat might be the source for the detection of some genetically borne diseases. It is an easily available biological sample containing sodium, potassium, calcium and other ions. A multisensing biosensor might provide several analytic information at the same time [46].

The wearable sensor attached to the human body takes sweat as a sample and measures the concertation of ions and lactate. A structure to accommodate a minor amount of fluidics is designed and it will guide the sweat to pass through our biosensor. Transducers help to convert the physicochemical signal generated on account of biological interaction to the electrical signal. The acquired signal is amplified and displayed as an output. The main advantage is that the microliter volume of solution can be considered as a sample and analyzed.

Sweat rate, concentration and composition are the factors that influence the overall output of the measurement. Measurements taken during some specific exercise or activity will be compared to

the previous standard data. The deviation between standard and actual measurements help to derive one's respective performance results [47].

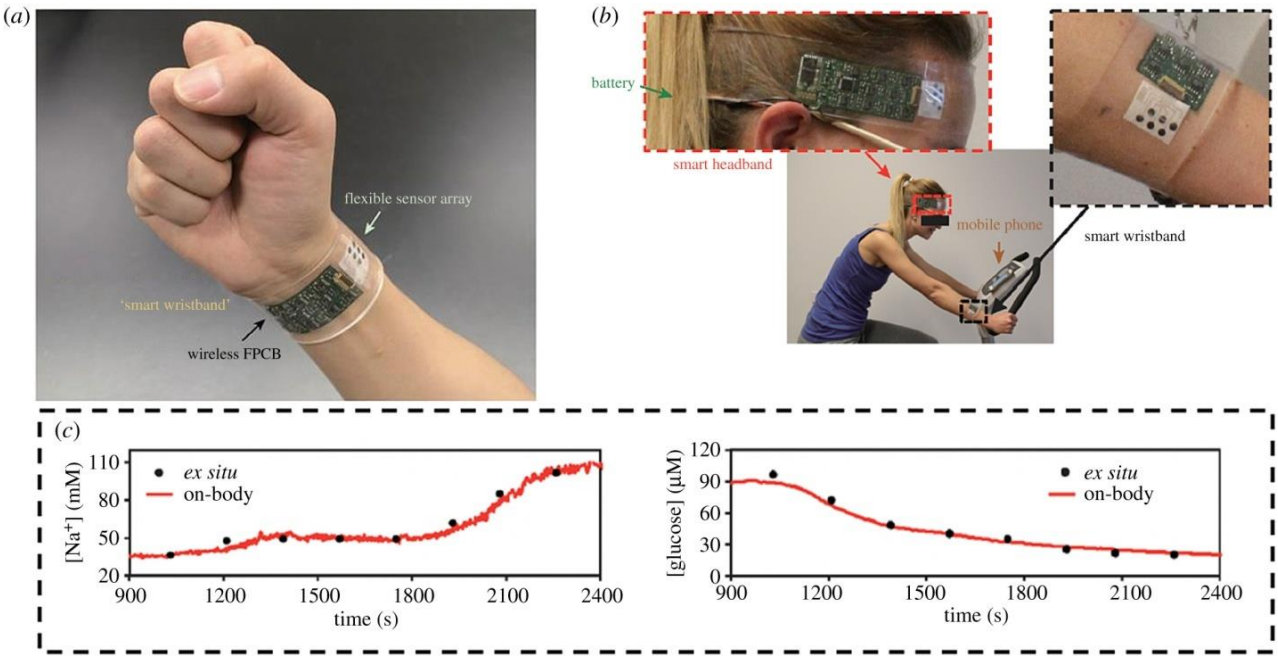

Figure 1.12: (a) *FISA and FPCB worn on the wrist;* (b) *sensor on the forehead, arm and wrist while cycling and* (c) *analysis for sodium and glucose [47]*

1.6 Organic Electronics

Organic electronics is a multidisciplinary field in the research and development of organic synthetic material, which can be applied in the electronic environment for the measurement of electrical properties. Instead of using traditional inorganic silicon based electrical components, carbon based organic electrical components were used. It is highly economical and has high electrical conductivity with minimal resistivity.

The first breakthrough in organic bioelectronics dates back to 1862, where Henry Letheby discovered the conductive properties of polyaniline, an organic polymer. Since then organic electrical components were used as a source of conductivity [48].

Improving the electrical conductivity of organic polymers is challenging and research has been conducted to improve their performance. By electrochemical oxidation or reduction, the conductive properties of an organic polymer can be improved. Polyacetylene is the most widely used organic polymer in research and in commercial applications. Doping of polyacetylene was successfully done by Hideki Shirakawa and coauthors, which contributed to the immense development of technologies related to organic semiconductors. Their contributions were well recognized by rewarding the Noble prize in 2000 [49]. Organic field effective transistor (OFET), Organic light emitting diode (OLED), Organic solar cell (OSC), Organic Photovoltaic cell (OPC) and organic photoelectrochemical cell (PEC) are some of the organic polymer used devices. Such devices offer flexibility, low cost, low maintenance, increased efficiency and clean power generation [50].

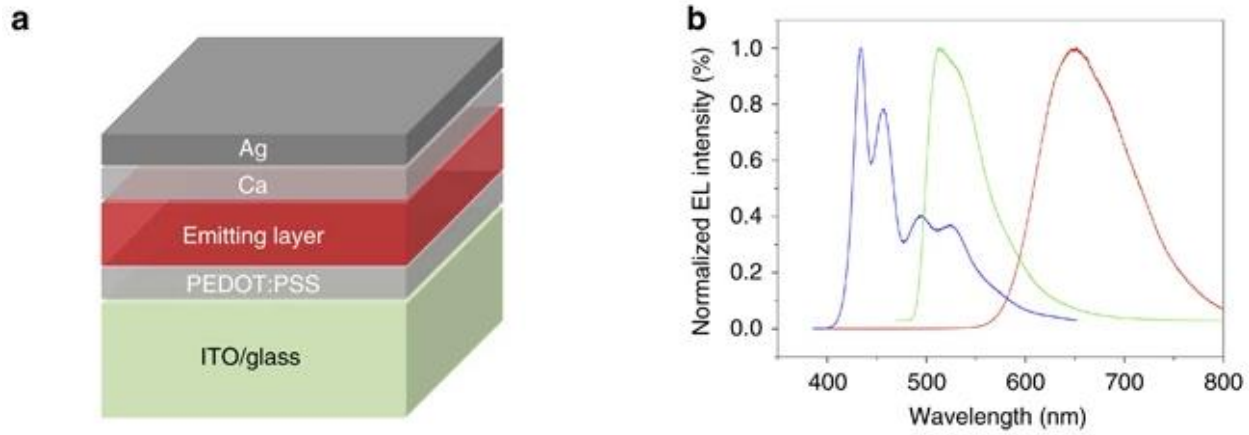

*Figure 1.13: a) Schematic architecture of the single-junction reference cell with a device structure of 'ITO/ PEDOT: PSS/Emitting layer/Ca/Ag'. (**b**) Electroluminescent spectra of the red, green and blue OLED devices. [51]*

In OLED, organic polymers are used as semi conducting materials, which reduces power consumption, operating voltage and provides high light emission. It is applied predominantly in digital appliances and also in displays of consumer appliances [52]. High resolution, faster responsive rate, robust and environment compatible design are the added advantages.

In the modern world, the usage of organic polymers in different fields of electrical and electronic devices is steadily increasing. They have become an integral part of our daily life both directly and indirectly. Its applications are expanded to multidisciplinary sectors, as we are steadily moving towards a sustainable living environment.

1.6.1 Evolution of Organic bioelectronics

Organic bioelectronics is the combination or alliance of organic electronics and biological elements and structures. This technology helps to regulate, control and monitor biological elements like blood, urine, saliva, tissue, cells, enzymes and other body fluids. Organic bioelectronics materials are capable of processing electronic and ionic signals.

With an effective synthesis process, they can enhance their physical, chemical and biological characteristics. They demonstrate adequate flexibility, excellent elasticity, stability and high durability. The emerging technology is the bridging stone for the merge of biology and organic electronics [53]. Their profound ability to detect ionic and electronic signals makes them extremely reliable to measure weak biochemical signals from the biological element.

Biotic-abiotic interface plays a vital role in effective electronic signal transmission. The output defines sensitivity and effective signal transmission between biological and electronic environment. The organic bioelectronics are classified as abiotic interface and it is found that increase in biological compatibility will subsequently improve the signal transmission between the biological and electronic system. This is an interface between two extreme mediums that is soft biological system and hard electronic system [53].

Conjugated polymers are efficient to create an interface between electronic and biological systems in a three-dimensional manner, whereas in traditional organic semiconductor interacts in two-dimensional mode. They are capable of interacting with ions and water molecules of the biological system of the entire capacity of the polymer.

Since there is no ionic barrier between semiconducting material and electrolyte, signal transmission is possible. PEDOT: PSS is one of the most widely applied conjugated polymers in

the research and development of organic bioelectronics. They are comprehensively applied in organic photovoltaic cells (OPV) [54].

In addition to the electrical, mechanical and chemical properties, the biocompatibility of organic bioelectronics elements plays a crucial role in signal processing and transmission. Biocompatibility can generate variable responses, depending on the interaction between the nature of the biological elements and electronic mediums.

Generally, such devices have a close interaction with tissue, cells and body fluids to generate signals. Specific biocompatibility tests need to be taken considering the type or nature of the biological element tested. Implantable organic bioelectronics devices need to be tested in three different environments such as in vitro, ex vitro and in vivo conditions. It is quite important to check its performance against several conditions before being implanted in the living body. Interaction of such devices with living matter can be toxic, Bioinert, Bioactive and Bioresorbable.

When the bioelectronic implant has a negative effect on implanted tissue or living matter, then it is defined as toxic. Bioinert devices exhibit no toxic reactions and remain biologically inactive. Bioactive devices have positive interactions with the biological element. They are able to transmit signals and measure output effectively. Bioresorbable devices are subject to non-rejecting inclusion in the tissue and eventually degradation after the implementation of the device in the host environment. They exhibit no toxic reactions [55].

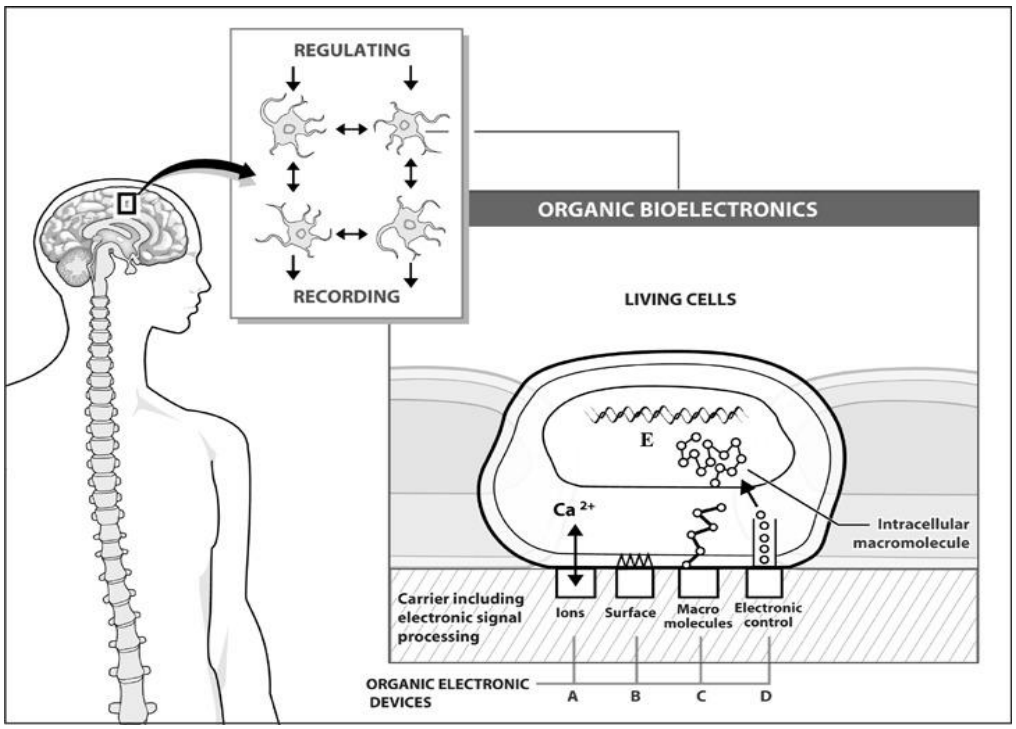

Figure 1.14: Application of Carbon based Organic Bioelectronics (OBOE) are carbon-based devices engineered from conductive polymers, in order to regulate and record the neuron signals [56]

Bioelectronic devices and related technologies are emerging for diagnostics and also treatment for specific diseases or disabilities. Fair biocompatibility, easy wearable properties, and low cost, easy accessibility, a wide range of buying options are the attractive benefits of organic bioelectronic devices.

1.7 Electrolyte-Gated Organic Field-Effect Transistor (EGOFETs)

Electrolyte-gated Organic Field-Effect Transistors (EGOFET) have emerged as potential biosensors due to their simplicity and highly sensitive nature to the interfacial changes at both gate/electrolyte and semiconductor/electrolyte interfaces. So, the target-specific bioreceptor can be immobilized either on the gate surface or at the semiconductor surface.

Transistor is a three terminal (base, collector, and emitter) semiconducting device and plays an important role in the field of electronics. In general, transistors have been used as transducing and sensing components due to the capability to amplify small signals arising at the interface between the active area and the external environment. Transistors can also act like as an ON/OFF switch for the electronic signals and electrical power. In short, transistors help to conduct or to regulate the current across the collector- emitter path, when the voltage is been applied to the base. When the base voltage is applied, the transistor is in an ON state and when no base voltage is applied, it switches to the OFF state.

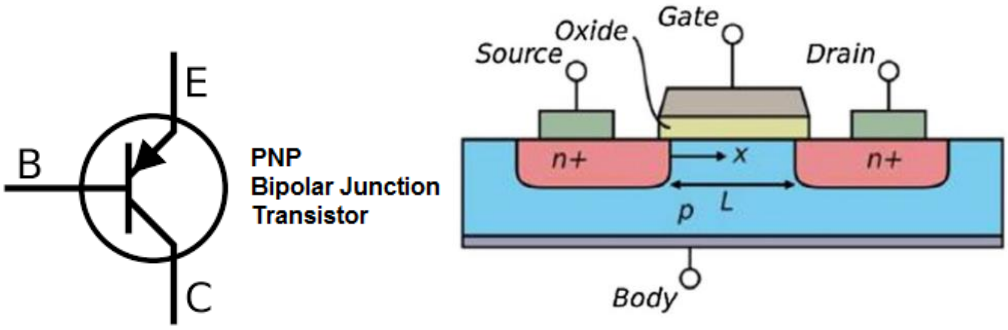

Figure 1.15: One of the pictogram representation of field effect transistor (left), schematics of silicon based FET [57]

In the family of transistors, there exist Field-Effect Transistors (FETs) which consist of three metallic conducting electrodes: Source (S), Drain (D) and Gate (G), and a thin solid insulating layer. Based on the location of the Gate electrodes, FETs can display either top-gate or bottom-gate architecture (cf. Figure 1.16). Similarly, the location of the Source and Drain electrodes classifies the architecture of the device in two main configurations: top Source-Drain contacts (top-contacts) and bottom Source-Drain contacts (bottom-contacts). However, widely bottom Source and Drain contacts are used in the FET fabrication. In addition, FET is a unipolar transistor that involves a single-carrier-type operation (either electrons or holes) based on the semiconductor used. [57]

The operation of the field-effect transistors implies the use of electric field to control the flow of current. The voltage applied at the Gate modifies the charge carrier density in the semiconductor

layer, where the semiconductor thin film acts like a conducting channel for the charges between the Source and Drain. [57]

Research in organic chemistry, synthesizing of conducting polymers and other small molecule crystalline materials lead to the development of Organic Field-Effect Transistor (OFETs) by Tsumura et.al in 1986. OFETs adopt the same configuration and the working mechanism of FETs but using an organic semiconducting material for the conduction path.

Organic semiconductors (OSC) which have been commonly used are: terthiophene and α-sexithiophene, P3HT (Poly (3-hexylthiophene)), Perlyene derivatives, Pentacene and TIPS-Pentacene(6,13-Bis(triisopropylsilylethynyl)Pentacene**)** [58]. In OFETs, electron donating organic semiconductors involving the highest occupied molecular orbital (HOMO) level are good candidates for p-type semiconductors, while electron- accepting ones with low HOMO levels are used as an n-type semiconductor.

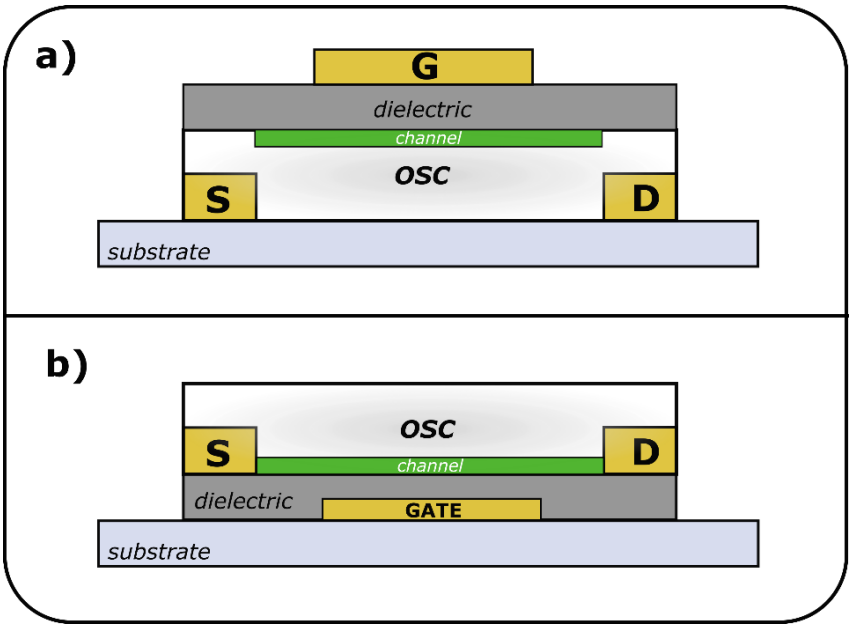

Figure 1.16: Configurations of FET: a) bottom-contacts with top gate electrode, b) bottom-gate contact with top Source-Drain electrodes [59]

Like in Field-effect transistors, the OFETs have also a solid insulating layer with capacitance (C). This insulating layer (dielectric) separates the gate from the semiconductor. The dielectrics, which can be used, are oxides, polymers, and self-assembled monolayers. When the gate is negatively polarized, for the p-type semiconductor, the free holes in the semiconducting channel are shifted towards the dielectric-semiconductor interface to compensate for an equivalent negative charge at the gate-dielectric interface (cf. Figure 1.17a). Then, the negative potential is applied between the Source and Drain, the holes are injected from Source and the current flows inside the channel.

OFET has been successfully fabricated and used as a high-performance sensing device, yet has some disadvantages like the biasing voltages applied to operate the OFETs are generally 10V or higher, which does not allow for operation in. In order to overcome these disadvantages, a door opened to the liquid world during the last decade by using a liquid dielectric medium instead of solid dielectrics. The resulting architecture was called Electrolyte-Gated Organic Field-Effect transistors. [58, 60]

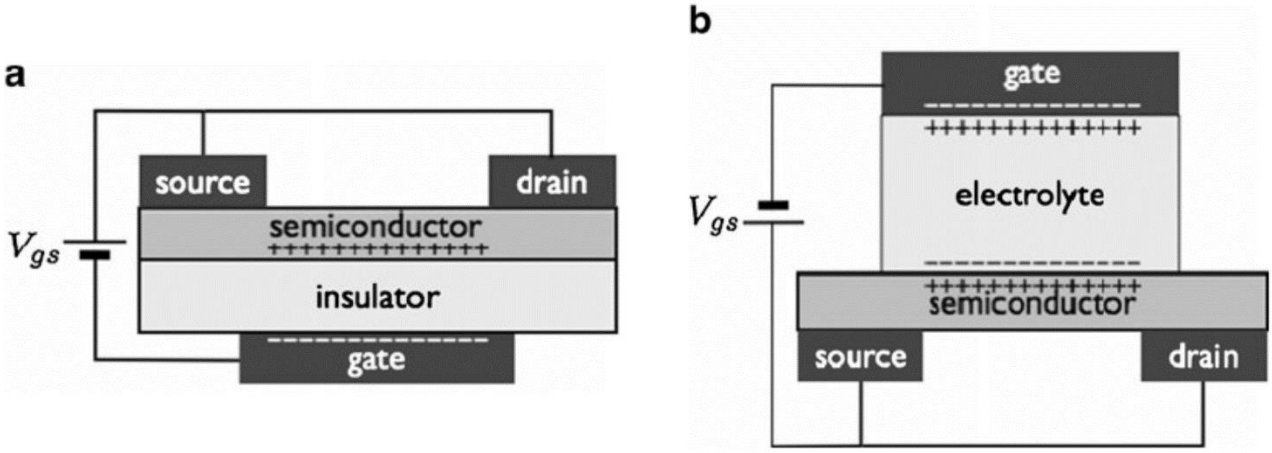

Figure 1.17: a) Organic field effect transistor working in air environment, b) Electrolyte gated organic field effect transistor, working with liquid medium [61]

EGOFET is a good alternative to conventional OFET, because in OFETs a solid dielectric (SiO_2 or PMMA (Poly (methyl methacrylate)) has been used, whereas in EGOFET an electrolyte (liquid) dielectric medium (for example, PBS buffer) was employed. This results in much higher capacitance ($\approx 10^1$-10^2 µF/cm^2) and low biasing voltage properties (< 1V). These two properties

are important for biosensing. Since the device is operating in a liquid environment, it is now possible for the biomolecules to bind with the respective bio receptors. [59, 62–70]

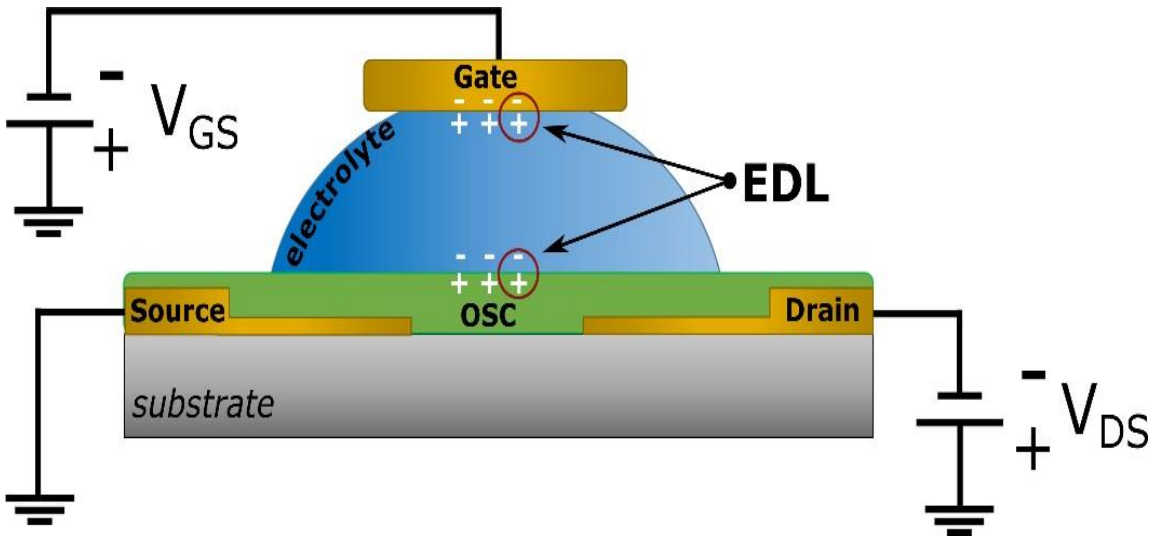

Figure 1.18: Schematics of EGOFET with formation of Electrical Double Layer at the interface between OSC and electrolyte and between electrolyte and gate electrode [59]

In order to turn ON the device (start the conduction), a negative gate potential has to be applied because the conducting channel is made of p-type semiconductor (Holes as a majority charge carriers) [61]

Once the negative potential is applied between Gate and Source electrodes, the excess of electrons at the gate electrode surface produces the accumulation of cations at the Gate-electrolyte interface. Whereas, the accumulation of anions at the electrolyte-semiconductor interface produces the accumulation of the holes at the topmost layer of the semiconductor (cf. Figure 1.18), modulating the hole transport inside the semiconductor channel. [61, 71, 72]

The interface layer at the electrolyte-gate and electrolyte-semiconductor material boundaries account for the formation of an Electrical Double Layer (EDL), which is responsible for the modulation of output current (I_{DS}) of the device. EDL is very sensitive to interfacial changes. In a very simplistic model, it is composed of two layers (cf. Figure 1.19), Helmholtz layer (HL) and

Diffusion layer (DL). Helmholtz layer is composed of ions arranged in a monolayer and Diffusion layer is set as a region of highly concentrated ions (cations and anions), based on the potentials applied to the gate. The concentration of ions in the Diffusion layer decreases with respect to the increase in distance from the interface. The region where the EDL forms look like a parallel plate capacitor having a thin layer of dielectric polarized solvent molecules separating them. The thickness of the EDL is in the range of thesub-nanometer (nm) length scale. Therefore, the capacitance is higher at the EDL due to the small distance between the charged layers. The energy storing capacity in terms of dielectric polarization results in a locally high internal field at the interface and the field stays constant in the bulk resulting in very low capacitance (due to the increase of distance). Potential < 1V is sufficient to produce a high field at the interface. When the device is been operated in the linear regime (V_{DS}=-0.2V), the output current produced is the amplified form of the capacitance value at the interface. The output current changes when the capacitance changes with respect to the interfacial changes with the target analyte. [61, 71]

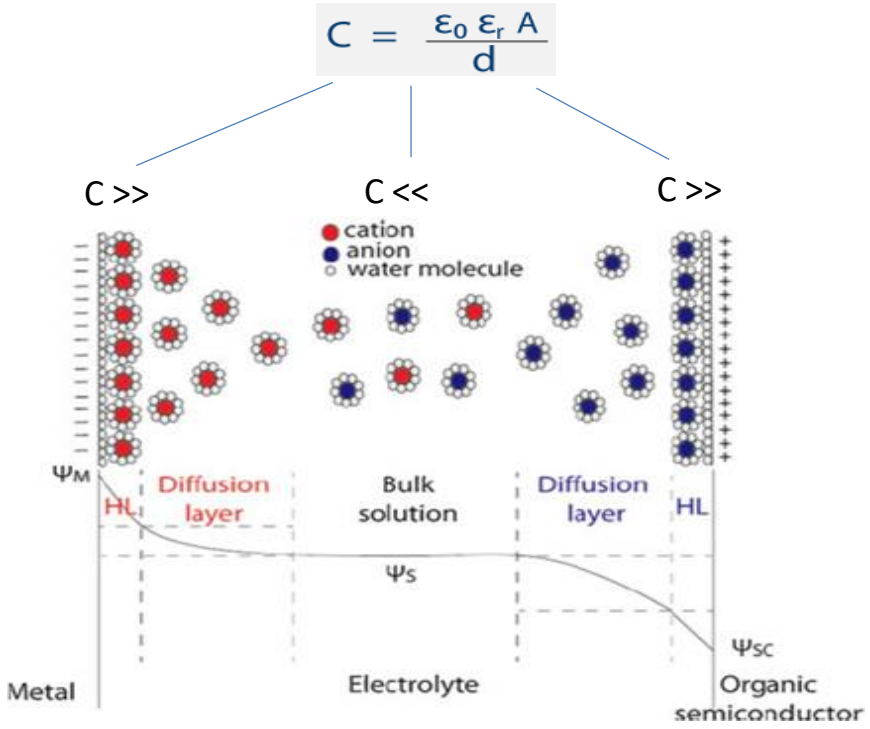

Figure 1.19: Ion distribution across the EDL and potential drop inside the electrolyte solution. [61]

Since the current measured at the S-D terminals of the transistor is highly non-linear, the I_{DS} is traditionally parametrized as in the following expressions for the two regimes of the output curve (see Figure 1.20):

$I_{DS} = W/L\ \mu\ C\ (V_{GS}-V_{Th}-V_{DS}/2)V_{DS}$, for $|V_{DS}| << |V_{GS}-V_{Th}|$ (Linear Regime)

$I_{DS} = W/2L\ \mu\ C\ (V_{GS}-V_{Th})^2$, for $|V_{DS}| >> |V_{GS}-V_{Th}|$ (Saturation Regime)…… (1)

Equation 1: Characteristic OFET equations for Linear and Saturation regimes

EGOFET device can be operated in two regimes, linear regime and Saturation regime (cf. Equation 1), in which the W and L are the width and length of the channel, while C is the capacitance of the insulating layer. By recording electrical characteristics of these devices, parameters such as μ (carrier mobility in the channel specific to the semiconductor) and V_{th}(threshold voltage representing the minimum voltage necessary to turn on the device) can be extracted and used as figures of merit, while performing sensing [73, 74].

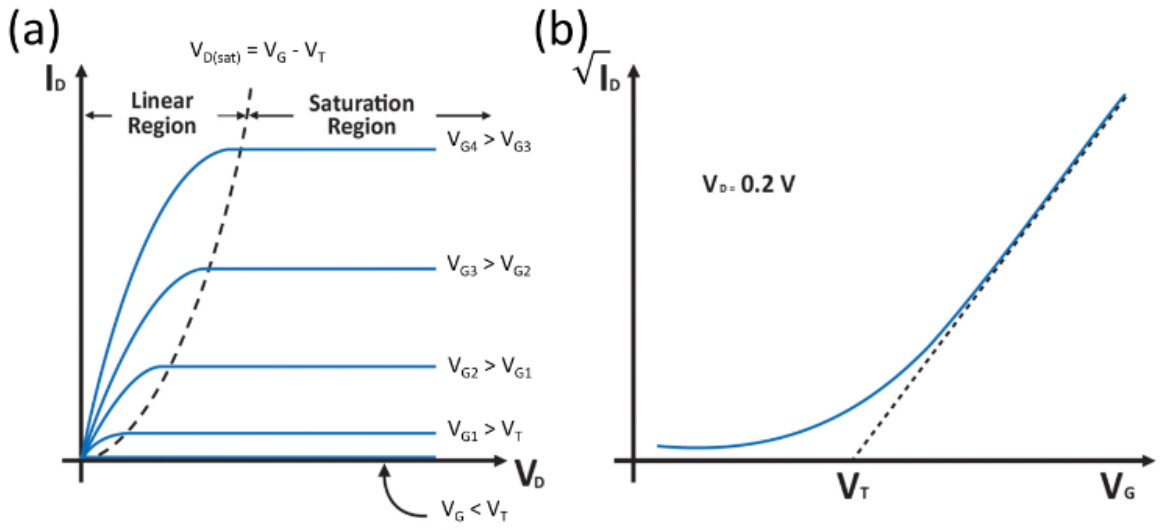

Figure 1.20: a) Output and (b) transfer curves of a generic n-type transistor [75]

The best operative conditions to perform biosensing stay near the linear regime because, at the state where the device starts conducting, dI_{DS}/dV_{DS} is maximum, whereas at the saturation regime the conducting path is completely filled with the charge carrier and reaches the saturation. The

state of reaching the saturation in the channel is called the pinch-off state (where the device acts like an OFF switch) and the voltage where the pinch off will happen is V_T.

EGOFET biosensors have been designed and prototyped recently in a number of different architectures by organic electronics research groups. I report in the following chapter some examples related to protein and nucleic acid specific biorecognition elements.

The detection of enzyme activity was achieved fabricating EGOFET with channel made with (α-sexithiophene) (α6T) [76]. The bioreceptor (penicillinase enzyme) was immobilized on the semiconductor surface and the target penicillin was detected with the limit of detection about 5µM, through the acid-base titration (cf. Figure 1.22). In this case, the field-effect transistor mobility stated was $4*10^{-2}cm^2V^{-1}S^{-1}$, with the on/off ratio between 10^2 and 10^3. at V_{DS} = -50mV

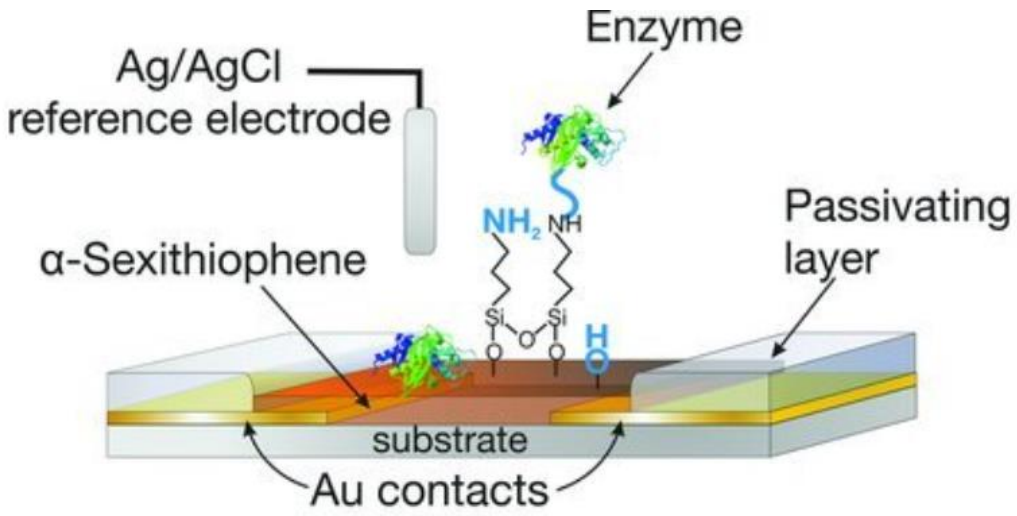

Figure 1.21: Schematics of α-sexithiophene based EGOFET with biorecognition element anchored on the semiconductor [76]

Poly(3-hexylthiophene) (P3HT) based EGOFET device was used for DNA detection using phosphate buffer saline (PBS, pH 7.2) solution as the dielectric medium and the device was operated below 1V. The ODN (oligonucleotide) probe modified at one end with the carboxylic acid (-COOH) group was covalently grafted upon the P3HT semiconducting layer. Platinum (Pt

wire) was used as a gate electrode and the sensing was performed at the semiconductor layer. DNA hybridization with 100nM concentration, the gate voltage was shifted between 40 to 60mV in the negative values which attribute to the negative charges carried by the DNA backbones. The importance of Debye length which could screen negative charges of the DNA can be analyzed with other experiments by using buffers having various ionic strengths [77].

Another interesting example of P3HT based EGOFET biosensor was developed for the protein (streptavidin) detection. Here, the semiconducting channel was created using a copolymer of P3HT, P3HT- COOH and biotinylated P3HT acting as an active sensing platform (cf. Figure 1.23). The -COOH group prevents or reduces a non-specific interaction and also, it can be further reduced by pre-treating the polymer surfaces with 1-octanol. The non- covalent interactions of the C8 alkyl chain (from 1-Octanol) with P3HT reduces furthermore non- specific interactions. As a proof-of-concept, biotin-streptavidin couples were used due to their very low dissociation constant. The transfer curve shows, no effect on human serum albumin exposure, whereas the Drain-Source current decreases due to streptavidin exposure [78].

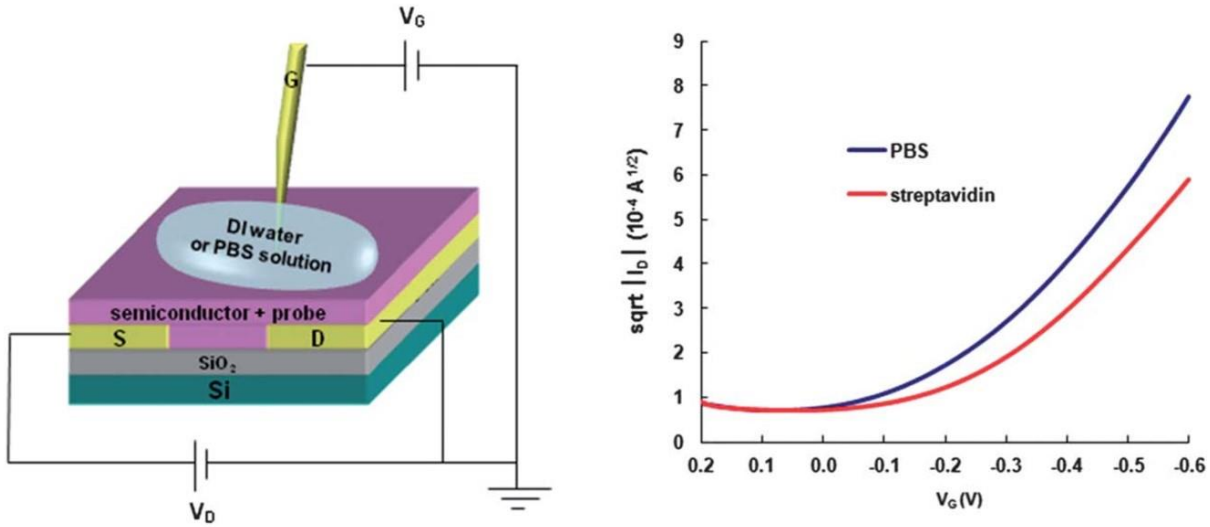

Figure 1.22: Schematics of P3HT based EGOFET biosensor was developed for the protein (streptavidin) detection [78]

EGOFET device transduction mechanism was investigated with respect to the sensitivity of the device as a function of Debye's length, receptor charge and the distance where the binding event takes place. Experiments were performed using phospholipid film with biotin/avidin and antigen/antibody interactions (C-reactive protein (CRP) and anti- CRP, respectively) which were immobilized on the semiconductor layer. It has been shown that the CRP was successfully detected, at the binding events which occurred at the distance that is 30 times of the Debye's length value obtained from the transistor semiconducting channel (cf. Figure 1.23). Also, the performance of the device was better towards high concentration of salts and the response obtained was due to the capacitive changes (Donnan's equilibria was formed within the protein layer, which leads to an additional capacitance (C_{DON})) at the electrolyte/semiconductor interface rather than the electrostatic effect of the charges carried by the target molecules [79].

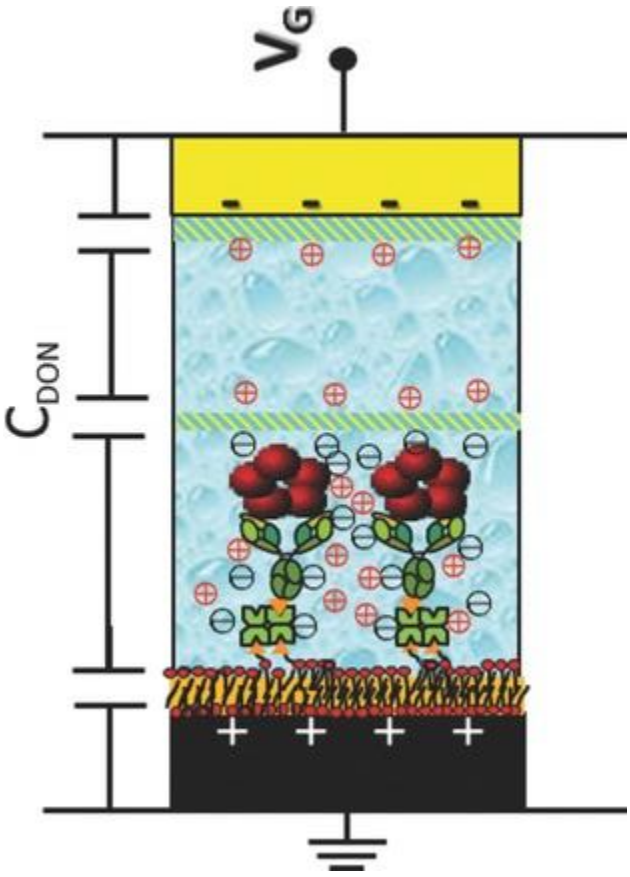

Figure 1.23: Schematic of the charge arrangements in a PL/SA/Ab/CRP multilayer. The striped regions denote the locations of the ionic double layers. The equivalent circuit of the capacitances involved is also shown [79].

Phospholipid bilayer thin film on top of the semiconductor layer became promising to avoid the penetration of ions from the electrolyte to OSC surface even at high ionic strength. This non-covalent approach led to EGOFET biocompatibility with no bio-probe immobilization in or onto the phospholipid bilayer. The development of biotin-labeled phospholipids for the streptavidin bindings with the LOD of 10 nM (cf. **Error! Reference source not found.**). The sensing effect is t he result of capacitive changes at the phospholipid bilayer together involving the charge carrier of streptavidin. This opened a way for the immunosensors, because of the promising feature of a phospholipid bilayer that can be virtually functionalized with any bioreceptors. In this case, streptavidin modifies the capture antibodies for heterogeneous ELISA immunoassay [80].

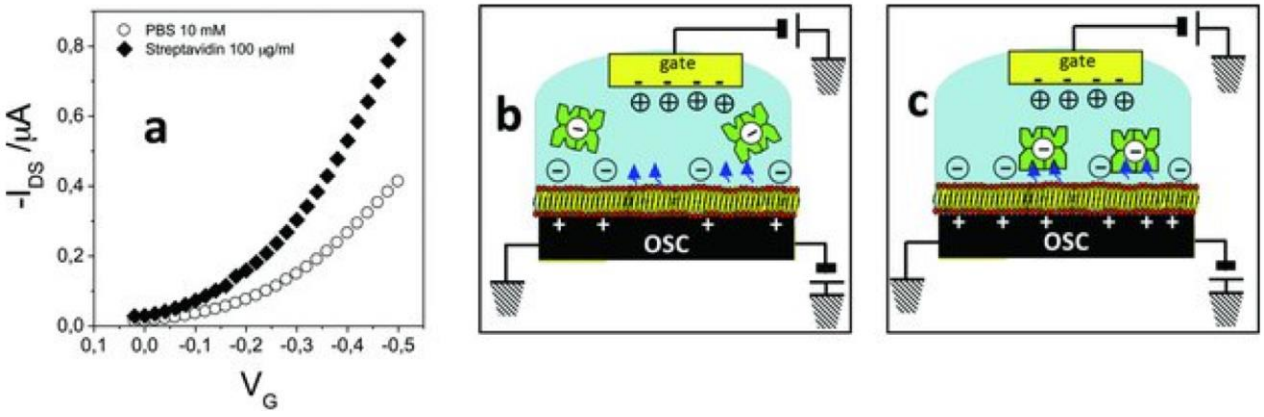

Figure 1.24: (a) Transfer characteristics of the biotin-functionalized phospholipid bilayer-EGOFET in PBS, pH 7.4 (open symbols) and streptavidin (full symbols) solutions. (b,c) Diagram for the rationale leading to the I_{DS} current increase [80].

EGOFET biosensing with gate functionalization plays a significant role in the detection of dopamine. Gate electrode (Au) acts as a sensing area instead of the semiconductor layer (cf. **Error! R eference source not found.**). Gate electrode was functionalized with a self-assembled monolayer of cysteamine and 4-formylphenyl boronic acids. Here, the transduction mechanism occurs with the modulation of capacitive changes of the electrical double layer formed at the Gate/electrolyte

interface. The transfer curve changes, upon the binding of the dopamine with boronic acid, also the work function of the gold electrode changes together with the gate capacitance changes [68].

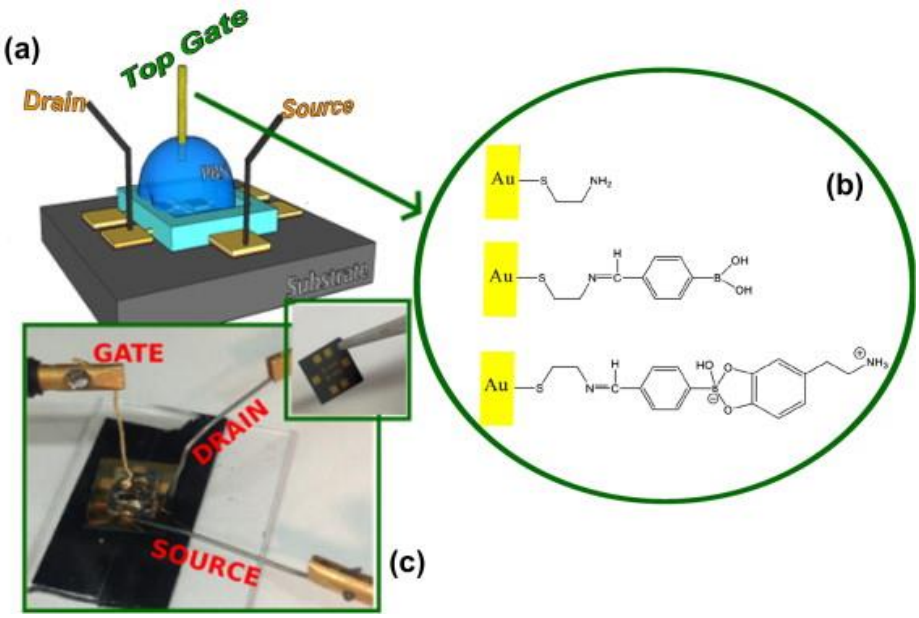

Figure 1.25: (a) Schematic picture of the test pattern integrated with a poly(dimethylsiloxane) pool for confining a droplet of phosphate buffer solution (PBS). (b) The SAM steps are (1) cysteamine, (2) 4-formylphenyl boronic acid and (3) dopamine. (c) picture of the device [68].

Another example for EGOFET sensing, based on gate functionalization technique is the detection of Interleukin (IL)-6 which is a multifunctional cytokine. (IL)-6 are small proteins and their increased levels are linked with infections, cancer and inflammation. It has been reported that two different bioreceptors such as monoclonal antibodies and peptide aptamers can be used to obtain label-free detection of protein (IL-6) (cf. Figure 1.26). Both the strategies were employed with two different EGOFETs and the results were compared. Antibodies were functionalized on the gate surface of one EGOFET biosensor and aptamer (Affimer^{TM}) was functionalized on the gate surface of the second EGOFET biosensor. When two EGOFET biosensor results were compared, where both leads to the limit of detection about 1 pM concentration of IL-6 [81].

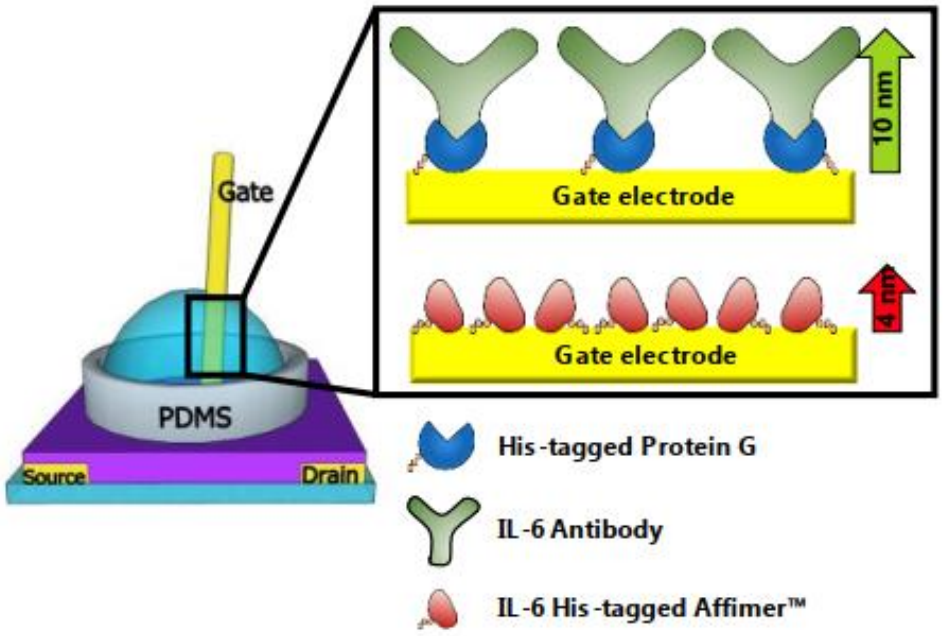

Figure 1.26: Schematic experimental setup in which are highlighted Source, Drain and Gate electrodes, the PDMS pool, the organic semiconductor layer on the quartz substrate and the electrolyte (left) and the two gate functionalization strategies (right): IL-6 Antibodies are immobilized on the gate surface through His-tagged Protein G, while anti-IL-6 Affimers are directly immobilized on the gold surface by means of the His-tag [81].

Using Pentacene semiconductor based EGOFET device, an article was reported for the label free detection of (TNF α) which is an inflammatory cytokine. TNF α – Antibody was immobilized on the gate surface using His-tag protein G. The target analyte Tumor Necrosis Factor (TNF α) was detected with the limit of detection of 100pM (cf. Figure 1.27). High selectivity of the target analyte was achieved, when the detection was performed in PBS solutions containing different concentrations of Bovine Serum Albumin (BSA) [82].

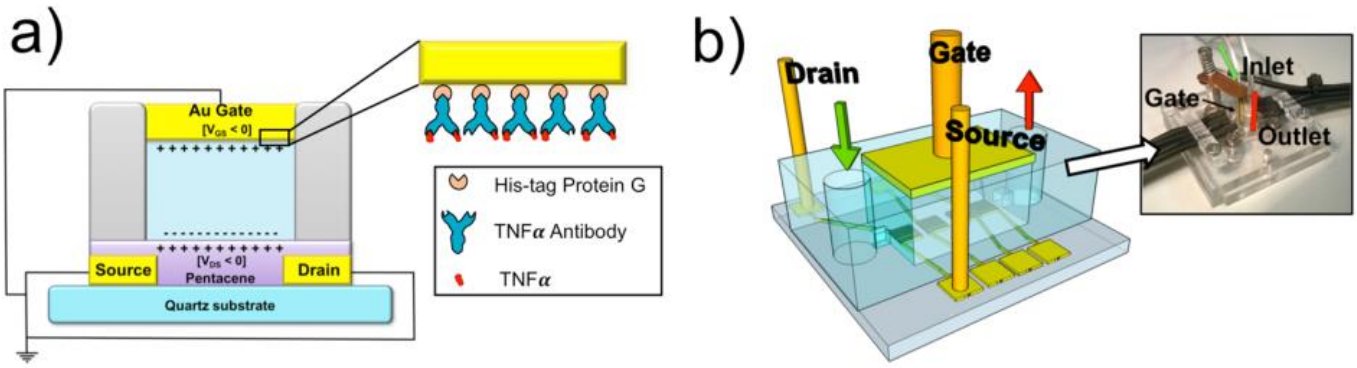

Figure 1.27: (a) Schematics of the EGOFET device with a zoom of the functionalized gate. (b) Schematic drawing of the microfluidics and a photo of the experimental setup comprising the electrical connections and fluidic inlets [82].

Single molecule with a large transistor (SiMoT) platform based on electrolyte gated organic field effect transistors was employed in order to detect the genomic biomarker for multiple sclerosis (miR-182). A label-free and LOD as single molecule detection was achieved (cf. Figure 1.28). Biotinylated oligonucleotides were used as a biorecognition elements at the gate surface and an organic semiconductor used as pentacene, in order to create the conducting channel [83].

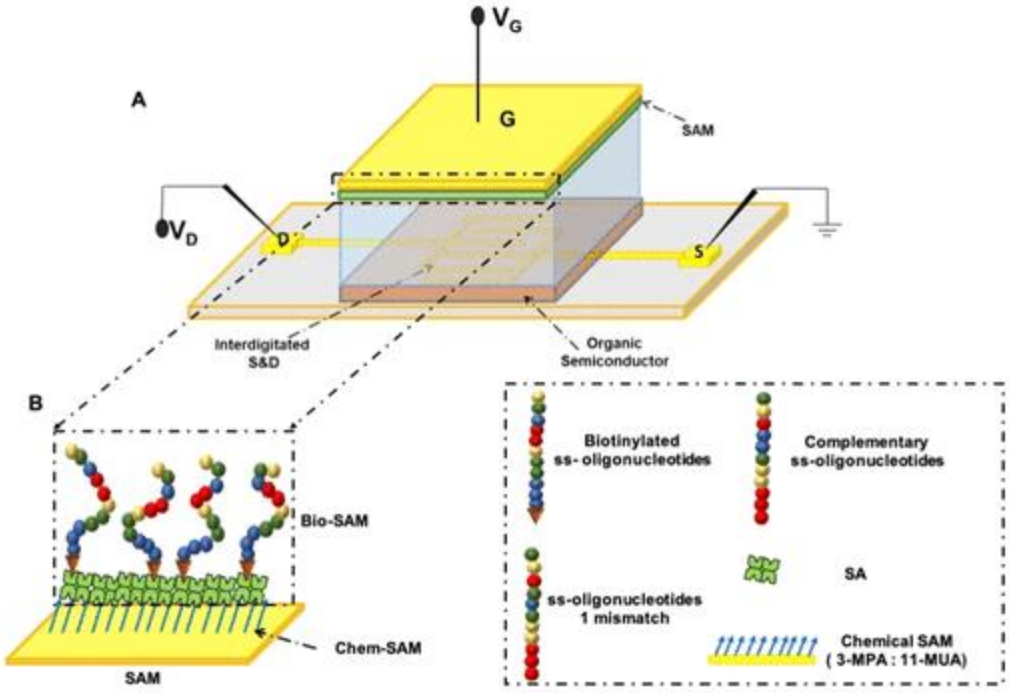

Figure 1.28: (A) Three-dimensional schematic representation of the SiMoT device. (B) Schematic representation of the gate surface biofunctionalized with a biotinylated single-strand oligonucleotide. Chem-SAM is depicted by blue arrows, and the structures of bio-SAM and target oligonucleotides (miR-182-5p) are sketched in the right panel [83].

1.8 Aim of the thesis

Glioblastoma (GBM) are a range of devastating and progressive brain tumors affecting around 25,000 people each year in Europe and responsible for the majority of deaths from primary brain tumors. My PhD dissertation aims at developing biosensors based on EGOFETs and integrated microfluidic devices, in order to detect GBM related biomarkers with high sensitivity and selectivity.

I adapted protocols reported in literature for a specific class of glioblastoma related biomarkers represented by miRNAs, in particular strands derived from the main stem of human miRNA-21. The transduction mechanism provides high sensitivity to hybridization reactions between probe and target sequences happening on the Gate electrolyte interface for oligonucleotide biosensor the probe sequence can be immobilized on the gold Gate surface, by means of thiol derivative

termination. High capacitance changes and low biasing voltages make EGOFETs ideal candidates for the next generation of biosensors, together with the integration of microfluidic devices. These objectives constitute the aim of the Marie Sklodowska Curie Action AiPBAND **"An integrated platform for developing brain cancer diagnostic techniques"**, in which I was involved as Early Stage Researcher

In Chapter 2 the Material and Methods are reported to highlight the design and fabrication protocols for a simple, low-cost and portable EGOFET on a flexible Kapton substrate metallized with gold. The laser ablation process of interdigitated electrodes geometry was carefully tested because it represents the enabling technology to easily fabricate geometries with different W/L ratios on a range of polymeric substrates. The 3D printing modelling was also equally assessed to integrate external Gate electrodes functionalized with different biorecognition moieties or to prepare master structures for microfluidic elastomeric devices. Then in Chapter 3, I discuss about the characterization techniques employed to assess the electrical performance of the organic transistors, as well as the physical-chemical properties of their components. In particular the interdigitated electrodes and the semiconductor thin film were characterized by atomic force microscopy to understand the important morphology features and discard the low performing samples. Electrochemistry methods were used to investigate the reproducibility of the functionalization protocol with oligonucleotide probes and self-assembled monolayers. In Chapter 4, different prototypes of EGOFET with the integration of PDMS based microfluidic device are reported, focusing on the effect of diffusion in solution streams across the microfluidic compartments. I investigated the geometry of the fluidic channels aligned on top of the transistor semiconductor channel and separated from the corresponding fluidic chamber coupled with the Gate, in particular addressing the diffusion of α-synuclein with respect to I-V recording time requirements. Similar microfluidic structures were assessed also for functionalization of electrodes in parallel, aiming at demonstrating an application for multiple biomarkers sensing.

Finally in Chapter 5, I present the experimental results on miRNA-21 sensing by analyzing the transfer curves and parameters of biosensors working with different concentrations of the analyte. The data collected were quantitatively analyzed, in order to evaluate the limit of detection of the biosensor with statistical confidence. In order to study the bio recognition events and extract the kinetic constant for validation of the results, a new reactions model has been proposed to analyse

the dose curves of the EGOFET biosensor. Finally, the molar electrostatic free energy upon hybridization (ΔG_e) was compared to the output of hybridization modelling algorithm, although developed for reaction happening in solution.

1.9 References

[1] Mehrotra P. Biosensors and their applications – A review. J Oral Biol Craniofac Res 2016; 6(2):153–59.

[2] Hughes WS. THE POTENTIAL DIFFERENCE BETWEEN GLASS AND ELECTROLYTES IN CONTACT WITH THE GLASS. J Am Chem Soc American Chemical Society 1922; 44(12):2860–67.

[3] Clark LC, Wolf R, Granger D, et al. Continuous recording of blood oxygen tensions by polarography. J Appl Physiol 1953; 6(3):189–93.

[4] Gao N, Gao T, Yang X, et al. Specific detection of biomolecules in physiological solutions using graphene transistor biosensors. PNAS National Academy of Sciences 2016; 113(51):14633–38.

[5] Freitag R. Applied biosensors. Current Opinion in Biotechnology 1993; 4(1):75–79.

[6] Atanasov P, Wilkins E. Biosensor for continuos glucose monitoring. Biotechnology and Bioengineering 1994; 43(3):262–66.

[7] Cuzick J, Babiker AG. Pancreatic cancer, alcohol, diabetes mellitus and gall-bladder disease. International Journal of Cancer 1989; 43(3):415–21.

[8] Meir EGV, Hadjipanayis CG, Norden AD, et al. Exciting New Advances in Neuro-Oncology: The Avenue to a Cure for Malignant Glioma. CA: A Cancer Journal for Clinicians 2010; 60(3):166–93.

[9] Holland EC. Glioblastoma multiforme: The terminator. Proc Natl Acad Sci USA 2000; 97(12):6242.

[10] Senders JT, Staples P, Mehrtash A, et al. An Online Calculator for the Prediction of Survival in Glioblastoma Patients Using Classical Statistics and Machine Learning. Neurosurgery Oxford Academic 2020; 86(2):E184–92.

[11] Brain cells | The Brain Tumor Charity [cited 2020]. Available at: https://www.thebraintumorcharity.org/brain-tumor-diagnosis-treatment/how-brain-tumors-are-diagnosed/brain-tumor-biology/brain-cells/.

[12] Lum DJ, Halliday W, Watson M, et al. Cortical ependymoma or monomorphous angiocentric glioma? Neuropathology 2008; 28(1):81–86.

[13] Jiang Y, Boije M, Westermark B, et al. PDGF-B Can Sustain Self-renewal and Tumorigenicity of Experimental Glioma-Derived Cancer-Initiating Cells by Preventing Oligodendrocyte Differentiation. Neoplasia 2011; 13(6):492-IN1.

[14] Ernest NJ, Sontheimer H. Glioma☆. In: Reference Module in Biomedical Sciences Elsevier 2015;

[15] Alix-Panabières C, Pantel K. Circulating Tumor Cells: Liquid Biopsy of Cancer. Clin Chem Oxford Academic 2013; 59(1):110–18.

[16] Tsermoulas G, Mukerji N, Borah AJ, et al. Factors affecting diagnostic yield in needle biopsy for brain lesions. British Journal of Neurosurgery Taylor & Francis 2013; 27(2):207–11.

[17] Cappabianca P, Cinalli G, Gangemi M, et al. APPLICATION OF NEUROENDOSCOPY TO INTRAVENTRICULAR LESIONS. Neurosurgery Oxford Academic 2008; 62(suppl_2):SHC575–98.

[18] Markwardt N, Berg A von, Fiedler S, et al. Optical spectroscopy for stereotactic biopsy of brain tumors. Medical Laser Applications and Laser-Tissue Interactions VII 2015[Online] International Society for Optics and Photonics 2015.

[19] Crowley E, Di Nicolantonio F, Loupakis F, et al. Liquid biopsy: monitoring cancer-genetics in the blood. Nature Reviews Clinical Oncology Nature Publishing Group 2013; 10(8):472–84.

[20] Wit S de, Dalum G van, Terstappen LWMM. Detection of Circulating Tumor Cells. Scientifica (Cairo) 2014; 2014.

[21] Yang C, Xia B-R, Jin W-L, et al. Circulating tumor cells in precision oncology: clinical applications in liquid biopsy and 3D organoid model. Cancer Cell International 2019; 19(1):341.

[22] Centrifugation Of Blood Diagram. Freepik 2018[Online] 2018 [cited 2020]. Available at: https://www.freepik.com/premium-vector/centrifugation-blood-diagram_3459696.htm.

[23] Rosenberg R, Gertler R, Friederichs J, et al. Comparison of two density gradient centrifugation systems for the enrichment of disseminated tumor cells in blood. Cytometry 2002; 49(4):150–58.

[24] Guiochon G. Monolithic columns in high-performance liquid chromatography. Journal of Chromatography A 2007; 1168(1):101–68.

[25] Tamaoka J, Katayama-Fujimura Y, Kuraishi H. Analysis of bacterial menaquinone mixtures by high performance liquid chromatography. Journal of Applied Bacteriology 1983; 54(1):31–36.

[26] Saenz-Antoñanzas A, Auzmendi-Iriarte J, Carrasco-Garcia E, et al. Liquid Biopsy in Glioblastoma: Opportunities, Applications and Challenges. Cancers Multidisciplinary Digital Publishing Institute 2019; 11(7):950.

[27] Linde ME van, Mijn JC van der, Pham TV, et al. Evaluation of potential circulating biomarkers for prediction of response to chemoradiation in patients with glioblastoma. J Neurooncol 2016; 129(2):221–30.

[28] Best MG, Sol N, Kooi I, et al. RNA-Seq of Tumor-Educated Platelets Enables Blood-Based Pan-Cancer, Multiclass, and Molecular Pathway Cancer Diagnostics. Cancer Cell Elsevier 2015; 28(5):666–76.

[29] Shin VY, Siu JM, Cheuk I, et al. Circulating cell-free miRNAs as biomarker for triple-negative breast cancer. British Journal of Cancer Nature Publishing Group 2015; 112(11):1751–59.

[30] Andersen GB, Tost J. Circulating miRNAs as Biomarker in Cancer. In: Schaffner F, Merlin J-L, Bubnoff N von, Eds. Tumor Liquid Biopsies Springer International Publishing: Cham 2020; pp. 277–98.

[31] Feng Y-H, Tsao C-J. Emerging role of microRNA-21 in cancer (Review). Biomedical Reports Spandidos Publications 2016; 5(4):395–402.

[32] Santangelo A, Tamanini A, Cabrini G, et al. Circulating microRNAs as emerging non-invasive biomarkers for gliomas. Ann Transl Med 2017; 5(13).

[33] Yang CH, Yue J, Pfeffer SR, et al. MicroRNA-21 Promotes Glioblastoma Tumorigenesis by Down-regulating Insulin-like Growth Factor-binding Protein-3 (IGFBP3). J Biol Chem American Society for Biochemistry and Molecular Biology 2014; 289(36):25079–87.

[34] Baldassarre A, Mucci N, Lecca LI, et al. Biosensors in Occupational Safety and Health Management: A Narrative Review. International Journal of Environmental Research and Public Health 2020; 17(7).

[35] Piccolino M. Luigi Galvani's path to animal electricity. Comptes Rendus Biologies 2006; 329(5):303–18.

[36] Piccolino M. Visual Images in Luigi Galvani's Path to Animal Electricity. Journal of the History of the Neurosciences Routledge 2008; 17(3):335–48.

[37] Lai A. The Experiment That Shocked the World | Helix Magazine. 2017[Online] 2017 [cited 2020]. Available at: https://www.helix.northwestern.edu/article/experiment-shocked-world.

[38] DiFrancesco D. Pacemaker Mechanisms in Cardiac Tissue. Annu Rev Physiol Annual Reviews 1993; 55(1):455–72.

[39] Ouyang H, Liu Z, Li N, et al. Symbiotic cardiac pacemaker. Nature Communications Nature Publishing Group 2019; 10(1):1821.

[40] Arzuaga P. Cardiac pacemakers: past, present and future. IEEE Instrumentation Measurement Magazine 2014; 17(3):21–27.

[41] Irisawa H. Comparative physiology of the cardiac pacemaker mechanism. Physiological Reviews American Physiological Society 1978; 58(2):461–98.

[42] Araki Y, Nomura M, Tanaka H, et al. MRI of the brain in diabetes mellitus. Neuroradiology 1994; 36(2):101–03.

[43] Foulds NC, Lowe CR. Enzyme entrapment in electrically conducting polymers. Immobilisation of glucose oxidase in polypyrrole and its application in amperometric glucose sensors. J Chem Soc, Faraday Trans 1 The Royal Society of Chemistry 1986; 82(4):1259–64.

[44] Bogue R. Developments in biosensors – where are tomorrow's markets? Sensor Review Emerald Group Publishing Limited 2005; 25(3):180–84.

[45] Ghasemi-Varnamkhasti M, Apetrei C, Lozano J, et al. Potential use of electronic noses, electronic tongues and biosensors as multisensor systems for spoilage examination in foods. Trends in Food Science & Technology 2018; 80:71–92.

[46] Kim J, Campbell AS, Ávila BE-F de, et al. Wearable biosensors for healthcare monitoring. Nature Biotechnology Nature Publishing Group 2019; 37(4):389–406.

[47] Chung M, Fortunato G, Radacsi N. Wearable flexible sweat sensors for healthcare monitoring: a review. Journal of The Royal Society Interface Royal Society 2019; 16(159):20190217.

[48] Rasmussen SC. The Early History of Polyaniline: Discovery and Origins. Substania 2017; 1(2):99–109.

[49] Rasmussen SC. Conjugated and Conducting Organic Polymers: The First 150 Years. ChemPlusChem 2020; 85(7):1412–29.

[50] Simonet J, Rault-Berthelot J. Electrochemistry: A technique to form, to modify and to characterize organic conducting polymers. Progress in Solid State Chemistry 1991; 21(1):1–48.

[51] Guo F, Karl A, Xue Q-F, et al. The fabrication of color-tunable organic light-emitting diode displays via solution processing. Light: Science & Applications Nature Publishing Group 2017; 6(11):e17094–e17094.

[52] Geffroy B, Roy P le, Prat C. Organic light-emitting diode (OLED) technology: materials, devices and display technologies. Polymer International 2006; 55(6):572–82.

[53] Simon DT, Gabrielsson EO, Tybrandt K, et al. Organic Bioelectronics: Bridging the Signaling Gap between Biology and Technology. Chem Rev American Chemical Society 2016; 116(21):13009–41.

[54] Lu B, Yuk H, Lin S, et al. Pure PEDOT:PSS hydrogels. Nature Communications Nature Publishing Group 2019; 10(1):1043.

[55] Liu H, Zhao T, Jiang W, et al. Flexible Battery-Less Bioelectronic Implants: Wireless Powering and Manipulation by Near-Infrared Light. Advanced Functional Materials 2015; 25(45):7071–79.

[56] Richter-Dahlfors A, Berggren M. Organic Bioelectronics. In: Bhushan B, Ed. Encyclopedia of Nanotechnology Springer Netherlands: Dordrecht 2012; pp. 2014–22.

[57] Obite F, Ijeomah G, Bassi JS. Carbon nanotube field effect transistors: toward future nanoscale electronics. International Journal of Computers and Applications Taylor & Francis 2019; 41(2):149–64.

[58] Stewart Z. Organic Thin-Film Transistors and TIPS-Pentacene. Lewis Honors College Capstone Collection 2013; 11.

[59] Parkula V. Organic Electronic Transistors for Biosensing. 2019[Online] [Ph.D dissertation] Università degli Studi di Modena e Reggio Emilia: Modena 2019.

[60] Kim SH, Hong K, Xie W, et al. Electrolyte-Gated Transistors for Organic and Printed Electronics. Advanced Materials 2013; 25(13):1822–46.

[61] Wang D, Noël V, Piro B. Electrolytic Gated Organic Field-Effect Transistors for Application in Biosensors—A Review. Electronics Multidisciplinary Digital Publishing Institute 2016; 5(1):9.

[62] Klauk H, Zschieschang U, Pflaum J, et al. Ultralow-power organic complementary circuits. Nature Nature Publishing Group 2007; 445(7129):745–48.

[63] Meijer EJ, Leeuw DM de, Setayesh S, et al. Solution-processed ambipolar organic field-effect transistors and inverters. Nature Materials Nature Publishing Group 2003; 2(10):678–82.

[64] Melzer K, Brändlein M, Popescu B, et al. Characterization and simulation of electrolyte-gated organic field-effect transistors. Faraday Discuss The Royal Society of Chemistry 2014; 174(0):399–411.

[65] Di Lauro M, Casalini S, Berto M, et al. The Substrate is a pH-Controlled Second Gate of Electrolyte-Gated Organic Field-Effect Transistor. ACS Appl Mater Interfaces American Chemical Society 2016; 8(46):31783–90.

[66] Cramer T, Kyndiah A, Murgia M, et al. Double layer capacitance measured by organic field effect transistor operated in water. Appl Phys Lett American Institute of Physics 2012; 100(14):143302.

[67] Borges-González J, Kousseff CJ, Nielsen CB. Organic semiconductors for biological sensing. J Mater Chem C The Royal Society of Chemistry 2019; 7(5):1111–30.

[68] Casalini S, Leonardi F, Cramer T, et al. Organic field-effect transistor for label-free dopamine sensing. Organic Electronics 2013; 14(1):156–63.

[69] Macchia E, Manoli K, Holzer B, et al. Single-molecule detection with a millimetre-sized transistor. Nature Communications Nature Publishing Group 2018; 9(1):3223.

[70] Berto M, Vecchi E, Baiamonte L, et al. Label free detection of plant viruses with organic transistor biosensors. Sensors and Actuators B: Chemical 2019; 281:150–56.

[71] Kergoat L, Herlogsson L, Braga D, et al. A Water-Gate Organic Field-Effect Transistor. Advanced Materials 2010; 22(23):2565–69.

[72] Cardoso AR, Moreira FTC, Fernandes R, et al. Novel and simple electrochemical biosensor monitoring attomolar levels of miRNA-155 in breast cancer. Biosensors and Bioelectronics 2016; 80:621–30.

[73] Kergoat L, Piro B, Berggren M, et al. Advances in organic transistor-based biosensors: from organic electrochemical transistors to electrolyte-gated organic field-effect transistors. Anal Bioanal Chem 2012; 402(5):1813–26.

[74] Mithu M, Fantoni G, Ciampi J. Effect of electrolyte temperature on Faradaic effect in electrochemical microdrilling. International Journal of Precision Technology Inderscience Publishers 2017; 7(1):17–31.

[75] Boratto M. Semiconducting and Insulating oxides applied to electronic devices. 2018[Online] 2018.

[76] Buth F, Donner A, Sachsenhauser M, et al. Biofunctional electrolyte-gated organic field-effect transistors. Adv Mater 2012; 24(33):4511–17.

[77] Kergoat L, Piro B, Berggren M, et al. DNA detection with a water-gated organic field-effect transistor. Organic Electronics Elsevier 2012; 13(1):1–6.

[78] Suspène C, Piro B, Reisberg S, et al. Copolythiophene-based water-gated organic field-effect transistors for biosensing. J Mater Chem B The Royal Society of Chemistry 2013; 1(15):2090–97.

[79] Palazzo G, Tullio DD, Magliulo M, et al. Detection Beyond Debye's Length with an Electrolyte-Gated Organic Field-Effect Transistor. Advanced Materials 2015; 27(5):911–16.

[80] Magliulo M, Mallardi A, Mulla MY, et al. Electrolyte-Gated Organic Field-Effect Transistor Sensors Based on Supported Biotinylated Phospholipid Bilayer. Advanced Materials 2013; 25(14):2090–94.

[81] Diacci C, Berto M, Di Lauro M, et al. Label-free detection of interleukin-6 using electrolyte gated organic field effect transistors. Biointerphases American Vacuum Society 2017; 12(5):05F401.

[82] Berto M, Casalini S, Di Lauro M, et al. Biorecognition in Organic Field Effect Transistors Biosensors: The Role of the Density of States of the Organic Semiconductor. Anal Chem American Chemical Society 2016; 88(24):12330–38.

[83] Macchia E, Manoli K, Di Franco C, et al. Organic Field-Effect Transistor Platform for Label-Free, Single-Molecule Detection of Genomic Biomarkers. ACS Sens American Chemical Society 2020; 5(6):1822–30.

CHAPTER 2

MATERIALS AND FABRICATION

2.1 Introduction

In this chapter the fabrication techniques, materials used and gate functionalization protocols for the detection of [miRNA-21] and α-synuclein will be reported. Experimental details and features will include also Surface plasmon resonance (SPR) and electrochemical setups.

Low cost fabrication of interdigitated Source (S) and Drain (D) electrodes on a flexible Kapton substrate (metallized with Au), which I designed and fabricated inorder to create a EGOFET model has been discussed. Gold (Au) electroplating technique employed to create a multi-gate EGOFET model will be also reported.

In my PhD work, I optimized the volume of organic semiconductor (TIPS-Pentacene) used. Only about 1µl volume of TIPS-Pentacene was drop casted on top of interdigitated S and D electrodes in order to create a fine micro crystalline structure, thus leading to the formation of good conduction channel with high carrier charge mobility which has been reported in the sub chapter 2.2.9

I also developed a simple regeneration process for the interdigitated Source (S) and Drain(D) electrodes, using few amounts of solvents. The cleaning protocol which I developed in my PhD has allowed to reuse the same interdigitated S and D electrodes for multiple experiments without loss of performance. This has been discussed in the final sub chapter of 2.2.10

2.2 Fabrication techniques

2.2.1 Microfabrication using UV photolithographic techniques

The microfabrication process shares common aspects with MEMS (micro electro mechanical systems) device production, since the scope is still oriented towards the study and control of flow dynamics at the microscopic scales.

Besides control of the volume and boundaries, which is usually the target in fluidic analytical devices, the fluidic cell must be sealed on the sensing device, therefore non conformal geometry, roughness and chemistry of the interface are important.

One of the most important microfabrication techniques is UV photolithography (cf. Figure 2.1). In the following, some detail on contact mode photolithography and the fabrication of easily affordable high contrast masks for photolithography is reported.

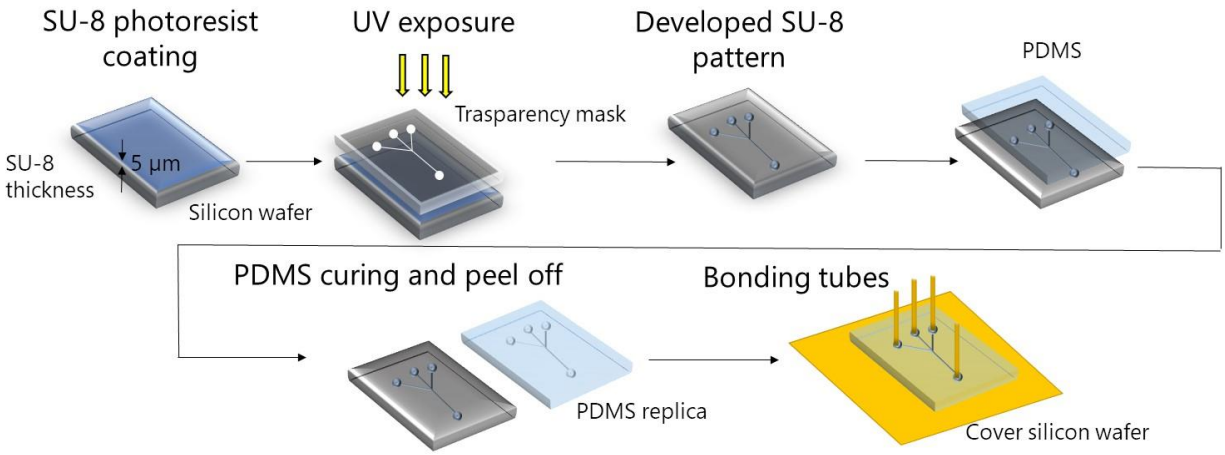

Figure 2.1: Simple scheme to summarize the steps of microfluidic device fabrication employing UV photolithography with SU8 Microchem photoresist and polydimethylsiloxane elastomer for replica molding.

2.2.2 Use of mask aligner

In order to fabricate a 3D master with UV photolithography, a film with desired thickness of photoresist must be exposed to UV light source through a high-contrast mask.

The mask can be prepared by ultra high vacuum metal evaporation upon a quartz or borosilicate glass substrate patterned with requested design. The pattern on the mask substrate is obtained by a pattern generator consisting of a UV laser focused beam scanned on a thin film of photoresist, according to polarity defined by the design and type of photoresist. After solvent development of the exposed thin film, a thin layer of metal is sputtered on the substrate and a lift-off process is performed to remove the photoresist and leave only the metal patterned according to design. The area covered by the metal will be approximately 100% opaque to UV radiation, whereas the rest of the transparent features will allow exposure through,

UV photolithography can be split into projection photolithography and contact photolithography. In projection mode, the mask is held in the optical path between the light source (collimated rays) and the substrate put in the focal plane. In between the mask and the substrate there is an objective lens which will focus the projected image correctly, with the desired magnification.

In contact photolithography, the mask is put in contact with the photoresist, so that the features reported in the mask will be faithfully reproduced in the photoresist without any scaling. Depending on the chemical composition of the photoresist, there might be a cross-linking induced by the UV radiation, making the exposed patterned insoluble in the development processing (negative photoresist). Viceversa in positive photoresists, there is a polymeric degradation induced by UV radiation which increases solubility in water based developing solutions made with potassium hydroxide (cf. Figure 2.2a,b).

Contact photolithography allows to reproduce features up to 1 μm, but the thickness of the structural photoresist will affect the final results achievable. In particular, the exposure system employed in the present work is based on a mask aligner with UV light source having intensity approximately equal to 0.5 W/cm^2.

With this intensity, it is possible to expose features with aspect ratio height/width maximally equal to 1, for the smallest feature sizes. High aspect ratio could not be achieved because the summing effect of diffraction and exposure time could lead to overexposure of the features.

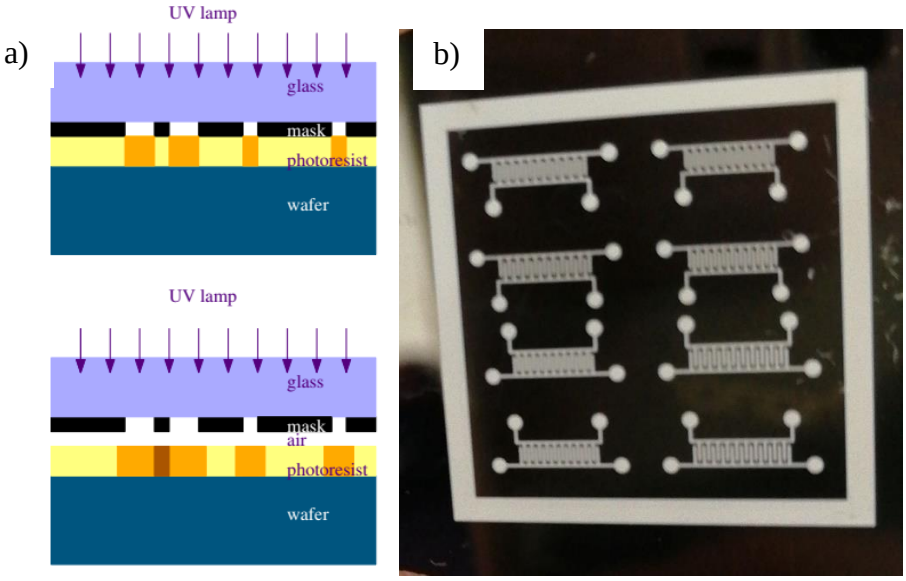

Figure 2.2: a) Schematics of layers involved in contact photolithography (top) and proximity photolithography (bottom). Contact photolithography allows to have the best resolution among the two methods b) Example of UV high contrast mask, obtain with laser lithography starting from a film of aluminium on glass.

2.2.3 Digital Light Processing (DLP) 3D Printer

Among the 3D printing processes available in the market, two most common process for photopolymer resin 3D printings are Stereo lithography (SLA) and Digital light processing (DLP) 3D printings [1]. 3D Printed structures with these technologies have high accuracy, isotropicity, high resolution and surface with smooth finish. (cf. Figure 2.3)

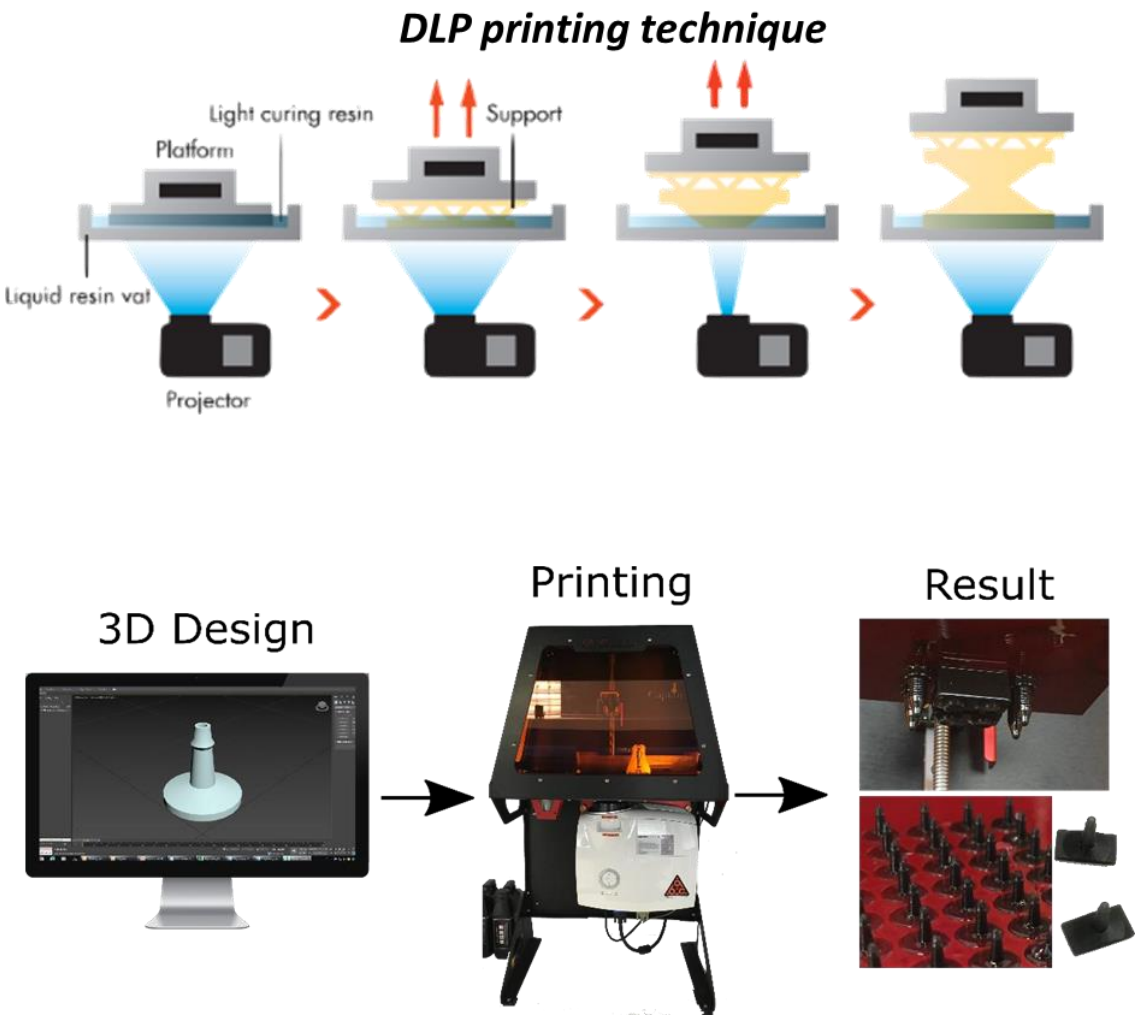

Figure 2.3: Schematics of the DLP 3D printing process including exposure steps and spread of the liquid resin (top). Example of manufactured microfluidic connector, from design to printed final components [2]

Thanks to technological development, there exist small-format DLP printers in today's market which produces quality 3D printed objects/ parts at affordable price. DLP 3D printer is similar to the conventional SLA printer. The desktop DLP (B9 Creator) 3D printer is composed of a resin tank with a transparent window sliding back and forth to refill the photoresin near the exposure area next to the build table that moves vertically into the photopolymer resin, in order to build up the model layer by layer [1, 3].

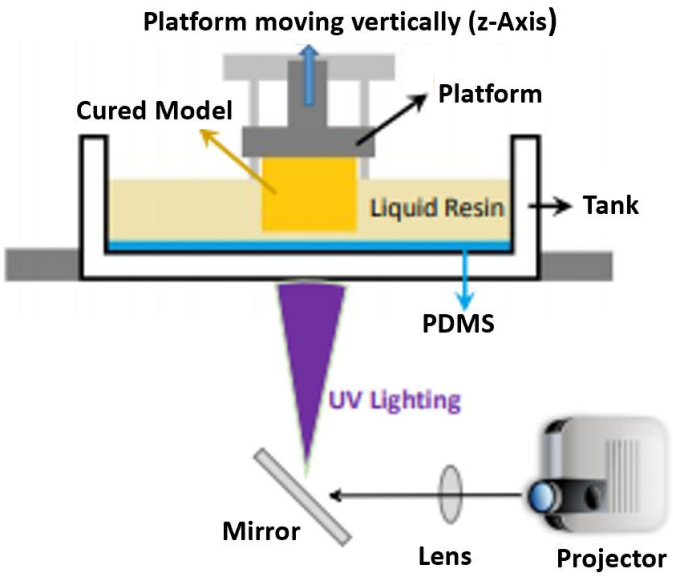

Figure 2.4: Schematic detail of the positioning of the micro mirror device inside the optical system of the DLP printer [1, 3]

The main difference between SLA and DLP is the light source. Conventional light source such as arc lamp with a liquid crystal display panel has been used in DLP. The light source is projected on an entire surface of the transparent vat containing photopolymer resin in a single step. The pattern created by the Digital Micro mirror Device (DMD) will perform projection of the image by reflecting the light source and in particular UV component of the incoming radiation. DMD is composed of microscopic sized mirrors laid out in a matrix on a semiconductor chip. (cf. Figure 2.4)

Toggling rapidly these mirrors, which reflect the light source, will polymerize part of the photoresin, whereas unexposed resin will be washed away by the sliding of the tank. Once the printing is been completed, the vat will be drained of liquid, revealing the solidified model. DLP 3D printing is faster and can print objects with a resolution of 150 µm in X, Y axis, and up to 25 µm along Z axis.

2.2.4 Laser Lithography

Laser lithography has been increasingly used in microfabrication to achieve controlled micrometric size ablation of thin metallic films. Desired patterns can be converted into a binary image and used to ablate metal (gold, aluminium, titanium, etc) deposited on a substrate (rigid or flexible), i.e. for the fabrication of shadow mask (ref. the UV photolithography Chapter 2.2.1) or for the fabrication of planar electrodes for sensors.

For the work reported here in the thesis, the laser marker has been used also to ablate 70 nm gold deposited on Kapton substrate to make Source (S) and Drain (D) interdigitated electrodes test pattern for Electrolyte Gated Organic field effect transistors (EGOFETs) [4].

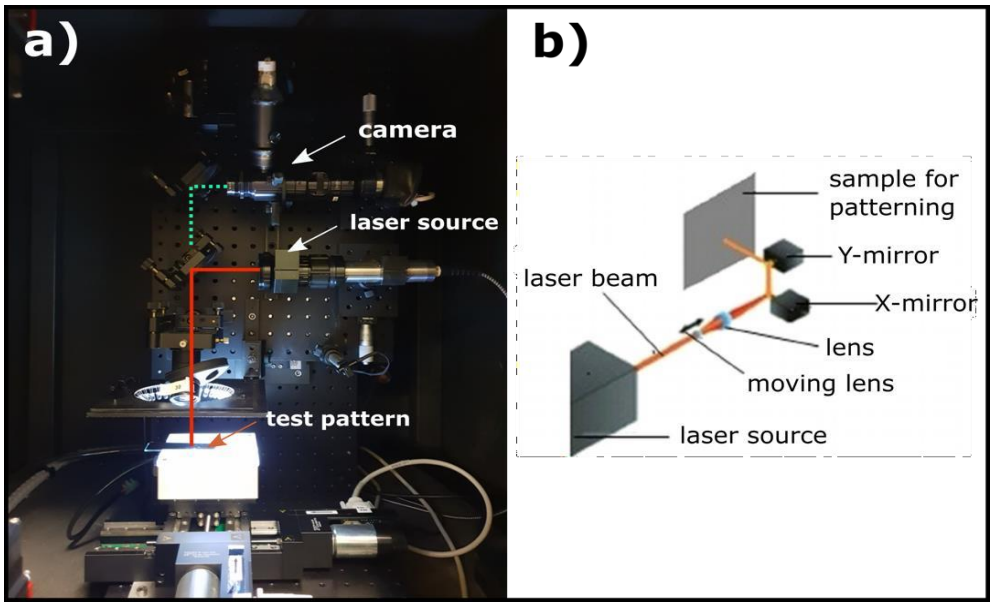

Figure 2.5: a) Optical setup of the ScribaR laser marker, b) schematics of scanning head component [4]

The laser marker ScribaR^{TM} (cf. Figure 2.5) was manufactured by Scriba nanotecnologie S.r.l, Bologna (IT). It has a laser source, which produces a short-pulsed Nd: YAG – infrared (IR) – laser (centre wavelength k ¼ 1064 nm). For the safer ablation of the metallic coatings or other coatings on top of underlying substrate (for example, biodegradable scaffolds), process parameters have to be studied in preliminary study. The pulse width, the repetition frequency, power, the speed of the laser beam have to be selected according to power map of the laser source., The infrared absorption

of the metallic compound and the thermal resistivity of both the metal and the substrate play a substantial role in throughput and quality of the printing.. The focus and displacement of the laser beam is being controlled by scanning head, whereas a motorized stage featuring an encoder is moving the sample across a range of 12 cm both in X and Y directions. In order to control the position and the ablation parameters in real time, a software developed by Scriba was used allowing the operator to have a controlled operativity.

The controller unit inside the instrument guides the translation of the stage under the focused beam via CAD (Computer- Aided- Design) file containing the drawings. Fast prototyping and high-resolution ablation of 10 µm - 20 µm can be obtained in X, Y and Z-axis with the help of described infrared laser printer [4].

2.2.5 EGOFET Device Fabrication using Laser Lithographic Technique

One of the objectives pursued in PhD thesis work, is to develop a highly sensitive, selective and stable EGOFET device, as per the literature model [5] with the top gate and bottom source and drain contacts configuration. The bio receptors moieties are confined on the gate electrode and the target analyte has to be injected, through the microfluidic channel via an external peristaltic pump in buffer with controlled ionic strength.

The sensing has to be performed by recording the current between Source and Drain in time, varying the potential between the Gate and Source electrodes. The organic semiconductor layer covers completely the electrodes, therefore the electrolyte solution containing the biomolecules is confined between the semiconductor layer and the Gate electrode.

A change in the ion distribution within the fluidic compartment, upon applying the Gate Source potential, is reflected in a change in capacitance on the Gate/electrolyte interface and OSC/electrolyte interface, which in its turns affects the charge transport within the organic semiconductor [5]. I will describe in the following paragraphs the fabrication of EGOFET components.

The interdigitated Source and Drain electrodes have been designed using the 2D software (Draftsight, Dessault Systems). The design geometry was made with objective Width/ Length (W/ L) ratio of 3000. This design is producing an output current (I_{DS}) of about 2µA - 3µA for the voltages applied in the linear regime (see Chapter 5.2.1) for clean Au as gate electrodes. The 2D design CAD was optimized considering the laser ablation process (cf. Figure 2.6) and was then imported into the laser marker control software for fabrication.

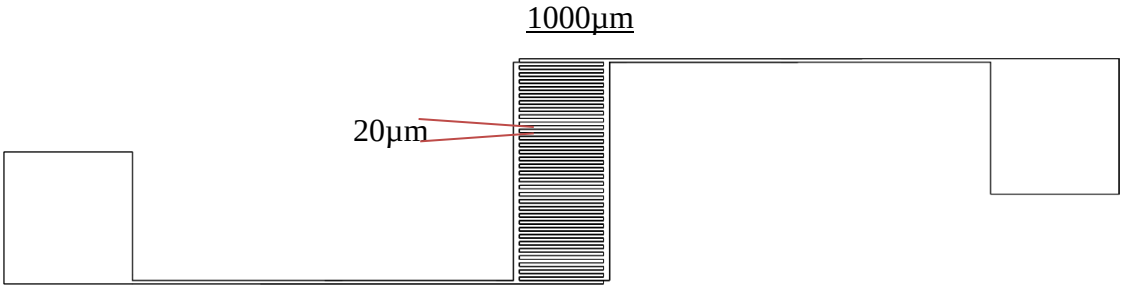

Figure 2.6: 2D Geometry of the interdigitated electrodes prepared for laser ablation using DraftSight®

The flexible substrate, which was used to create such Source and Drain interdigitated electrodes, was a thin foil of Kapton (50µm thickness). 99.99% pure gold Sputtering was accomplished by Creavac, Dresden, Germany to metallize the surface of the polymeric foil. Single side coated Kapton substrate , obtained in Ultra High Vacuum Evaporation contains the following:

1. 10 nm Nickel Chromium (NiCr) as adhesion improver
2. 70 nm Au± 15%

The metallized Kapton substrate with the size of 10 mm * 6 mm was placed on the sample stage of the Infrared Laser marker to ablate the desired geometry for interdigitate electrodes (cf. Figure 2.6). The parameters set for the process where the following:

1. Power = 0.3 Watt,
2. Scanning speed = 180 mm/s
3. Pulse repetition frequency = 20 kHz

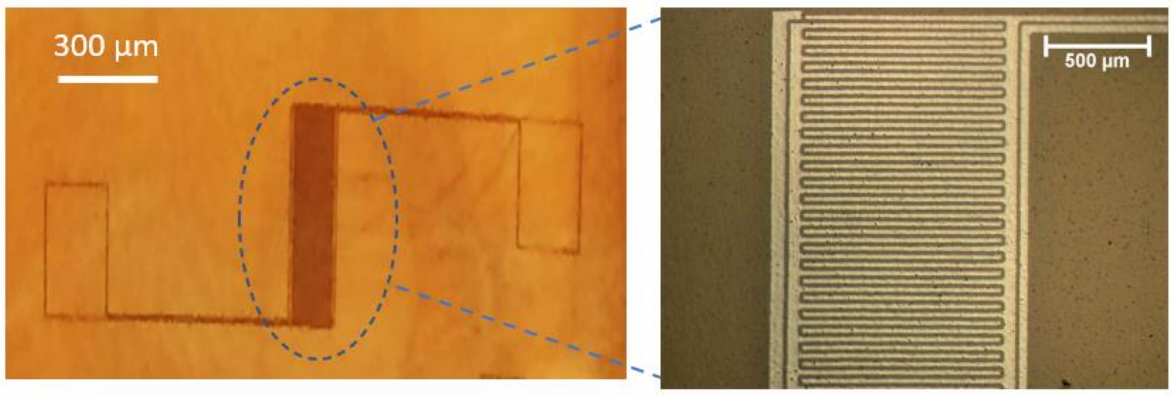

Figure 2.7: Images obtained with optical microscope (magnification 5X and 20X) of the Au – Kapton after ablation with laser marker [4]

Once the interdigitated electrodes pattern has been ablated (cf. Figure 2.7), the substrate was removed from the printer stage and sonicated with DMF (Dimethylformamide) for 5 minutes. Later it was rinsed with distilled water, in order to remove the ablation residues and to increase the surface tension of the interdigitated pattern. At last, the flexible substrate(cf. Figure 2.8) was dried with the Nitrogen gas.

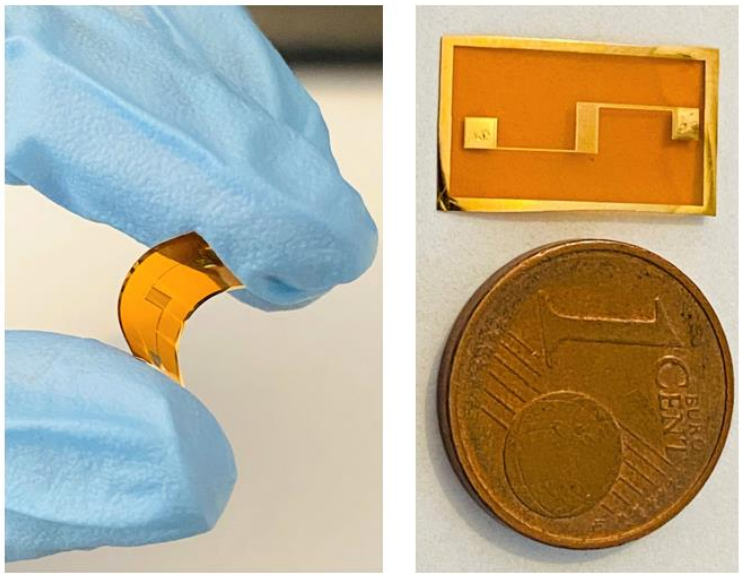

Figure 2.8: Flexibility (Left) and transparency (Right) of the interdigitated Source (S) and Drain (D) electrodes of the EGOFET device

Before the drop casting of the organic semiconductor (Tips- Pentacene) [6], the substrate was checked with the optical microscope for the pattern continuity in the interdigitating electrodes. Moreover, the kapton layer between them isolates the interdigitated electrodes (cf. Figure 2.7 right)

2.2.6 Electroplating with metal aqueous solution

Other architecture of multigate (multisensing) EGOFET device were designed employing thin silver wires or stripes as gate electrodes. Functionalization with bioreceptors are reported for different metallic and dielectric substrates in literature were proposed, but frequently employing thiol termination to establish a covalent bond with gold surface.

Therefore, in-house gold electroplating technique was performed to deposit a thin layer a gold upon thin silver wire with good adhesion properties. So, the electroplating principle makes a gold coating on the thin silver wire by reducing the cations of that silver wire by the application of direct electric current. The localized area in silver wire to be coated, acts as a cathode (negative electrode) of an electrodeposition cell.

The electrolyte used was the potassium gold cyanide $kAu(CN)_2$ and it is the most frequent gold plating chemical employed in literature. Whereas, the anode (positive electrode) is connected to the same block or small area in the thin silver wire, left uncovered (prevention of direct contact) by the electrolyte while performing brushing electroplating technique (cf. Figure 2.9). Direct electric current of 5.4 V was applied to the anode and cathode through external power supply with a desired plating time at room temperature [7].

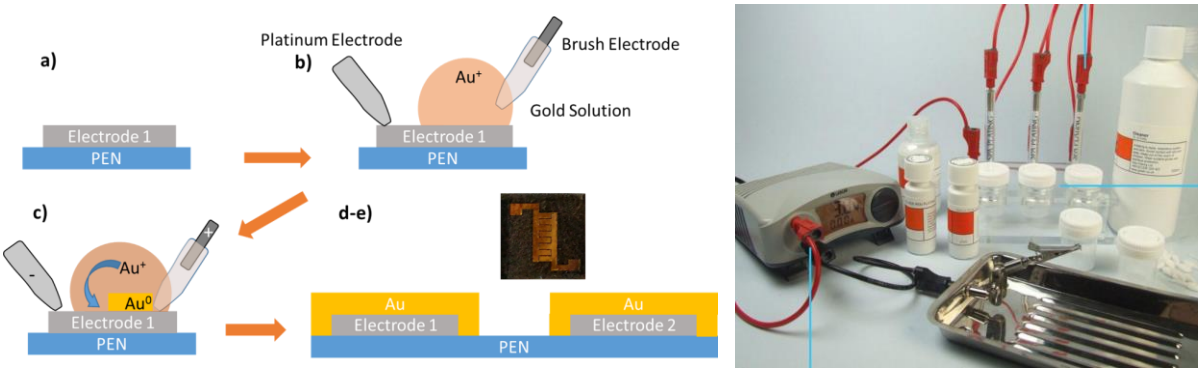

Figure 2.9: a-e) Scheme of electroplating process, performed on silver or steel interdigitated electrodes, f) the pen-brush electroplating instrument with voltage rectifier.

Electroplating solution was applied through a brush made of a metal (stainless steel) which was covered with small cotton on both sides. So, the electrolyte was soaked with the cotton pads, then by applied manually (rubbing or brushing) on top of the thin silver wire by evenly distributing the plating solution [7, 8].

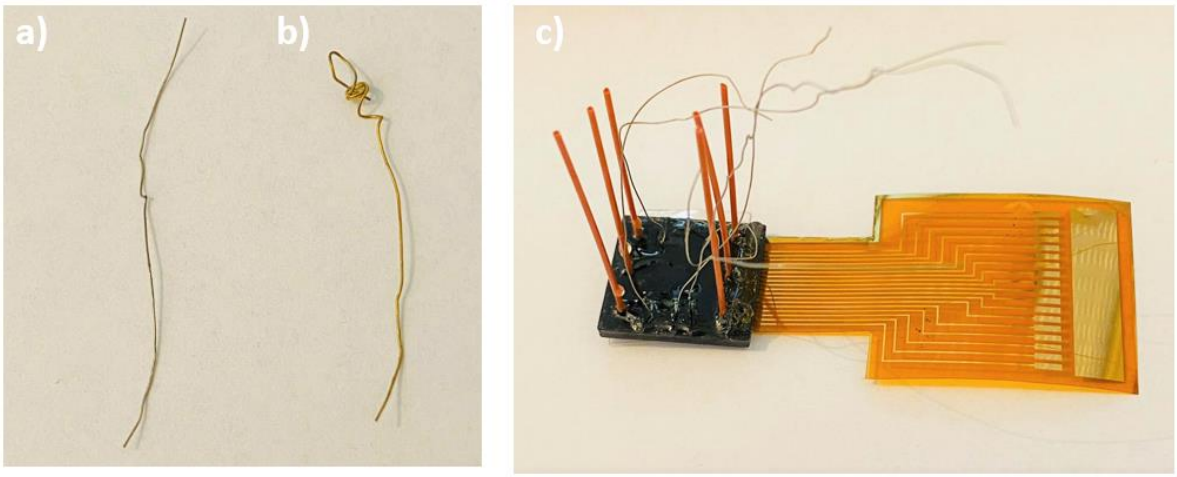

Figure 2.10: a) Thin silver wire with a ∅ 0.3mm before electroplating b) after Au electroplating c) Multigate EGOFET model with the electroplated gate electrodes

The main advantage of this process includes low volume usage of the electroplating solution compared to the tank electroplating technique and a specific or small objects needed to be

electroplated (cf. Figure 2.10 a) can be achieved without the need of any masks as used in tank electroplating techniques [8].

2.2.7 Drop casting of organic semiconductor

Drop casting techniques have been extensively tested to deposit organic semiconductors in the channel geometry of organic electronic field effect transistors. For the experimental results reported in the present thesis (Chapters 5.2 and 5.3), TIPS-pentacene has been selected as charge transport material for Electrolyte Gated Organic Field Effect Transistors (EGOFET).

Drop casting technique also allows us to control the rate of deposition of the semiconductor , in order to gain more control in the crystalline morphology and achievebetter transistor performance. With this deposition method,an homogeneous and crystalline thin film layer can be created with good adhesion on polyimide. In case of another organic semiconductor named “pentacene” for creating a thin film deposition, it has to undergo thermal evaporation in high vacuum conditions. So, vacuum evaporation can’t be always applicable to ionic materials without being evaporated. In case of spin coating considerably large volume of semiconducting material will be used. For spin coating techniques, the deposition rate can’t be always controlled [9–11].

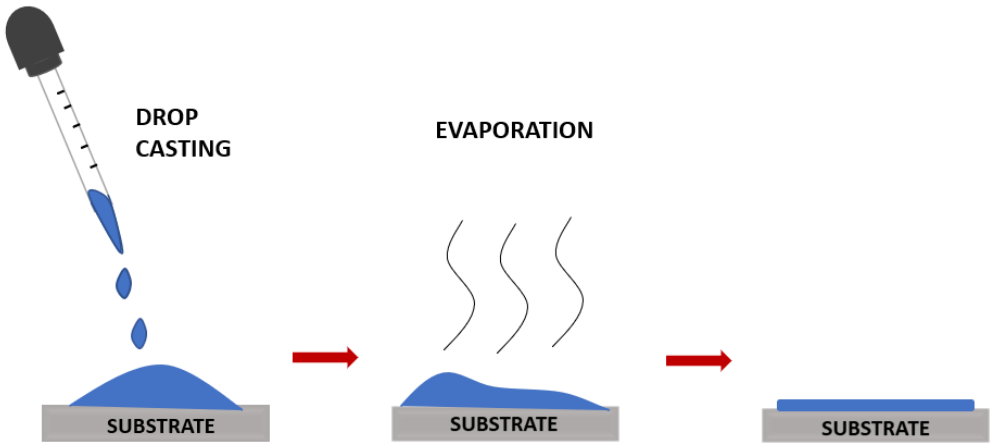

Figure 2.11: Simple block diagram of the drop casting process

Also, it is critical to obtain multilayer organic material. The main advantage of drop casting (cf. Figure 2.11) methods can be summarized in the following points:

- controlled area can be coated,
- usage of low volume of the organic material
- no pre annealing and post annealing steps are needed.
- highly cost efficient,

This last point merits a specific highlighting. In order to fabricate a thin film organic field effect transistor, only 1µl of TIPS-pentacene solution (cf. Figure 2.12 a) was used to create the conductive channel and after drop casting, the solvents in the material were dried at room temperature in less than 5 minutes. (cf. Figure 2.12 b,c)

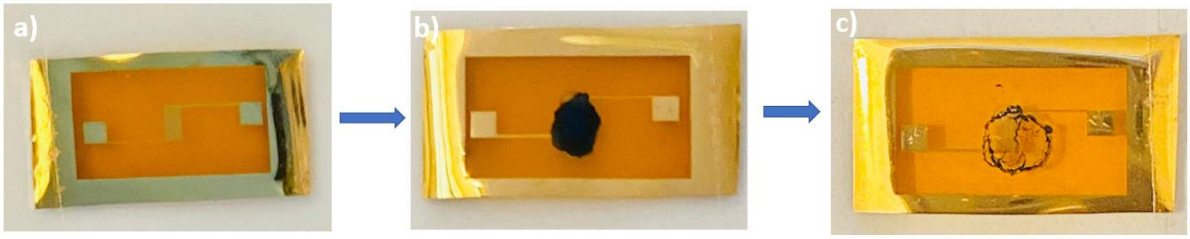

Figure 2.12: a) Picture of the interdigitated S and D electrodes before drop casting process b) After 1µl volume of TIPS-pentacene drop casting c) evaporation and the solvents and formation of fine crystalline structure.

2.2.8 Replica molding for microfluidic devices

In order to fabricate the microfluidic devices a well tested elastomer, polydimethylsiloxane (PDMS) was used. PDMS is highly cost efficient and widely used material to fabricate microfluidic devices. The special features of PDMS based microfluidics include: transparency in the range of 230-700 nm wavelength, typically used in UV spectroscopy), conformal bonding to sensor substrate and permeability to gases for specific biological applications with cell cultures [12–14].

Curing agent and PDMS pre polymer (SYLGARD 184 Silicone Elastomer Kit) were mixed in the weight ration of 1:10. After thorough mixing, the PDMS mixture was kept inside a vacuum chamber for 1 hour, in order to remove any air bubbles or gas trapped into the fluid. After degassing, PDMS was poured upon the 'masters' fabricated through 3D printer and photolithographic techniques (Chapter 2.2.1). Almost all the 3D masters included an external structure to contain the liquid PDMS, defining in this way the overall thickness of the microfluidic structure [13, 15].

Then PDMS mixture was thermally cured in the oven at 70°C for 12h -15h or it can be also cured at room temperature for 48 hours. Then the PDMS replica with the desired channel thickness (10-15μm) based on the design in the master was created. Usually, the thickness of the PDMS microfluidic devices will be 3mm to 4mm in height. Then the PDMS replica is peeled off gently and sealed on top of glass or Lab on chip devices or sensors either using O2 Plasma sealing or mechanical sealing. Since PDMS is very hydrophobic, the fabrication of pools to contain electrolyte seemed a good option for integration with organic based devices. But in case of droplet microfluidics or other fluidics devices involving a controlled flow of solution, surface modification of the PDMS microfluidic device can be performed to generate hydrophilic boundaries reducing the pressure acting on the sealed parts, although this hydrophilic performance is not permanent in time [12, 16].

When PDMS polymer based microfluidic devices are used, there leads to important compromise between the rigidity for processing (i.e, thermal expansion) and flexibility based on the specific application. Since the soft polymeric material (PDMS) is highly versatile and has elastic modulus 1M Pa, it can be tuned by changing the hardening agent to PDMS base and also by changing the temperature of curing processes accordingly to the time. The stiffness of PDMS can be controlled from 800kPa to 10MPa with a certain rupturing limit and contact angle wetting issues [17].

2.2.9 TIPS-Pentacene organic semiconductor (materials and crystallization processes)

With the development of organic thin-film transistors in the past decade, 613-Bis(Triisopropylsilylethynyl) pentacene (TIPS-pentacene) was widely used as organic semiconducting material (conductive channel of the transistor). The main advantage of TIPS-pentacene includes its good electronic properties, solubility and stability onto the substrate after deposition. Organic semiconductors have some specific advantages with respect to inorganic semiconductors. In particular they are highly flexible, easy to process and allow a large number of fine chemistry reactions to tune the chemical, mechanical and electrical properties of the material and to link other bioactive molecules as side substituents [6].

Among the organic semiconductors, “pentacene” was first studied for its crystalline structure and molecular orbitals. In order to have high carrier change transfer, it is important to have highest occupied molecular orbital (HOMO) orbitals overlap of molecular orbitals, which is difficult to achieve due to electron-electron repulsion of such orbitals. It has been figured out that Pentacene, as a small organic molecule undergoes a poor overlap between HOMO Orbitals.

For Pentacene forming herring-bone crystalline structure and acene backbone [6] are arranged perpendicular to its neighbor resulting in poor overlap between the HOMO orbitals. Also, Pentacene is not easily dissolvable in available other common organic solvents and its prone to photo-dimerization in solution, which reduces carrier charge mobility. Incase of pentacene after deposition on the substrate, it undergoes an interaction with oxygen which loses its conjugation to freshly formed bond or bridge. Another disadvantage of using pentacene is that for deposition onto the substrate, it undergoes thermal evaporation under high vacuum conditions, resulting in increasing processing time and cost [6, 18].

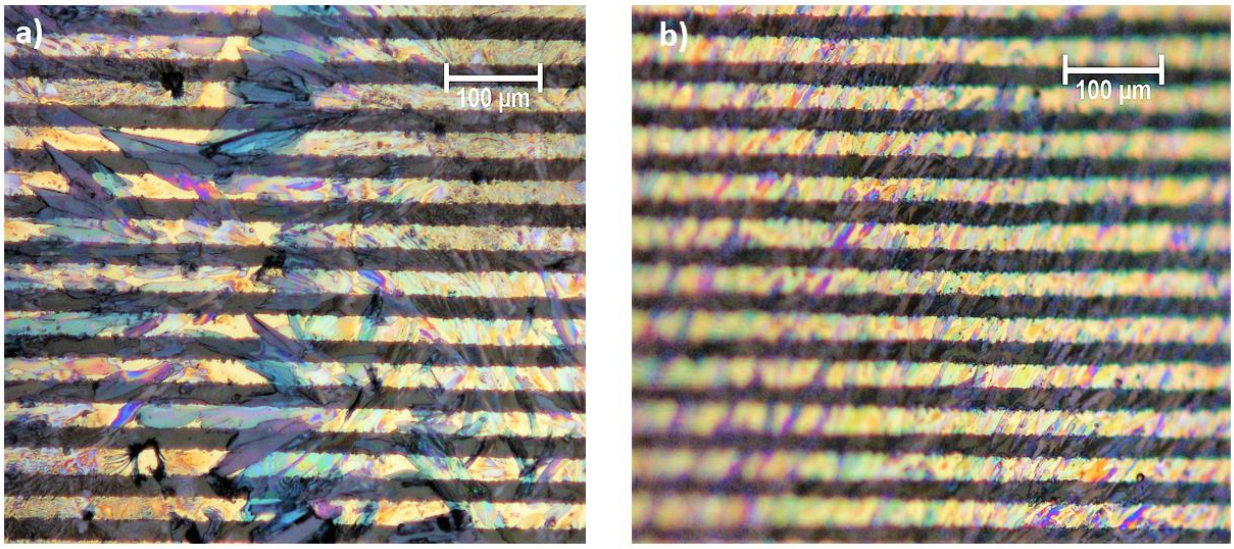

Figure 2.13: optical images represented in 20x magnification a) after 2.5 µl volume of TIPS-pentacene drop casting which leads to bigger crystalline formation b) after 0.5 µl volume of TIPS-pentacene drop casting leading to very smaller crystalling formation.

The addition of 2 triisopropylsilylethynlyl acetylene groups to pentacene generates TIPS-pentacene. The molecule solubility in an organic solvent was increased due to the substitution on to pentacene with isopropyl. Also, Photo-oxidation and favorability to dimerization was reduced. Because, the reaction must be coordinated as opposed to radical or zwitterionic forms and the large functional group decreases the tendency to form dimers.

The addition of TIPS containing large functional group to pentacene makes the crystalline structure to flatten out and acene backbone performs stacking on top of one another. Hence the HOMO overlap can be maximized by changing acene backbone [6]. Acene backbone overlap can be modified by changing the groups attached to the silicon, thus twitching the structure of the crystalline structure. After obtaining the optimal overlap, the carrier mobility is greatly increased.(cf. Figure 2.14)

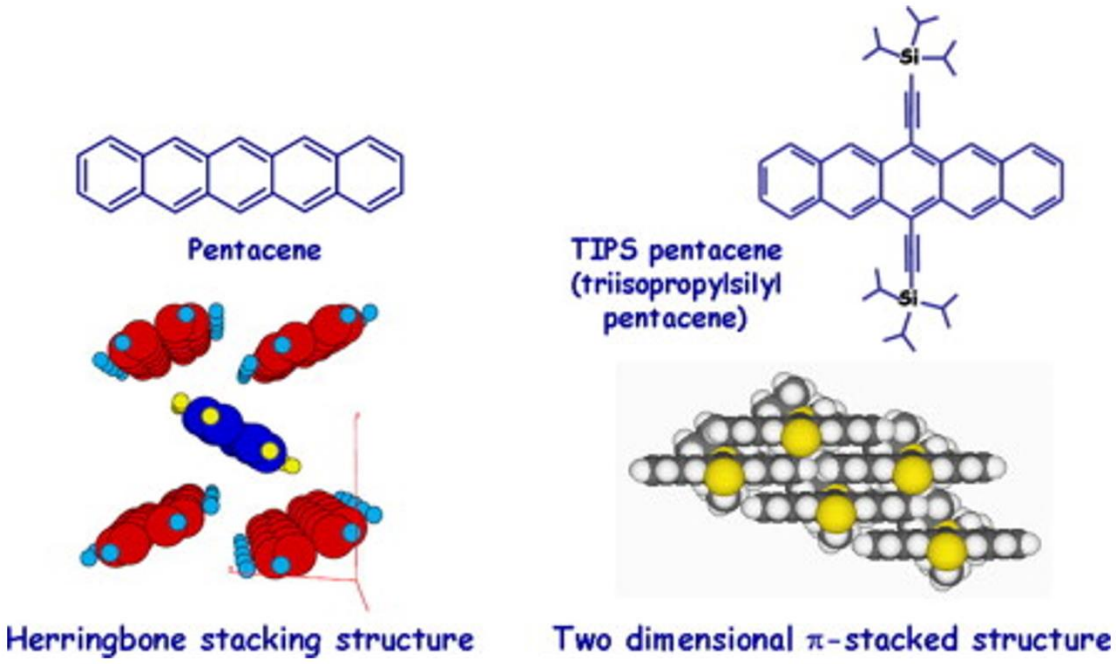

Figure 2.14: Structure of pentacene with it's respective Herringbone structure (Left) and Structure of TIPS-pentacene with the two dimensional π – stacked structure (Right) [19]

In this PhD work, TIPS-Pentacene was used to create a conducting channel between S and D interdigitated electrodes present in the Electrolyte Gated Organic field effect transistors. Also an optimization was achieved in the volume of organic semiconductor (1 µl volume of TIPS – Pentacene) used for deposition on top of the interdigitated S and D electrodes, in order to create a high carrier charge mobility.(cf. Figure 2.15 a, c)

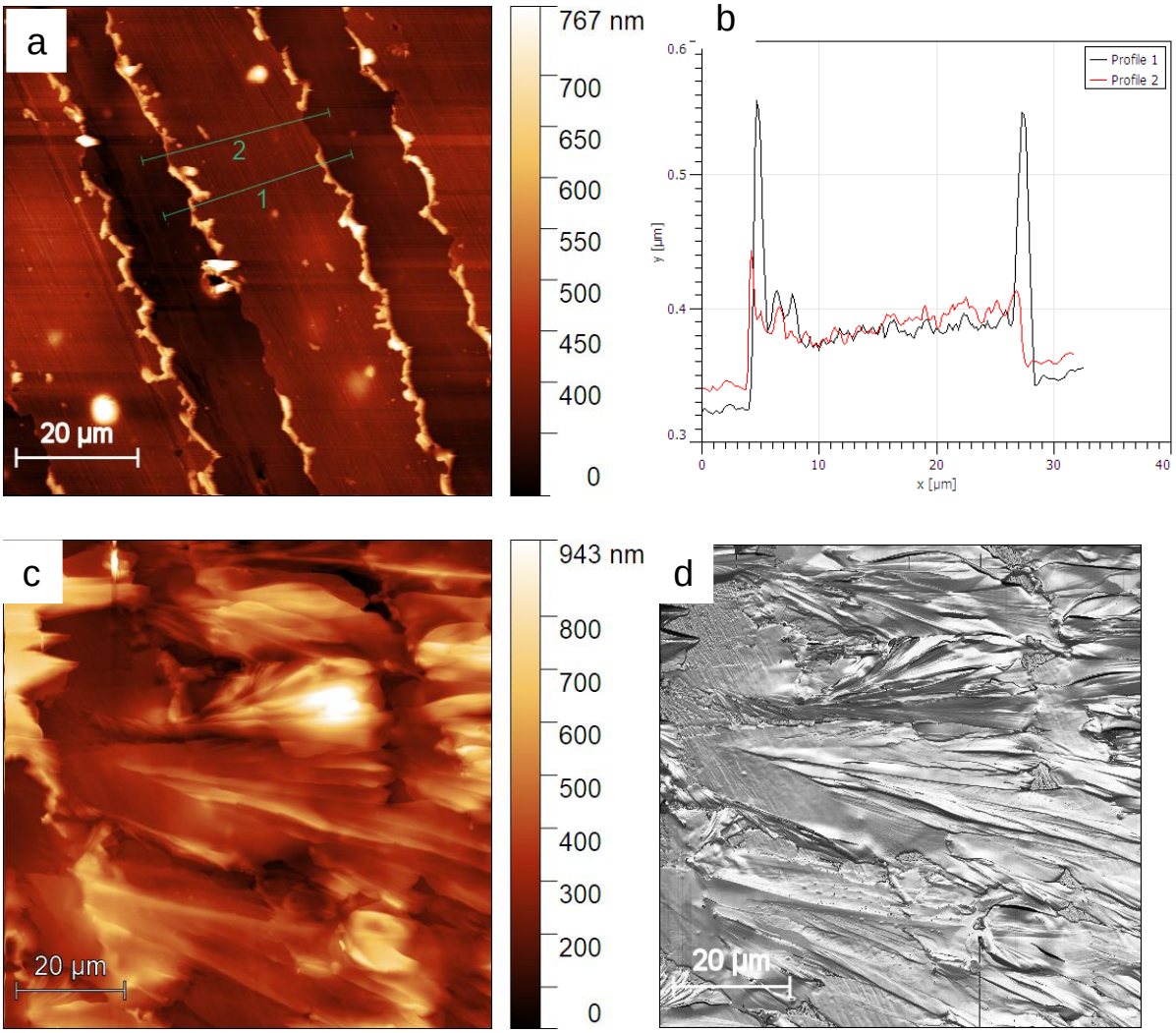

Figure 2.15: a) AFM image of the Au interdigitated electrodes before deposition of organic semiconductor. From the topography it is possible to appreciate the roughness of the borders induced by the laser ablation process. b) Profiles of the electrodes taken in position 1 and 2 in a. The thickness of the border is larger than 250 nm versus an average thickness of the film of 70 nm. c) AFM topography of the TIP-pentacene crystalline domains after drop casting on the interdigitated electrodes. It is still possible to appreciate the electrode morphology underneath the organic film. d) Phase image contrast recorded for c, where the boundaries of domains are more pronounced.

The solvents used to dissolve the TIPS-pentacene molecules are toluene and hexane (80:20) ratio. With 1% wt of TIPS-pentacene molecule (25 mg) for 3ml total volume of the solvent (Toluene: Hexane). The solution was well mixed using the stirrer for 3 hours at 70° C [18]. Many depositions

using drop casting technique with different volume of TIPS-Pentacene solution were performed to confirm reproducibility in EGOFET device performance. 1 µl volume of TIPS-pentacene solution drop cast on top of the interdigitated source (S) and drain (D) electrodes was sufficient enough to form a good micro crystalline structure. The solvents evaporates in few seconds, thus allowing the molecules to form homogeneous crystalline domains. It is reported in literature that TIPS-pentacene domains with slipped $\pi - \pi$ stacking helps the charge carriers to "hop" from one molecule to the other and increases the mobility measured on organic transistors [20].

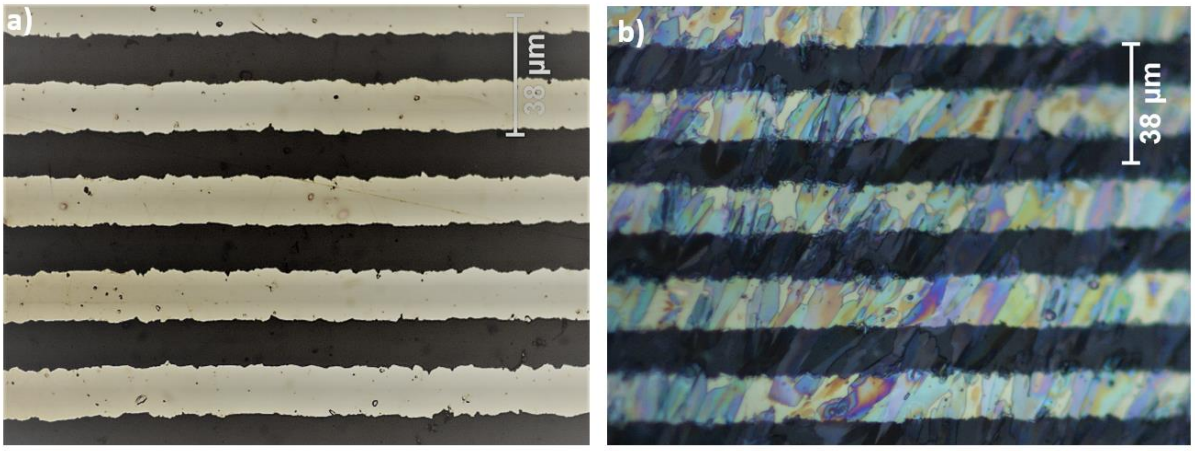

Figure 2.16: optical images represented in 50x magnification a) interdigitated S and D electrodes before drop casting b) 1 µl volume of TIPS-pentacene creating a fine micro crystalline formation and creating a good conducting channel

Tips- Pentacene has the ability to form a high crystalline structure; the optical image (cf. Figure 2.16) shows the crystalline formation on top of the interdigitated pattern. The important concern with the drop casting of Tips-pentacene, for more than 1 µl, is the increase of crystallinity [6]. Thick crystal structures lead to the formation of small solid blocks on top of the pattern and will not passivate the complete interdigitated pattern (cf. Figure 2.13).

2.2.10 Surface treatment protocols on gold/Kapton substrates

Regeneration process for the interdigitated electrodes was achieved in this PhD work, by using simple protocols with less amounts of solvents. The substrate of the organic transistor device, i.e. the Kapton polymeric foil with interdigitated electrodes ablated by laser, may be regenerated after use with electrolyte solution by removing the organic semiconductor pattern and cleaning completely the surface before repeating drop casting of organic semiconductor. The cleaning protocol can be summarized in the following steps (cf. Figure 2.17)

1. Manual agitation of the flexible Kapton-Au interdigitated S and D electrodes with Ethanol for 5 minutes and gently remove the semiconductor with dabbing a piece of tissue paper immersed with ethanol.

2. Rinsing with distilled water to remove the semiconductor residues and dry with N_2 gas

3. Manual agitation of the flexible Kapton-Au interdigitated S and D electrodes for 5 minutes in Dimethylformamide (DMF), in order to increase the surface tension of the interdigitated pattern

4. Wash the interdigitated S and D with distilled water and dry with N_2 gas

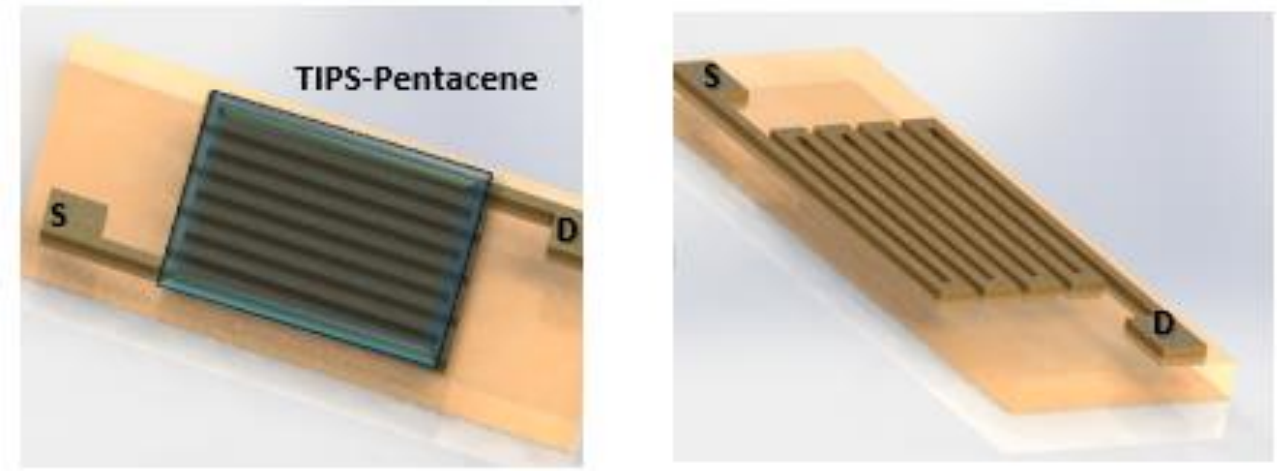

Figure 2.17: Interdigitated Source (S) and Drain (D) electrodes drawn using TINKERCAD® and depicts the S and D electrodes before regeneration (Left) and after regeneration (Right) steps.

2.3 Materials and methods for miRNA-21 detection

2.3.1 Gate electrodes for miRNA-21 biosensor

Gold wires were purchased from Nanovision S.r.l, Brugherio (IT) with purity of 99.99%, a length of 2.5 cm (for dual-gate EGOFET architecture, Chapter 5.2.1), or a length of 1 cm (for multi-gate EGOFET architecture, Chapter 5.3) and all with a diameter of 1 mm. The gold wire has proven to be an alternative to the classical planar / flat surface, due to the possibility to regenerate the surface with sulfuric acid cleaning procedure, and easy operation for functionalization and contact making. In order to assemble the gate electrode on top of the electrolyte and to obtain a final model, a 3D printed gate holder was designed and fabricated (cf. Figure 2.18).

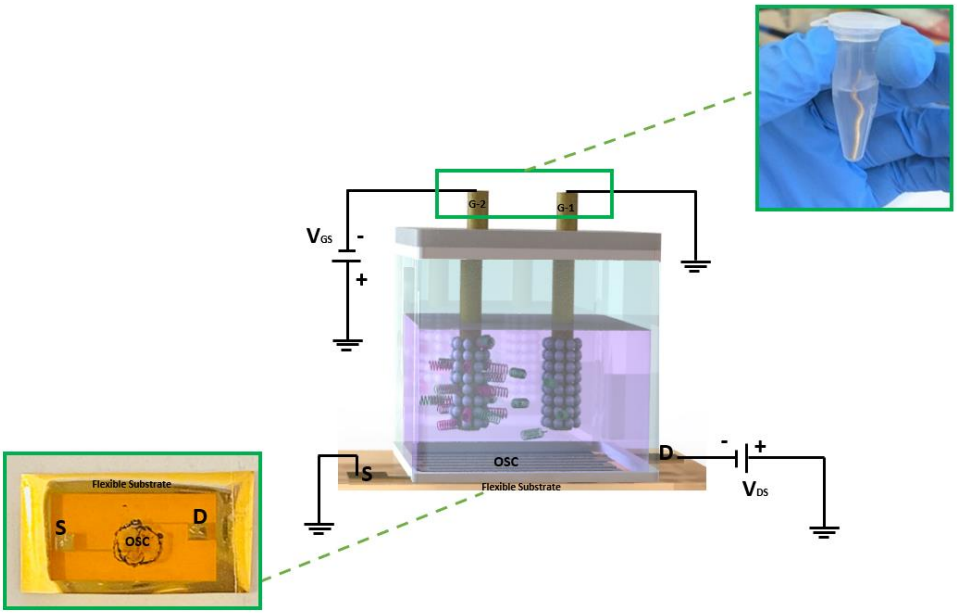

Figure 2.18: 3D model of the Dual gate EGOFET model developed using TINKERCAD® with the insight images showing the pictures of Au gate wire (Ø1mm) and a picture of Interdigitated Source (S) and Drain (D) electrodes with a TIPS-pentacene (1 µl) drop casted

2.3.2 miRNA-21 functionalization protocol

Synthetic oligonucleotides were purchased from Metabion Internation AG, according to the following sequences:

- miRNA-21-3p derived sequence (5'- CAACACCAGUCGAUGGGCUGU- 3'), as the target analyte for the experiments reported in Chapter 5.1
- Thiol-C6-AAA AAAA-5'- UAGCUUAUCAGACUGAUGUUGA – 3', synthetized with thiol group, C6 and 7 adenine spacers, as the probe
- miRNA-141 derived sequence (5'-CAUCUUCCAGUACAGUGUUGGA- 3'), as the control unrelated sequence (CTR).

The stock solution for 'Probe' containing segments of miRNA sequences was prepared in SSPE buffer (Sodium Chloride-Sodium Phosphate-EDTA) (2g/10ml ultrapure water) from Sigma-Aldrich, containing 0.02 M EDTA (Ethylenediaminetetraacetic acid), 2.98 M NaCl (Sodium Chloride) and 0.2 M PBS buffer (Phosphate-buffered Saline) (20* diluted, pH 7.4). 100 μM concentration of probe normalized solution was obtained by adding 788 μl of SSPE stock solution [21].

The stock solution of miRNA-21 was prepared in Tris-HCl (Tris Hydrochloride) containing 0.02 M Tris (tris(hydroxymethyl)aminomethane), 0.14 M NaCl (Sodium Chloride), 0.001 M $MgCl_2$ (Magnesium chloride), 0.005 M KCl (potassium chloride) and 0.001M $CaCl_2$ (Calcium chloride) (pH 7.4).100 μM concentration of mir-21 normalized solution was obtained by adding 652 μl of Tris-HCl stock solution and stored in 65 aliquots (10 μl each) at -20° C.

2-mercaptoethanol (2-ME) (Merck) blocking agent was selected to reduce the direct interaction between the target analyte and the gold surface.

Different concentrations (10 pM to 300 pM) in the Pico molar (pM) range of miRNA-21 standards were prepared by adding 0.001M Tris buffer containing 0.001M EDTA and 0.05 M NaCl (pH 7.4). This Tris-EDTA (TE)-NaCl buffer was also used as hybridization buffer and immobilization buffer. The water used for dilution is Mili-Q laboratory grade (conductivity <0.1 μ S/cm) in order to increase the stability of the miRNA by decreasing the RNase activity [22, 23].

The following gate functionalization steps were performed:

1) G1 was functionalized with 2-mercaptoethanol (1 mM) for 2 hours at the room temperature, then rinsed with the ultrapure water before assembling (cf. Figure 2.19 a).

2) G2 was functionalized with probe (2 µM), for the whole night at room temperature. Later G2 was rinsed with ultrapure water and then placed in the vial containing 1 mM concentration of the blocking agent (2-ME) for 2 hours, in order to block the non-specific bindings. (cf. Figure 2.19 b).

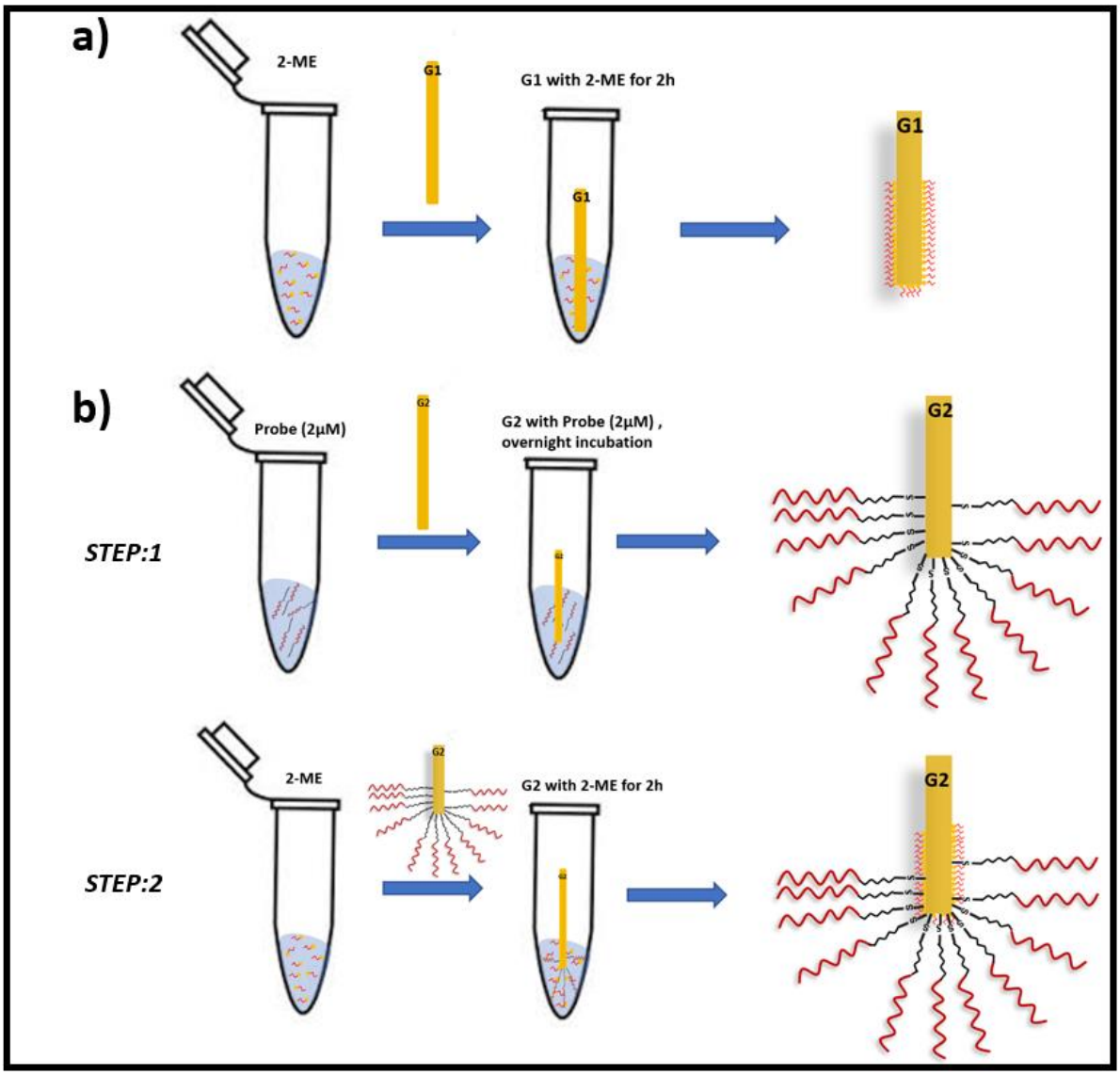

Figure 2.19: a) Gate(G1) functionalized with 2-Mercaptoethanol (2-ME) for 2 hours b) Two step process functionalization for the sensing gate (G2), STEP:1 Functionalization of Gate (G2) with 2µM or 5µM probe

concentration for the whole night, STEP:2 Functionalization of the Gate (G2) which was already immobilized with Probe into the blocking agent (2-ME) for 2 hours , in order to block the non-specific adsorption on the uncovered gate surface (G2)

Hybridization with the different concentrations of the target analyte (miRNA-21) was done by incubation the Gate-2 at 37°C for 30 minutes in the oven [24]. The vial containing different miRNA-21 concentrations was prepared using hybridization (Tris-EDTA-NaCl) buffer. The procedure of incubation for hybridization has to be done starting from the vial of lower concentration to higher concentration, of each vial incubation at 37 °C for 30minutes with the same Gate -2 electrode [22, 24]. Then after the hybridization, both the gates (Reference gate and Sensing gates) were electrically characterized using the faraday cage containing source measurement unit (SMU).

2.3.3 Electrochemical characterization for [miRNA-21-3p]

The impedance spectroscopy data were acquired by using a CH Instrument potentiostat 760c model with a three-electrodes set-up, where the gate electrode was connected as working electrode, alongside an Ag/AgCl reference electrode (Elbatech, Livorno Italy) and a Pt wire as counter electrode, all in an electrochemical cell, filled with an aqueous solution of 5 mM $K_3(FeCN_6)$, 0.1 M KCl. The impedance spectra were recorded between 0.1 Hz and 100 MHz, at a fixed potential of 0.2 V. The Nyquist plots fits were obtained with the EIS Spectrum Analyzer software.

2.3.4 Surface Plasmon Resonance Imaging (SPRI) experiments for [miRNA-21-3p]

Gold chips for SPRI were purchased from Xantec Bioanalytics (Germany). The biochips were washed with ethanol and dried under a nitrogen stream. An SPR Imaging apparatus (GWC Technologies, USA) equipped with a white light source and an SF-10 prism coupled with a poly(dimethylsiloxane) microfluidic device was used for the experiments as elsewhere described. [25]. SPR image data were converted into percentage of reflectivity (%R) using the equation %R

= 85 (I_p/I_s) where I_p and I_s refer to the intensity of the reflected p- and s-polarized light, respectively. Kinetic data was obtained by plotting the difference in %R (Δ%R) from selected regions of interest of SPR images as a function of time. PDMS microfluidic device with six parallel microchannels (80 μm depth, 1.4 cm length, 400 μm width) was used to achieve independent control of parallel interactions occurring on the gold chip surface.

The probe was immobilized on the gold surface by introducing solution (0.2 μM in PBS, flow rate 10 μL min^{-1} for 30 minutes) in the microfluidic device in contact with the SPRI gold surface. After the probe immobilization and equilibration with PBS, the modified surface was passivated with 2-mercaptoethanol (1 mM in PBS) for 15 minutes.

miRNA-21 target and miRNA-141 (CTR, control scrambled sequence) solutions (100 pM in PBS + $MgCl_2$ 10 mM) were injected (10 μL min^{-1}) into parallel channels of the microfluidic device for 30 minutes. The discrimination between target and control sequences was assessed by comparing SPRI signals produced by PBS running buffer before and after target and CTR adsorption.

2.4 Materials and methods for α-synuclein

2.4.1 Gate electrodes for α-synuclein biosensor

The substrate used for EGOFETs α-synuclein biosensor was Kapton®. Source, Drain, and Gate electrodes when required, were patterned by positive photolithography. A thin layer of Au was evaporated, namely 5 nm of Cr (as an adhesive layer) and 40 nm of Au. The channel length (L) and width (W) were fixed to 30 μm and 18400 μm (i.e. W/L ratio equal to 613) respectively. After the metal deposition, the substrates were cleaned by sonication in acetone and isopropanol. The devices were then exposed to UV Ozone cleaner for 25 minutes. Subsequently, the chip was immersed in a solution of 2,3,4,5,6-pentafluorothiophenol (PFBT, 2 μL/mL in isopropanol) for 15 minutes to functionalize the gold source-drain contacts, rinsed with isopropanol and dried over N_2. In the devices with the coplanar gate electrode, before the source-drain PFBT functionalization, the planar gate electrode was passivated by a thick coating of dextran (i.e. drop-casting of a dextran solution 10 mg/mL) [26]. Such a sacrificial layer was removed by immersing the device in water after the deposition of the organic semiconductor in order to leave the gate electrode uncovered.

The organic semiconductor deposition method selected was the so-termed Bar-Assisted Meniscus Shearing (BAMS) ands was performed by collaborator group of Prof. Marta Mas Torrent in CSIC, Barcelona, Spain. [27]. A blend of 2,8-Difluoro-5,11-bis(triethylsilylethynyl)anthradithiophene (diF-TES-ADT) and polystyrene Mw= 10000 g/mol (viz. PS_{10k}) was dissolved in chlorobenzene 2% wt with a ratio of 4:1. The solution was deposited at 10 mm/s and at 105 ºC as previously reported [28].

The electrical characterization was performed by using a two-channel Keithley Source Meters 2400 and 2601 controlled with a homemade Matlab script, under ambient temperature and dark condition. The device was conditioned by applying V_{GS} = -0.1 V and V_{DS} = -0.1 V until the I_{DS} reached a steady state. Afterwards, transfer characteristics were recorded in the linear regime. For each functionalization step at least three transfers were measured in PBS 0.01x at physiological pH.

2.4.2 α-synuclein functionalization protocol

Human α-synuclein, glutaraldehyde (25% wt), potassium chloride, sodium phosphate dibasic, iron(III) ferrocyanide, polystyrene (MW 10000 g/mol), chlorobenzene, 2,3,4,5,6-pentafluorothiophenol, dextran (from Leuconostoc Mesenteroides, MW= 64.000-76.000 g/mol), and gold wire (Ø 0.5 mm) were purchased from Sigma Aldrich. Sodium chloride and glycerol were purchased from Panreac Quimica. Recombinant His-tagged Protein G was obtained from BioVision, Inc. $HS–(CH_2)_{11}–(OCH_2CH_2)_6–NH_2·HCl$ (abbreviated as $HSC_{11}EG_6NH_2$) was purchased from ProChimia Surfaces. The anti-(α-synuclein) antibody, α-synuclein(211) that binds to monomeric α-synuclein, was purchased from Santa Cruz Biotechnology, Inc. The organic semiconductor, 2,8-Difluoro-5,11-bis(triethylsilylethynyl)anthradithiophene (diF-TES-ADT), was obtained from Lumtec. Acetone and isopropanol were purchased from Chem-Lab and used without further purification.

2.4.3 Functionalization of gold wire gates

The polycrystalline Au wire was cleaned according to the following protocol: (i) immersion in NaOH 1 M, heating at above 100 ˚C for 15 minutes, (ii) immersion in concentrated H_2SO_4 heating at above 100 ˚C for 15 minutes, (iii) Au electropolish by sweeping the potential from -0.1 V to 1.6 V (15 cycles in H_2SO_4 1 M, as solvent). The functionalization protocols consisted of the following steps:

(i) incubation in the solution of $HSC_{11}EG_6NH_2$ (1 mM EtOH) at 4 °C overnight. The Au wire was successively rinsed with EtOH and bidistilled water and dried by N_2 flow.

(ii) Activation of the amino-group by dipping the $HSC_{11}EG_6NH_2$-coated wire in a solution of glutaraldehyde (2.5% wt in water) at 4°C for 1 h, and successively rinsed with bidistilled water.

(iii) Incubation into the anti-(α-synuclein) antibody solution (40 µg/mL in PBS 1x pH 7.2) at RT for 15 minutes.

An alternative approach for functionalization was tested and relidon the following steps:

(i) Incubation in Recombinant His-tag protein G solution (140 µg/mL in PBS 1x pH 5.5) at RT for 15 minutes.

(ii) Incubation into the anti-(α-synuclein) antibody solution (40 µg/mL in PBS 1x pH 5.5) at RT for 15 minutes.

The α-synuclein solutions were prepared by subsequent dilution starting from 1 mg/mL concentration in PBS 1x pH 7.2. The Ab-coated Au surfaces were incubated with α-synuclein solutions of increasing concentrations (0.25 pM, 2.5 pM, 10 pM, 25 pM, 50 pM, 250 pM, 2.5 nM, 25 nM, 250 nM) for 15 minutes at R.T. and finally abundantly rinsed with PBS 1x pH 7.2 before measurements.

2.4.4 Functionalization of coplanar gates in microfluidic device

The microfluidic device was constituted by two main parts: i) the inner chamber in Polydimethylsiloxane (PDMS) which contains the PBS solution and ii) the outer holder that serves as a support for the Kapton® substrate and properly fixes the PDMS chamber on it. In order to fabricate the chamber and the holder, 3D drawings were made using SketchUp 2017 software . A master for the PDMS chamber and the holder were printed by means of Digital Light Processing (DLP) 3D printer model "B9Creator V1.2HD". The resin of choice was "B9R-2-Black". A Sylgard® 184 silicone elastomer was used to create a liquid solution of PDMS and was deposited over the 3D printed mould and cured in oven at 70 °C for 12 h. When the curing process was finished, PDMS microfluidic chamber was removed from the mould and fixed over the planar electrodes on the Kapton® substrate. It features a microfluidic channel of 500 μm height and a flexible channel connecting both chambers.

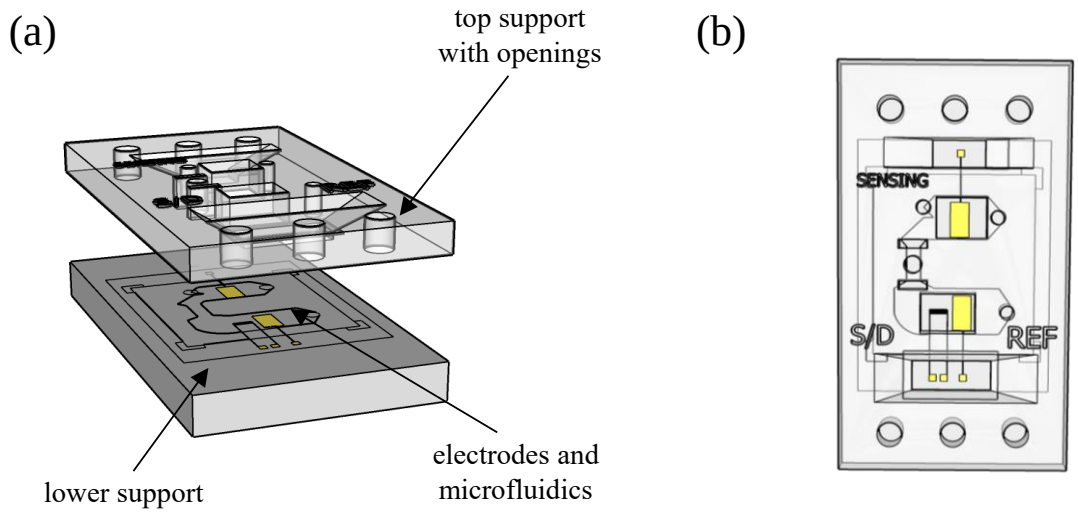

Figure 2.20: Microfluidics setup. (a) Since no chemical processes were used to bond PDMS to silicon substrate and to insure a proper liquid isolation and closing and opening of the middle channel that connect both chambers, a 3D support was designed and printed. It was made of two parts: a bottom one on which the silicon substrate with microfluidic chamber was located, and a top part (featuring openings for tubing

and electrical connections as well as "windows" for controlling solution flow) was fixed on top of the microfluidic chamber. (b) Top view of the setup.

The self-assembled monolayer formation on the coplanar gate electrode was carried out ex-situ by PDMS-assisted printing technique [26]. Afterwards, the microfluidics setup was assembled and the chambers were filled with the electrolyte solution from Inlet, employing a peristaltic pump from Watson-Marlow (400 series pump). At this point, activation of the SAM amino-groups by glutaraldehyde (100 µL, 2.5% v/v) and subsequent Ab (50 µL, 40 µg/ml) immobilization was performed in-situ, by injecting the corresponding solutions from Inlet2 at a flow rate equal to 10 µl/min, connecting simultaneously a peristaltic pump at the Outlet to pump out the same fluid. Then, buffer solution (PBS 1mM) was injected at 10 µl/min through Inlet2 in order to wash away physisorbed biomolecules, approximatively for 5 minutes.

The subsequent α-synuclein sensing was performed in-situ, by injecting the solution containing the receptors (50 µl) at a flow rate of 10 µl/min from Inlet2, for about five minutes. After each functionalization step, a fresh PBS 1x solution was streamed through Inlet2 for at least 3 minutes in order to remove the physisorbed molecules. Finally, the flow was stopped and three transfers were recorded in the linear regime, measuring the device with the sensing gate. The concentrations of α-synuclein solution sensed were the following: 2.5 pM, 25 pM, 250 pM, 2.5 nM, 25 nM, 250 nM. Each sensing experiment started and finished with an electrical characterization by exploiting the reference gate electrode in order to cross-check the overall operation status of the organic semiconductor.

2.4.5 Electrochemical characterization for α-synuclein

Electrochemical characterization of the sensing platform was realized with a potentiostat/galvanostat Autolab (PGSTAT128N). The measurements were carried out in a standard three-electrode configuration cell by using Pt, Ag/AgCl, and Au as the counter, reference, and working electrode, respectively.

Electrochemical Impedance Spectroscopy (EIS) was recorded between 0.1 MHz to 0.1 Hz with an AC amplitude equal to 10 mV. The setpoint voltage was the redox potential of the ferricyanide probe. The impedance response was fitted by means of Randles circuit, whose components are the solution resistance (R_s) in series with the charge transfer resistance (R_{CT}) and the Warburg element (W), whereas in parallel the double-layer capacitance (C_{dl}) [29].

Cyclic voltammetry (CV) was measured at different scan rates (10 mV/s, 30 mV/s, 60 mV/s, 90 mV/s, 100 mV/s, 200 mV/s, 300 mV/s, 400 mV/s, 500 mV/s), sweeping the potential from -0.1 V to 0.45 V. Differential Pulse Voltammetry (DPV) was recorded sweeping the potential from -0.1 V to 0.5 V, at a sweep rate equal to 10 mV/s and its modulation amplitude equal to 25 mV. For the reductive desorption of thiols from Au surface, DPV was recorded sweeping the potential from -0.1 V to -1.4 V in NaOH 1 M.

The whole batch of electrochemical measurements was performed in an aqueous solution containing $K_3[Fe(CN)_6]$ 5 mM, KCl 100 mM, and 50 mM of sodium phosphate buffer. The different pHs were adjusted by using small aliquots of NaOH or HCl 1 M. The non-faradaic measurements were carried out in a solution of KCl (100 mM) and sodium phosphate (50 mM) at pH 7.2.

2.4.6 Surface Plasmon Resonance (SPR) experiments for α-synuclein

For the characterization of the bio-functionalized Au surface by means of Surface Plasmon Resonance (SPR) technique, it was used a SPR platform (Sensia ß-SPR), that employs the Kretschmann configuration and incorporates two flow cells (300 nL each) for an independent analysis. The sample is a 1 cm^2 gold chips (2 nm Cr, 50 nm Au), whereas the whole setup works in a semi-automated way. The flow rate was set at 25 μL/min. The sensor surface was excited with a 670 nm light source. Gold chips were cleaned according to the following protocol: sonication in Acetone, EtOH, and bidistilled water for 1 min respectively. The final step consisted of exposing the surface to the UV Ozone cleaner for 30 minutes. All the functionalization steps were carried out in-situ and measured in real-time except for the amino-terminated thiols adsorption, which was carried out ex-situ because of the incompatibility of the microfluidics tubes with EtOH.

2.5 References

[1] Wu C, Yi R, Liu Y-J, et al. Delta DLP 3D printing with large size. 2016 IEEE/RSJ International Conference on Intelligent Robots and Systems (IROS) 2016[Online] 2016.

[2] Parkula V. Organic Electronic Transistors for Biosensing. 2019[Online] [Ph.D dissertation] Università degli Studi di Modena e Reggio Emilia: Modena 2019.

[3] Ko D-H, Gyak K-W, Kim D. Emerging Microreaction Systems Based on 3D Printing Techniques and Separation Technologies. Journal of Flow Chemistry 2017; 7(3):1–10.

[4] Campana A, Cramer T, Greco P, et al. Facile maskless fabrication of organic field effect transistors on biodegradable substrates. Appl Phys Lett American Institute of Physics 2013; 103(7):073302.

[5] Magliulo M, Mulla MY, Manoli K, et al. Ultrasensitive printable biosensors for point-of-care applications. 2015[Online] 2015 [cited 2020]. Available at: https://spie.org/news/5961-ultrasensitive-printable-biosensors-for-point-of-care-applications.

[6] Stewart Z. Organic Thin-Film Transistors and TIPS-Pentacene. Lewis Honors College Capstone Collection 2013; 11.

[7] Grot W. 5 - Applications. In: Grot W, Ed. Fluorinated Ionomers (Second Edition) William Andrew Publishing 2011; pp. 81–156.

[8] Schlesinger M. Electroplating. In: Kirk-Othmer Encyclopedia of Chemical Technology American Cancer Society 2004;

[9] Farag AAM, Yahia IS. Structural, absorption and optical dispersion characteristics of rhodamine B thin films prepared by drop casting technique. Optics Communications 2010; 283(21):4310–17.

[10] Park J, Lee S, Lee HH. High-mobility polymer thin-film transistors fabricated by solvent-assisted drop-casting. Organic Electronics 2006; 7(5):256–60.

[11] Kajal P, Ghosh K, Powar S. Manufacturing Techniques of Perovskite Solar Cells 2018; pp. 341–64.

[12] Toepke MW, Beebe DJ. PDMS absorption of small molecules and consequences in microfluidic applications. Lab Chip The Royal Society of Chemistry 2006; 6(12):1484–86.

[13] Fujii T. PDMS-based microfluidic devices for biomedical applications. Microelectronic Engineering 2002; 61–62:907–14.

[14] Jo B-H, Van Lerberghe LM, Motsegood KM, et al. Three-dimensional micro-channel fabrication in polydimethylsiloxane (PDMS) elastomer. Journal of Microelectromechanical Systems 2000; 9(1):76–81.

[15] Mata A, Fleischman AJ, Roy S. Characterization of Polydimethylsiloxane (PDMS) Properties for Biomedical Micro/Nanosystems. Biomed Microdevices 2005; 7(4):281–93.

[16] Anderson JR, Chiu DT, Jackman RJ, et al. Fabrication of Topologically Complex Three-Dimensional Microfluidic Systems in PDMS by Rapid Prototyping. Anal Chem American Chemical Society 2000; 72(14):3158–64.

[17] Seghir R, Arscott S. Extended PDMS stiffness range for flexible systems. Sensors and Actuators A: Physical Elsevier 2015; 230:33–39.

[18] Ryno SM, Risko C, Brédas J-L. Impact of Molecular Packing on Electronic Polarization in Organic Crystals: The Case of Pentacene vs TIPS-Pentacene. J Am Chem Soc American Chemical Society 2014; 136(17):6421–27.

[19] Park SK, Mourey DA, Han J-I, et al. Environmental and operational stability of solution-processed 6,13-bis(triisopropyl-silylethynyl) pentacene thin film transistors. Organic Electronics 2009; 10(3):486–90.

[20] Giri G, Verploegen E, Mannsfeld SCB, et al. Tuning charge transport in solution-sheared organic semiconductors using lattice strain. Nature 2011; 480(7378):504–08.

[21] Cardoso AR, Moreira FTC, Fernandes R, et al. Novel and simple electrochemical biosensor monitoring attomolar levels of miRNA-155 in breast cancer. Biosensors and Bioelectronics 2016; 80:621–30.

[22] Cardoso AR, Moreira FTC, Fernandes R, et al. Novel and simple electrochemical biosensor monitoring attomolar levels of miRNA-155 in breast cancer. Biosensors and Bioelectronics 2016; 80:621–30.

[23] Yagi N, Satonaka K, Horio M, et al. The Role of DNase and EDTA on DNA Degradation in Formaldehyde Fixed Tissues. Biotechnic & Histochemistry Taylor & Francis 1996; 71(3):123–29.

[24] Bhagavan NV, Ha C-E. Chapter 21 - Structure and Properties of DNA. In: Bhagavan NV, Ha C-E, Eds. Essentials of Medical Biochemistry (Second Edition) Academic Press: San Diego 2015; pp. 381–400.

[25] Grasso G, D'Agata R, Zanoli L, et al. Microfluidic networks for surface plasmon resonance imaging real-time kinetics experiments. Microchemical Journal 2009; 93(1):82–86.

[26] Leonardi F, Tamayo A, Casalini S, et al. Modification of the gate electrode by self-assembled monolayers in flexible electrolyte-gated organic field effect transistors: Work function: Vs. capacitance effects. RSC Advances 2018; 8(48):27509–15.

[27] Temiño I, Pozo FG Del, Ajayakumar MR, et al. A Rapid, Low-Cost, and Scalable Technique for Printing State-of-the-Art Organic Field-Effect Transistors. Advanced Materials Technologies 2016; 1(5):1–7.

[28] Zhang Q, Leonardi F, Casalini S, et al. High performing solution-coated electrolyte-gated organic field-effect transistors for aqueous media operation. Scientific Reports Nature Publishing Group 2016; 6:1–10.

[29] Bard AJ, Faulkner. LR. Electrochemical Methods: Fundamentals and Applications,. America 2002[Online] 2002.

CHAPTER 3

CHARACTERIZATION METHODS

3.1 Introduction

In the following Chapter, I will report on the characterization techniques employed to gather sensor responses or to assess the quality of the device components. In particular, electrical characterization instrumentation and protocols are described in subchapter 3.2, with a focus on the organic electronics target application, where low voltage/low current operations and the capability to spot leakage currents between Gate and Source electrodes are two of the critical requirements of a measurement tool. In subchapters 3.3 and 3.4, I will give a brief overview of the electrochemistry methods used to characterize the gold electrodes after the functionalization step. Cyclic voltammetry and impedance spectroscopy were used consecutively to evaluate the relationship between functionalization time and apparent coverage of the electrode. In subchapter 3.5, I will describe the atomic force microscopy technique, employed to characterize the surface morphology of the organic transistor device. Finally, in subchapter 3.6, I will briefly report on the surface plasmon resonance, as a gold -standard analytical tool to determine the binding constant between antibody and target analyte, or also other affinity-based interactions.

3.2 Electrical Characterization using Faraday Cage

In order to electrically characterize organic transistors, and in particular, EGOFETs, a Source - Measurement Unit (SMU) with a Faraday cage was used. With SMU instrumentation it is possible to apply varying potentials and to record the respective output current of the device. Employed Agilent (California, U.S.A) model B2912 SMU features high-resolution recording, up to 10 fA / 100 nV, and low-noise electronics. SMU has two independent source and measurement channels. Channel 1 was used for applying the potentials between Gate and Source whereas Channel 2 was used to apply the potentials between Source and Drain. SMU communicates with the customized software with user interface, while applying the potentials simultaneously and measuring each channel's resulting current.

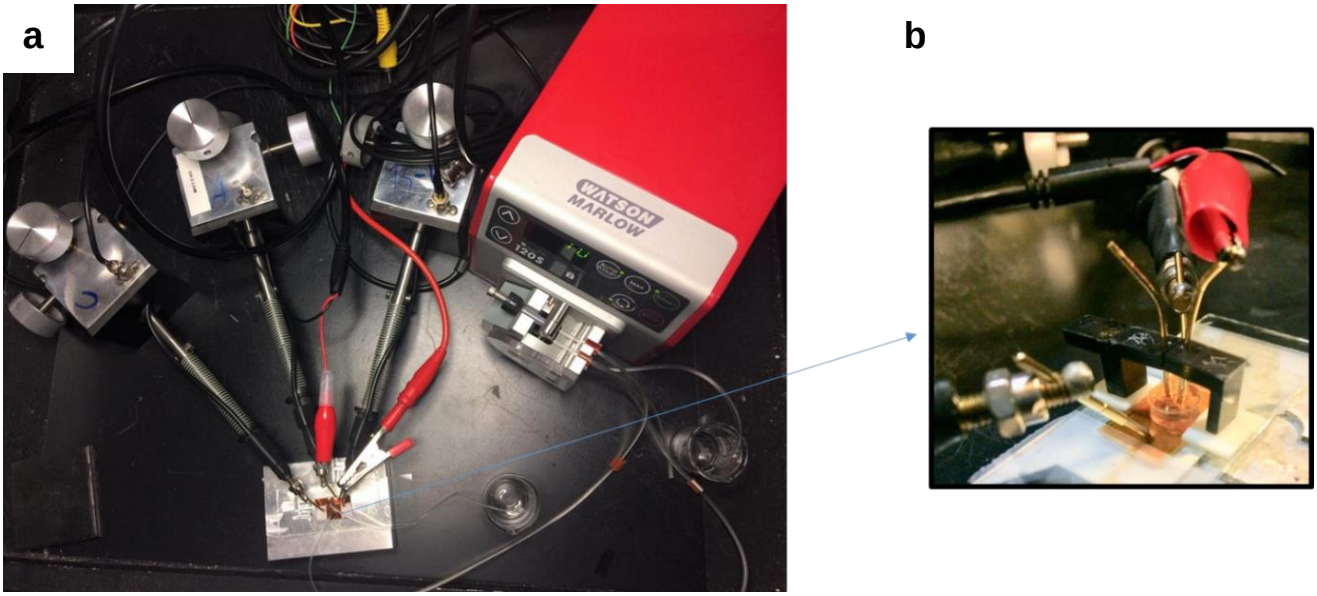

Figure 3.1:a) Snapshot inside the Faraday cage including probes, peristaltic pump and connectors (left).b) Detail of the EGOFET device during measurement

Since the EGOFET can be operated in less than 1V, usually the varying potentials applied between Gate and Source will be between -0.3 V to -0.9 V and Drain-Source voltages are kept at constant value -0.2 V, thus the EGOFET devices are operated in the so-called linear regime.

Once the potentials are fixed, the other parameters of choice such as the delay between steps in Gate Source potential or repeated cycling were chosen accordingly. By neglecting the electromagnetic interferences from the surrounding ambiance, the low-noise signals were recorded. This was possible due to the connection of the SMU with the Faraday cage via the triaxial cable.

The device, fabricated according to what was reported in the Chapter on Materials and methods (Chapter 2.3), has been placed inside the Faraday's cage and contacted by means of high-precision micromanipulators. Finally, the data recorded during the measurement was processed by Origin lab Origin Pro 2018 Software.

3.3 Cyclic Voltammetry

In the last fifteen years, cyclic voltammetry has become a prominent tool for researching electrochemical reactions. Organic chemists have used it to investigate biosynthetic reaction pathways as well as electrochemically generated free radicals [1]. CV is widely used in the domains of electrochemistry, inorganic chemistry, organic chemistry, and biochemistry due to its versatility and ease of measurement [2].

CV (Cyclic Voltammetry) is an electrochemical technique for determining the current that occurs in an electrochemical cell when the voltage exceeds that predicted by the Nernst equation.

Cyclic Voltammetry can be used to investigate qualitative information about electrochemical processes under a variety of situations, such as the presence of intermediates in oxidation-reduction reactions and a reaction's reversibility. CV can also be used to estimate a system's electron stoichiometry, an analyte's diffusion coefficient, and the formal reduction potential, which can be used as a tool for identification.

CV is accomplished by varying the voltage of a working electrode with respect to a reference electrode and measuring the resulting current [3]. The working electrode's potential is compared to a reference electrode that maintains a constant potential, and the resulting applied potential provides an excitation signal similar to that seen in Figure 3.2. The potential first scans , starting with a higher potential (a) and finishing at a lower potential (b) (d). The potential extrema (d), called the switching potential, is the point at which the voltage is high enough to cause an analyte to oxidize or reduce. The potential is later scanned in reversal , which takes place from (d) to (g). This cycle can be repeated as needed, with the scan rate varying. The scan rate is determined by the slope of the excitation signal [3].

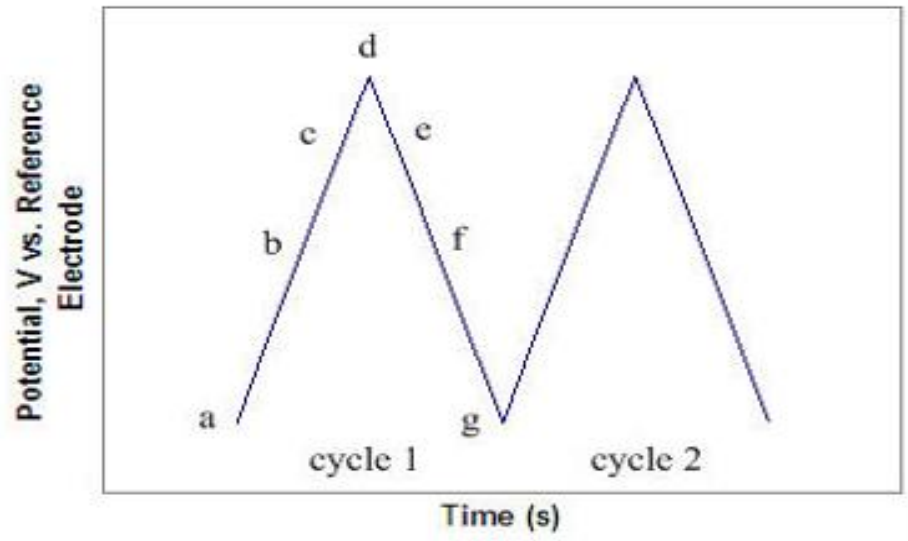

Figure 3.2: Cyclic Voltammogram Excitation Signal

The potential scan is generally applied as an excitation signal using a waveform generator applied to an electrochemical cell via a potentiostat. A current-to-voltage converter measures the resulting current, and an XY recorder or oscilloscope displays the voltammogram (Figure 3.3). Although modular instruments are also utilized, the first three parts are usually combined into a single electrical device.

A potentiostat is an electronic device that employs a dc power supply to provide a stable and precise potential while enabling small currents to be taken into the system without affecting the voltage. The potentiostat ensures that the potential of the working electrode is not changed by the reaction(s) [3].

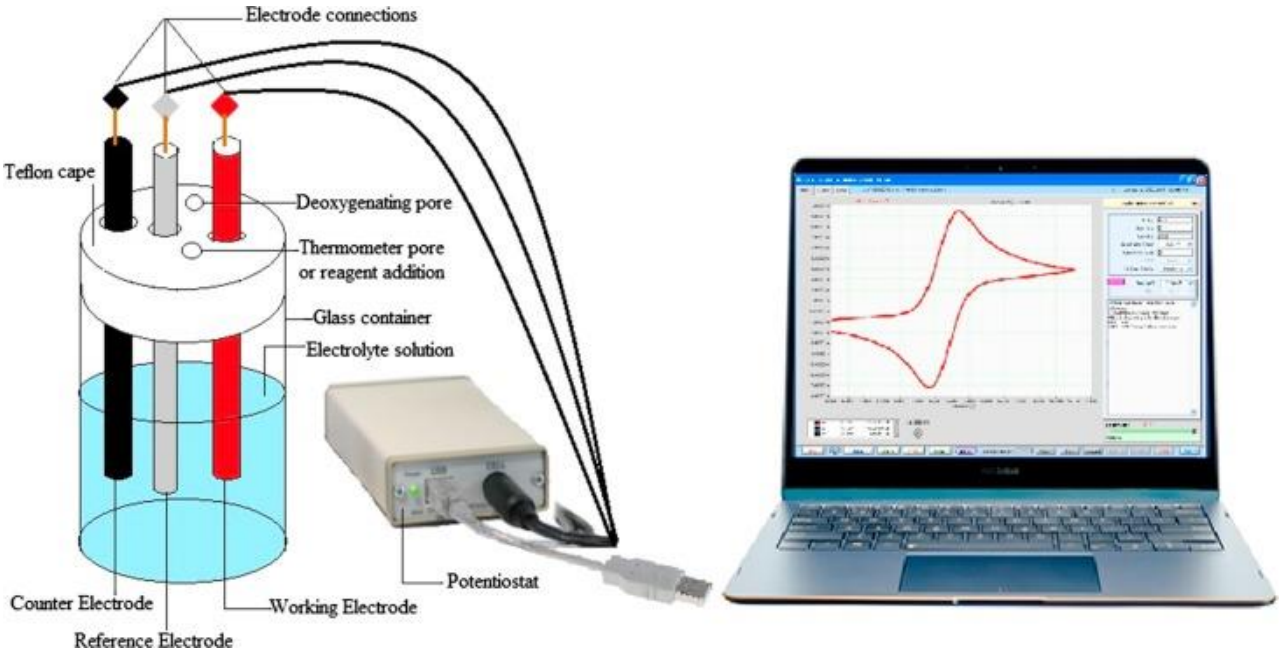

Figure 3.3: Instrumentation for cyclic voltammetry [4]

Because concentration is proportional to the current in a reversible, Nernstian system, the concentration of an unknown solution can be estimated by creating a calibration curve of current vs. concentration [3, 5]. In Figure 3.4 which is reported from Reference [2] the concentration profiles for the redox couple Ferrocyanide(Fc)/Ferricyanide(Fc+) (mM) as a function of distance from the electrode, during the consecutive stages of the voltammogram.

It is possible to correlate the presence of the reduced or oxidize form of the moiety, considering the value of the applied potential. The characteristic values depend also on the scan rate at which the voltammogram is performed, because of the interplay between diffusion and kinetic constants of reactions [6].

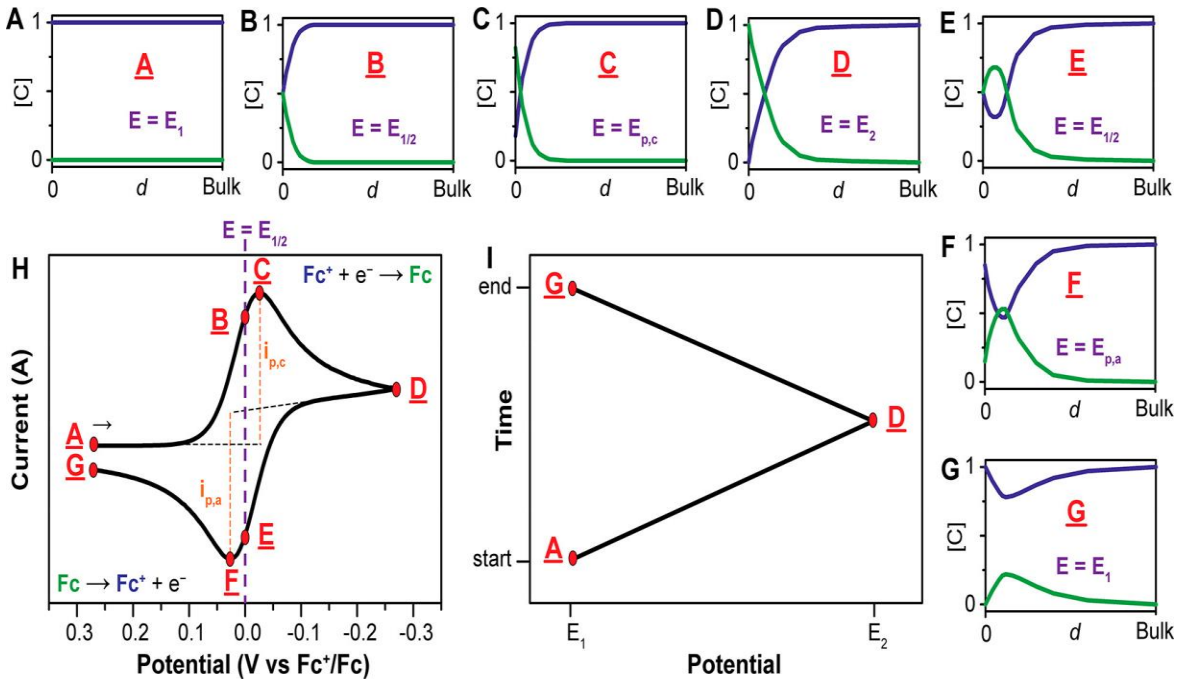

Figure 3.4: (A–G): Concentration profiles of Ferrocyanide/Ferricyanide couple vs distance d from the electrode in bulk solution (H): Voltammogram measurements of the reversible reduction of a 1 mM Fc^+ solution to Fc, with a scan rate of 100 mV s^{-1}, whereas $i_{p,c}$ is the peak cathodic current and $i_{p,a}$ is the peak anodic current.Also $E=E_{1/2}$ is the average potential between F and C. (I): Applied potential as a function of time for a generic cyclic voltammetry experiment, with the initial, switching, and end potentials represented (A, D and G, respectively). The negative potential is swept from the starting potential E_1 to the switching potential E_2 and it is referred as cathodic trace. The direction of the scan is then reversed, and a positive potential is swept back to E_1, referred as the anodic trace [2].

3.4 Impedance Spectroscopy

Impedance Spectroscopy (IS) is emerging as a more acceptable approach with some distinct characteristics, among other non-invasive approaches for diagnostics, besides being a standard electrochemical technique for analysis. Oliver Heaviside was the first to introduce impedance spectroscopy in the 1880s. Impedance spectroscopy (IS) is widely used to measure the capacitance of optimally polarizable electrodes, resulting in the development of models for the different functionalised electrodes [7]. As a result of modeling the low signal findings obtained with the alternating current setup, the focus in electrochemistry has switched from time/concentration dependence to frequency-related phenomena.

The relaxation times, or more practically, the distribution of their relaxation periods, is characteristic of the electrical double layers and their inherent capacitive reactance. The electrical response of a heterogeneous cell can vary significantly depending on the charge species present, the electrolyte chemical composition, and the texture and composition of the electrodes. Impedance Spectroscopy is a potent and relatively recent method of assessing numerous electrical characteristics of materials and their interactions with electrically conducting electrodes [8].

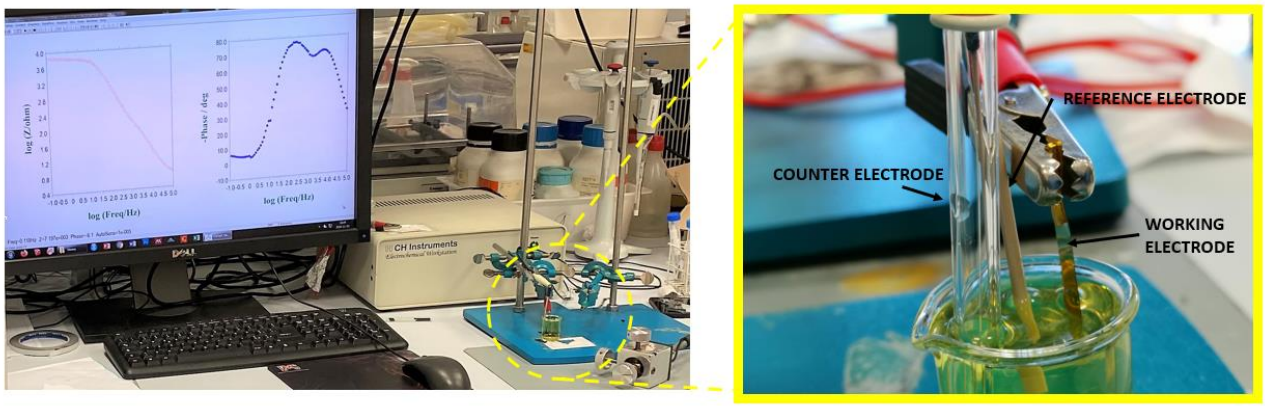

Figure 3.5: Set up used for Impedance Spectroscopy measurement (left). The counter electrode used was platinum (Pt)wire, working electrode used was gold (Au) wire and reference electrode asAg/AgCl (right)

Impedance spectroscopy (IS) encompasses the measurement of material's linear electrical response to low – potential excitation (including electrode effects) and subsequent analysis of the response to obtain relevant information about the system's physicochemical qualities. The analysis is generally carried out in the frequency domain, although measurements are sometimes made in the time domain and then Fourier is transformed to the frequency domain [8].

Impedance spectroscopy is a non-destructive technique and so can provide time-dependent information about the properties of a system but also about ongoing processes such as corrosion of metals, discharge and charge of batteries, electrochemical reactions in fuel cells, capacitors or any other electrochemical process [9].

Nyquist and bode plots depict the correlations between simple circuits and impedance spectra. The Nyquist plot shows the impedance spectra of an electrode/electrolyte contact as a semicircle. The

charge transfer resistance and the interfacial capacitance are connected in parallel in the equivalent circuit for this interface, and a comparison of this circuit with the impedance spectra yields structural and physical information about the interface [10].

$$Z=E/I= Z_0 \exp(i\Phi) = Z_0 (\cos\Phi + i\sin\Phi) \quad (1)$$

There is a real and an imaginary portion to the statement for Z (ω). A “Nyquist plot” is created by plotting the real part on the X-axis and the imaginary component on the Y-axis of a chart.

$$1/Z= (1/R) + (1/i\omega C) \quad (2)$$

The Nyquist plot results from the RC circuit (Figure 3.6). The semicircle is characteristic of a single "time constant”.

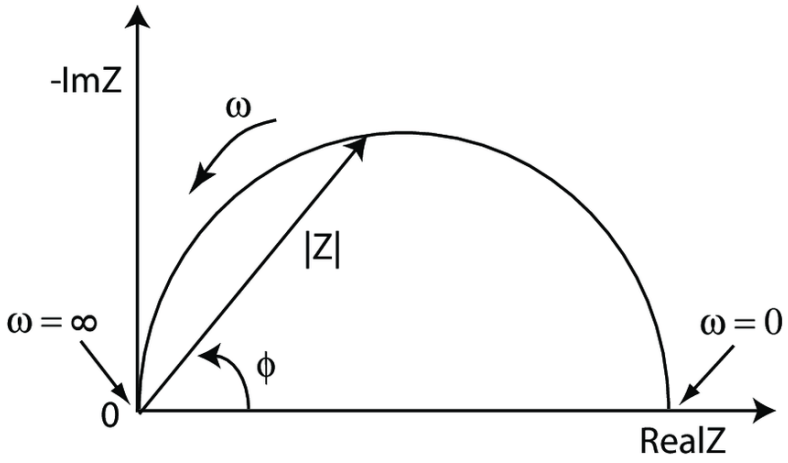

Figure 3.6: Nyquist plot with Impedance vector [11]

The "Bode plot" is another prominent presenting approach. The impedance is plotted on the X-axis with log frequency (log ω) on the X-axis and absolute impedance ($|Z| = Z_0$) and phase-shift on the Y-axis. Unlike the Nyquist plot, the Bode plot displays frequency information explicitly (Figure 3.7).

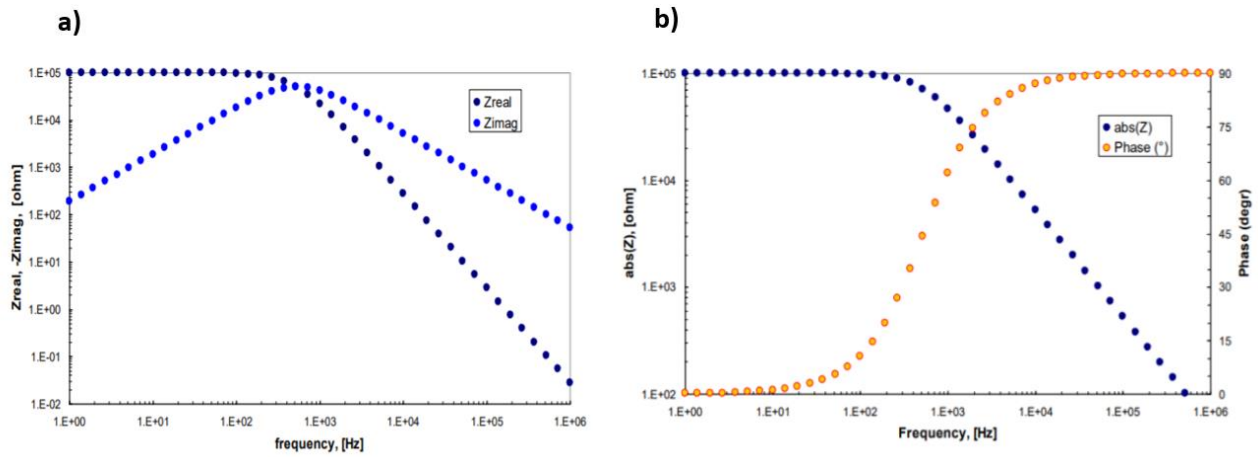

Figure 3.7: a) Bode plot with Frequency Vs Zreal , Zimag [9] b)Bode Plot with absolute(Z) phase vs Frequency [9]

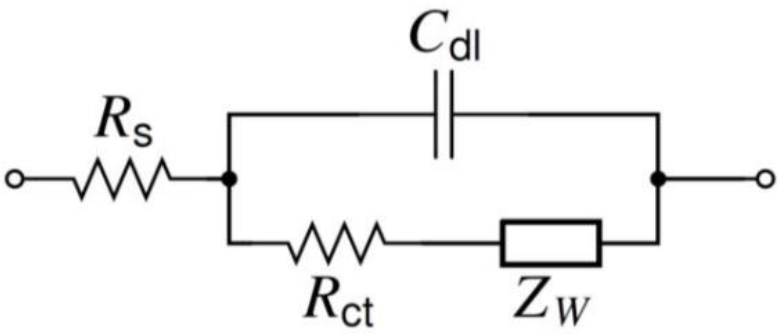

Figure 3.8: Equivalent Randles circuit [12]

- where Rs is the electrical resistance of the electrolyte
- Cdl the double-layer capacitance of the electrolyte interface
- Rct the charge transfer resistance

The Nyquist plot is used to describe the electrical circuit (Figure 3.8, Figure 3.9). Ion diffusion (Warburg impedance) is the dominating impact at low test frequencies, and the figure is practically

a straight line with a slope of 45˚. The figure is defined by a semi-circle with a diameter equal to the charge transfer resistance Rct at high frequencies, when the diffusion time constant is substantially longer than the signal period [12].

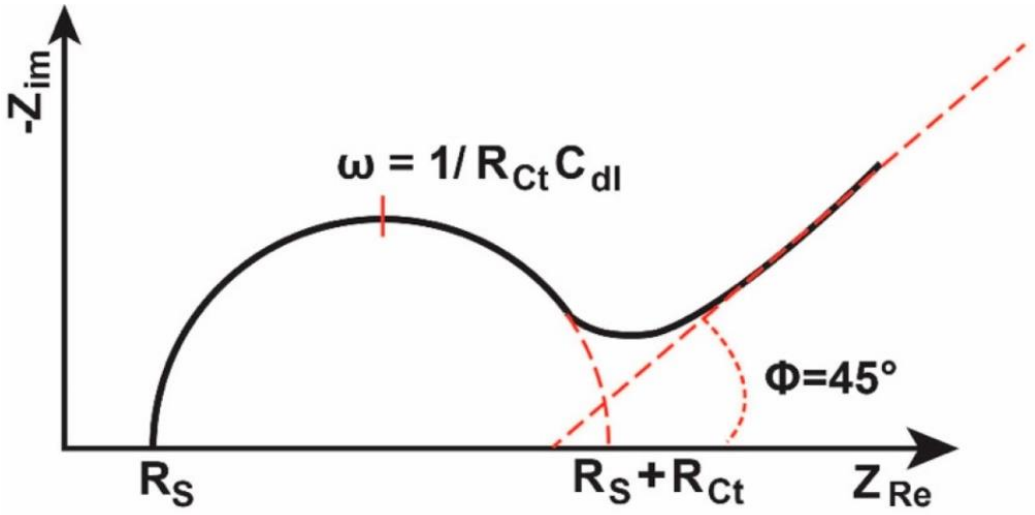

Figure 3.9: Nyquist plot of the equivalent circuit [13]

Other applications include Impedance spectroscopy as a most useful tool for determining the electrical structure of cells and tissues and it can predict aspects of the performance of chemical sensors and fuel cells and it has been used extensively to investigate membrane behaviour in living cells [8]. Impedance Spectroscopy is a technique with exquisite resolution since it resolves linear electrical properties into uncorrelated variables, as a function of frequency also provides biologically useful insight into the pathways for current flow in film of adsorbed bioreceptors, or several cells and tissues [14].

3.5 Atomic Force Microscopy (AFM)

The invention of the scanning tunneling microscope (STM) in 1981 laid the foundation for the visualization of layers of molecules at the atomic level and won ‘BINNING and ROHRER’ the Nobel Prize in 1986 [15]. STM is based on the tunneling effect and uses the tunneling current between an electrically conductive STM-tip and the sample as a parameter to determine the surface

topography. If tip and sample are several angstroms apart from each other a tunneling current will flow respectively to the distance. A piezo actuator can adjust and measure the distance to keep the current constant and therefore map the surface [16]. Unfortunately, in order to use the tunneling current, the sample has to be electrically conductive. Thus, STM is restricted to conductive and semi-conductive layers making the selection of materials rather small. However, during their experiments with the STM, 'BINNING and co-workers observed accompanying forces acting on the tip when it was close to the surface. The usage of that forces later led to the invention of the atomic force microscope (AFM) in 1985 [17].

Compared to STM, AFM uses a force sensing cantilever with a sharp tip at the end instead of the conductive STM-tip. This small change in the setup also allows scanning of non-conductive surfaces, making AFM one of the most common techniques in topographical measurement. The range of application reaches from classical inorganic layers, over composite layers, to biological samples. The force sensing principle of the cantilever is based on Hooke's law:

$$F = -k\Delta z \tag{3}$$

with F being the interacting force between sample and cantilever, k is the spring constant of the cantilever, and Δz being its deflection. The spring constant is a material parameter that is defined by the Young's modulus E and the dimensions of the cantilever. Nowadays, AFM cantilevers typically consist of Si or Si_3N_4. The radius of the tip-curvature is usually a couple of nm to 20 nm at the end.

Figure 3.10 shows the working principle of AFM and its key components. During scanning, the piezo-driven xyz scan table adjusts the sample position towards the tip of the cantilever. Depending on the scan mode, the cantilever is either excited to oscillate by a driving voltage or firmly pressed against the surface. If the cantilever tip approaches the sample surface, the cantilever deflects due to surface forces or direct contact. A laser beam, directed on the flat upper side of the cantilever, is reflected of the cantilever and detected by a position-sensitive photodiode, resulting in tracking every slight change in cantilever deflection. According to the diode-signal, a feedback loop can regulate the position of the xyz scan table.

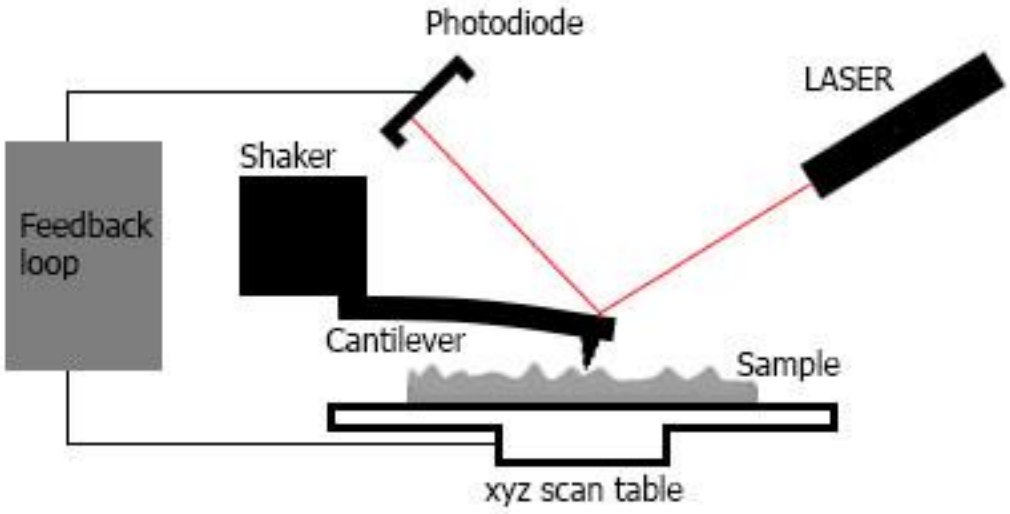

Figure 3.10: Working principle and key components of AFM

There are several ways to operate the AFM each having its respective advantages and disadvantages [18]. The 3 most common ones are contact, non-contact and tapping mode.

In contact mode, the cantilever pushes directly against the surface with a defined force set by the user. Laser and photodiode measure the deflection of the cantilever and the feedback loop adjusts the z-parameter, keeping the deflection constant. The advantages of this mode are high scan speeds and high resolution. But due to constant direct contact, the surface can be damaged, making contact mode unsuitable for delicate samples, like biological materials. It is also not suited for detecting single atoms and small molecules.

In non-contact mode, as the name implies, the tip is not in direct contact with the surface. Instead, the shaker component causes the cantilever to continuously oscillate at resonance frequency over the surface. If the tip approaches the surface, surface forces, like van der Waals forces, act on the tip resulting in a change in amplitude and frequency. Laser and photodiode detect the change and the feedback loop can compensate it by varying the z-parameter, resulting in the tip scanning over the sample at a constant height. Due to not touching the surface, even soft samples can be scanned. A major disadvantage, however, is the slow scan speed and the lower resolution compared to contact mode.

The tapping mode is a mixture between contact and non-contact mode. Like in non-contact mode, the cantilever is excited by the shaker and oscillates near or at resonance frequency over the surface, but this time, the amplitude is much higher. This causes the tip to touch the surface for a short period of time. The impact can alter the amplitude and frequency of the cantilever which can be detected by the laser and the photodiode. In order to acquire the topographical image, the feedback loop can keep the amplitude constant. Despite the higher impact force during surface contact compared to contact mode, it is a much gentler interaction due to the very short duration. Hence, tapping mode has the advantages of a high resolution, a mediocre scan speed and a minimal sample damage, which also allows scanning of soft structures like biological samples. Besides amplitude and frequency alteration during impact, there can also be a phase angle shift of the cantilever [19]. This shift occurs when the surface properties (elasticity, crystallinity, etc.) change and can be used to generate a material mapping of the sample.

In this work, all AFM were generated using a SMENA AFM (see Figure 3.11). Tapping mode was used to acquire the topographical pictures and phase shift for material contrast. The roughness was calculated using Gwyddion software.

Figure 3.11: a) SMENA AFM and b) Gwyddion software [20]

3.6 Surface Plasmon Resonance

SPR is a real-time, optical based label-free technique applied in detection of interaction of bio molecules with specific bioreceptors adsorbed or covalently linked to the gold biochip surface. SPR stands for gold-standard technique to study Ligand binding protein interactions, with many applications in medical science, i.e.study of potential molecular targets in drugs validation process [21–23]. SPR sensorgrams allow to extract binding affinities and measure kinetics with smaller sample sizes. Current instrumentation has the potential to provide medium to high throughput [22, 23].

Traditional SPR technique requires two binding molecules for its molecular protein interaction assay. One binding molecule is fixed permanently on the chip of sensor either by covalent bond or by adsorption and the other binding material is allowed to flow over the sensor interface [23].

SPR technique measures minute changes in the refractive index, which is the key for sensing bio molecular interactions. It helps to identify, monitor and analyze the interaction of analyte and receptor molecules within a close vicinity [21–23]. SPR finds applications in various fields such as biotechnology, electro chemistry, electronics and instrumentation, molecular physics, food industry, laboratory and testing.

Historically, SPR technique was experimented during the early 1960s, when excitation of Surface Plasmons during interaction were studied and analyzed [24]. In 1990, the first commercially available SPR product named Biocare came into the market and it became the most reliable, accurate, real time instrument effectively measuring the interaction of bio molecules [25]. Research and development in Surface Plasmon Resonance in the last three decades have been steadily increasing since the release of first commercially successful product.

Propagating SPR sensors and localized SPR sensors are the two main types of SPR sensors. As the name suggest PSPR sensors get excited on gold film and their resonance will propagate into the interface. Localized SPR sensors do not exhibit propagation, when the sensor gets excited on nano-structured gold film [26].

Prism, metal coating, light source, detector, cover glass and solution phase are the main components of the fundamental SPR setup. One of the most familiar configurations for SPR is

Kretschmann and Otto Configuration. It excites the Surface plasmon resonance, where prism is being coated with metal film to a thickness ranges upto 50 nm [27]. The light travels from medium of higher refractive index to medium of lower refractive index.

The angle of incidence is greater than the critical angle and is referred to as the Total critical angle. In the lower refractive index, Evanescent waves are formed. In the solution, these electromagnetic waves can travel up to a distance up to 250 nm [28]. When the light source interacts with the interface, it generates waves of electron charges which are referred as Plasmons. [29].

BioReceptor molecule is generally immobilized on the gold films by means of continuous aqueous flow. In order to detect the binding between Analyte and receptor molecule. Analyte molecule is introduced into the aqueous solution.

A solution of our interest, which generally have low refractive index with respect to the prism, is flown on the interface. Parallel polarized light is passed into the Prism, under the thin layer of gold film, which gets excited causing generation of surface Plasmons at a critical angle. The angle of incident light decreases inversely to the light absorption [28]. Evanescent waves excite the Plasma of the metal film, at an angle greater than the critical angle. Electron charges in the form of waves are generated, thereby causing Surface Plasmon Resonance. SPR angle indicates the angle where reflectivity is smaller than the incident angle [29].

Sensogram helps to visualize the real time response of an experiment conducted with an SPR instrument. During binding between receptor and Analyte molecules, the refractive index changes, thereby increasing the intensity of the signal. This increase of signal is referred to as Response units (RU). At the start of the experiment, binding between analyte and receptor molecules doesn’t occur and this shows the initial critical angle. As soon as the analyte is being injected into the flow cell, they start to bind with the immobilized receptor, which is referred to as the association phase. The binding sites are occupied causing a change in the refractive index. The curve indicates the rate of association [28].

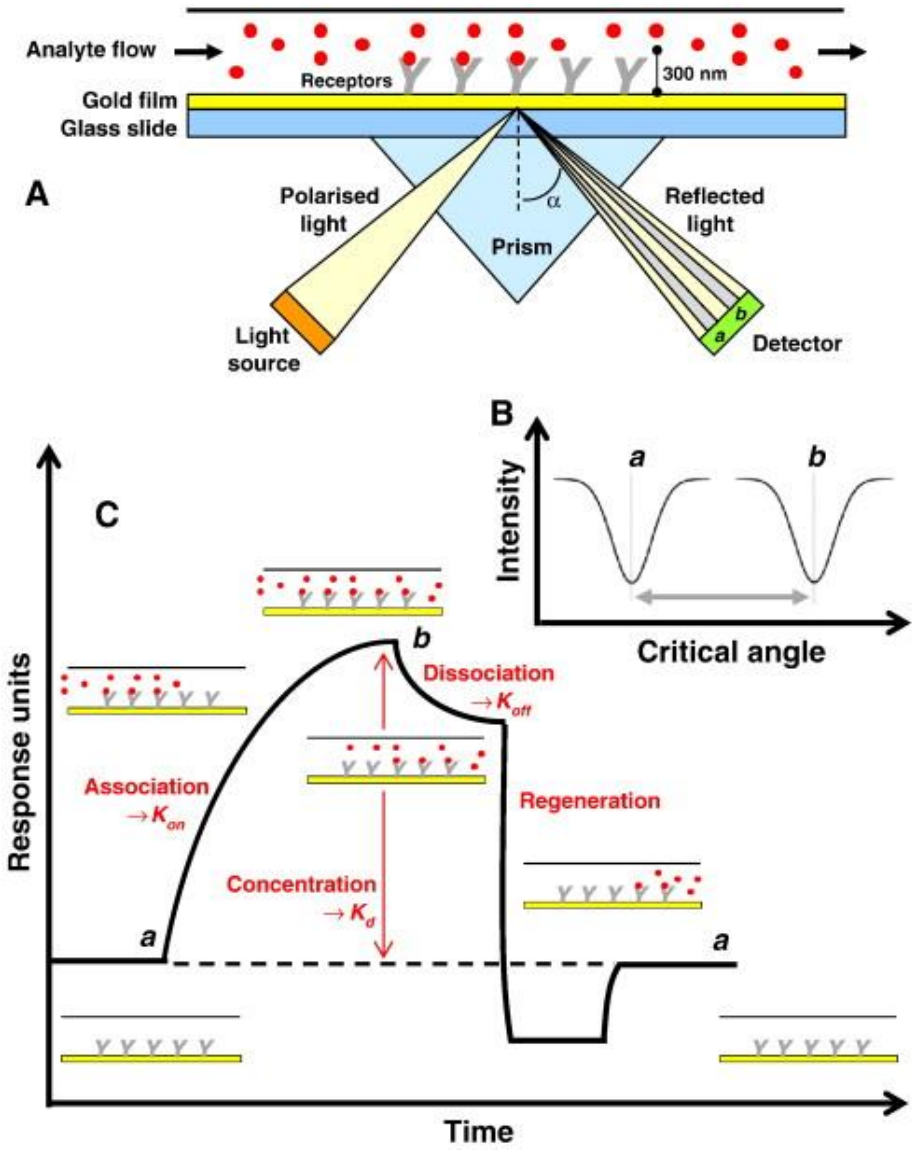

Figure 3.12: A. Instrument set up for an SPR experiment based on BIAcore™ technology inorder to detect the binding of an analyte molecule to a receptor molecule, the receptor molecule is usually immobilised on the sensor surface and the analyte molecule is injected in the aqueous solution through the flow cell B. Change in the critical angle of incident light from angle a to angle b on binding of an analyte molecule to a receptor molecule C. Response of the SPR experiment in the form of a sensorgram. If interaction between the immobilised receptor molecule and the analyte molecule occurs, the refractive index at the surface of the gold film changes and this is seen as an increase in signal intensity [28].

Concentrations of analyte ad receptor molecules are measured and provide Binding affinity. Rate of dissociation is measured when the analyte is removed during the flow of buffer, thereby

inducing dissociation of the target to reach equilibrium. Dissociation curve depicts the rate of dissociation of the experiment. Molecular weight of bio molecules, affinity constant, refractive index, analyte molecule, receptor molecule, light source and type of prism determine the detection abilities of SPR [28].

3.7 References

[1] Mabbott GA. An introduction to cyclic voltammetry. J Chem Educ American Chemical Society 1983; 60(9):697.

[2] Elgrishi N, Rountree KJ, McCarthy BD, et al. A Practical Beginner's Guide to Cyclic Voltammetry. J Chem Educ American Chemical Society 2018; 95(2):197–206.

[3] Kissinger PT, Heineman WR. Cyclic voltammetry. J Chem Educ American Chemical Society 1983; 60(9):702.

[4] Gomaa EA, Negm A, Abu-Qarn RM. Cyclic voltammetry study of the electrochemical behavior of vanadyl sulfate in absence and presence of antibiotic. Measurement 2018; 125:645–50.

[5] Chooto P. Cyclic Voltammetry and Its Applications 2019;

[6] Aristov N, Habekost A. Cyclic Voltammetry - A Versatile Electrochemical Method Investigating Electron Transfer Processes. World Journal of Chemical Education Science and Education Publishing 2015; 3(5):115–19.

[7] Macdonald DD. Reflections on the history of electrochemical impedance spectroscopy. Electrochimica Acta 2006; 51(8):1376–88.

[8] Macdonald JR. Impedance spectroscopy. Ann Biomed Eng 1992; 20(3):289–305.

[9] Markovsky B. Basics of Impedance Spectroscopy. 2014[Online] Bar - Ilan University 2014.

[10] Itagaki M. Principle and Analytical Method of Impedance Spectroscopy. Hyomen Kagaku 2012; 33(2):64–68.

[11] Addy SA. Electrochemical arsenic remediation for rural Bangladesh. 2008[Online] Lawrence Berkeley National Lab. (LBNL), Berkeley, CA (United States) 2008.

[12] Grossi M, Riccò B. Electrical impedance spectroscopy (EIS) for biological analysis and food characterization: a review. Journal of Sensors and Sensor Systems Copernicus GmbH 2017; 6(2):303–25.

[13] Khan NI, Song E. Lab-on-a-Chip Systems for Aptamer-Based Biosensing. Micromachines Multidisciplinary Digital Publishing Institute 2020; 11(2):220.

[14] Macdonald JR, Johnson WB. Fundamentals of Impedance Spectroscopy. In: Impedance Spectroscopy John Wiley & Sons, Ltd 2005; pp. 1–26.

[15] Binnig G, Rohrer H, Gerber Ch, et al. Tunneling through a controllable vacuum gap. Appl Phys Lett American Institute of Physics 1982; 40(2):178–80.

[16] Giessibl FJ. Advances in atomic force microscopy. Rev Mod Phys American Physical Society 2003; 75(3):949–83.

[17] Binnig G, Quate CF, Gerber Ch. Atomic Force Microscope. Phys Rev Lett American Physical Society 1986; 56(9):930–33.

[18] Marrese M, Guarino V, Ambrosio L. Atomic Force Microscopy: A Powerful Tool to Address Scaffold Design in Tissue Engineering. J Funct Biomater 2017; 8(1):7.

[19] Jagtap R, Ambre A. Overview literature on atomic force microscopy (AFM): Basics and its important applications for polymer characterization. undefined 2006;

[20] Parkula V. Organic Electronic Transistors for Biosensing. 2019[Online] [Ph.D dissertation] Università degli Studi di Modena e Reggio Emilia: Modena 2019.

[21] Silin V, Plant A. Biotechnological applications of surface plasmon resonance. Trends in Biotechnology 1997; 15(9):353–59.

[22] Gopinath SCB. Biosensing applications of surface plasmon resonance-based Biacore technology. Sensors and Actuators B: Chemical 2010; 150(2):722–33.

[23] Altintas Z, Uludag Y, Gurbuz Y, et al. Development of surface chemistry for surface plasmon resonance based sensors for the detection of proteins and DNA molecules Elsevier Science B.V., Amsterdam. 2012;

[24] Homola J, Yee SS, Gauglitz G. Surface plasmon resonance sensors: review. Sensors and Actuators B: Chemical 1999; 54(1):3–15.

[25] Schasfoort RBM. Chapter 2:History and Physics of Surface Plasmon Resonance. In: Handbook of Surface Plasmon Resonance 2017; pp. 27–59.

[26] Zeng S, Baillargeat D, Ho H-P, et al. Nanomaterials enhanced surface plasmon resonance for biological and chemical sensing applications. Chem Soc Rev The Royal Society of Chemistry 2014; 43(10):3426–52.

[27] Vinogradov AP, Dorofeenko AV, Pukhov AA, et al. Exciting surface plasmon polaritons in the Kretschmann configuration by a light beam. Phys Rev B American Physical Society 2018; 97(23):235407.

[28] Patching SG. Surface plasmon resonance spectroscopy for characterisation of membrane protein–ligand interactions and its potential for drug discovery. Biochimica et Biophysica Acta (BBA) - Biomembranes 2014; 1838(1, Part A):43–55.

[29] Tang Y, Zeng X, Liang J. Surface Plasmon Resonance: An Introduction to a Surface Spectroscopy Technique. J Chem Educ 2010; 87(7):742–46.

CHAPTER 4

MICROFLUIDICS AND INTEGRATION WITH ORGANIC ELECTRONIC DEVICES

4.1 Introduction

In literature multiple microfluidic devices for the purpose of analysis and synthesis processes are reported. They are considered part of micro electromechanical systems (MEMS) or microscale biochemical systems. Also, at the microscale level, these microfluidic devices make use of the physical and chemical properties of both liquid and gases. The main advantages of using a microfluidic device also include the usage of low sample volume, chemicals and other reagents with a precise controlled behaviour. It is also possible to operate fluids in geometrically constrained environment to a micro scale level at which the volumetric forces are overwhelmed by the surface forces. Microfluidic chips were used for the purpose of mixing the fluids, transport, filtering, separating, dilution and for other fluid processing techniques.

Due to excellent features of mass transport control, less energy consumption, reduced and compact size, they were widely used for the development of Lab-on-chip technology, inkjet printheads and micro-thermal technologies. Employing microfluidic devices, factors like resistance of the fluidics, surface tension and dissipation of energy can be studied. Based on the applications, different kinds of microfluidic devices with a desired flow rate, due to their geometrical constraints can be modelled and integrated. In the present chapter I will present a case study of using microfluidic device plus EGOFET biosensor for the detection of α-synuclein, a model biomarker for Parkinson disease. The response of the device obtained with standard electrolyte drop is compared with engineered prototype with fluidic compartment for electrolyte and for sample solution, where diffusion is controlled with steps of the perfusion protocol.

The microfluidic device puts in electrical contact the buffer flowing on top of the transistor channel with the sample solution flowing on top of the gate, but increases the diffusion time to 30 min, thereby not influencing the measure of the target concentration. I will report also on the activities performed in the PhD program to design and fabricate simple microfluidic prototypes for EGOFET biosensors detecting oligonucleotides and microfluidic devices for optical biosensors, SPR and fluorescence based, also employed for quantification of oligonucleotides Finally, I will describe an example of elastomeric mold with microchannels employed to functionalize electrodes patterned on PCB substrate.

4.2 Label-free immunodetection of α-synuclein by using a microfluidics coplanar electrolyte-gated organic field-effect transistor

Label-free immunosensors that exploit an organic semiconductor channel as the transducer of the biorecognition events are emerging as ultrasensitive and highly specific devices for bioanalytical assays, with figures of merit often comparable, sometimes even superior (with levels of detection down to a few target molecules), to those characterizing the workhorse of bioanalytical techniques viz. the enzyme-linked immunosorbent assays (ELISA) [1]. With comparison to label-free electronic sensors based on inorganic semiconductors, as CHEM-FETs (i.e., chemical field-effect transistors [2]) or MOSFETs (i.e., metal-oxide field-effect transistors [3]), organic biosensors offer other important advantages, such as the closer proximity with the aqueous environment (the organic semiconductor channel is immersed in the biologically relevant fluid), the stability of operations in aqueous electrolytes (the typical hysteresis and bias stress observed in ambient operations of organic electronics devices disappear in immersion conditions), the possibility to be interfaced or integrated as arrays with living systems, thanks to the large-area manufacturing on flexible substrates and a suitable bio/functional interface.

Two main device architectures are used in biosensing in aqueous liquids: i) electrolyte-gated organic field-effect transistors (EGOFETs) [4] and ii) organic electrochemical transistors (OECTs) [5]. EGOFETs rely on the capacitive coupling between the gate electrode and the active material, whereas OECTs exploit the ion diffusion along with the electrochemical doping of the active material [6]. Relevant bio-applications include electroceuticals [7], bioelectric signal recording [8, 9], neuromorphic devices [10, 11], and biosensors [12–14].

In the case of EGOFET biosensors, the functionalization with a biorecognition group can be done either at the gate electrode [12], or at the organic semiconductor channel [15, 16]. Magliulo et al. [17] successfully demonstrated both physisorption and chemical grafting of sensing receptors onto the semiconducting channel achieving excellent results towards the quantification of streptavidin and C-reactive protein in a wide range of concentrations, namely from 1μM to 10nM and from 2μM to 2pM, respectively. The most viable route is the modification of the gate electrode by means

of different functionalization strategies with antibodies or aptamers mediated either by the Protein G or by self-assembled monolayers (SAMs) [13–15, 17–20]. State-of-the-art level of detection down to single-molecule was reported for the sensing of immunoglobulins G/M by co-functionalizing the gate electrode with a SAM endowed with hydrogen-bonding interactions that amplify the individual biorecognition event by a cooperative reorientation of the SAM [21]. As the limits of detections are pushed down to such low concentrations, and since many relevant biomarkers, even when overexpressed, are present at extremely low concentration during their patho-physiological condition (*e.g.* inflammatory cytokines), it is crucial in these label-free devices to guarantee the stability of performance together with the temporal control of the temperature and concentration conditions.

This is particularly important if the aim is a new generation of biosensing point-of-care (POC) systems or early diagnostic tools for the detection of relevant biomarkers. Thus, the effort on engineering the optimal interface immunochemistry must be paralleled by the effort in endowing the sensor with compact microfluidics able to guarantee the required stability of parameters during the measurement. Other promising label-free techniques that are also being developed in the field of biosensing include the more conventional electrochemical devices [22, 23] as well as optical-based devices, such as those exploiting the Surface Enhanced Raman Spectroscopy (SERS) [24, 25]. In both cases, efforts are devoted to fabricate compact devices embedded in chips to develop novel POC tests [26].

This work is aimed to design and develop an EGOFET immunosensor for detecting monomeric *α*-synuclein, which is a small protein formed by 140 amino acids (19-20 kDa). In its pathological condition, *α*-synuclein is a component of the so-called Lewy Body inclusions. This protein has been considered as a possible hallmark of a group of neurodegenerative diseases, known as *synucleinopathies*, which include Parkinson's disease (PD), the second most common neurodegenerative disease [27–30]. Furthermore, α-synuclein has also been shown to play a role in the pathophysiology of Alzheimer's disease (AD) [31, 32]. Specifically for PD, there are still no conclusive results about the correlation between the specific levels of circulating *α*-synuclein in plasma and cerebrospinal fluid (CSF) with the clinical diagnosis and progression of this illness, which has been mainly accounted by variations in the assays detection and sensitivity/accuracy [33, 34]. Thus, the development of devices able to detect this protein in the range from nM down

to pM is required for the diagnosis and prognostics of PD and the understanding of the correlation of the α-synuclein levels on its evolution.

Aiming at this goal, reported sensor relies on the electronic transduction of an EGOFET, whose gate electrode is functionalized by a monoclonal anti-(α-synuclein) antibody. Two different surface functionalization strategies to graft the anti-(α-synuclein) antibody (i.e. SAM and Protein G) are explored. The EGOFET sensor is integrated into a novel microfluidics layout designed *ad-hoc* to standardize the measurements. This microfluidics consists of separately accommodating the gate and the organic semiconductor, thereby avoiding cross-contamination during the sample dispensing, even though their electrical connection is always preserved for its proper operation. Additionally, the microfluidic is crucial to avoid the fast evaporation of solvent/water, which would produce a temporal drift of the target concentration and hence of the relevant electrochemical potentials in the device. The microfluidic embedded EGOFET featuring a coplanar gate reaches a sensitivity up to 37(±5) mV/dec and a limit-of-detection (LOD) as low as 2 pM in a phosphate buffered saline solution at pH= 7.2 performing analytical tests that take around 8 minutes.

4.2.1 Characterization of the sensing platforms

Anti-(α-synuclein) antibodies (Abs) have been tethered onto the polycrystalline Au by means of two different approaches, the so-termed "approach I" and "approach II" (Figure 4.1). The former relies on an amino-terminated pegylated thiol ($HSC_{11}EG_6NH_2$), whose amino groups have been successively activated with glutaraldehyde (Gl) [35, 36].

This leads to a functionalized Au extremely reactive towards primary amines, which are usually abundant in the Abs backbone (see Figure 4.1a). The second approach does not covalently graft the antibody to the surface but instead tethers it to the His-tagged recombinant Protein G (PG), that is anchored to the Au electrode. PG is able to target efficiently the crystallizable Ab region [37–39]. Furthermore, PG is robustly anchored to the polycrystalline Au thanks to its His tag that exhibits an affinity towards different metals such as Ni and Au (Figure 4.1b) [40, 41].

Since there is not an established protocol for tethering a bio-molecule onto a metal surface without affecting partially its bio-functionality, I pursued both approaches that have pros and cons and compared the outcomes of the sensing devices in order to establish the most suitable approach. For instance, approach I yields covalent albeit random Ab grafting, whereas approach II guarantees more oriented Ab immobilization onto the Au surface although non-covalent interactions are involved.

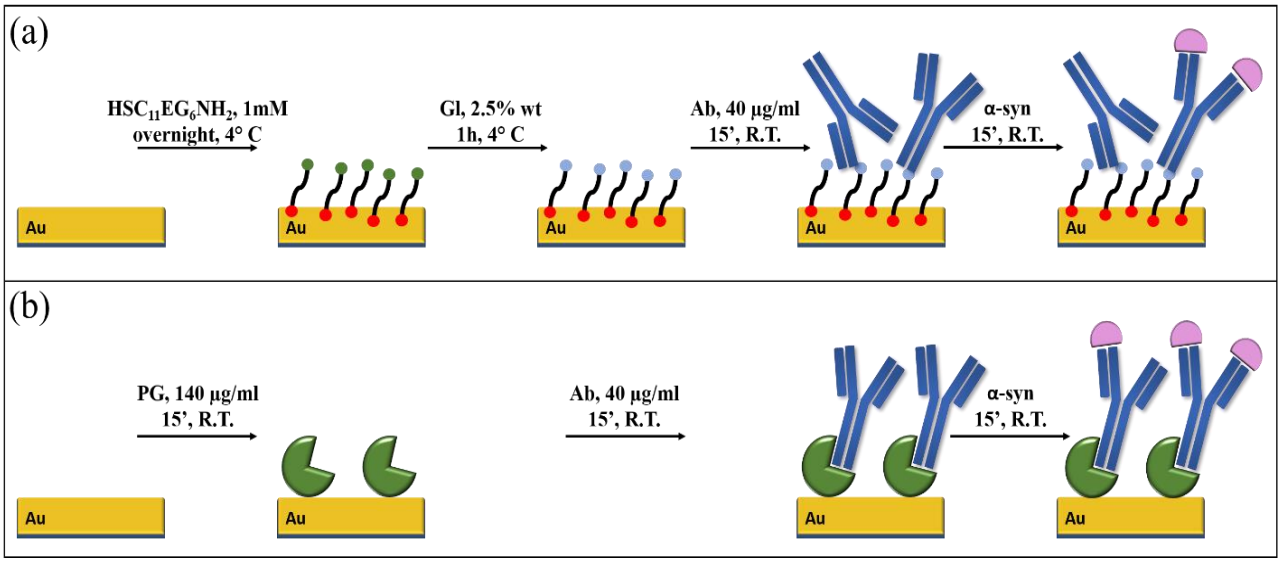

Figure 4.1: Scheme of the Au surface functionalization protocol with Approach (a) I and (b) II.

4.2.2 Impedance spectroscopy and differential pulse voltammetry

The first goal was to verify the presence of the surface binders (*viz.* $HSC_{11}EG_6NH_2$-based SAM and PG), their reactivity towards Abs and consequently, their sensitivity towards α-synuclein. By electrochemistry (i.e., electrochemical impedance spectroscopy and differential pulse voltammetry), the PG grafting yielded a pronounced area normalised R_{CT} increase (ΔR_{CT}) up to 20 $k\Omega/cm^2$ and a consequent decrease of the current density (ΔJ) down to 440 $\mu A/cm^2$ (Figure 4.2a,b). As expected, the $HSC_{11}EG_6NH_2$-based SAM features higher ΔR_{CT} (~120 $k\Omega/cm^2$) than PG due to its more ordered and compact packing onto the Au surface (see Figure 4.2 c). Both functionalization approaches were successfully tested towards a 0.25 µM solution of α-synuclein

proving their sensing ability towards this analyte. In particular, the two approaches exhibit opposite trends of the response with respect to Abs adsorption and detection of α-synuclein.

The $HSC_{11}EG_6NH_2$-based SAM (i.e. higher coverage and molecular packing) showed an increase of ΔR_{CT} and a consequent ΔJ decrease (Figure 4.2 d) after being incubated with α-synuclein. Conversely, PG showed a decrease of ΔR_{CT} and a consequent ΔJ increase (i.e. lower coverage and molecular packing). Albeit it is beyond the scope of this paper, these experimental proofs hint at a relevant redistribution of the surface charge on the metal due to the pairs Ab-PG as well as Ab-PG-synuclein. In addition, the different response could also be influenced by the Au SAM bond formation that leads to permanent electric dipoles.

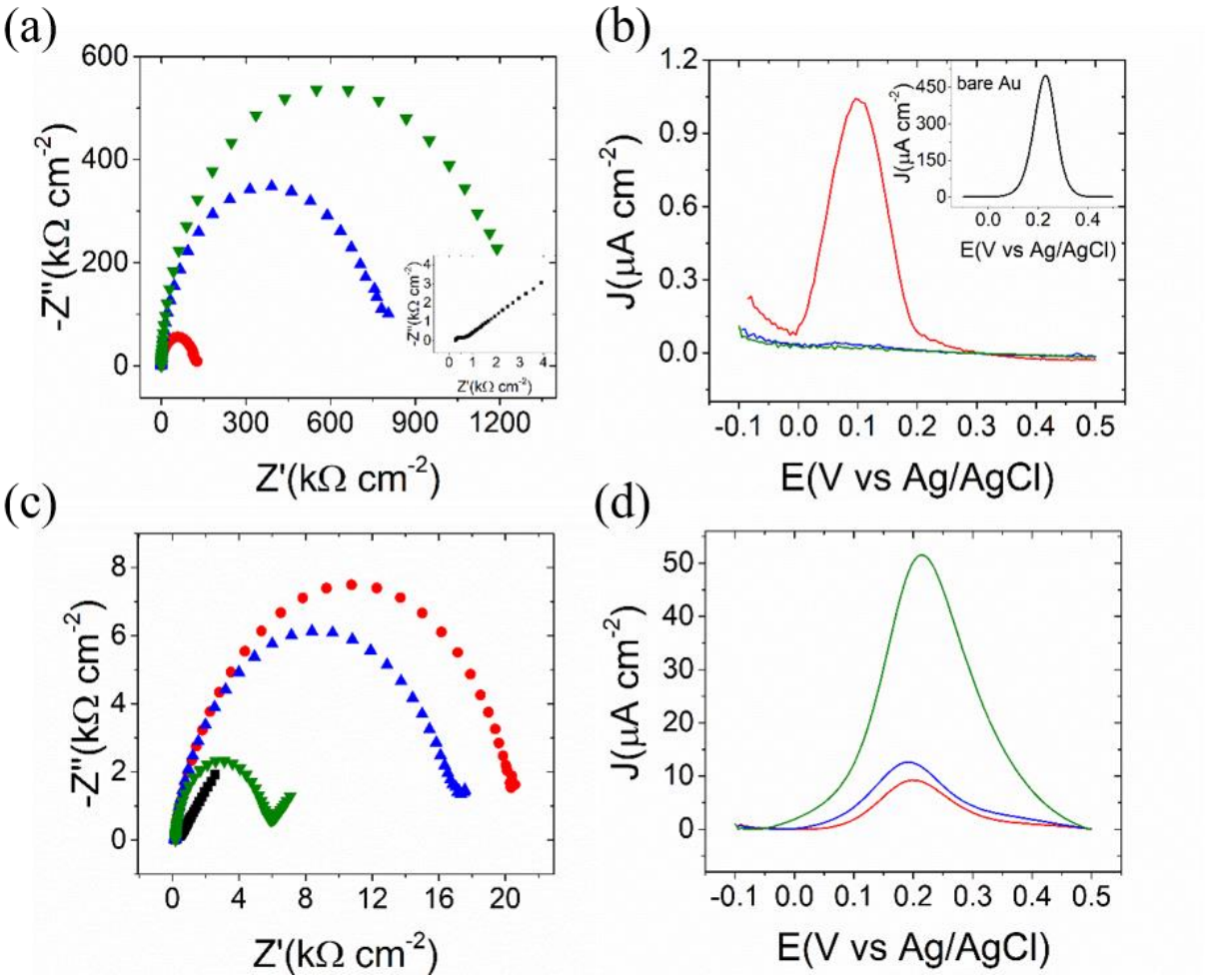

Figure 4.2: EIS and DPV characterization of the Ab functionalized surface. Approach I. (a) EIS: SAM-coated Au (red curve), Ab-SAM-coated Au (blue curve), after incubation in a solution of α-synuclein 0.25

μM (green curve). In the inset, the curve relative to pristine Au is represented, (b) DPV: SAM-coated Au (red line), Ab-SAM-coated Au (blue line), after incubation in a solution of α-synuclein 0.25 μM (green line). In the inset, the DPV of pristine Au is reported. Approach II. (c) EIS: bare Au (black curve), PG-coated Au (red curve), Ab-PG-coated Au (blue curve), after incubation in a solution of α-synuclein 0.25 μM (green curve). (d) DPV: PG-coated Au (red line), Ab-PG-coated Au (blue line), after incubation in a solution of α-synuclein 0.25 μM (green line).

4.2.3 Surface Plasmon Resonance (SPR) characterization

In order to further characterize the functionalized substrates, surface plasmon resonance (SPR) has been used to assess the two approaches on a planar Au film (Figure 4.3 a,b). As explained in the Chapter 2.4.6, the SPR is equipped with microfluidic channels that allow real-time monitoring of the absorption process. The excellent sensitivity of this technique allowed us to track the reflected light variation (*%ΔR*), which is directly related to the Au surface grafting. In particular, *ΔR* as a function of time allows one to monitor the kinetics of this phenomenon.

Apart from demonstrating the successful glutaraldehyde activation of $HSC_{11}EG_6NH_2$-based SAM in approach I, as well as the PG adsorption on gold in approach II, the transient *ΔR* change related to the surface functionalization with anti-(α-synuclein) Ab was monitored and exponentially fitted for both approaches (Ab concentration was fixed at 40μg/ml).

It turned out that approach I was faster than approach II yielding f = 112 (±1) s and f = 212 (±1) s, respectively. Although a calibration curve and more advanced measurements would be required for achieving a quantitative analysis, it can be stated that approach II leads to the adsorption of more anti-(α-synuclein) Ab (*ΔR* = 12) with respect to approach I (*ΔR* = 6). Concerning the α-synuclein recognition (concentration selected equal to 250 nM), a larger *ΔR* is recorded for approach II with respect to approach I. Thus, these data do not only hint a larger amount of anti(α-synuclein) Ab in approach II, but also an improved control of Ab orientation onto the Au surface.

In agreement with the electrochemistry results, SPR measurements confirm the successful Ab functionalization of the surfaces employing both approaches, as well as their capability to sense α-synuclein.

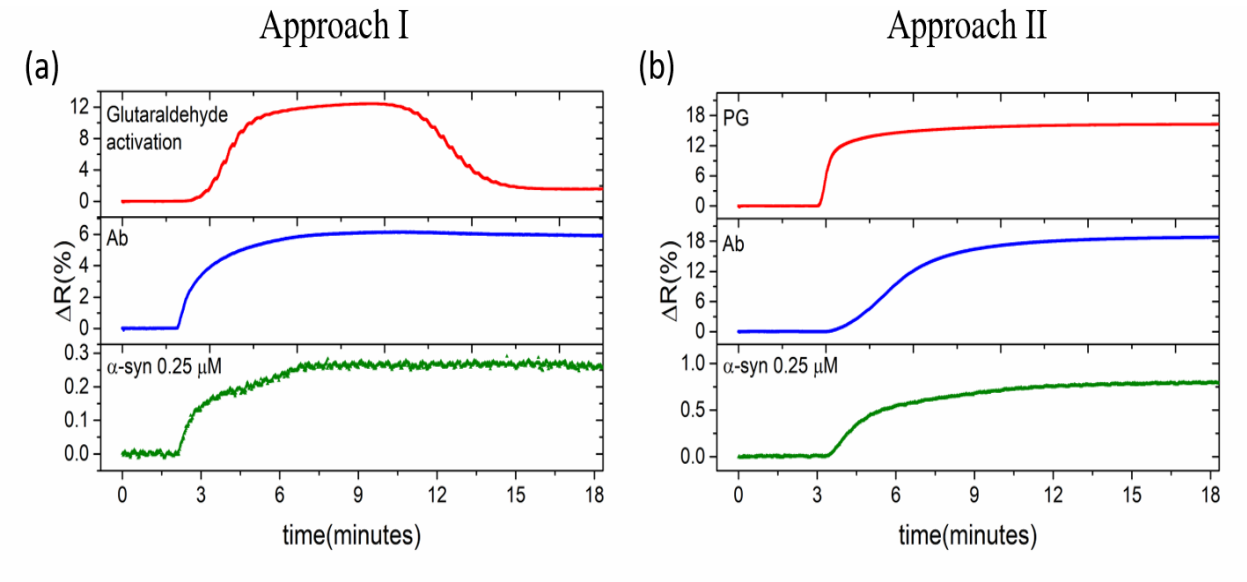

Figure 4.3: SPR characterization of the functionalized substrates:(a) approach I and (b) approach II.

4.2.4 Top-gated EGOFETs: α-synuclein detection

Since both approaches turned out to be extremely responsive towards α-synuclein, It has been then employed as gate terminals into a standard EGOFET architecture (see Figure 4.4 a). This allows one to monitor the detection of α-synuclein by using a transistor. Concerning the general architecture of the device, *Kapton*® as a flexible supporting substrate for the interdigitated electrodes has been choosen. The channel area was coated by a thin-film blend composed of the organic semiconductor 2,8-Difluoro-5,11-bis(triethylsilylethynyl)anthradithiophene (diF-TES-ADT) and polystyrene (PS) deposited by bar-assisted meniscus shearing (BAMS), as reported earlier [42–45].

As previously published, the role of PS improves the general stability of the electrical performances, especially when operated in liquid [45–52]. This is achieved due to the vertical phase separation of the two components that takes place during the deposition; in other terms, the organic semiconductor crystallizes sandwiched between a bottom PS layer and a top thin skin PS layer.

Finally, the device was exposed to phosphate-buffered saline (PBS) solution at pH 7.2, where a top gate electrode was immersed, namely an Au wire (Figure 4.4 a).

The *I-V* transfer characteristics were acquired after the *ex-situ* functionalization of the gate with anti-(*α*-synuclein) Ab. Subsequently, the electrode was immersed in benchmark solutions of *α*-synuclein and, afterwards, implemented as top gate electrode in the standard EGOFET layout (Figure 4.4 a). This guaranteed no chemical and/or biological contamination onto the organic semiconductor surface. Prior to any sensing experiment, electrical conditioning was always performed (*i.e.*, V_{DS} and V_{GS} equal to -0.1 V for 20 minutes) and the *ex-situ* functionalization was verified step by step by recording at least three transfers for each step (Figure 4.4 b,c).

Aiming at avoiding misleading interpretation, additional *I-V* transfer characteristics were acquired at the end of each sensing experiments by using a freshly cleaned Au wire (*viz*. gate electrode). This allowed us to verify if any extrinsic phenomena (such as bias stress or damaging of the semiconducting film) related to the device were contributing to the recorded trends. These final cross-checks clearly elucidated the direct interplay between the functionalization steps and the electrical changes occurring at the transistor.

Two well-defined trends were observed corresponding to the two approaches. In particular, approach I shows a positive shift of the *I-V* transfer after exposure of the gate to an increasing concentration of *α*-synuclein, whereas approach II exhibits a negative one (Figure 4.4d,e).

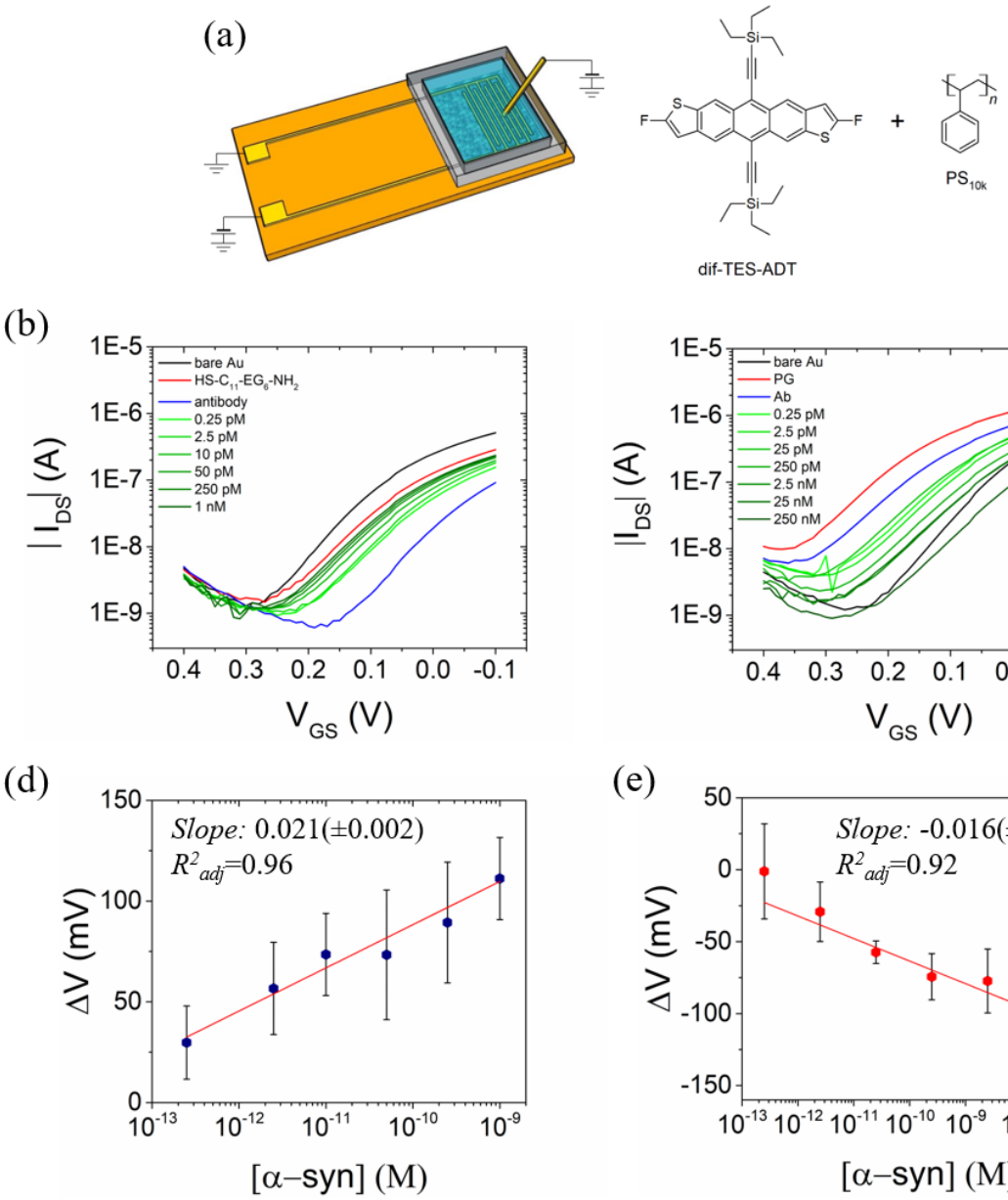

Figure 4.4: (a) Schematic image of the top-gated EGOFET and molecular structure of diF-TES-ADT and PS. I-V transfer characteristics of the EGOFET (V_{DS} = -0.1 V) with (b) Ab-SAM-coated Au gate (approach I) and (c) Ab-PG-coated Au gate (approach II), upon interaction with α-synuclein. The sensing response for both approaches in terms of ΔV is depicted, respectively, in (d) and (e) plots. The bar error is relative to three measurements.

As widely reported in the literature, an organic or biological coating assembled onto the gate surface or the semiconducting material can drastically affect the electrical performance of the transistor operated in aqueous media [12, 15, 18, 53–55]. The introduction of surface dipoles can either build-up an additional potential into the device or lead to a relevant change of the electrical double-layer capacitance. Aiming at a more quantitative description, an extraction of ΔV solely related to the bio-molecular recognition event regardless of the device-to-device variability, which affects usually the threshold voltage was performed. For this reason, the data have been extracted by adopting the mathematical elaboration suggested by *Ishikawa et al*. [56–58], as follows:

$$\Delta V = \frac{\Delta I}{g_m} \tag{1}$$

where ΔI=($I_{DS,ini}$-$I_{DS,fin}$) is the difference between the I_{DS},ini related to the device functionalized by the anti-(α-synuclein) Ab and the $I_{DS,fin}$ corresponding to a specific concentration of antigen, and g_m is the maximum transconductance (namely the first derivative of I_{DS} versus V_{GS}). In particular, it has been decided to verify the device sensitivity at the gate bias, where the g_m is the highest, namely -0.07 V. At the end of the sensing experiments, approach I yields a shift of +111(±20) mV, while an opposite shift of -111(±29) mV is found in approach II. In accordance with the electrochemical data, our EGOFETs sensed two opposite trends corresponding to the two functionalization approaches (Figure 4.4 d,e).

Concerning approach I, the sensing trend can be explained by considering the outer charges arising from the *α*-synuclein [59]. As reported in the literature, α-synuclein has an isoelectric point (pI) equal to 4.67, thus it is negatively charged at physiological pH (*viz.* pH > pI) [60]. As a result, a *p*-doping effect takes place due to an increase of negative charges onto the gate electrode. This leads to an extra accumulation of positive charge carriers into the conductive channel of diF-TES-ADT. Furthermore, the response ranges from 0.25 pM to 1 nM featuring a sensitivity equal to 21(±2) mV/dec.

On the contrary, a rationalization based on simply the PI of *α*-synuclein does not hold for approach II due to the presence of different bio-molecules on the surface. In this case, the sensing range appears wider than in approach I, namely from 0.25 pM to 0.25 µM, with a sensitivity of -16(±2) mV/dec. In other terms, both approaches reveal similar sensitivities, but approach II reached two orders of magnitude higher the upper limit of the sensitivity range (i.e., up to 0.25 µM). This

outcome is consistent with the SPR assays, which qualitatively pointed to a more efficient Au electrode for the detection of α-synuclein in approach II. Furthermore, both approaches show comparable LOD values, namely at pM concentration. This high sensitivity makes these devices well-suited to study pathological versus physiological levels of this biomarker [61].

4.2.5 Coplanar gating: in-situ (bio)-functionalization

Although top-gated architecture allowed us to verify the sensibility of the functionalized EGOFET, this technology can be solely used at the laboratory scale for proof-of-concept. Aiming at more sound technology, a coplanar gate architecture is demanded along with a well-suited microfluidic cell for the sample handling. The coplanar architecture improves intrinsically the electrical characterization of such device, because it exerts an ideal control of the gate area immersed in the aqueous solution.

Furthermore, it allows a straightforward implementation to more sophisticated circuitry, because no mobile electrodes are used like the Au wire in the top gate architecture. In this case, two planar gates termed “reference” and “sensing” (Figure 4.5 a) has been designed. According to this layout, a microfluidic cell composed of two well-defined chambers, so-termed “chamber 1” and “chamber 2” was manufactured.

The former contains the reference gate along with the source/drain electrodes covered by the organic semiconductor, whereas the latter hosts the sensing gate. These chambers are joined together by a “connecting channel”, whose role is fundamental for the overall functioning of this self-standing chip (Figure 4.5 b). This connecting channel guarantees the electrical connection between the sensing gate and the organic semiconductor through the electrolyte media. Furthermore, it enables to inject the sample containing α-synuclein or antibodies in “chamber 1” avoiding the cross-contamination of the organic semiconductor.

In other terms, chamber 1 together with the connecting channel are always filled by phosphate buffer, and chamber 2 is filled with different solutions (as mentioned in the Chapter 2.4.4). The

use of peristaltic pumps together with the narrow section of the connecting channel guarantee the proper functioning of the chip.

This has been experimentally verified by using the reference electrode, which allowed us to verify the electrical performance of the organic semiconductor at the beginning as well as at the end of the sensing experiments.

Such coplanar architecture was tested by using approach I. The sensing gate was *in-situ* functionalized (ref. chapter. 2.4.4). Subsequently, the sensing experiments were also performed *in-situ* by injecting the α-synuclein solutions for 5 minutes and then rinsing 3 minutes with the electrolyte media. The *I-V* transfer characteristics were acquired by spanning the gate-source voltage from 100 mV to -400 mV and with a V_{DS} = -0.1 V. (Figure 4.5 c).

The data turned out to be coherent with the previous experiments related to the top gated EGOFETs. As a result, a positive doping was observed by increasing the α-synuclein concentrations, reaching a LOD of 2 pM, ΔV value as high as +166(±52) mV and a slight increase in sensitivity (37(±5) mV/dec) with respect to the top gated devices (Figure 4.5 d).

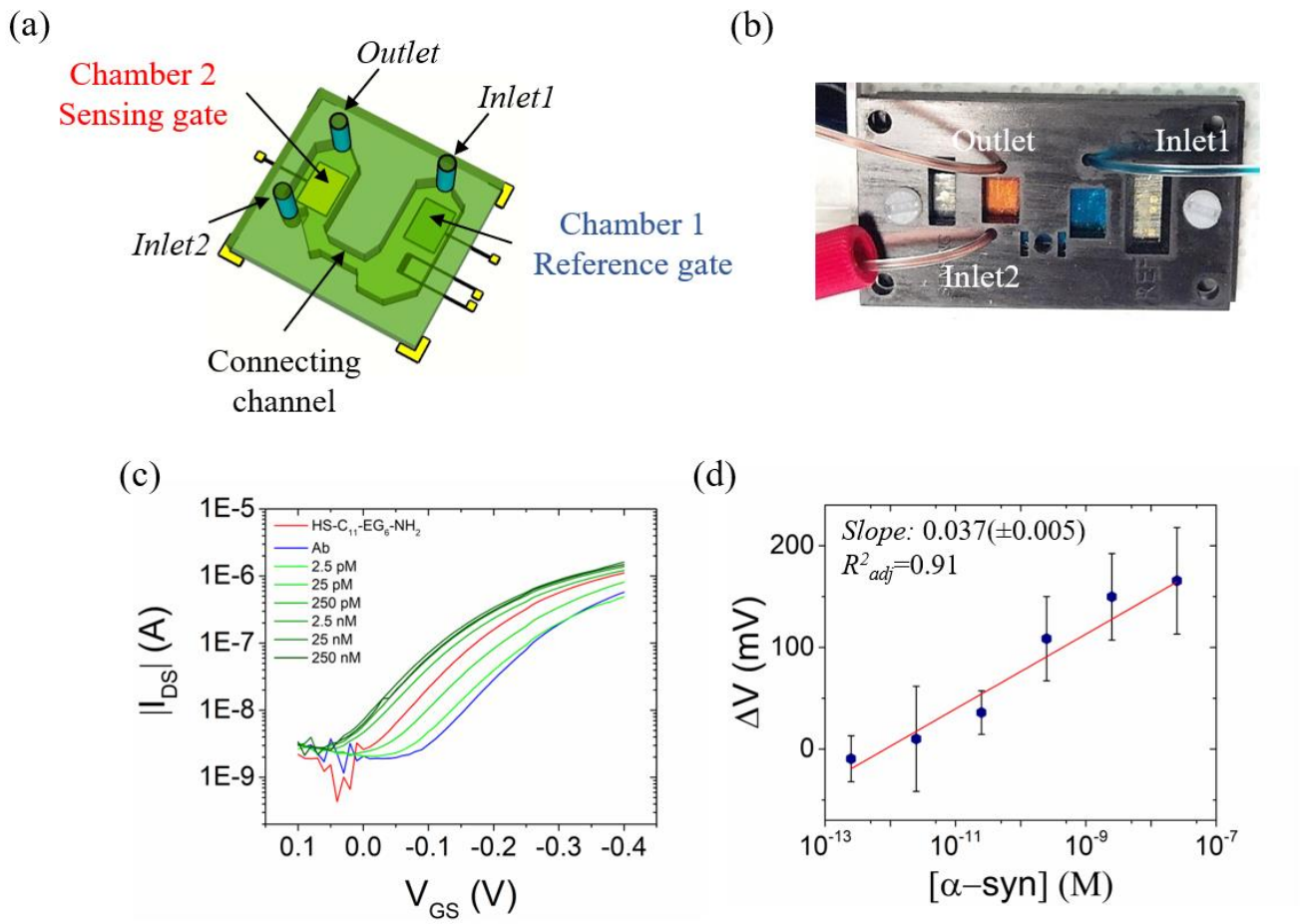

Figure 4.5: (a) 3D scheme of the microfluidic setup. (b) Real image of the microfluidic setup filled with red and blue dyes, the sensing chamber and the device chamber, respectively . (c) Transfer characteristics (V_{DS} = -0.1 V) of the sensing experiment employing the EGOFET with Ab-SAM-coated coplanar-gate Au gate (approach I) and (d) relative calibration curve.

4.3 Microfluidics Simulation

Time evolution of the concentration of *α*-synuclein inside the sensing chamber of the microfluidic device is calculated using commercial finite element solver Comsol Multiphysics ®.

The simulation involved coupled time-dependent solution of Navier-Stokes (NS) and convection-diffusion equations for the interior geometry of the full microfluidic device, including both chambers and inlets and outlet sections [62]. The fluid velocity field and pressure were calculated according to the following form of NS, neglecting the inertial term.

$$\rho \partial \mathbf{u} / \partial t = +\rho \mathbf{u} \cdot \nabla \mathbf{u} + \nabla \cdot [-p2\mathbf{I} + \mu(\nabla \mathbf{u} + \nabla \mathbf{u}^T)] \quad (2)$$

where **u** is the velocity field of the fluid, ρ the fluid density (for PBS buffer assumed equal to 1), *p* the pressure, **I** the identity tensor and μ the fluid viscosity. A quadratic dependence of viscosity with respect to the analyte concentration was assumed, according to:

$$\mu = 0.001 + 0.0005 c^2 \quad (3)$$

The disjoining pressure in Navier-Stokes equation was not considered, although it may a dominant effect in short distances close to the PDMS walls [63].

The α-synuclein concentration was determined according to convection diffusion equation:

$$\partial c / \partial t + \nabla \cdot (-D \nabla c + c\mathbf{u}) = 0 \quad (4)$$

Where *c* is the concentration and *D* the diffusion coefficient for α-synuclein ($D = 10^{-9}$ m^2/s).

The mesh for the computation was generated with tetrahedral assembly, with approximately $190 \cdot 10^3$ domain elements.

The iterative and coupled solution of Equation 2, 3 and 4 returned the values for the velocity and pressure field inside the microfluidic chambers and time evolution for α-synuclein concentration, as depicted in Figure 4.6 a,b

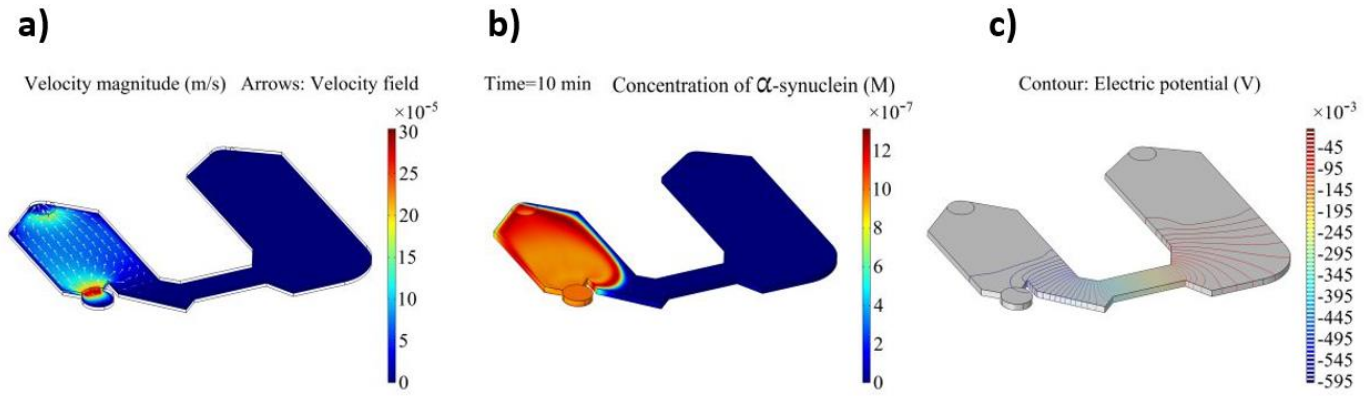

Figure 4.6: (a) Velocity field inside the microfluidics during sample injection resulting from finite element simulation. (b) Concentration of α-synuclein within "Chamber 2" after 10 min from the injection. (c) Potential contour plot in electrolyte between sensing gate and interdigitated electrodes.

The volume defined for NS and convection-diffusion simulation was also employed to calculate the potential across the electrolyte solution, by finite element calculation of the combined system of equations:

$$\nabla \cdot (\varepsilon_0 \varepsilon_r \mathbf{E}) = \vartheta_V \quad (5)$$

$$\mathbf{E} = -\nabla V \quad (6)$$

where **E** is the electric field, V is the potential, ε_r is the relative permittivity of PBS buffer (ε_r = 80) and ϑ_V is the charge volume density where, it was imposed that no charge is moved across the boundary (**n**·**D** = 0), except for the electrodes of gate and source where the potential was set to -0.6 and 0 V, respectively. The potential contour resulting from the simulation is reported in Figure 4.6 c.

4.3.1 Summary of microfluidic based α-synuclein detection

A sensing platform based on a dual coplanar electrolyte-gated organic field-effect transistor in a microfluidic chamber has been demonstrated to detect *α*-synuclein, a hallmark of neurodegeneration in important pathologies like Parkinson's and Alzheimer's down to LOD equal to 0.25 pM. The optimum immuno-detection strategy based on anti-(*α*-synuclein) monoclonal antibody was inferred by a comparative study of two surface functionalisation routes of the gate electrode. Both showed similar sensitivities and LOD values, but they showed different response ranges, namely approach II had a wider range than approach I (*viz*. 0.25 pM - 250 nM versus 0.25 pM - 1 nM, respectively). The microfluidics layout has been designed to avoid cross-contamination between the sensing gate and the organic semiconductor. Such an approach allowed the *in-situ* functionalisation of the sensing gate and the electrical tests with reference solutions of *α*-synuclein. The herein reported devices combine the high sensitivity and short measurement tests, with the electrical readout and the simplicity and upscaling compatibility of the fabrication methods employed. Thus, these devices showed excellent potential for the prognostics and diagnosis of synucleinopathies such as PD, and also can provide a promising label-free tool for gaining insights into the role of *α*-synuclein and its aggregation mechanism, which is pivotal for a comprehensive understanding of such neurodegenerative diseases. Future work will be devoted to fabricating technologically more advanced devices to validate them in a larger set of samples and test the label-free sensors reported using real samples from patient's fluids.

4.4 Integration of microfluidic devices with EGOFET: different geometries

Some examples of using microfluidic devices for point of care (POC) diagnosis, include development of chip-based diagnostic techniques with a reduced sample volume and analysis time, droplet based microfluidic devices, also called as digital microfluidic devices, provide amazing possibilities. With the combination of digital microfluidic devices and a Molecular-Beacon (MB)-assisted isothermal circular-strand-displacement polymerization (ICSDP) technique, it is possible to detect miRNA-210 sequences in the range of 10^{-18} mol in 20nL droplets compartment. MiRNA-

210 is primary and upregulated hypoxia inducible factor. It was detected using, low temperature isothermal-amplification methods without the need for additional thermal cycling by using a simple droplet microfluidic device [64].

Another point of care (POC) device for diagnosis of circulating miRNAs amplification and detection can be achieved using passive poly(dimethylsiloxane) (PDMS) microfluidic chip with laminar flow-assisted dendritic amplification (LFDA) technique. The multiplex target miRNAs (miRNA-500a-3p, miRNA-21-5p and miRNA-16) detections with the LOD (limit of detection) at femto-to-Pico molar level with the assay time of 20 minutes can be achieved using capture DNA probes (CP-DNA) and detection DNA probes (DP-DNA). The CP-DNA probes was immobilized on the deep-set pattern of three parallel line shaped microchannels (300μM width and 25μM height) present on to one of the PDMS chip. The second PDMS chip is with the sunken pattern of 'Y' shaped channel (100μM width and 25μM height) with CP-DNAs for the detection of miRNAs. A charge-coupled device camera was used to capture fluorescence signals and analysed using ImageJ software. [65].

A significant technique named 'Integrated comprehensive droplet digital detection' (IC 3D) was used to digitally count the enzymatically amplified miRNA targets directly from plasma sample. The target miRNAs are encapsulated into a microdroplets and counted digitally by the novel high-throughput 3D particle counter. Also, exponential amplification reaction (EXPAR) for the detection of miRNA targets in plasma was analysed through the fluorescent signal generated in the presence of the targets. So let-7a, let-7b and let-7c miRNAs were detected from the plasma sample of colon cancer patients and healthy donors. The limit of detection obtained was around 50 copies per mL in less than 3 hours [66].

To obtain a rapid, sensitive and specific detection of miRNA-134 biomarker, which has been found to be upregulated in unprocessed human plasma and cerebrospinal fluid samples of epilepsy patients, electrochemical detection based on electrocatalytic platinum nanoparticles was reported. The detection was performed with centrifugal microfluidic device, where it forms a sandwich assay by using an event triggered release system. The advantages of such a kind of disc microfluidics are that the centrifugal device rotation speed can be controlled, in order to pump specific nanolitre volume of fluid at a set time and to improve mass transport rate of the fluid by manipulating them within the device. The limit of detection achieved through the centrifugal

device platform was 1pM with low hybridization time. Also, due to the improved reaction rates and yields, an efficient mixing was achieved by overcoming diffusion-limited processes [67].

In the following paragraphs I will present the results of simple microfluidic device fabrication for conveying the electrolyte in contact with the transistor channel, either in static condition as open pool microfluidics or in continuous flow.

4.4.1 Open pool microfluidics

In this PhD thesis a simple and a low cost, PDMS based microfluidic devices such as , open pool microfluidics , continuous – flow microfluidics and droplet - based microfluidics was designed and fabricated using the "masters" created by the two techniques described in Chapter 2 (3D printing – replica moulding and photolithographic techniques).

Open pool microfluidic devices, help to contain 70-80µl volume of Tris-EDTA-NaCl buffer. This pool microfluidics can be integrated to confine the liquid on top of the semiconducting channel (present in EGOFET) without the need of any mechanical sealing or plasma bonding or glues.

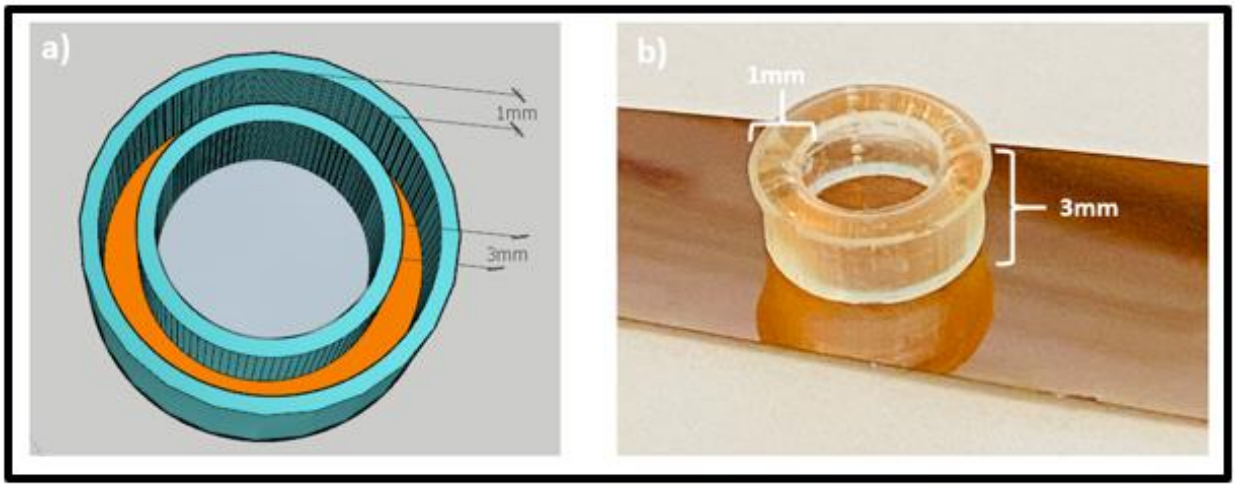

Figure 4.7: a) Snapshot of the 3D printed master for the pool fluidics and PDMS mixture has to be poured in the orange color highlighted area b) PDMS replica of the open pool microfluidics

The main advantage of this pool microfluidic devices is the easy accessibility to the buffer filling, no need of external peristaltic pump and no bubble formation. The pool can be filled every time when the electrolytic buffer is evaporated. The height of the pool is 3mm with the thickness 1mm and internal diameter of 3mm

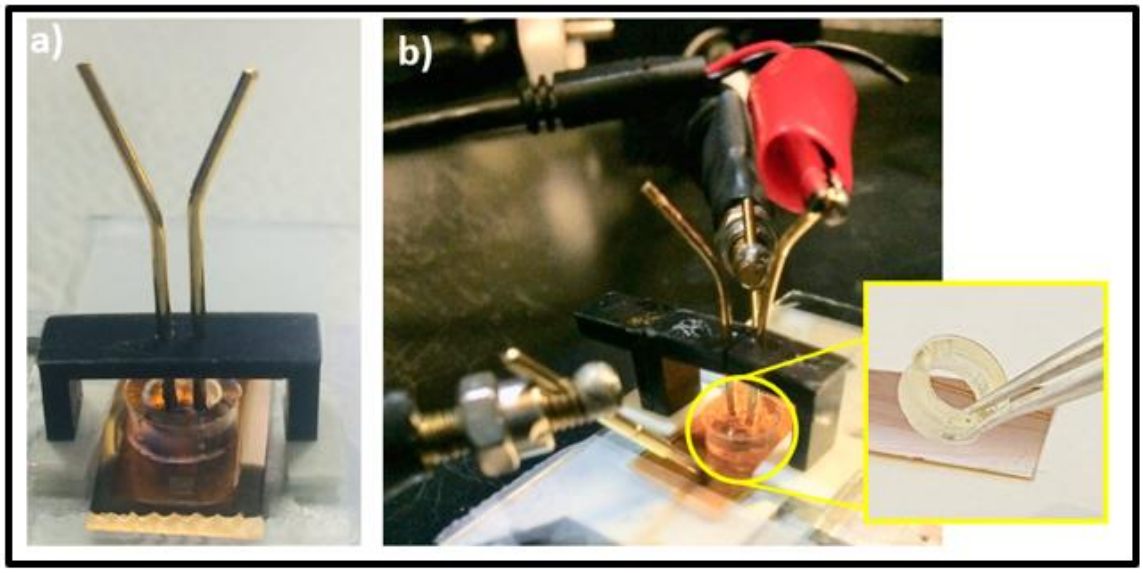

Figure 4.8: a) Assembly of the pool fluidics with Au wires and interdigitated Source (S) and Drain (D) electrodes b) Pool filled with approximately 70µl volume of the buffer and electrical contacts applied to Source, Drain and Gate electrodes

4.4.2 Continuous - flow microfluidic device

In case of Continuous- flow microfluidics, the fluidic device has to be sealed completely without any buffer leakage. So, a mechanical sealing was developed and the flow rate was controlled by external peristaltic pump.

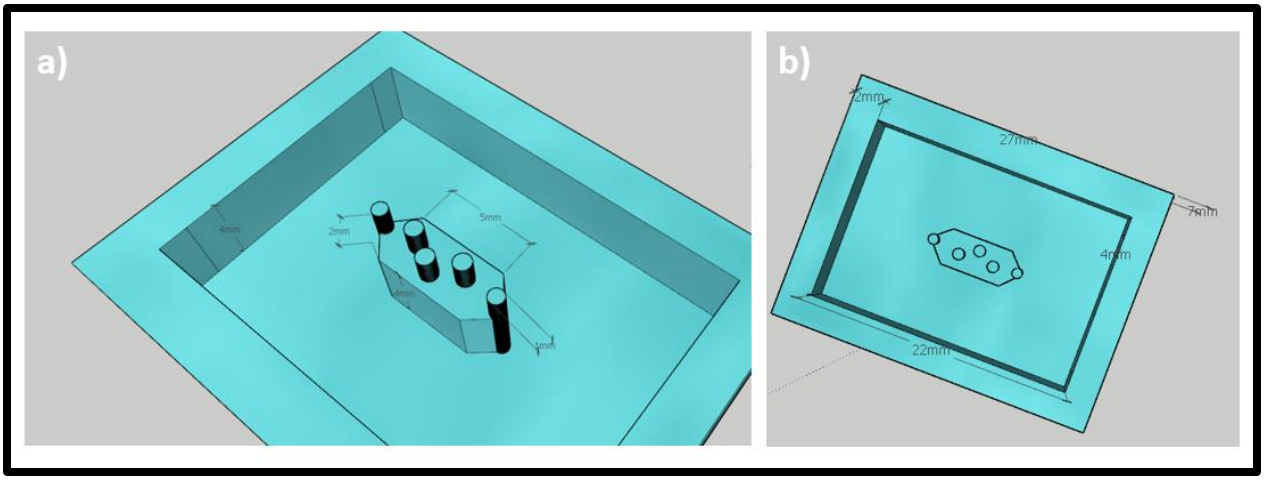

Figure 4.9: a) 3D master created for the multigate microfluidic cell fabrication containing pillars for the inlet, outlet tubes and electrodes b) Top view of the 3D master of the multigate microfluidic cell

The buffer flow rates, in the range between 0.1 to 100 µl/min, can be changed based on the specific application requirements. Using continuous flow microfluidic setup, hybridization process of sensing probes and target bindings were performed (inside the microfluidics) using three gate electrodes which were integrated on the top boundary of the microfluidic compartment.

The microfluidic cell is similar to the shape of an elongated hexagon and the measurements of length,width and height of the fluidic cell are 8 mm * 3 mm * 4 mm respectively. The total volume of the buffer solution inside the fluidic cell is 96 µl. The bore size of the holes for the gold (Au) wire electrode used was Ø0.9 mm and the distance between gold wires are approximately 0.5 mm placed apart with respect to one another. The length of each Au wire electrode in contact with the electrolyte solution is about 3 mm and the total surface area of each Au electrode immersed in the electrolyte is about 11 mm^2.

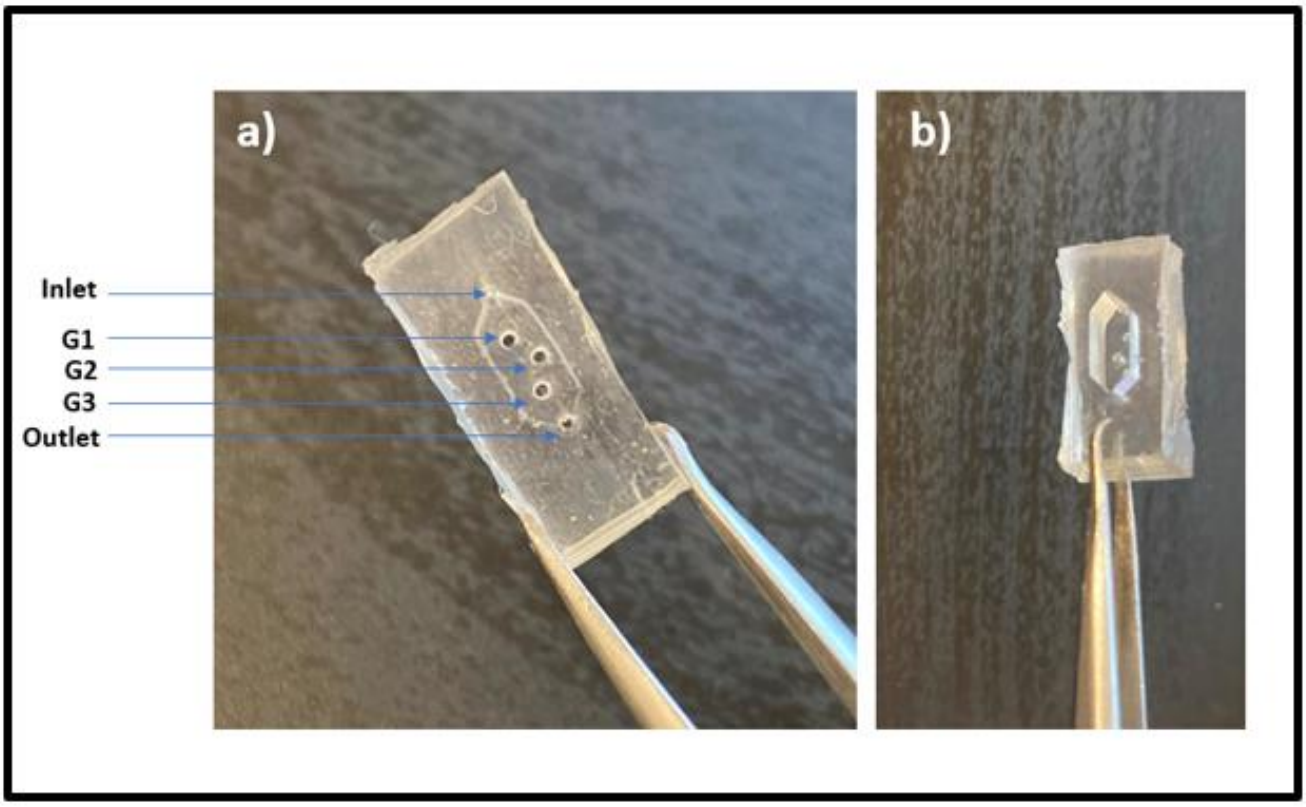

Figure 4.10: a) PDMS replica of the microfluidic cell (top view) for the 3 Au wire integration b) Bottom view of the fluidic cell

The 3D printed structures are designed according to the mechanical properties of elastomeric PDMS [68]. Deformation of the PDMS under clamping of the rigid 3D structures ensured sealing with the Au Kapton substrate, but the microfluidic chamber was not subject to sagging effect.

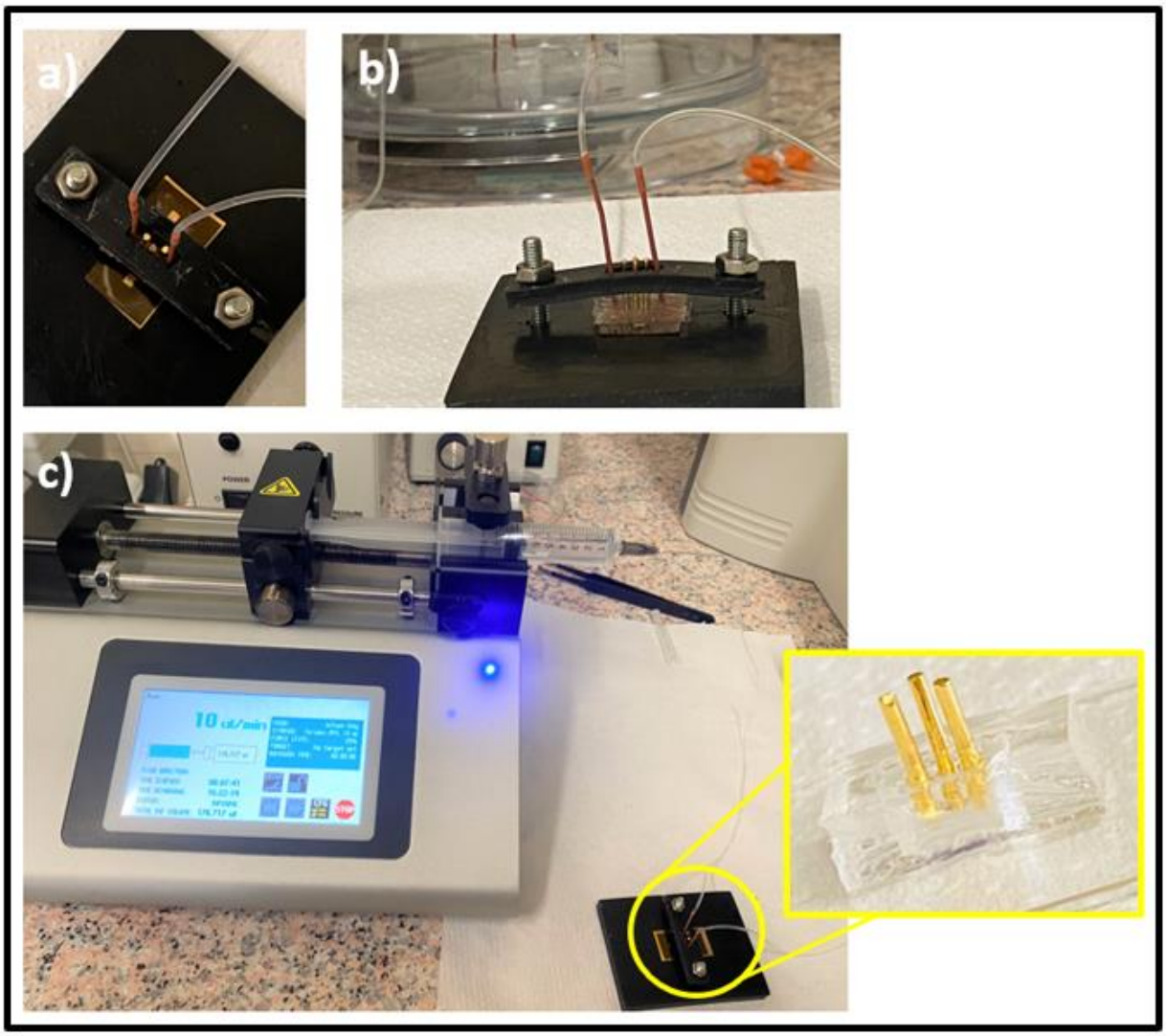

Figure 4.11: a)Top view showing Source , Drain , Au wires (G1,G2 and G3) electrodes and it's possibilities to make electrical contacts b)mechanical sealing using screws, 3D printed top holder and bottom holder by sandwiching the microfluidic device on top of the channel , also showing the connections of inlet and outlet tubes c) connecting with the external peristaltic pump and the flow rate used was 10µl/minute for in filling the microfluic cell with a suitable buffer and leakage was also checked.

4.4.3 Planar gates enclosed in microfluidic devices

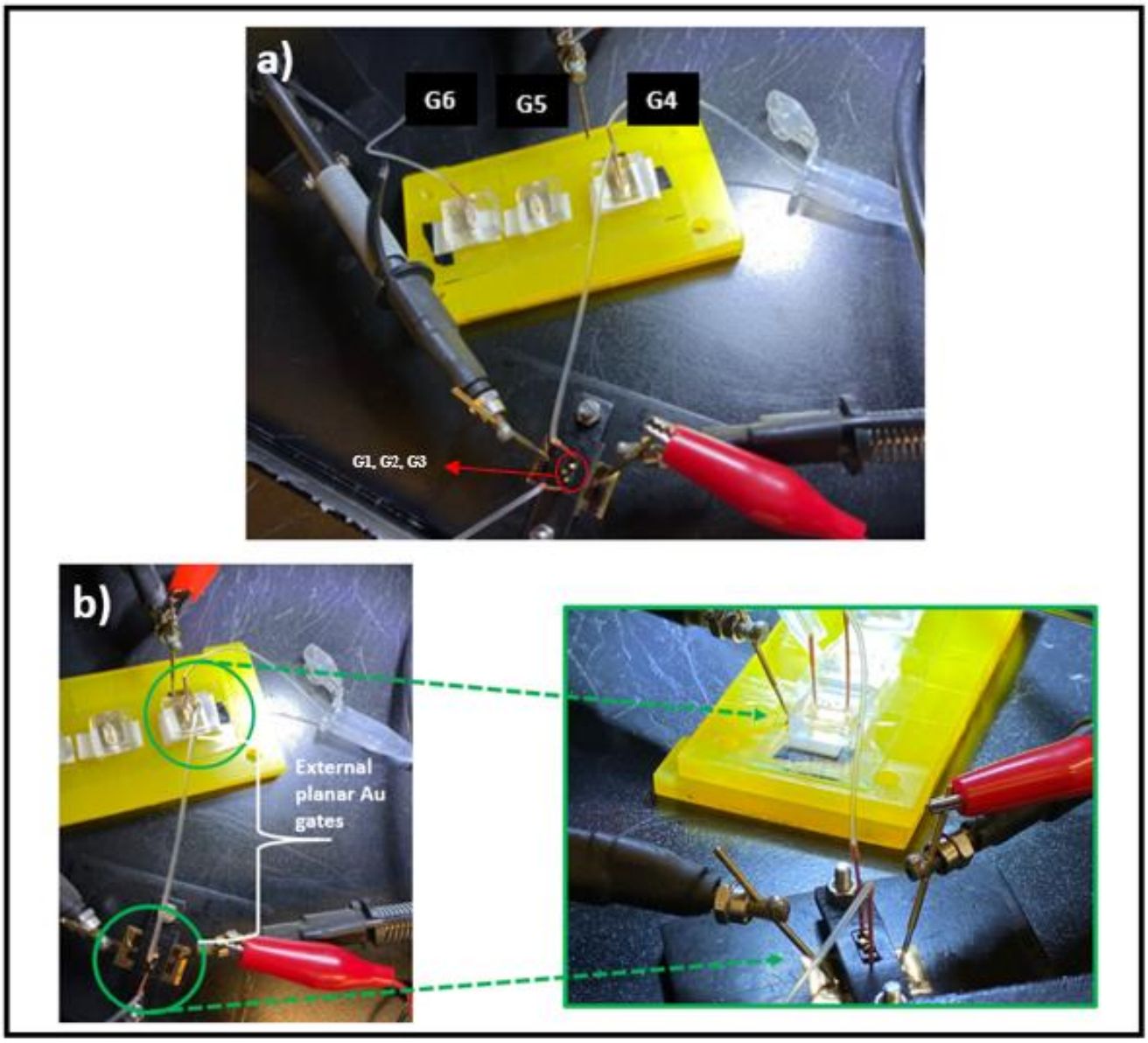

Figure 4.12: a)Top view of the internal Au wires (G1,G2,G3) and external flexible planar Au electrodes (G4, G5,G6) connected through the silicone tubing b) EGOFET device operation when gate (G4) is given the potential together with Source and Drain contacts, insight showing the contacts made for S,D and G4

A prototype of multisensing platform was achieved using multi-gated EGOFET with the integration of microfluidic devices and planar gates. External flexible planar Au gates (G4, G5 and G6) were connected to the interdigitated Source (S) and Drain (D) electrodes through a connecting silicone tubing (ID = 0.5mm). The solution inside the silicone tubing acts as a bulk and fills the microfluidic devices sealed on top of the flexible planar Au electrodes individually. Each external microfluidic device contains approximately 96µl volume of the buffer. The silicone tubing with the buffer connected from the main device acts a conducting path (capacitive coupling) to the external gates, when the potentials are applied to Gate, Source and Drain (i.e., V_{DS} = -0.2V, V_{GS} = -0.1V to -0.8V). Internal gates (G1, G2, G3) are Au wires (Ø 1mm each) were placed on top of the channel through continuous -flow microfluidic device. This multi-gate EGOFET architecture (G1 to G5) was operated in linear regime.

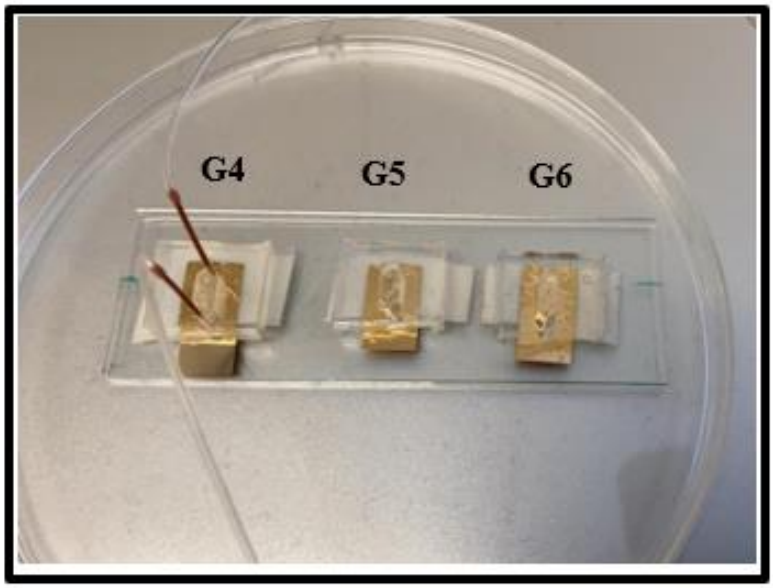

Figure 4.13: Picture of the external flexible planar Au electrodes containing individual microfluidic device to infill the buffer through PEEK tubings and small projection of planar gates outside each microfluidic device inorder to apply gate potential

Both the transfer curve measurements and output curve measurements were performed in order to understand the working mechanism of this setup. From the transfer curves obtained, the output

current (I_{DS} in µA) for G1, G2 and G3 are around 2µA. But the output current for G4 and G5 are about 1.8µA. This reduction in current might be explained with the distance between the electrical double layer (EDL) formation at electrolyte/semiconductor and gate/electrolyte interface.

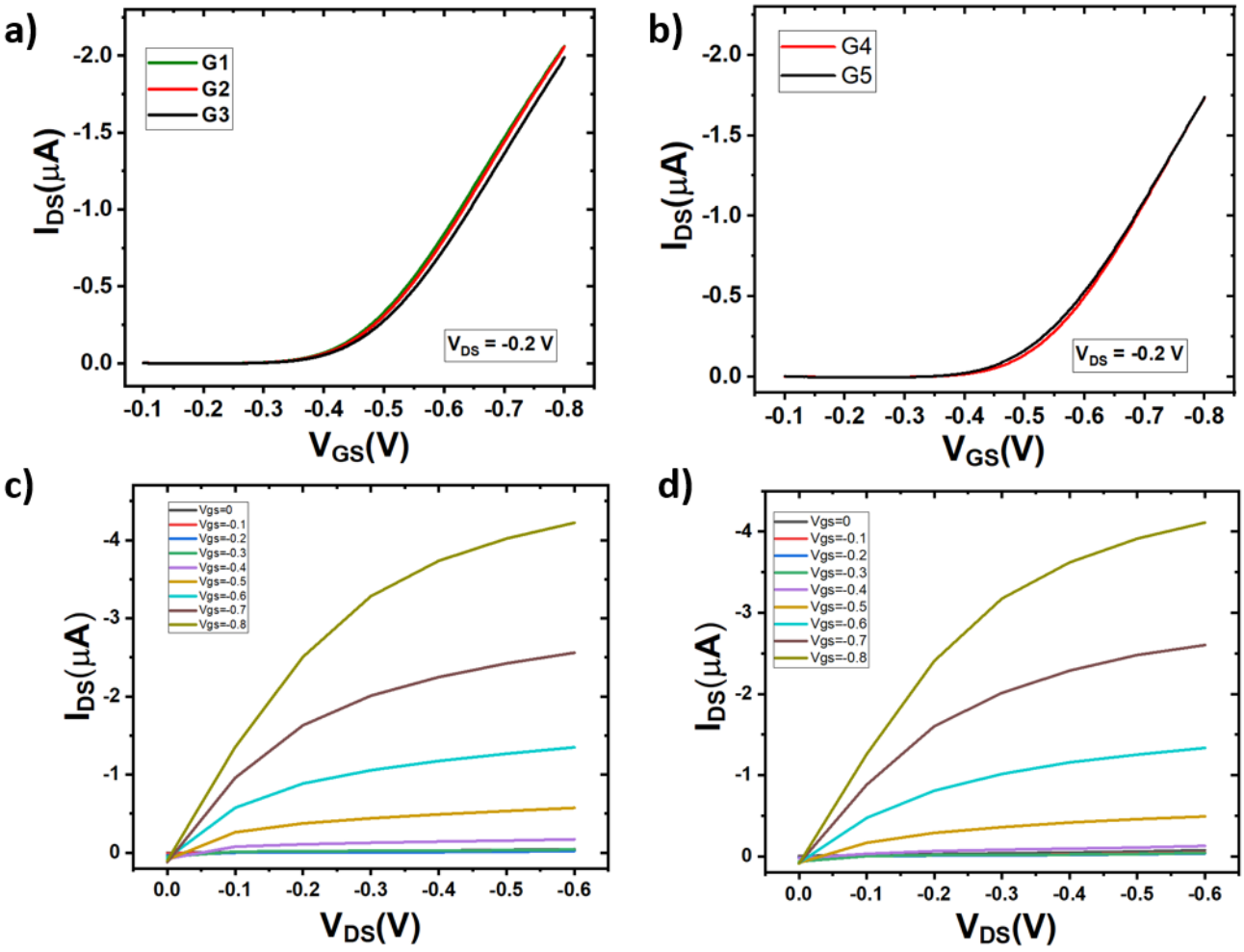

Figure 4.14: Transfer curve curves of the gates (G1,G2 and G3) operated in linear regime at V_{DS} = -0.2V b) Transfer curve of the external flexible planar gate electrodes (G4 and G5) with a threshold shift in the negative direction c) output curve measurement of the gate G1 d) output curve measuremnt for gate G4 showing the device was turned ON from V_{GS} = -0.5V

The threshold voltage of G4 is shifted to more negative biases. Analysing the output curve measurements obtained for one of the internal gates (G1) and an external gate (G4), the device was turned ON only at V_{GS} = -0.5V for G4, whereas for G1 it was turned ON for V_{GS} = -0.4V.

On the positive note, an array of external gate architecture, opens a way to perform multiple sensing with different gate functionalized bioreceptors at the same time. Each external Au flexible planar gate has it's own inlet and outlet tubings leading to separate contacting of the gate once the fluidic are filled.

4.5 Integration of microfluidic devices with optical based sensor platforms

4.5.1 Microchannels integration with SPR biochip

An array of microchannels were designed to couple with SPR biochip gold surface. In each channel a specific biomarker functionalization is achieved by incubation with the corresponding reagents.

The geometric properties of the microchannel are defined mainly by the imaging capability of the SPR instruments but also by the possibility to exert a pressure on the elastomeric mold containing the microchannels, in order to achieve good sealing and a controlled perfusing flow. Moreover, the final cross section of the microchannel in operative conditions is affecting the velocity profile of the liquid and the mass transport towards the surface-active sites.

3D printing of the master has been carefully optimized in order to reach x-y feature size of 200 µm and z resolution of 100 µm. The design for 3D master has been studied so to add pillars to act as vertical fluid channels in the final microfluidic replica.

These pillars, with diameter larger or equal to 800 µm, are very straight forward to integrate in the 3D drawing and 3D printing, whereas, with traditional UV photolithography substrates and processes, they would imply a large number of complex fabrication steps.

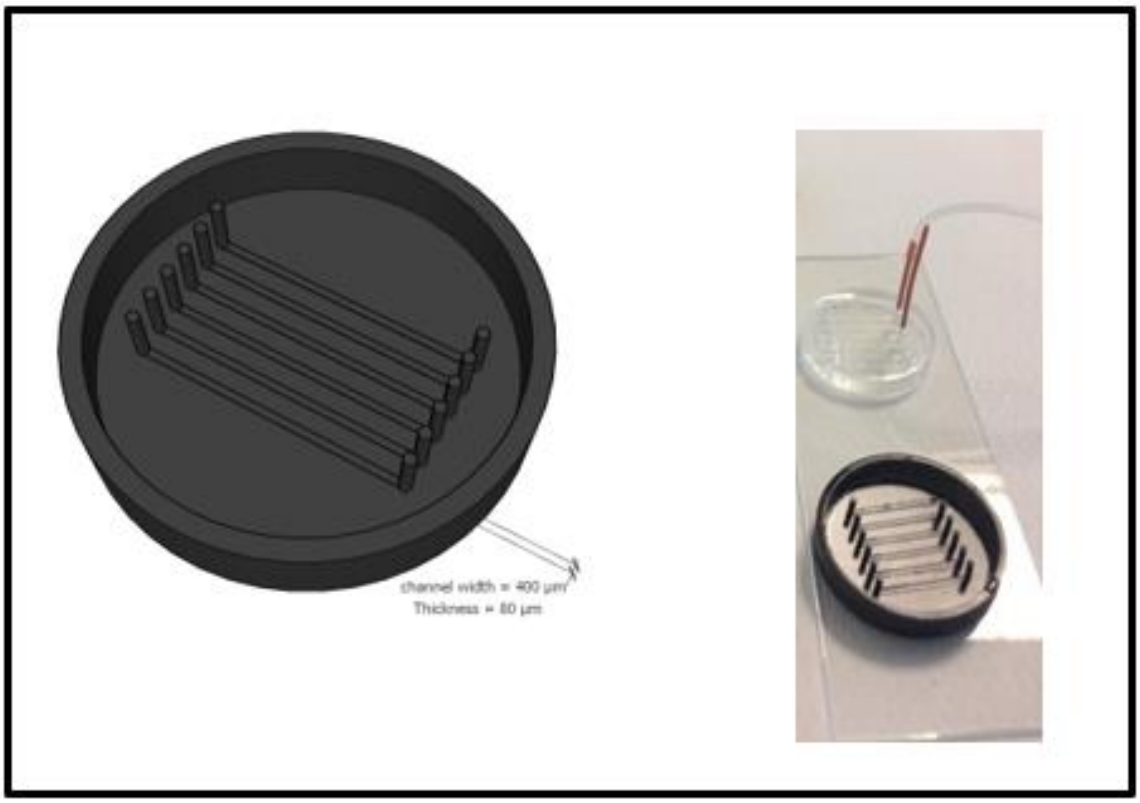

Figure 4.15: Master geometry after design with 3D cad software SketchUP®. Snapshot of the 3D printed master(Left) and a PDMS replica with PEEK tubings for connection with external(Right)

4.5.2 Droplet microfluidic device

Replica molding of UV photolithographic masters for microfluidic devices have been fabricated according to design optimized in collaboration with Prof. Spoto in University of Catania, to perform experiments on droplet generation and fluorescence analysis to detect genomic target in low copy number.

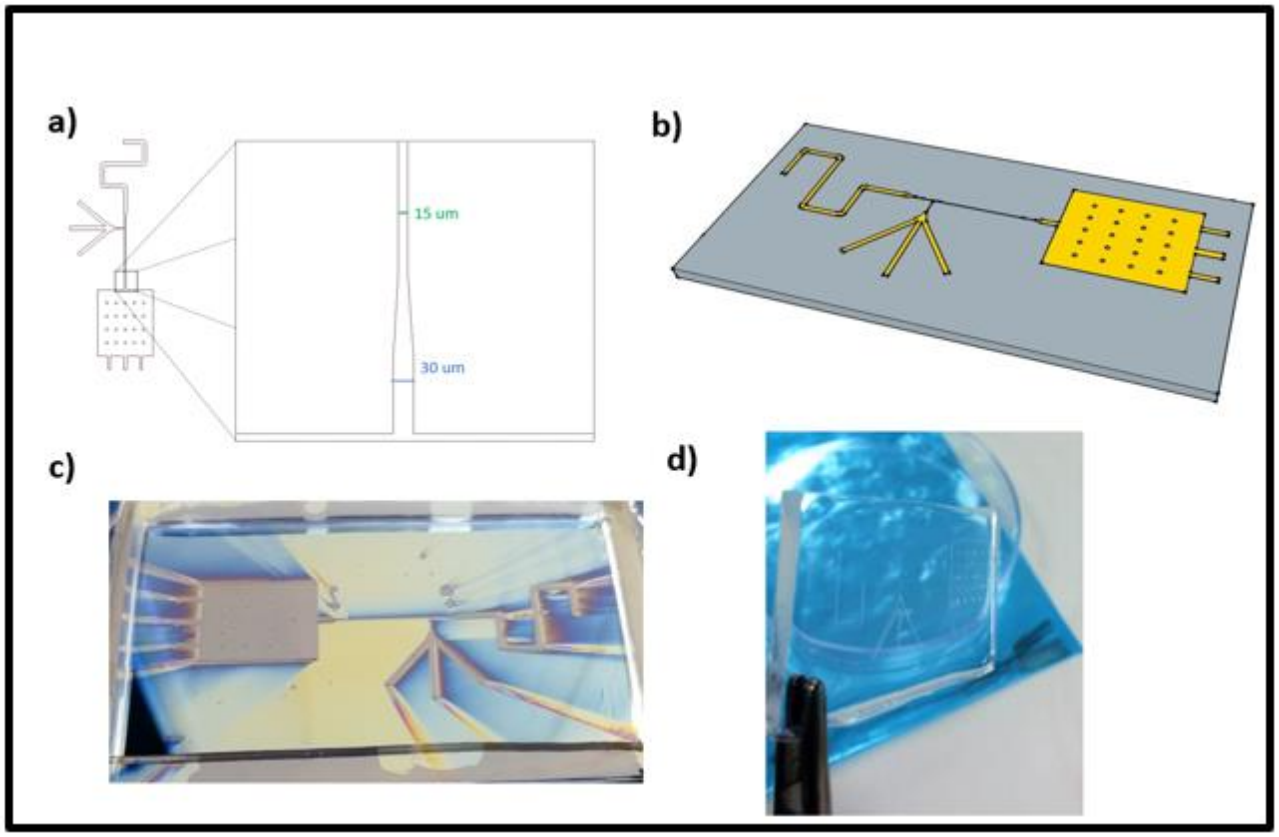

Figure 4.16: a) 2D design with the channel thickness of 15µm and 30µm at the T-junction of the droplet fluidics b) 3D model of the droplet microfluidics created using SketchUP® c)Master fabricated with UV photolithography, ready for replica molding d) Elastomeric replica in PDMS obtained in University of Catania after replica molding, for droplet generation.

4.6 Microchannel fabrication for the functionalization of the multi gate electrodes

A microfluidic device with 4 parallel channels was designed and fabricated in order to functionalize the 4 gate electrodes (Au), present on a rigid polymeric substrate. The 4 gate (Au) electrodes were fabricated by Esseti S.r.l. (Bologna, Italy) with an Electroless Nickel Immersion Gold (ENIG) surface plating technique, on a 2.5 mm thick Printed Circuit Board (PCB) (FR4 glass epoxy) substrates. Thickness of electrodes varies throughout the design, starting from 400µm up to 200µm with a fixed spacing of 200µm between them.

The main purpose of this multi-parallel channel microfluidics with a desired architecture is to functionalize each Au electrode with different functional moieties. The microfluidic channels were placed on top of the printed gate electrodes and each channel was filled with specific biomolecules to be functionalized.

The functional molecules are transported through the individual inlet tubings of the fluidic channels and collected through the outlet tubings. Once the channels were filled, the edges of both inlet and outlet tubings which contains remaining fluids are sealed using paraffin wax. In this way, remaining (or excess) solution available at both inlet and outlet tubings will helps to maintain the channel always filled for the whole night.

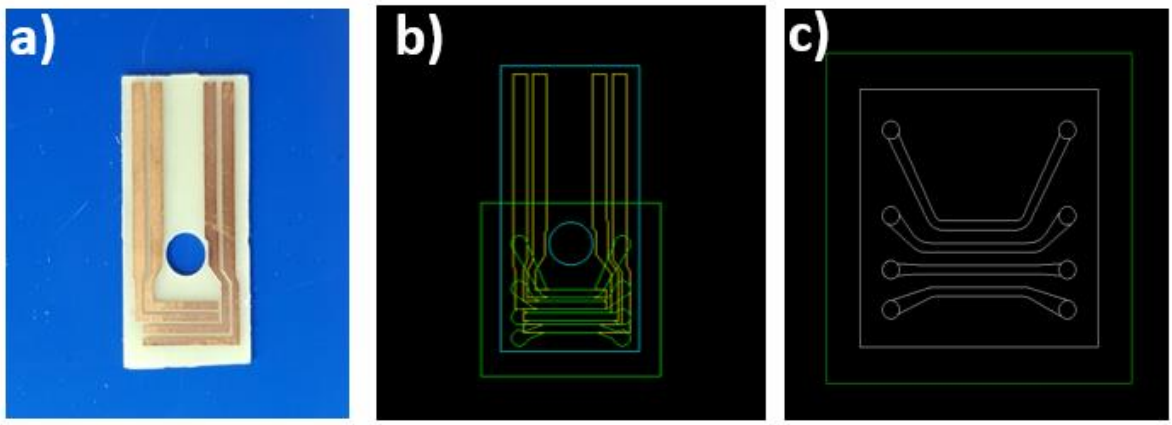

Figure 4.17: a) 4 Au electrodes and deposited with industrial process (electroless nickel gold plating) b)2D design of the electrode with channel footprint including the inlets and outlets c) 2D design of the multi-parallel channel microfluidic device created using DraftSight®

Before the channels are filled with the suitable biomolecules, both the gate electrodes and microfluidic channels were gently placed on the 3D printed bottom holder (contains specific slit to hold the printed electrodes and fluidics). Then, a 3D printed top holder was used which contains a small window opening for monitoring fillings of the fluid and the leakage between the channels was checked after each channel gets filled.

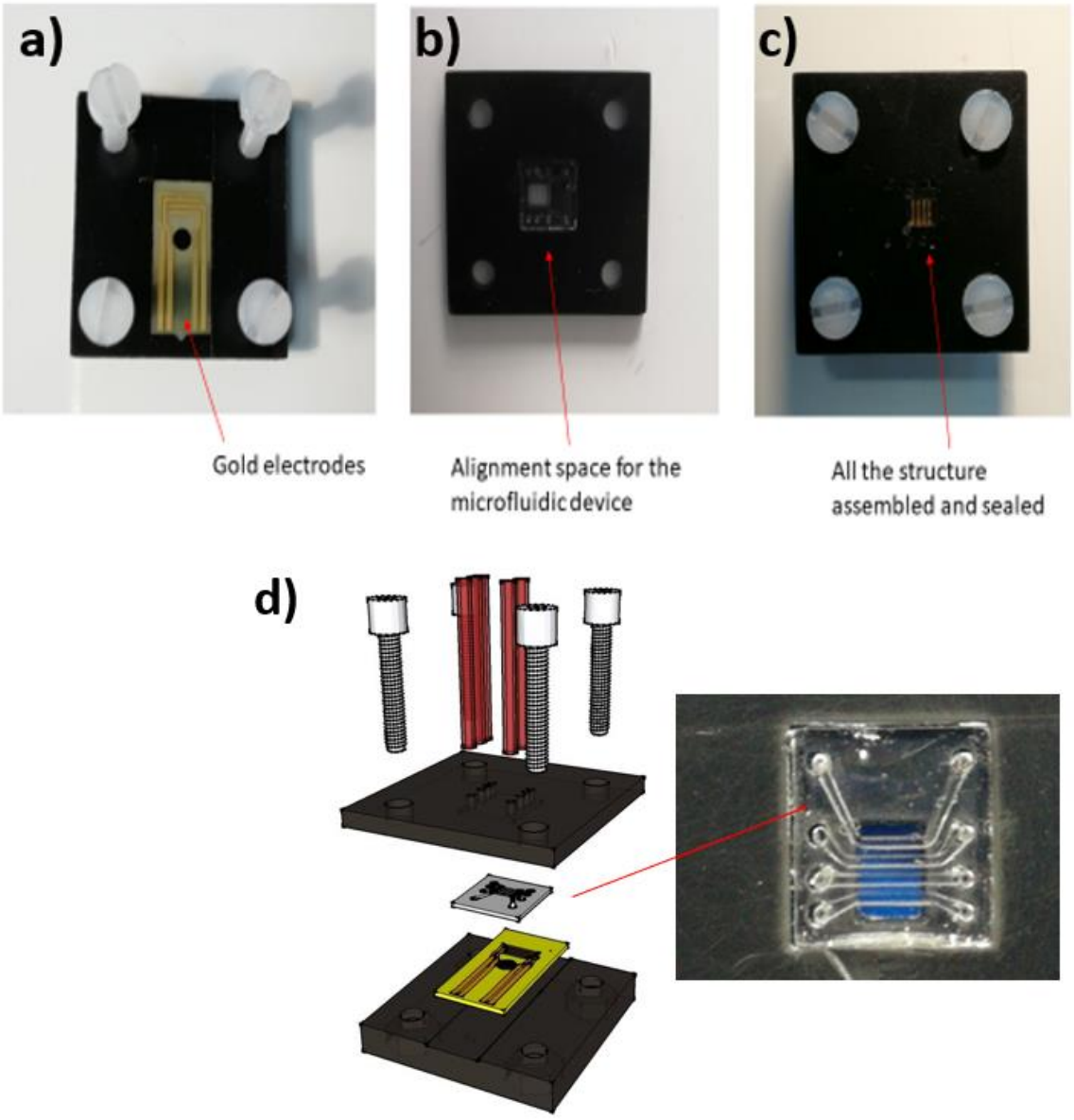

Figure 4.18: a) 3D printed bottom holder for Au electrodes b) 3D printed top holder containing an alignment space for the multi channel microfluidic device, window to view the channel fillings and ports for the inlet and outlet PEEK tubings c) sealed and assembled parts together with gate electrodes and microfluidic device d) 3D model of the complete assembly and insight showing the microfluidic device placement on the top holder containing a window openening

The top holder also consists of ports for the inlet and outlet tubings. All the parts were then sealed together using mechanical clamps (3D printed screws). After filling one of the microfluidic

channel with a sample blue dye, it was then viewed with the optical microscope for the leakage through the window present on the top holder. With a development of a simple, cost efficient multi-parallel channel microfluidic device and 3D printed holders, a leakage less individual channel filling with different functional moieties in order to functionalize gate electrodes , all at at a same time can be achieved.

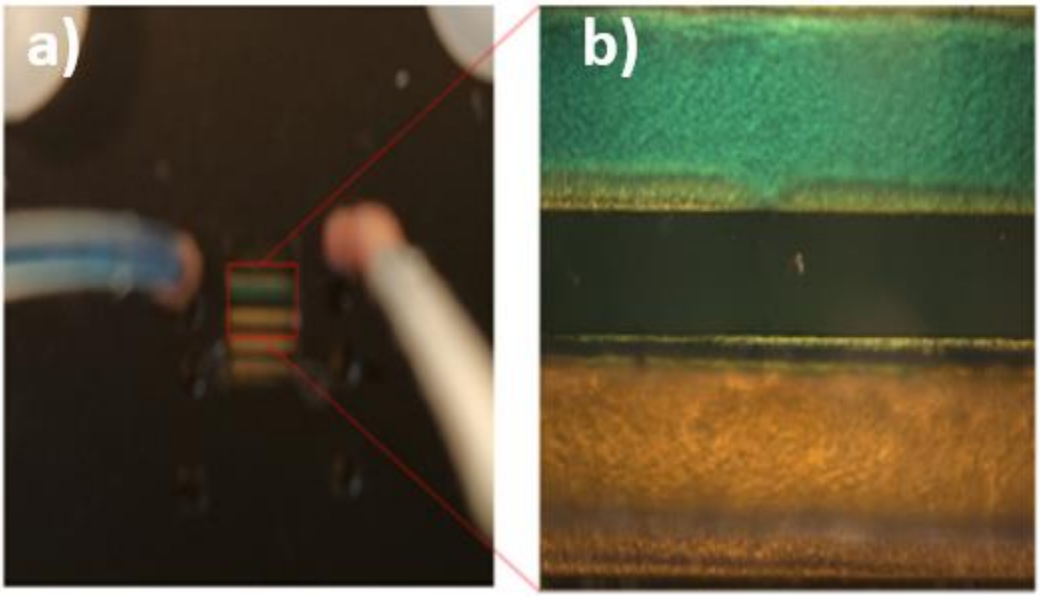

Figure 4.19: a) filling the top channel with a sample blue dye using inlet tubes connected to the persistaltic pump with the flow rate of 5µl/minute and collected using oulet tubes and remaining channels were left unfilled b) optical image showing the 1st channel filled with blue dye with no leakage and the 2nd channel left empty (also visible Au surface underneath the channel)

This also opens a path to perform different functionalization at any sensing electrode platform based on the desired microfluidic channel design and applications. It is advantageous to perform over night different functionalization all together on the same or different sensing electrode.

4.7 References

[1] Engvall E, Perlmann P. Enzyme-linked immunosorbent assay (ELISA) quantitative assay of immunoglobulin G. Immunochemistry 1971; 8(9):871–74.

[2] Kaisti M. Detection principles of biological and chemical FET sensors. Biosensors and Bioelectronics Elsevier B.V. 2017; 98:437–48.

[3] Guo J, Ai Y, Cheng Y, et al. Volumetric measurement of human red blood cells by MOSFET-based microfluidic gate. Electrophoresis 2015; 36:1862–65.

[4] Kergoat L, Herlogsson L, Braga D, et al. A water-gate organic field-effect transistor. Advanced Materials 2010; 22(23):2565–69.

[5] Kergoat L, Piro B, Berggren M, et al. Advances in organic transistor-based biosensors: From organic electrochemical transistors to electrolyte-gated organic field-effect transistors. Analytical and Bioanalytical Chemistry 2012; 402(5):1813–26.

[6] Rivnay J, Inal S, Salleo A, et al. Organic electrochemical transistors. Nature Reviews Materials 2018; 3:17086.

[7] Jonsson A, Inal S, Uguz L, et al. Bioelectronic neural pixel: Chemical stimulation and electrical sensing at the same site. Proceedings of the National Academy of Sciences 2016; 113(34):9440–45.

[8] Cramer T, Chelli B, Murgia M, et al. Organic ultra-thin film transistors with a liquid gate for extracellular stimulation and recording of electric activity of stem cell-derived neuronal networks. Physical Chemistry Chemical Physics 2013; 15(11):3897–905.

[9] Campana A, Cramer T, Simon DT, et al. Electrocardiographic recording with conformable organic electrochemical transistor fabricated on resorbable bioscaffold. Advanced Materials 2014; 26(23):3874–78.

[10] Desbief S, Casalini S, Guerin D, et al. Electrolyte-gated organic synapse transistor interfaced with neurons. Organic Electronics Elsevier B.V 2016; 38:21–28.

[11] Burgt Y Van De, Lubberman E, Fuller EJ, et al. A non-volatile organic electrochemical device as a low-voltage artificial synapse for neuromorphic computing. Nature Materials 2017; 16(4):414–18.

[12] Casalini S, Leonardi F, Cramer T, et al. Organic field-effect transistor for label-free dopamine sensing. Organic Electronics Elsevier B.V. 2013; 14(1):156–63.

[13] Casalini S, Dumitru AC, Leonardi F, et al. Multiscale Sensing of Antibody À Antigen Interactions by Organic Transistors and Single-Molecule Force Spectroscopy. ACS Nano 2015; 9(5):5051–62.

[14] Wang N, Yang A, Fu Y, et al. Functionalized Organic Thin Film Transistors for Biosensing. Accounts of Chemical Research American Chemical Society 2019; 52:277–87.

[15] Torsi L, Magliulo M, Manoli K, et al. Organic field-effect transistor sensors: A tutorial review. Chemical Society Reviews 2013; 42(22):8612–28.

[16] Torsi L, Farinola GM, Marinelli F, et al. A sensitivity-enhanced field-effect chiralsensor. Nature Materials 2008; 7(5):412–17.

[17] Magliulo M, Tullio D De, Vikholm-Lundin I, et al. Label-free C-reactive protein electronic detection with an electrolyte-gated organic field-effect transistor-based immunosensor. Analytical and Bioanalytical Chemistry Analytical and Bioanalytical Chemistry 2016; 408(15):3943–52.

[18] Berto M, Casalini S, Lauro M Di, et al. Biorecognition in organic field effect transistors biosensors: The role of the density of states of the organic semiconductor. Analytical Chemistry 2016; 88(24):12330–38.

[19] Berto M, Vecchi E, Baiamonte L, et al. Label free detection of plant viruses with organic transistor biosensors. Sensors and Actuators, B: Chemical Elsevier B.V. 2019; 281:150–56.

[20] Magliulo M, Mallardi A, Mulla MY, et al. Electrolyte-gated organic field-effect transistor sensors based on supported biotinylated phospholipid bilayer. Advanced Materials 2013; 25(14):2090–94.

[21] Macchia E, Manoli K, Holzer B, et al. Single-molecule detection with a millimetre-sized transistor. Nature Communications Springer US 2018; 9(1).

[22] Guo J. Uric Acid Monitoring with a Smartphone as the Electrochemical Analyzer. Analytical Chemistry 2016; 88:11986–89.

[23] Huang X, Xu D, Chen J, et al. Smartphone-based analytical biosensors. Anales de la Quimica Royal Society of Chemistry 2019; 143:5339–51.

[24] Zeng F, Duan W, Zhu B, et al. Paper-Based Versatile Surface-Enhanced Raman Spectroscopy Chip with Smartphone-Based Raman Analyzer for Point-of-Care Application. Analytical Chemistry 2019; 91:1064–70.

[25] Xu K, Zhou R, Takei K, et al. Toward Flexible Surface-Enhanced Raman Scattering (SERS) Sensors for Point-of-Care Diagnostics. Advanced Science 2019; 6(16):1900925.

[26] Xu D, Huang X, Guo J, et al. Biosensors and Bioelectronics Automatic smartphone-based micro fl uidic biosensor system at the point of care. Biosensors and Bioelectronic Elsevier B.V. 2018; 110(February):78–88.

[27] Goedert M, Jakes R, Spillantini MG. The Synucleinopathies: Twenty Years on. Journal of Parkinson's Disease 2017; 7:S53–71.

[28] Gould N, Mor DE, Lightfoot R, et al. Evidence of native α-synuclein conformers in the human brain. Journal of Biological Chemistry 2014; 289(11):7929–34.

[29] Spillantini MG, Goedert M. The Alpha-Synucleinopathies : Parkinson's Disease, Dementia with Lewy Bodies, and Multiple. Annals New York Academy of Sciences 2000; 920:16–27.

[30] Chang CW, Yang SY, Yang CC, et al. Plasma and Serum Alpha-Synuclein as a Biomarker of Diagnosis in Patients With Parkinson's Disease. Frontiers in Neurology 2020; 10(January):1–7.

[31] Twohig D, Nielsen HM. α -synuclein in the pathophysiology of Alzheimer ' s disease. Molecular Neurodegeneration Molecular Neurodegeneration 2019; 14:1–19.

[32] Wennström M, Surova Y, Hall S, et al. Low CSF Levels of Both α-Synuclein and the α-Synuclein Cleaving Enzyme Neurosin in Patients with Synucleinopathy. PLoS ONE 2013; 8(1).

[33] Shi M, Zabetian CP, Hancock AM, et al. Significance and confounders of peripheral DJ-1 and alpha-synuclein in Parkinson's disease. Neuroscience Letters Elsevier Ireland Ltd 2010; 480(1):78–82.

[34] Bougea A, Stefanis L, Paraskevas GP, et al. Plasma alpha-synuclein levels in patients with Parkinson's disease: a systematic review and meta-analysis. Neurological Sciences Neurological Sciences 2019; 40(5):929–38.

[35] Betancor L, López-Gallego F, Hidalgo A, et al. Different mechanisms of protein immobilization on glutaraldehyde activated supports: Effect of support activation and immobilization conditions. Enzyme and Microbial Technology 2006; 39(4):877–82.

[36] Walt DR, Agayn VI. The chemistry of enzyme and protein immobilization with glutaraldehyde. TrAC - Trends in Analytical Chemistry 1994; 13(10):425–30.

[37] Choe W, Durgannavar TA, Chung SJ. Fc-binding ligands of immunoglobulin G: An overview of high affinity proteins and peptides. Materials 2016; 9(12):994.

[38] Song HY, Zhou X, Hobley J, et al. Comparative study of random and oriented antibody immobilization as measured by dual polarization interferometry and surface plasmon resonance spectroscopy. Langmuir 2012; 28(1):997–1004.

[39] Young MB, Oh BK, Lee W, et al. Study on orientation of immunoglobulin G on protein G layer. Biosensors and Bioelectronics 2005; 21(1):103–10.

[40] Iori F, Corni S, Felice RD. Unraveling the interaction between histidine side chain and the Au(111) surface: A DFT study. Journal of Physical Chemistry C 2008; 112(35):13540–45.

[41] Yang Z, Zhao YP. Adsorption of His-tagged peptide to Ni, Cu and Au (1 0 0) surfaces: Molecular dynamics simulation. Engineering Analysis with Boundary Elements 2007; 31(5):402–09.

[42] Pozo FG Del, Fabiano S, Pfattner R, et al. Single crystal-like performance in solution-coated thin-film organic field-effect transistors. Advanced Functional Materials 2016; 26:2379–86.

[43] Leonardi F, Tamayo A, Casalini S, et al. Modification of the gate electrode by self-assembled monolayers in flexible electrolyte-gated organic field effect transistors: Work function: Vs. capacitance effects. RSC Advances 2018; 8(48):27509–15.

[44] Temiño I, Pozo FG Del, Ajayakumar MR, et al. A Rapid, Low-Cost, and Scalable Technique for Printing State-of-the-Art Organic Field-Effect Transistors. Advanced Materials Technologies 2016; 1(5):1–7.

[45] Zhang Q, Leonardi F, Casalini S, et al. High performing solution-coated electrolyte-gated organic field-effect transistors for aqueous media operation. Scientific Reports Nature Publishing Group 2016; 6:1–10.

[46] Campos A, Riera-Galindo S, Puigdollers J, et al. Reduction of Charge Traps and Stability Enhancement in Solution-Processed Organic Field-Effect Transistors Based on a Blended n-Type Semiconductor. ACS Applied Materials and Interfaces 2018; 10(18):15952–61.

[47] Leonardi F, Casalini S, Zhang Q, et al. Electrolyte-Gated Organic Field-Effect Transistor Based on a Solution Sheared Organic Semiconductor Blend. Advanced Materials 2016; 28:10311–16.

[48] Paterson AF, Treat ND, Zhang W, et al. Small Molecule/Polymer Blend Organic Transistors with Hole Mobility Exceeding 13 cm2V−1s−1. Advanced Materials 2016; 28(35):7791–98.

[49] Pérez-Rodríguez A, Temiño I, Ocal C, et al. Decoding the vertical phase separation and its impact on C8-BTBT/PS Transistors properties. ACS Applied Materials & Interfaces 2018; 10:7296–303.

[50] Temiño I, Pozo FG Del, Ajayakumar MR, et al. A Rapid, Low-Cost, and Scalable Technique for Printing State-of-the-Art Organic Field-Effect Transistors. Advanced Materials Technologies 2016; 1:1600090.

[51] Zhang Q, Leonardi F, Casalini S, et al. High performing solution-coated electrolyte-gated organic field-effect transistors for aqueous media operation. Scientific Reports Nature Publishing Group 2016; 6(November):1–10.

[52] Zhao K, Wodo O, Ren D, et al. Vertical Phase Separation in Small Molecule:Polymer Blend Organic Thin Film Transistors Can Be Dynamically Controlled. Advanced Functional Materials 2016; 26:1737–46.

[53] Berto M, Diacci C, D'Agata R, et al. EGOFET Peptide Aptasensor for Label-Free Detection of Inflammatory Cytokines in Complex Fluids. Advanced Biosystems 2017; 2(2):1700072.

[54] Kergoat L, Piro B, Berggren M, et al. DNA detection with a water-gated organic field-effect transistor. Organic Electronics: physics, materials, applications Elsevier B.V. 2012; 13(1):1–6.

[55] Roberts ME, Mannsfeld SCB, Queralto N, et al. Water-stable organic transistors and their application in chemical and biological sensors. Proceedings of the National Academy of Sciences 2008; 105(34):12134–39.

[56] Ishikawa FN, Curreli M, Chang H, et al. A Calibration Method for Nanowire Biosensors to Suppress Device-to-Device Variation. ACS Nano 2009; 3(12):3969–76.

[57] Duan X, Li Y, Rajan NK, et al. Quantification of the affinities and kinetics of protein interactions using silicon nanowire biosensors. Nature Nanotechnology Nature Publishing Group 2012; 7(6):401–07.

[58] Lee BY, Sung MG, Lee J, et al. Universal parameters for carbon nanotube network-based sensors: Can nanotube sensors be reproducible? ACS Nano 2011; 5(6):4373–79.

[59] Hammock ML, Knopfmacher O, Naab BD, et al. Investigation of protein detection parameters using nanofunctionalized organic field-effect transistors. ACS Nano 2013; 7(5):3970–80.

[60] Gould N, Mor DE, Lightfoot R, et al. Evidence of native α-synuclein conformers in the human brain. Journal of Biological Chemistry 2014; 289(11):7929–34.

[61] Lee PH, Lee G, Park HJ, et al. The plasma alpha-synuclein levels in patients with Parkinson's disease and multiple system atrophy. Journal of Neural Transmission 2006; 113(10):1435–39.

[62] Greco P, Facchini M, Cavallini M, et al. Fabrication of ordered carbon nanotube structures by unconventional lithography. physica status solidi (b) John Wiley & Sons, Ltd 2010; 247(4):877–83.

[63] Transport Phenomena, Revised 2nd Edition | Wiley. Wiley.com [Online] [cited 2020]. Availableat:https://www.wiley.com/enit/Transport+Phenomena%2C+Revised+2nd+Edition-p-9780470508633.

[64] Giuffrida MC, Zanoli LM, D'Agata R, et al. Isothermal circular-strand-displacement polymerization of DNA and microRNA in digital microfluidic devices. Anal Bioanal Chem 2015; 407(6):1533–43.

[65] Ishihara R, Hasegawa K, Hosokawa K, et al. Multiplex MicroRNA Detection on a Power-free Microfluidic Chip with Laminar Flow-assisted Dendritic Amplification. Analytical Sciences 2015; 31(7):573–76.

[66] Zhang K, Kang D-K, Ali MM, et al. Digital quantification of miRNA directly in plasma using integrated comprehensive droplet digital detection. Lab Chip The Royal Society of Chemistry 2015; 15(21):4217–26.

[67] McArdle H, Jimenez-Mateos EM, Raoof R, et al. "TORNADO" – Theranostic One-Step RNA Detector; microfluidic disc for the direct detection of microRNA-134 in plasma and cerebrospinal fluid. Sci Rep 2017; 7(1):1750.

[68] Seghir R, Arscott S. Extended PDMS stiffness range for flexible systems. Sensors and Actuators A: Physical Elsevier 2015; 230:33–39.

CHAPTER 5

MULTIGATE ORGANIC TRANSISTORS FOR THE DETECTION OF OLIGONUCLEOTIDE BIOMARKERS

5.1 Introduction

MicroRNAs (miRNA) are a class of biomarkers whose relevance in oncology is increasing enormously, especially for neuroblastoma and lung cancer (Chapter 1). Detection of miRNA circulating in blood appears a potential strategy for cancer early diagnosis, patient monitoring, and explaining the cellular path of disease. Therefore the biosensor technology involved into miRNA detection and quantification is increasing momentum and competition between high sensitivity solutions. In the following chapter, I report the work I completed during my secondment at University of Modena and Reggio Emilia in the Laboratory of Organic Electronics under the supervision and tutoring of Prof. Fabio Biscarini. EGOFET device represent a viable and promising label free technology for the detection of miRNA as I demonstrate with the prototype which I built. The device allows one to measure the differential response between two gate electrodes, viz. one sensing and one reference, both immersed in the electrolyte above the transistor channel. I will describe the dose curves with an analytical function derived from a thermodynamic model of the reaction equilibria relevant in our experiment. The binding free energy characteristic of the hybridization on the device surface was found to be approximately 20% lower with respect to the reaction in solution, hinting to partially inhibiting effect of the surface and presence of competing reactions.

In subchapter 5.3, I will report the work done to prepare a prototype to demonstrate multiple biomarkers sensing with same concept but increased throughput thanks to integration of 3 gates in the same microfluidic device.

Finally I will report on the modelling of EGOFET with finite element software Comsol Multiphysics, that was tested to simulate and eventually predict the response of the EGOFET biosensor.

5.2 Label free detection of miRNA-21 with Electrolyte Gated Organic Field Effect Transistors

Since miRNAs with different sequences may act either as tumor promoter or tumor suppressor in the presence of interacting drugs [1], accurate methods for quantification of miRNA are of potential impact for both diagnostics [2] and study of therapeutic efficacy [3]. For these reasons, PCR-assisted low volume analytic protocols, as well as PCR-free isothermal amplification methods, are emerging as new techniques to tackle the difficult task of counting a small number of oligonucleotides in complex matrices [4].

Among the numerous miRNAs involved in disease diagnostics and therapy, miRNA-21 is one of the most studied because has been conserved through evolution of vertebrates up to humans and its main biological functions are linked with anti-apoptosis and pro-survival factors [5]. In the immune system, miRNA-21 has been shown to regulate the gene coding for inflammation biomarker IL-12 [6]. Temporary silencing of miRNA-21 was correlated with cell differentiation and development in thyroid cells [7], whereas in the large majority of cancer diseases, miRNA-21 is upregulated. High levels of miRNA-21 were correlated, as promoting progression, with breast cancer [8], pancreatic cancer [9], lung cancer [10], glioblastoma [11].

The concentration of oligonucleotides is measured in clinical studies with quantitative PCR. More recently, analytical tools based on PCR-free hybridization in microfluidics appeared, where surface plasmon resonance and droplet based microfluidics are exploited [12].

Electrochemical methods for miRNA detection were extensively investigated. An example consists of gold nanoparticles functionalized with DNA-bioreceptor and using iridium complexes for redox reactions. This approach yields femtomolar limit of detection (LOD) in controlled hybridization [13]. Another example features sensing probes, synthetized as complementary strands to the mature miRNA, anchored to a gold electrode surface by means of thiol chemistry [14], and capable to detect attomolar levels of miRNA-155 (marker of breast cancer).

Optical detection, based on either absorption or fluorescence, requires labelling of the probe with either gold nanoparticles [15] or fluorescent molecules whose signal changes upon the formation

of the duplex [16]. Molecular beacons, consisting of paired fluorophore and quencher [17], yield a fluorescent label upon the separation of the two parts induced by hybridization.

Label-free biosensors, based on electronic or ionic transport, transduce a specific reaction of the target analyte with a modulation of the charge transport in an inorganic [18] or organic semiconductor [19] channel, thus changing the current flowing in the channel. Electrolyte gated organic field-effect transistors (EGOFET) are able to quantify ultra-low concentrations of diverse biomarkers [20–23]. Moreover, this architecture offers the opportunity to integrate complementary techniques sensitive to biorecognition, such as fluorescence microscopy or surface plasmon resonance [24].

EGOFET enables ultrasensitive detection of antigens because the electrostatic potential of the gate electrode, which is sensitive to antigen binding at surface bound recognition sites, is capacitively coupled to the channel. An amplified shift of the Fermi level of the organic semiconductor is achieved even for low amount of biomolecules adsorbed or grafted on the gate electrode [19]. Multiple biomarkers detection is possible within the same integrated EGOFET microfluidic device, by miniaturization and multiplexing gate electrodes immersed in the electrolyte solution. Demonstration of multigate architecture was reported by our group for the detection of inflammatory biomarker TNFα using aptamer functionalization with standard manufacturing processes employed for printed circuit board production [25].

In the present work, I report the fabrication and assessment of an EGOFET device with dual gate architecture designed for sensing solutions containing a single-stranded segment of miRNA-21 (miRNA-21-3p, also termed target analyte (T), see Chapter 2.3.2) at concentrations down to tens picomolar range. Our device operates on the differential electronic response of the transistor to the two gate sweeps: one of the gate electrodes, termed G2, is grafted with the complementary sequence bioreceptor (miRNA-21-5p, also termed probe (P)), while the other gate electrode, termed G1, is functionalized with a tightly packed organic monolayer that reduces unspecific adsorption on the Au surface. The G1 electrode serves as an internal reference electrode, whereas the G2 electrode as the sensing electrode. Characterization of EGOFET devices allows us to quantify the current difference at each gate voltage, as modulated by the number of target nucleotides hybridized on the sensing gate surface. This number is correlated to the molar concentration of the target analyte [T].

Complementary information was then obtained by Surface Plasmon Resonance Imaging (SPRI) performed on the same oligonucleotide pair. There, the change in refractive index (SPRI) is correlated to the functionalization and the hybridization reaction. This provides an independent assessment of the surface coverage and hybridization efficiency of the sensing gate electrode of the EGOFET sensor.

5.2.1 EGOFET in dual gate configuration

I describe first the architecture of the dual gate EGOFET designed for miRNA sensing (Figure 5.1). The electrode G1 is a gold wire functionalized with 2-Mercaptoethanol (ME) monolayer, while the electrode G2 is a gold wire, symmetric to G1 with respect to the channel, functionalized with the thiolated probe P. The sequence of P was synthesized according to a sequence reported for human miRNA-21-5p [26]. According to my protocol, before the EGOFET operations, G2 is incubated in buffer solutions spiked with different target concentrations [T]. The incubation protocol is described in Chapter 2.3.2.

In Figure 5.1a, I schematically depict the hybridization of the probes P grafted to G2 with the target analyte T. The electrode G2 is then immersed together with G1 in the buffer electrolyte of the device that comprises an organic semiconductor channel patterned on polyimide substrate (Kapton™, 50 μm) (Figure 5.1b). The aqueous electrolyte is contained in a polydimethylsiloxane (PDMS) reservoir. Figure 5.1c shows optical images at two different magnifications of the semiconductor channel. In particular, the optical micrograph in polarized light reveals the presence of large crystalline domains across the channel. The functionalization steps of the gate electrodes are assessed by both SPR and the electrical characterization of each EGOFET before and after each step. Details on the fabrication procedure and functionalization steps are provided in Chapter 2.3.3 and Chapter 2.3.4.

The stage holder with gate electrodes (Figure 5.1c) was removed from the electrolyte reservoir and electrode G2 was incubated in vials each containing different concentrations of T, starting from 10 pM to 300 pM.

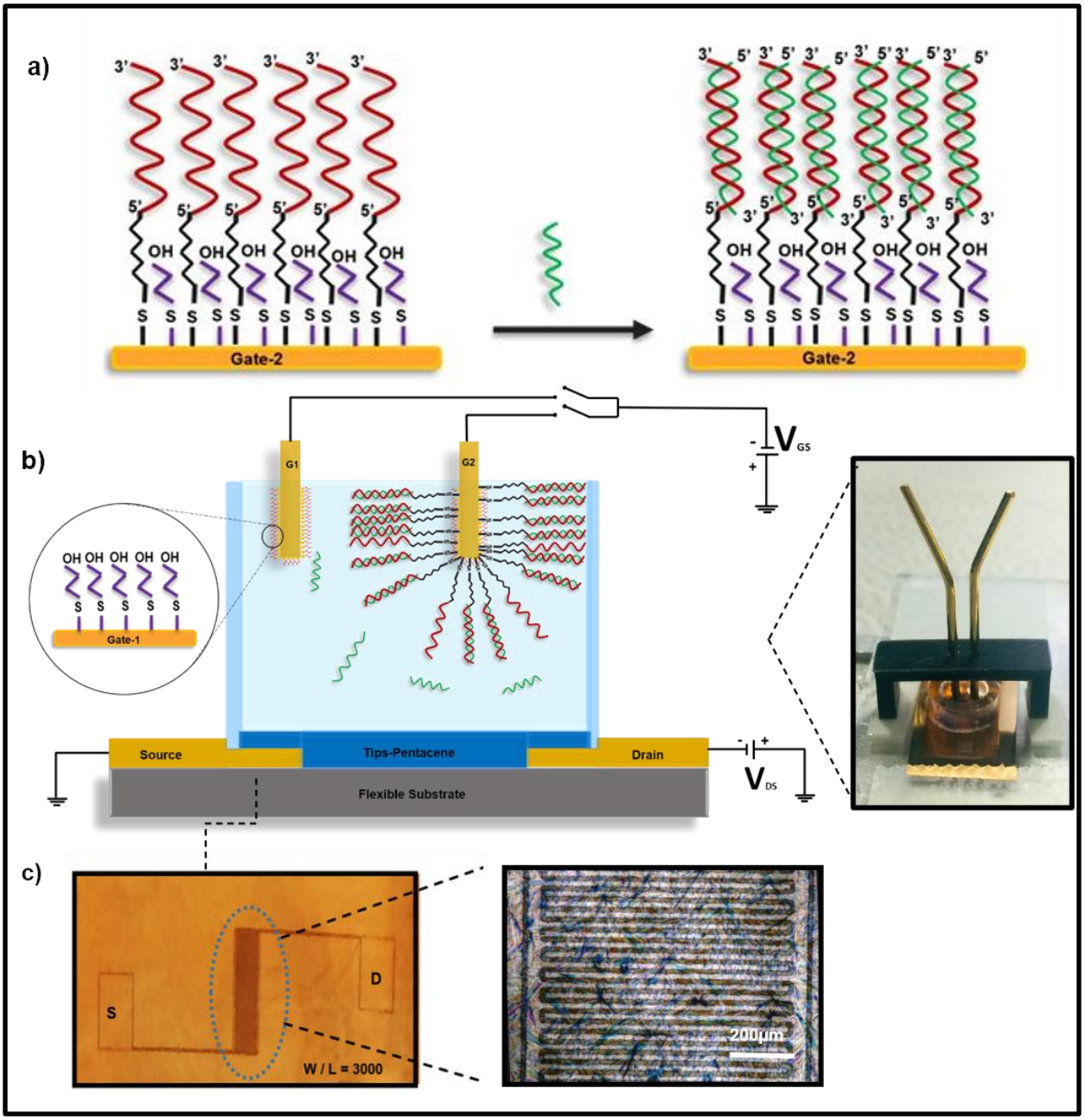

Figure 5.1: Functionalization of a) G2 with probe and 2-ME (left) and the hybridization process of the target analytes with G2 after incubation (right). b) Schematic drawing illustrating the architecture of the dual-gate EGOFET device featuring the PDMS microfluidics pool sealed on top of the Source and Drain interdigitated electrodes covered with TIPS-pentacene. c) Morphology of EGOFET showing a detail of the test pattern with interdigitated electrodes and contact pads, a polarized light microscopy image (10x objective) evidencing the crystals in the channel formed by TIPS-pentacene thin film.

5.2.2 EGOFET after hybridization

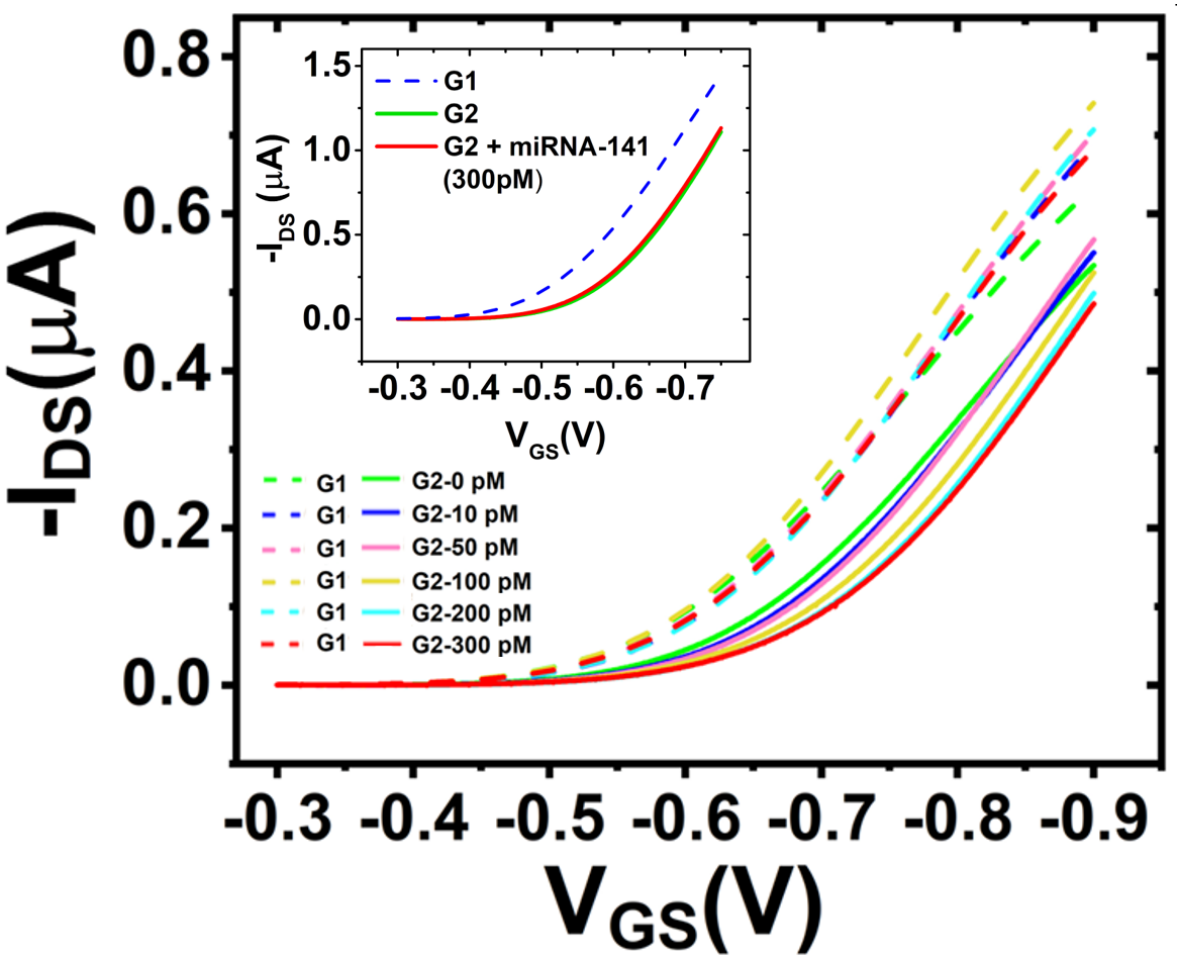

Figure 5.2: Transfer curves of EGOFET device with two-gate electrodes, characterized after incubation of both gates with solutions containing different concentrations of the target analyte; the solid lines obtained with G2 are markedly separated from the dashed curves obtained with G1 Transfer characteristics with G1 are plotted with the same color of G2 to indicate the measurement taken few minutes after G2. The response of the device to 300 pM concentrated miRNA-141 solution is plotted in the inset, confirming the selectivity of the probe.

Transfer curves of the device were obtained by measuring channel current (I_{DS}) upon sweeping Gate-Source voltages in the range from -0.2V to -0.9V with steps of -1 mV at a fixed Drain-Source voltage V_{DS} =-0.2 V. The transfer curves of the EGOFET are acquired first by sweeping the voltage bias of reference G1, while leaving sensing G2 floating. Then, within two minutes, they were

acquired by sweeping the voltage bias of sensing G2, while leaving G1 floating. The values of both Drain-Source and Gate-Source currents were acquired to ensure that no short-circuit or faradaic process occurred. In order to evaluate the precision and reproducibility of the measurement performed with EGOFET, the laser ablation of the interdigitated electrodes and the deposition of the organic semiconductor upon the transistor channel were repeated for each experiment.

Figure 5.2 shows an example of transfer curves recorded with G1 and G2 at different concentration [T]. The extent of residual leakage current was less than 30 nA, compared to the on-current measured in the range of 0.1 to 1 μA. I recall that only G2 was previously incubated in a buffer solution spiked with the target analyte at concentration [T]. The transfer curves for the G2 gate sweeps $I_{DS}([T],\ V_{GS})_{G2}$ show a decrease of current with increasing concentration [T]. Conversely, the transfer curves (dashed lines) $I_{DS}([T], V_{GS})_{G1}$ are narrowly distributed around a central value of the buffer transfer curve $I_{DS}(0, V_{GS})_{G1}$.

The first evidence suggests a sizable change in the charge distribution in the proximity of the gold surface of G2 is induced by the formed hybridized complex, with respect to the single-stranded oligonucleotide. This is not observed in the case of G1.

Indeed, the transfer characteristics acquired by sweeping G1 after the incubation of G2 in the target analyte solution exhibit modest fluctuations with respect to the curve recorded with the pure buffer solution, [T]=0. I ascribe these fluctuations to unspecific adsorption of target molecules on G1 during measurement, that may detach from G2 and diffuse through the solution. This process is depicted in the zoom of Figure 5.1b. The scarce sensitivity of the electrode G1 to [T] enables us to assume that the transfer curves driven by G1 are independent on [T] in the range of [T] explored, viz. $\langle I_{DS}([T], V_{GS})\rangle_{G1} \approx \langle I_{DS}(V_{GS})\rangle_{G1.}$

Mean transfer curves are estimated as the logarithmic mean of N=10 measurements for each concentration by sweeping G2, and N=15 measurements for each concentration by sweeping G1:

$$\langle I_{DS}([T], V_{GS})\rangle_{G2} = 1A \cdot \langle e^{\ln[I_{DS}([T],V_{GS})/1A]}\rangle_{G2} \approx 1A \cdot e^{\langle \ln[I_{DS}([T],V_{GS})/1A]\rangle_{G2}} \quad (1a)$$

$$\langle I_{DS}([T], V_{GS})\rangle_{G1} = 1A \cdot \langle e^{\ln[I_{DS}([T],V_{GS})/1A]}\rangle_{G1} \approx 1A \cdot e^{\langle \ln[I_{DS}(V_{GS})/1A]\rangle_{G1}} \approx \langle I_{DS}(V_{GS})\rangle_{G1} \quad (1b)$$

Here the pre-factor imparts the physical dimension, and the exponent of the right equation is the logarithmic mean:

$$\langle \ln[I_{DS}([T], V_{GS})/1A]\rangle = \frac{1}{N}\sum_{i=1}^{N} \ln\left[I_{DS,i}([\mathrm{T}], V_{GS})/1A\right] \quad (2)$$

The experimental error is estimated as:

$$\frac{\delta I_{DS}}{\langle I_{DS}\rangle} \approx \sqrt{\frac{1}{N-1}\sum_{i=1}^{N}(\ln(I_{DS}/1A) - \langle \ln(I_{DS}/1A)\rangle^2} \quad (3)$$

This procedure to calculate the mean is motivated by the transfer curve spanning by orders of magnitude in the small V_{GS} range of operations: since the arithmetic mean will wash out small features because the largest transfer curve overwhelms the others, even if it were an outlier, it is preferred to adopt the logarithmic mean as detailed previously [25].

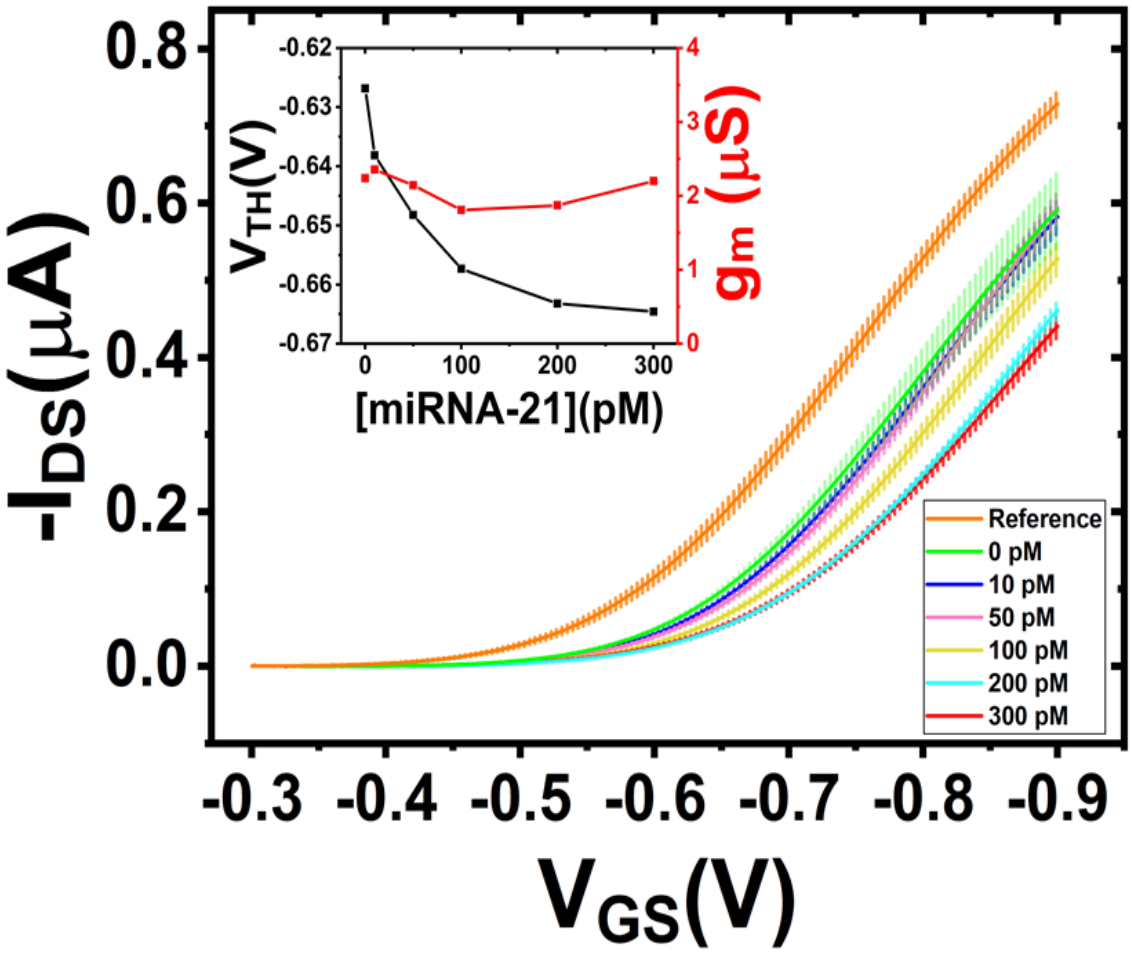

Figure 5.3: Plot of the logarithmic average of the transfer curves of G1 and G2 showing clear, distinct trends with statistical error. In the inset the decay of G2 threshold voltage is depicted with transconductance values reported to be almost constant at varying target concentration.

The logarithmic mean transfer curves, estimated from three devices each, are shown in Figure 5.3 with G1 (orange) and G2 (colors, each representing one concentration). The error is depicted by the corresponding color shades, and as also clear from eq. 3 increases with the current, hence with applied V_{GS}.

The transfer curves in Figure 5.2 and Figure 5.3 are recorded for hybridization with the target miRNA-21 solution. The measurement protocol is set to acquire the transfer curves mostly in the linear regime $|V_{DS}| << |V_{GS} - V_{Th}|$ that can be described according to the equation:

$$I_{DS}([T], V_{GS}) = g_m([T], V_{DS}) \cdot [V_{GS} - V_{Th}([T])]. \quad (4)$$

Here, g_m is the transconductance that depends linearly on both V_{DS} and W/L, where W and L are the channel width and length, respectively. V_{DS} and W/L are kept fixed. The threshold voltage V_{Th} represents the internal field to overcome for turning the device on. Both transconductance and threshold voltage are, in principle, sensitive to the interaction between P and T, and hence to [T]. In particular hybridization, that affects the surface potential of the gate G2, is reflected in the threshold voltage shift, and may also appear in g_m as the density of states may be changed.

The inset in Figure 5.2 shows the transfer curves for hybridization with unrelated miRNA-141 (mismatched sequence is reported in the chapter 2.3.2). The I_{DS} vs V_{GS} curve for [miRNA-141]=300 pM is not significantly different from those obtained with the pristine G2 probe, whereas miRNA-21 modulates sensibly the current with concentration.

In the inset of Figure 5.3 I show the threshold voltage and the transconductance extracted from the mean transfer curves $\langle I_{DS}([T], V_{GS})\rangle_{G2}$ by applying the linear fit eq. 4. I observe a logarithmic decay of $V_{Th,G2}$ vs [T]. On the other hand, I notice that the slope of the linear region of the transfer curves in Figure 5.3 does not change substantially even when the curves are progressively offset towards more negative voltage values with increasing concentration. This is evidenced by the transconductance values in Figure 5.3 right axis that exhibits a substantial invariance vs [T].

The presence of the negatively charged hybridized probe/target pair on the sensing gate explains both the absence of change in transconductance and the shift of the V_{TH} to more negative voltages. The more negative hybridized sensing layer induces a positive image charge on the electrode surface, thus making the gate electrode potential less negative.

In order to experimentally minimize the device-to-device variations, it is convenient referring the changes in the transfer curves to the mean curve of the reference electrode G1, the latter being largely insensitive to [T]. Therefore, I combine the transfer curves $\langle I_{DS}([T], V_{GS}\rangle_{G2}$ (obtained by

sweeping the voltage at the sensing electrode G2), with $\langle I_{DS}(V_{GS})\rangle_{G1}$ (obtained by sweeping the voltage the reference electrode G1) to yield the signal S_{ref}:

$$S_{ref}([\mathrm{T}], V_{GS}) = 1 - \frac{\langle I_{DS}([\mathrm{T}], V_{GS})\rangle_{G2}}{\langle I_{DS}(V_{GS})\rangle_{G1}} \tag{5a}$$

Similarly, in order to model the dose curve later, I define the signal *S* referred to G2 as:

$$S([\mathrm{T}], V_{GS}) = 1 - \frac{\langle I_{DS}([\mathrm{T}], V_{GS})\rangle_{G2}}{\langle I_{DS}(0, V_{GS})\rangle_{G2}} \tag{5b}$$

The brackets indicate the averaging process of the transfer curves that is described in the previous section. The definition imposes a relation between *S* and S_{ref} in terms of $A(V_{GS}) = \frac{\langle I_{DS}(V_{GS})\rangle_{G1}}{\langle I_{DS}(0, V_{GS})\rangle_{G2}}$:

$$S([\mathrm{T}], V_{GS}) = [1 - A(V_{GS})] + S_{ref}([\mathrm{T}], V_{GS}) \cdot A(V_{GS}) \tag{6}$$

Thus, the signal S_{ref} measured with respect to the reference electrode must be both rescaled and offset to be reconducted to the signal recorded with the gate G2 alone. The error δS on the signal is estimated by error propagation starting from the error eq. 3:

$$\delta S([\mathrm{T}], V_{GS}) = \delta A(V_{GS})\left[1 + S_{ref}([\mathrm{T}], V_{GS})\right] + A(V_{GS}) \cdot \delta S_{ref}([\mathrm{T}], V_{GS}) \tag{7a}$$

$$\delta S([\mathrm{T}], V_{GS}) = \left\{\frac{\delta\langle I_{DS}\rangle_{G1}}{\langle I_{DS}\rangle_{G1}} + \frac{\delta\langle I_{DS}\rangle_{G2}}{\langle I_{DS}\rangle_{G2}}\right\} \cdot A(V_{GS})\left[1 + S_{ref}([\mathrm{T}], V_{GS})\right] + A(V_{GS}) \cdot \left[1 - S_{ref}([\mathrm{T}], V_{GS})\right] \cdot \left\{\frac{\delta\langle I_{DS}([\mathrm{T}], V_{GS})\rangle_{G2}}{\langle I_{DS}([\mathrm{T}], V_{GS})\rangle_{G2}} + \frac{\delta\langle I_{DS}\rangle_{G1}}{\langle I_{DS}\rangle_{G1}}\right\} \approx 2 \cdot A(V_{GS}) \cdot \left\{\frac{\delta\langle I_{DS}([\mathrm{T}], V_{GS})\rangle_{G2}}{\langle I_{DS}([\mathrm{T}], V_{GS})\rangle_{G2}} + \frac{\delta\langle I_{DS}\rangle_{G1}}{\langle I_{DS}\rangle_{G1}}\right\} \tag{7b}$$

The assumption in eq. 7b is that the relative errors of the transfer curves acquired upon G2 sweeping are comparable. In eq. 7b, I omitted the dependence of V_{GS} for sake of brevity.

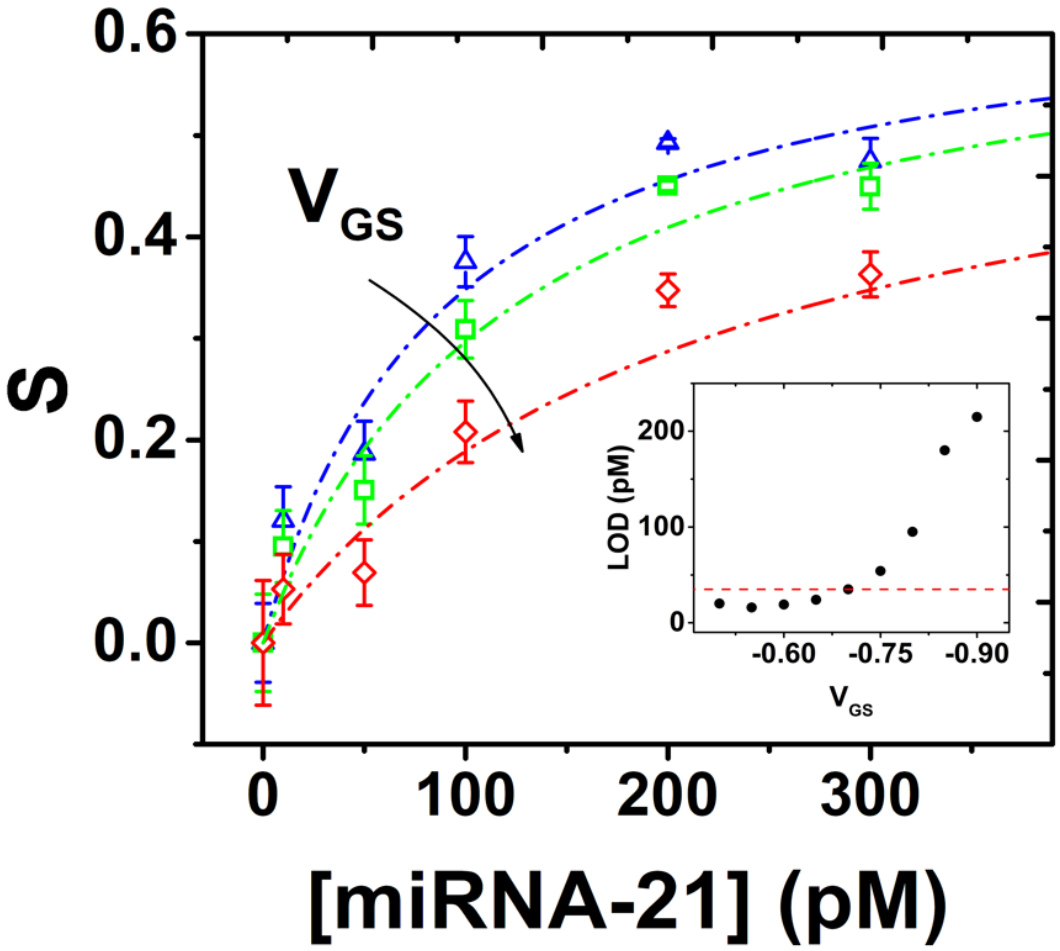

Figure 5.4: Fitting of the dose curves calculated at three different V_{GS} (-0.6 blue, -0.7 green, -0.8 red) V using eq. 18; inset, plot of LOD vs V_{GS}, extracted from the fitting curve value corresponding to three times the error reported for measurements without the target analyte (dashed line indicating the value of 35 pM as maximum for $V_{GS} \geq$ -0.7 V.

The dose curves shown in Figure 5.4 compare S_{ref} and the signal S from eq. 6 vs [T] both acquired at V_{GS}=-0.6, -0.7, -0.8 V. The signal S slows down at concentrations approaching 300 pM. I estimate, based on the transfer curves and the error width obtained from 20experiments, that the sensitivity of the biosensor is below 50 pM, with a LOD taken to be the value of concentration corresponding to $S = 3 \cdot \delta S([0], V_{GS})$ in the fit reported in Figure 5.4. The LOD is equal to 35 pM for gate voltages below -0.75 V (inset Figure 5.4), while the LOD increases and the sensitivity (slope) decreases as V_{GS} becomes more negative (see the curves in Figure 5.4).

5.2.3 Thermodynamics of the biorecognition events

I derive now an analytical function that describes the dose curves as in Figure 5.4 for the dual gate device. The aim is not only to devise an invertible function for the dose curve, but to derive it from a chemical model that enables us to understand how biorecognition is translated into the device response. In doing this, we assume that the device (system) is in quasi-equilibrium conditions, thus we neglect this time kinetic effects. Thus, drawing the different equilibria that characterize our system, and we envision four relevant equilibria.

We start from G2 that is functionalized with the probe P, whose activity (that we take equal to concentration) is termed p_0. G2 is first incubated in the solution containing the target T at initial concentration t_0, then a first equilibrium (hybridization on the G2 electrode surface) is attained:

$$P + T \rightleftharpoons PT \tag{8}$$

Here PT is the probe-target pair concentration whose equilibrium constant K_{PT} is the binding association constant on the electrode:

$$K_{PT} = \frac{[PT]}{[P][T]} = \frac{[PT]}{(p_0 - [PT])[T]} = \frac{(p_0 - [P])}{[P][T]} \tag{9a}$$

$$K_{PT} = \frac{x_{eq}}{(1 - x_{eq})(t_0 - x_{eq} \cdot p_0)} = \frac{x_{eq}}{(1 - x_{eq})(1 - x_{eq} \cdot p_0 / t_0) \cdot t_0} \tag{9b}$$

Here, $[T]$ is the concentration of target in solution, $[P]$ concentration of the free probe on the electrode, and $x_{eq} = [PT]/p_0$ is the equilibrium fraction of the hybridized probe. Langmuir modelling described the behaviour of DNA and RNA sensors based on fluorescence or electrochemistry, although the hybridization process may involve multiple reactions in competition with detection and characteristic reaction kinetics may also be regulated by hindrance effects between target and probe oligonucleotides or by the presence of the surface itself. [27]. The signal $S([T])$, dependence on x_{eq} can be described as in the Langmuir isotherm:

$$S = S_{max} x_{eq} = S_{max} \frac{K_{PT} \cdot [T]}{1 + K_{PT} \cdot [T]} \tag{10}$$

We record the signal after the electrode G2 has equilibrated in the buffer solution of the device. Hence we write the other equilibria involving G2 and the buffer solution:

$$P \rightleftharpoons C \tag{11a}$$

$$T + C \rightleftharpoons TC \tag{11b}$$

$$PT \rightleftharpoons TC \tag{11c}$$

that represent, respectively, the desorption of probe from the electrode surface (eq. 11a), the recognition between probe and target in the bulk solution (eq. 11b) where *C* is the probe that in limited amount has desorbed from the gate surface and diffuses nearby the surface free in solution, and *TC* accounts for the desorption of probe/target from the electrode surface (11c). The respective equilibrium constants are:

$$K_{des} = \frac{[C]}{[P]} \tag{12a}$$

$$K_a = \frac{[TC]}{[C][T]} \tag{12b}$$

$$K_{det} = \frac{[TC]}{[PT]} \tag{12c}$$

That represent respectively the desorption constant (12a), the binding association constant in solution (12b), and the detachment constant that leads to a partition of the associated pair between electrode and solution. Mass conservation imposes that:

$$[C] + [TC] + [P] = p_0 \tag{13a}$$

$$[T] + [TC] + [PT] = t_0 \tag{13b}$$

By multiplying eq. 12a and eq. 12b, dividing them by eq. 12c and comparing to eq. 9, we establish the relationship among the four constants:

$$\frac{K_a K_{des}}{K_{PT}} = K_{det} \tag{14}$$

We express $[C]$ from eq. 12a, $[TC]$ from eq. 12b, then we obtain:

$$[P] = \frac{p_0}{1+K_{des}+K_a K_{des}[T]} \tag{15a}$$

$$[T] = \left\{1 + \frac{K_{PT}+K_a K_{des}}{1+K_{des}+K_a K_{des}[T]} p_0\right\}^{-1} t_0 \tag{15b}$$

Upon simplification, eq. 15b yields the second order equation:

$$K_a K_{des}[T]^2 + [T]\{1 + K_{des} + (K_{PT} + K_a K_{des})p_0 - K_a K_{des} t_0\} - \{K_{des} + 1\}t_0 = 0 \tag{16}$$

Expressed also in terms of K_{det}

$$K_a K_{des}[T]^2 + [T]\left\{1 + K_{des} + K_a K_{des}\left(1 + \frac{1}{K_{det}}\right)p_0 - K_a K_{des} t_0\right\} - \{K_{des} + 1\}t_0 = 0 \tag{17}$$

Finally, if we solve for [T] and we plug it into eq. 10, we obtain the analytical function describing the signal $S([T])$:

$$S = S_{max} \frac{K_{PT}\cdot[(K_{PT}+K_a K_{des})p_0+1]\cdot(\sqrt{Wt_0+1}-1)}{K_{PT}\cdot[(K_{PT}+K_a K_{des})p_0+1](\sqrt{Wt_0+1}-1)+2K_a K_{des}} \tag{18}$$

where we indicate $W = \frac{4K_a K_{des}}{[(K_{PT}+K_a K_{des})p_0+1]^2}$ to simplify notation.

We notice from eq. 18 that *S* scales as $\sqrt{t_0}$ when $W \cdot t_0 \gg 1$, thus recovering the Hill-type power law dependence shown by [27]:

$$S \approx S_{max} \frac{\left\{\frac{2K_{PT}\sqrt{K_a K_{des}}}{\left[(K_{PT}+K_a K_{des})p_0+1\right]}\right\}\cdot\sqrt{t_0}}{1+\left\{\frac{2K_{PT}\sqrt{K_a K_{des}}}{\left[(K_{PT}+K_a K_{des})p_0+1\right]}\right\}\cdot\sqrt{t_0}} = S_{max}\frac{K_{1/2}\cdot\sqrt{t_0}}{1+K_{1/2}\cdot\sqrt{t_0}} \quad (19)$$

Instead, S scales linearly with t_0, hence recovering a Langmuir type dependence,

when $W \cdot t_0 \ll 1$:

$$S \approx S_{max} \frac{\left\{\frac{2K_{PT}K_a K_{des}}{\left[(K_{PT}+K_a K_{des})p_0+1\right]}\right\}\cdot t_0}{1+\left\{\frac{2K_{PT}K_a K_{des}}{\left[(K_{PT}+K_a K_{des})p_0+1\right]}\right\}\cdot t_0} \approx S_{max} \frac{\left\{\frac{2K_{PT}K_a K_{des}}{[K_{PT}p_0+1]}\right\}\cdot t_0}{1+\left\{\frac{2K_{PT}K_a K_{des}}{[K_{PT}p_0+1]}\right\}\cdot t_0} \approx S_{max}\frac{K_1\cdot t_0}{1+K_1\cdot t_0} \quad (20)$$

Thus, the simple model predicts these two important cases as limit behaviors. Hence, I used the generalized Langmuir isotherm function (18) to fit the dose curve of the EGOFET biosensor. The only free fitting parameter is the equilibrium constant K_{PT}, whereas the other parameters S_{max}, K_a, K_{des}, and p_0 were fixed. In particular, K_a=1.15 10^{17} is calculated from the interaction between miRNA sequences same of P and T in solution from software DINAMELT [28]. K_{des} was arbitrarily fixed at 10^{-15} to indicate that it is strongly unlikely, S_{max} =0.65 and p_0=30 pM. From the analysis of experimental signal data retrieved from EGOFET current output, I obtain the value for the binding constants, for instance at V_{GS}= -0.75 V as in the plot of Figure 5.4 is equal to K_{PT} = $8.8\times10^9 \pm 1.8\times10^9$. Similarly, fitting of data was applied to all the dose plots starting from V_{GS}=-0.5V to V_{GS}=-0.9V. This allows us to analyze the dependence of the binding constant with respect to the values of gate voltage. From the values of K_{PT} obtained by best fit with eq. 18, I plot the data in Figure 5.5, keeping the temperature equal to 37 °C (as in the incubation phase). I observe a non-linear monotonic trend of K_{PT} vsV_{GS}, that I interpret according to the combination of free energy of hybridization and electrostatic free energy contributions, as detailed in the following.

5.2.4 Calculation of free energy from Electrolyte-gated field-effect transistor (EGOFET) characteristics

The equilibrium constant K_{PT} is related to the molar free energy of hybridization at the G2 electrode (ΔG_0) and the electrostatic free energy (ΔG_e), according to the following factor expression:

$$K_{PT}(V_{GS}) = e^{-\frac{\Delta G_0}{RT}} \cdot \Delta e^{-\frac{\Delta G_e}{RT}} \quad (21)$$

Where R is the gas constant and T is the absolute temperature. When we expand the enthalpic part of ΔG_e at the second order, we obtain

$$\Delta G_e = \delta Q_{\text{eff}} \cdot (V_{\text{GS}} - V_0) + \delta C_{\text{eff}} \cdot (V_{\text{GS}} - V_0)^2 \quad (22)$$

The terms δQ_{eff} and δC_{eff} represent the variation of the effective charge and effective capacitance respectively, while the voltage V_0 annihilates the electrostatic free energy contribution eq. 22. In the present work V_0 has been selected equal to the minimum V_{GS} resulting from the fitting, as explained further.

By expanding equations (21) and (22) we get:

$$-RT \cdot \ln K_{PT} = \Delta G_0 + \delta Q_{\text{eff}} \cdot (V_{\text{GS}} - V_0) + \delta C_{\text{eff}} \cdot (V_{\text{GS}} - V_0)^2 \quad (23a)$$

and by grouping, we obtain the fitting function:

$$-RT \cdot \ln K_{PT} = \left(\Delta G_0 - \delta Q_{\text{eff}} V_0 + \delta C_{\text{eff}} {V_0}^2\right) + (\delta Q_{\text{eff}} - 2\delta C_{\text{eff}})\, V_{\text{GS}} + \delta C_{\text{eff}} \cdot {V_{\text{GS}}}^2 \quad (23b)$$

$$-RT \cdot \ln K_{PT} = A + B\, V_{\text{GS}} + C\, {V_{\text{GS}}}^2 \quad (23c)$$

Upon the binding of probe-target, the contribution due to the changes of the surface charge and of the surface dipole moment is represented by the linear term B in equation (23).

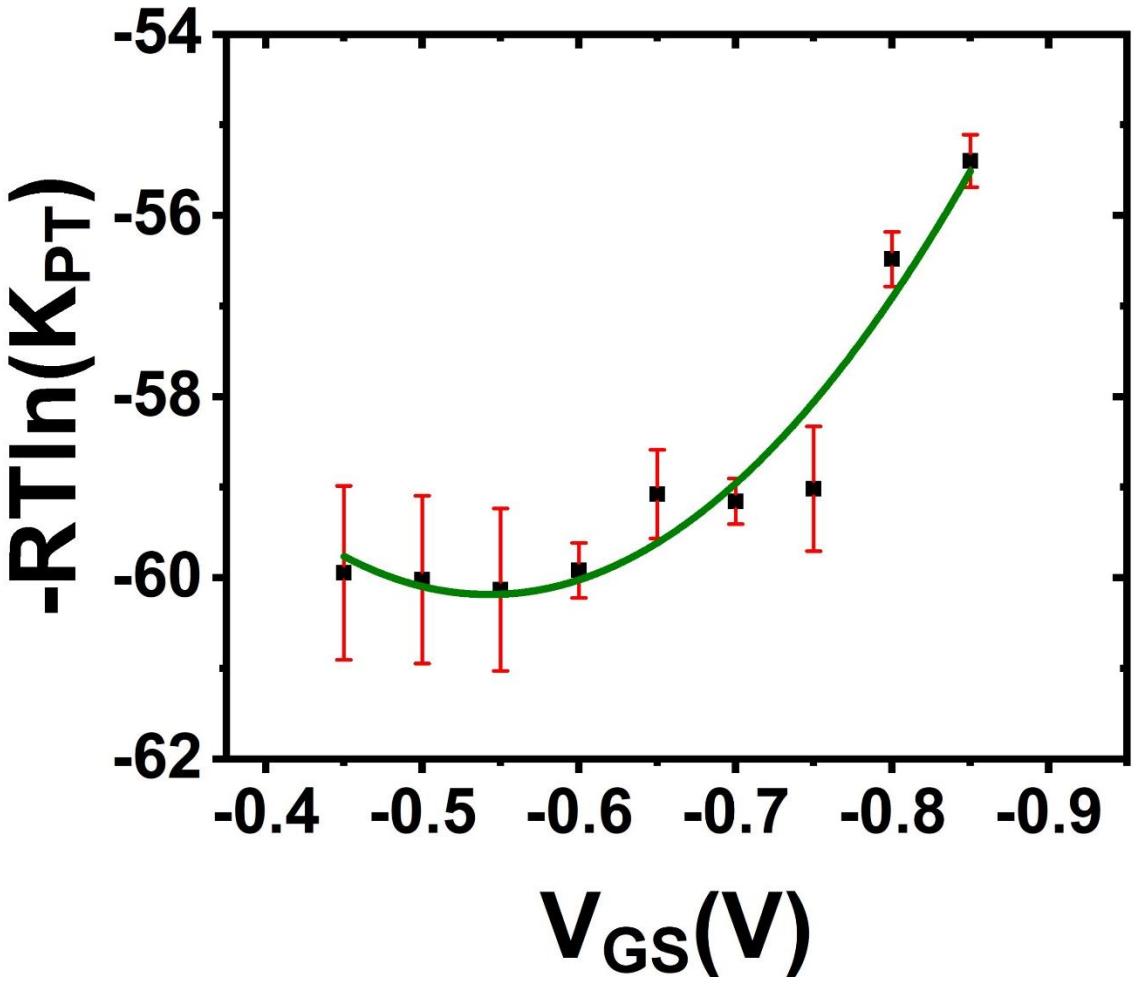

Figure 5.5: Gate–voltage dependent affinity constant K_{PT} extracted from all dose curves; green continuous line is the best fit from equation (23c).

The quadratic term *C* is the change of capacitance δC_{eff} and includes both the change of interfacial capacitance between electrolyte and the gate electrode and the change of polarizability upon hybridization.

I fit the data in Figure 5.5 with the parabolic equation (23c), then I extract the values of the physical properties from the best fit values *A*, *B*, and *C*. These are summarized in Table 1.

Table 1: Best fitting parameters obtained from eq.23c and the corresponding thermodynamics properties ΔG_0 and δQ_{eff} derived from eq.23b.

A (kJ/mol)	*B* (kC/mol)	$C = \delta C_{eff}$(kF/mol)	ΔG_0(kJ/mol)	δQ_{eff}(kC/mol)
-55.48±3.8	25.77±11.57	29.42±8.51	-83.3	54.77

Binding free energy was thus obtained as function of voltage. I find V_0= -0.45 V as the value of V_{GS} that zeroes the derivative of eq. 23c. I then extract ΔG_0 =-83.3kJ/mol. ΔG_0 was then compared with the binding energy generated by the simulation software DINAMELT [28] for the sequences of probe and target described in the chapter 2.3.2. The value of ΔG_0 calculated for the bulk reaction, according to [29], is -101.2 kJ/mol. I infer that our ΔG_0 value in Table 1 for the G2 electrode is comparable with respect to the binding constant in solution. The value extracted from our EGOFET measurement is approximately 20% lower and this reduced value hints to a reduced efficiency of hybridization because of spatial confinement, as it is also supported by the SPR experiments described below.

I obtained the electrostatic free energy at V_{GS} = -0.75V equal to -13.52kJ/mol from eq. 22. The capacitive contribution to ΔGe is 0.05kJ/mol at V_{GS} =-0.5V and increases as a power law with the drain-source voltage up to 5.8kJ/mol at V_{GS} = -0.9V. The charge contribution is dominant in the electrostatic free energy and shows a linear dependency with the applied gate-source voltage (from -2.4kJ/mol to -24.26kJ/mol at V_{GS}=-0.9V). The primary role of charge could be related to the presence of the negatively charged phosphate groups on the target RNA filaments, as observed also from the V_{TH} trend.

5.2.5 SPRI Characterization

I used surface plasmon resonance to obtain an independent evidence of the interaction between probe and miR-21-3p. With this aim, I immobilized probe on the gold surface of the SPR sensor through direct interaction between the thiol moiety available in the structure of probe and the gold surface. Figure 5.6 shows a representative sensorgram detected for the immobilization. The linear time-dependence of the signal detected during the adsorption of the probe is consequence of a mass-transport limited kinetics for the adsorption process.

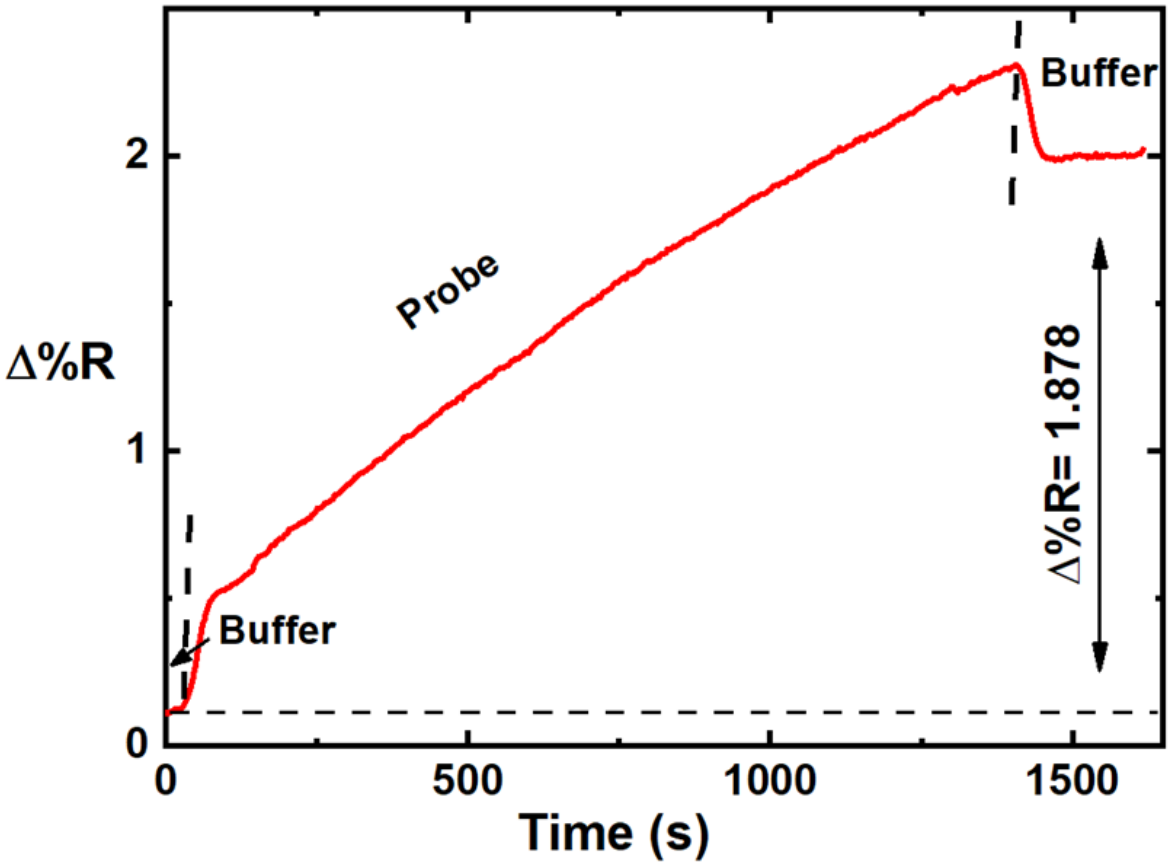

Figure 5.6: Representative changes in per cent reflectivity (Δ%R) over time detected for the immobilization of probe. The probe was immobilized through direct interaction of thiol moiety with the gold surface. The signal detected when the running buffer baseline was established after probe adsorption, allowed us to quantify the surface coverage of probe adsorbed on the surface corresponding to 4.7 10^{-12} molecules cm^{-2}.

I quantified the surface coverage of probe adsorbed on the surface (4.7 10^{-12} molecules cm^{-2}) measuring the variation of the detected signal after the adsorption of probe (Δ%R=1.878). The number of molecules per unit area was estimated on the basis of the theoretical model described by *Shumaker-Parry et al.* [30].

Figure 5.7 shows representative sensograms detected for the hybridization of miR-21-3p and the interaction of the control unrelated sequence (CTR). Both experiments were conducted using 100 pM solutions. The larger SPR shift detected for the interaction between miR-21-3p and provided an evidence of the capacity of the probe to interact with the miRNA-21 target sequence.

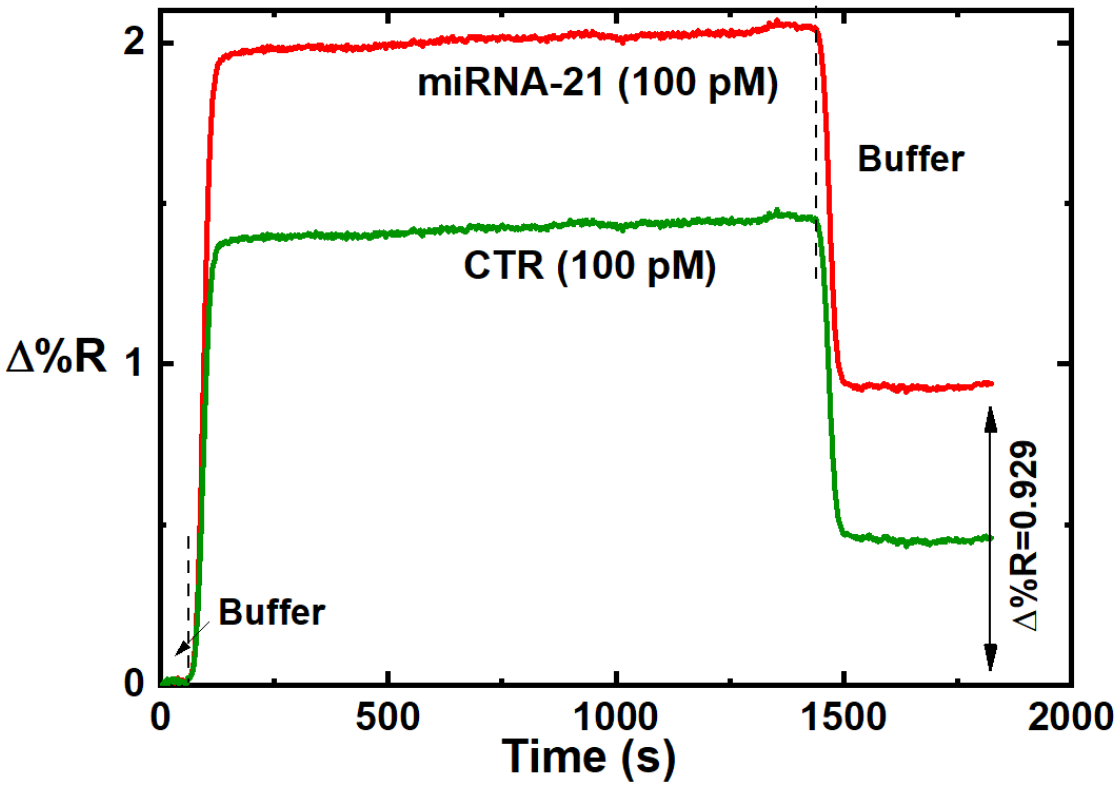

Figure 5.7: Δ%R over time detected for the parallel adsorption of 100 pM solutions of miR-21-3p and CTR (unrelated control sequence) on surface immobilized probe.

On the basis of the SPR data referring to probe immobilization and target hybridization, I calculated the hybridization efficiency (HE) as HE = ($\Delta\%R_{hybridization} \cdot MW_{probe} / \Delta\%R_{immobilization} \cdot MW_{miR\text{-}21\text{-}3p}$) where MW_{probe} and $MW_{miR\text{-}21\text{-}3p}$ correspond to the molecular weight of anti miR-

21-3p (probe) and miR-21-3p, respectively. HE represents the ratio of probes immobilized on the gold surface that formed a duplex with the target sequence [31]. HE=0.69 was obtained for the interaction of probe with 100pM miR-21-3p target, thus demonstrating the capacity of the surface immobilized probe to catch low concentrated miR-21-3p target molecules.

5.2.6 Impedance Spectroscopy

Impedance spectra in faradaic regime is reported in Figure 5.8 for G2. From the fit relative to the Nyquist plot, the charge transfer resistance undergoes an increase after functionalization with thiolated probe nucleotide equal to approximately 1.3 kΩ and a further increase of 2 kΩ after incubation with mercaptoethanol. Impedance was capable of detecting the presence of a hybridized probe-target system for a concentration of 300 pM target miRNA but was not sufficiently sensitive for a lower concentration.

The $[Fe(CN)_6]^{3-/4-}$ ions might interfere with the formation and stability of the duplex, therefore the hybridization reaction was performed in a separate incubation volume, and the gate was later transferred to the electrolyte for current/voltage measurement. More importantly, impedance was used to clarify the stability of the probe functionalization for perturbation of the equilibrium between the probe and blocking agent occurring in the thermal step of hybridization.

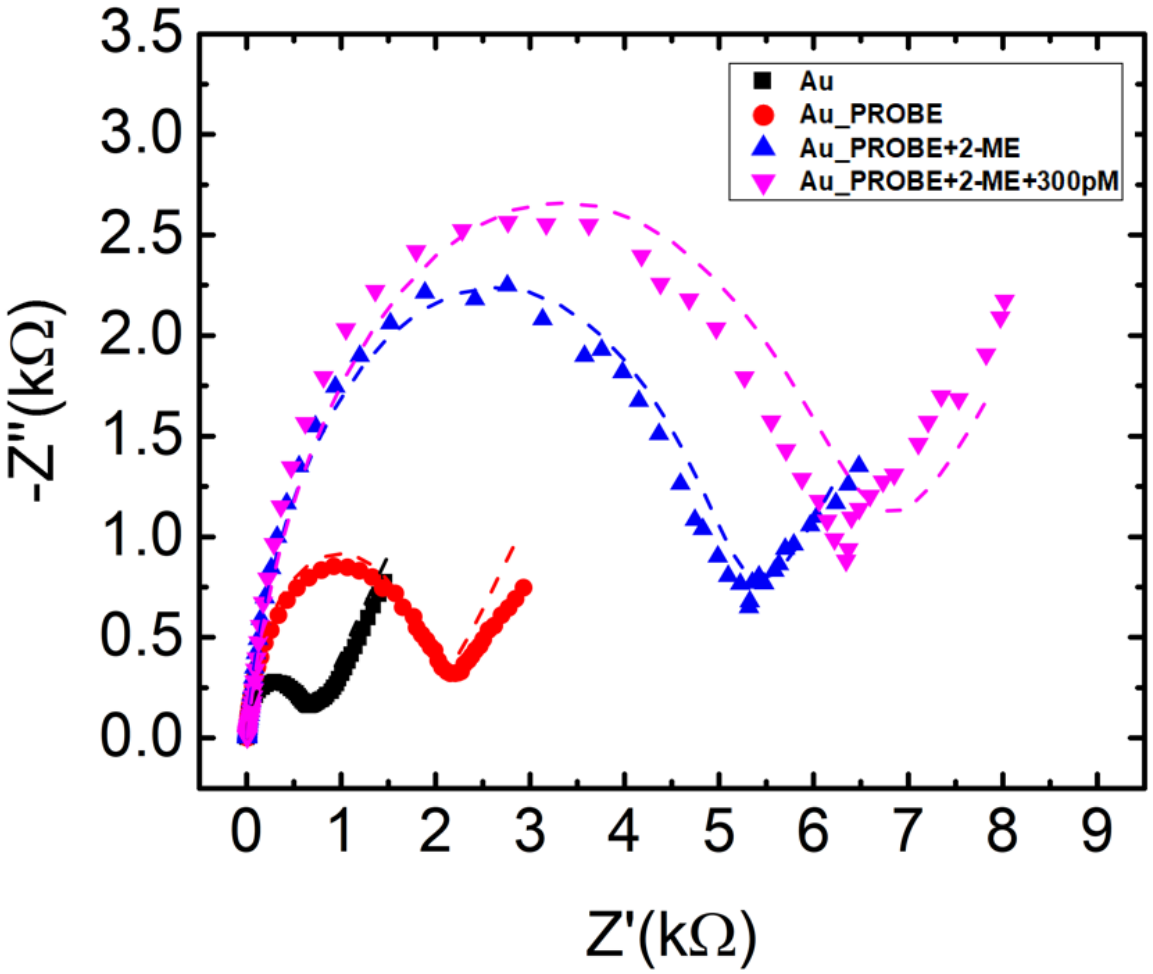

Figure 5.8: Nyquist plot characterizing the impedance of gate G2 taken on a clean gold surface (black), after the immobilization of the probe sequence obtained with thiol bonding (red), after the reaction with mercaptoethanol (blue) which is filling the available site left uncovered by the probe. The incubation with complementary miRNA-21 (300pM) derived sequence is further increasing both the real and imaginary part of impedance (pink). Dashed lines are the result of a Randles circuit (inset) fit

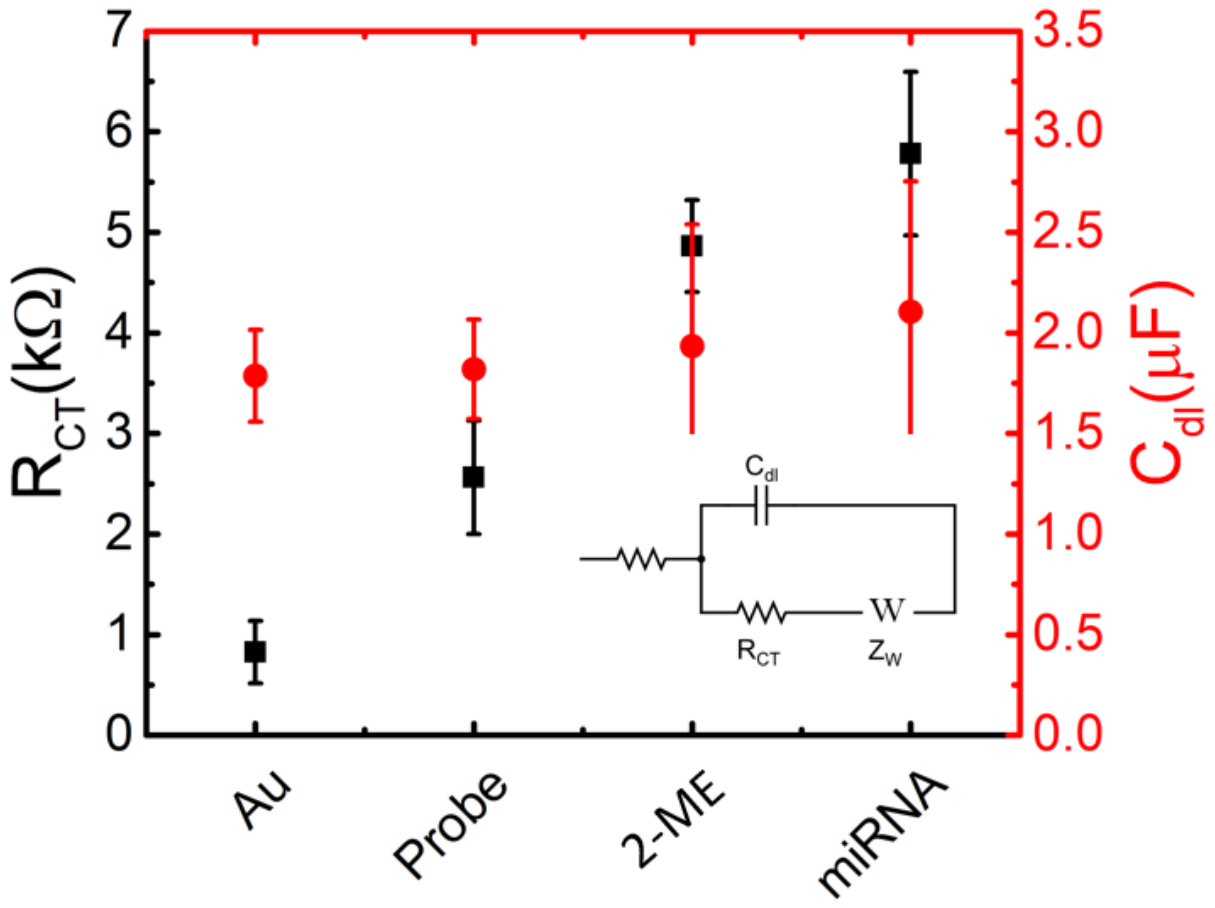

Figure 5.9: Resistance to the charge transfer and Capacitance of the double layer obtained by fitting a classic Randles circuit (shown in the inset) on the Nyquist plots for the consecutive functionalization steps of Gate 2.

From the plot reported in Figure 5.9 (equivalent circuit method reported in the Characterization Chapter 3.4) it is possible to appreciate a slight decrease of the imaginary part of impedance for the probe functionalized G2 after incubation at 37 °C in a solution containing just Tris-EDTA-NaCl buffer. The detached probe might be transferred in solution and be responsible for a competitive target-probe reaction affecting the sensitivity of the biosensor as reported in previous calculation of free energy. The resistance of the gate surface to the charge transfer (R_{CT}) of the redox probe (potassium ferricyanide), increases after every functionalization step and Error bars are the Standard Deviation calculated on 3 datasets (cf. Figure 5.9)

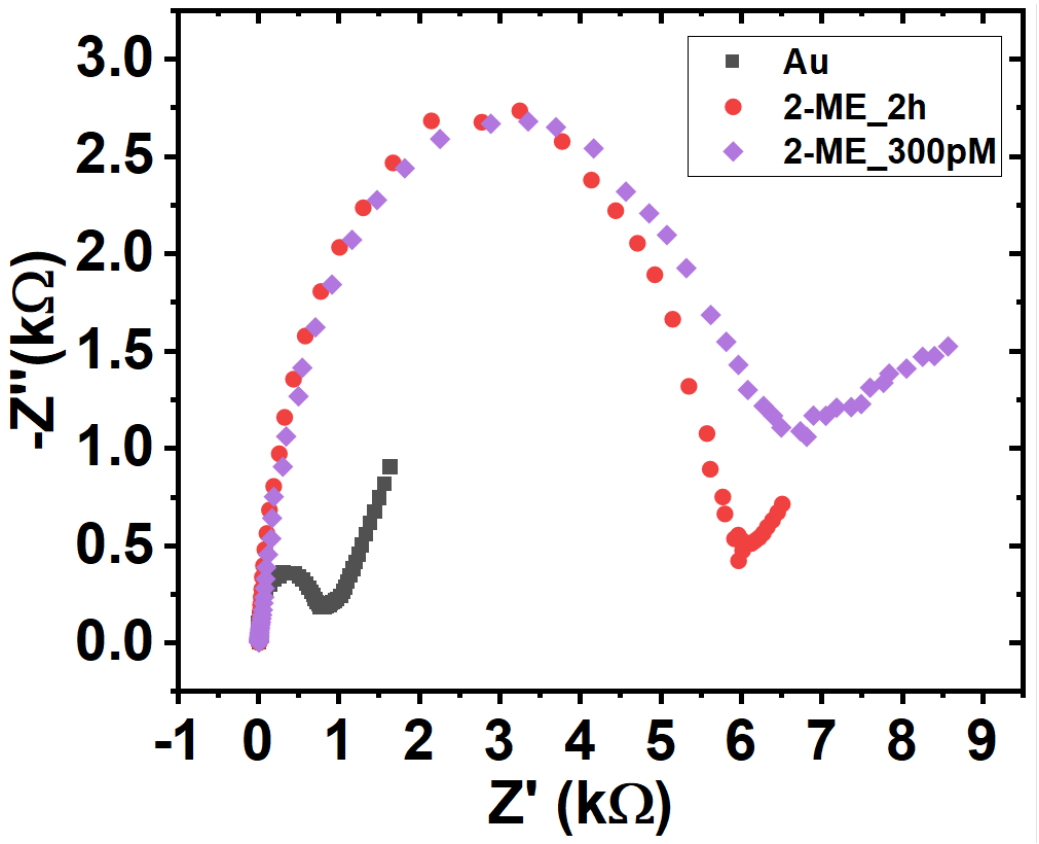

Figure 5.10: Nyquist plot characterizing the impedance of gate G1 taken on a clean gold surface (black), after the functionalization with mercaptoethanol (red). The incubation with complementary miRNA-21-3p (300pM) derived sequence is staying similar in signal with both the real and imaginary part of impedance (pink).

Another stability experiment was performed for the gate electrode (G1). So, the clean gold electrode (G1) was functionalized with 2-Mercaptoethanol for 2 hours and the impedance measurement was taken. Then the gate electrode (G1) covered with 2-ME was incubated in 300pM concentration of the target analyte [miRNA-21-3p] present in the hybridization buffer (Tris-EDTA-NaCl). This incubation process was carried out in an oven at 37˚C for 30 minutes (cf. Figure 5.10). Then the IS measurements was taken, the results obtained show unaffected real and imaginary parts of the impedance, thus, resulting in the same signal obtained before incubation procedure. This proves that the presence of mercaptoethanol (2-ME) compound was unaffected and 300pM concentration of the target analyte [miRNA-21-3p] was hindered by available 2-ME

on the gold electrodes. Also with this impedance measurement, one can witness the area coverage for the blocking agent (2-ME) after functionalising it on the clean gold electrode.

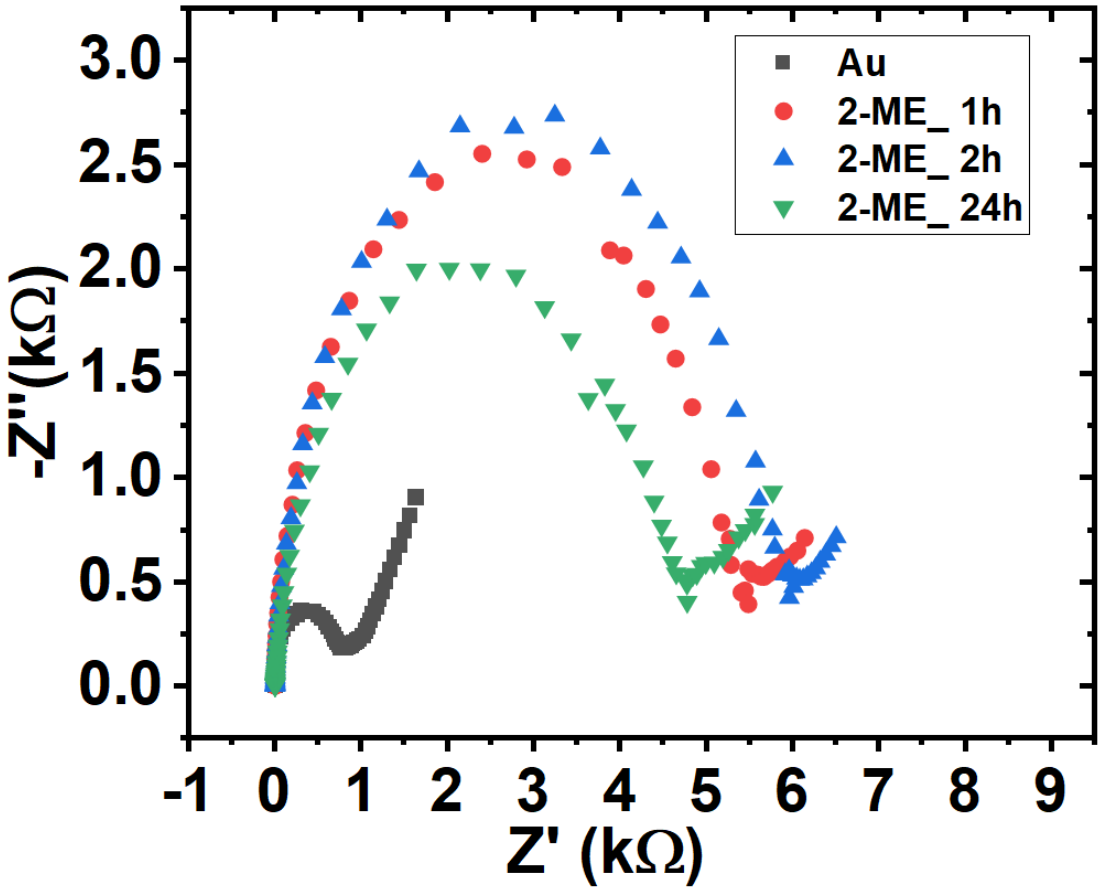

Figure 5.11: Nyquist plot characterizing the impedance of a clean gold surface (black), after the functionalization with mercaptoethanol for 1h (red), 2h (blue) and 24h (green).

An experiment to ensure the area coverage of 2-ME for different period of time (1h, 2h and 24h) was performed. From the impedance measurements obtained, we could see that a maximum area coverage by 2-ME on the clean gold (Au) electrode can be achieved even at 1 hour functionalization. So, the signal obtained after functionalization of 2-ME for 2 hours is similar to that of 1hour. Whereas, 24 hours functionalization of the gold electrode with 2-ME, shows the measurement shifts both in real and imaginary part of the impedance together with the reduction

in signal intensity (cf. Figure 5.11). This effect is due to the detachment or dissolving nature of the mercaptoethanol in the buffer with respect to long period of functionalization protocol (24h).

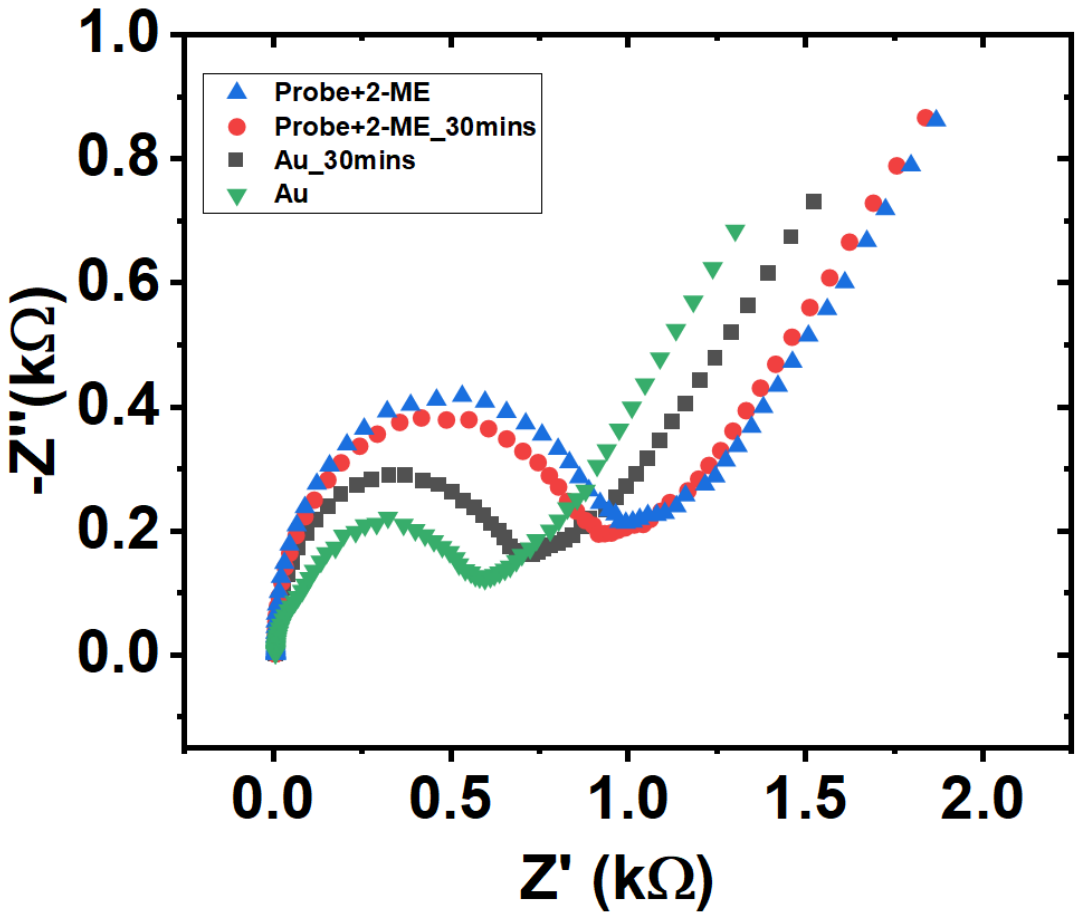

Figure 5.12: Nyquist plot characterizing the impedance of gate(G2) taken on a clean gold surface (green), impedance of the gate G2 has further increased at both real and imaginary parts after the incubation step of G2 in Tris-EDTA-NaCl at 37˚C(black), Gate (G1) taken with the immobilization of the probe sequence obtained with thiol bonding(2µM) and the blocking agent 2-Mercaptoethanol(1mM) (blue),the real and imaginary part of the impedance remains the same after the incubation step for G1 in Tris-EDTA-NaCl at 37˚C(red).

A stability experiment was performed to check the availability of the probe before and after incubation for 30 minutes at 37 ˚C in Tris-EDTA-NaCl buffer without the presence of target analayte. The impedance measurements obtained after incubation in the buffer was similar to the signal which was measured before incubation in the oven. This clearly shows that there is no

influence of the temperature (37˚C) in detaching the probe from the gold surface and the incubation time period of 30 minutes. Perhaps similar experiment was performed for clean bare gold electrode, after 30 minutes of incubation at 37 ˚C with the Tris-EDTA-NaCl buffer, there occurs a change in impedance measurement at both the real and imaginary parts of the impedance. This could be due to the influence of the temperature, incubation time and the salt contaminants available in the buffer which gets attached to the gold surface(cf. Figure 5.12).

5.2.7 Summary

I demonstrated that EGOFET biosensors are suitable label free devices for recognition of short sequences of genetic materials in the picomolar region. The oligomer miRNA-21 was selected as a relevant prototype to study the capability of EGOFET to detect the formation of probe-target duplex in the case of an almost complementary matching. This proof of concept was achieved in a buffer suitable for hybridization and should be assessed in biological fluids. The proposed architecture features a second gate electrode working as reference for the extraction of the genuine biorecognition signal. The intrinsic shift of response due to semiconductor change of performance in liquid media is now taken into account by dual gate measurement and data analysis. Statistical analysis of the transfer curves allowed us to reconstitute the trend common to different organic transistors fabricated with simple process steps. Gate electrodes functionalized with thiolated oligonucleotide probes are biorecognition interfaces suitable for EGOFET detection scheme since the charges distributed in the oligonucleotide backbone and the stabilizing surrounding media may contribute to signal enhancement and the main mechanism of transduction is based on capacitance. The regeneration of the functionalized gate electrode, although not targeted in the present experiment, will be crucial for transfer of the technology to diagnostic assays.

The free energy of the couple probe-target was inferred by fitting the trend of the binding constant vs V_{GS}. I find a value sensibly lesser than the binding energy extracted for the homogeneous reaction in solution. This is due to the detachment of the probe and the occurrence of uncontrolled hybridization also in solution even at low concentration, and to the presence of a surface hindered hybridization reaction. The dependence of the signal with respect to square root of target concentration affects the sensitivity, which, however, is still attractive for developing multiplexed

electronic biosensors for miRNA panel assays. Impedance spectroscopy measurements of the functionalized gate were used to validate the stability of the biorecognition layer positively, whereas SPR complementary detection confirmed a hybridization efficiency of 69 % for the probe-target interaction. Multiplexed EGOFET biosensors with dual gate may indeed represent a viable perspective for integrated devices for genic recognition whose data may be analyzed with good confidence and across-sample measurements. This would be very important, for instance, in the label-free detection not only of miRNA biomarkers, but also in the discrimination of point mutations of viruses and microrganisms, as it is very actual in the present epidemics.

5.3 Integration of microfluidic device with multi gate EGOFET architecture and detection of [miRNA-21-5p] at sub-pM range

Microfluidic compartment has been implemented with three gate electrodes (Au wires), in order to perform the hybridization process with the biorecognition moiety directly on top of EGOFET device (cf. Figure 5.13 a, b). A PDMS microfluidic cell was developed with specific design features for the three gates to be placed within the 80-90 μL of the electrolyte chamber aligned with the transistor channel (cf. Figure 5.13 b,c).

The PDMS microfluidic cell was integrated together with the EGOFET device through mechanical sealing by using 3D printed top and bottom holders (cf. Figure 5.13b) to ensure sealing and the possibility to substitute each part of the ensemble. The fluidic cell also includes inlet and outlet tubing for the electrolyte to flow by the gate surface, and putting in electrical contact the semiconductor layer which acts as an amplifier of the chemical reactions undergoing at the gate surface. Once the microfluidic cell was integrated with the device, the electrolytic buffer flow using peristaltic pump has been checked to avoid the leakage. The complete assembly with three gate architecture was used to perform sensing of oligonucleotides of different length and sequence, by having one gate acting as a reference electrode and other two gates as sensing electrodes.

For the hybridization process, the fluidic cell was filled with solutions with different concentration of the target analyte for a specific period of time, starting from concentration in the fM to pM range. After each hybridization step of target analyte concentration, the fluidic cell was emptied before filling the next target analyte concentration for the hybridization process. The electrical characterization of EGOFET devices were taken after each hybridization step (cf. Figure 5.13 d), sweeping the gate potential consecutively and not overlapping for all the three gate electrodes.

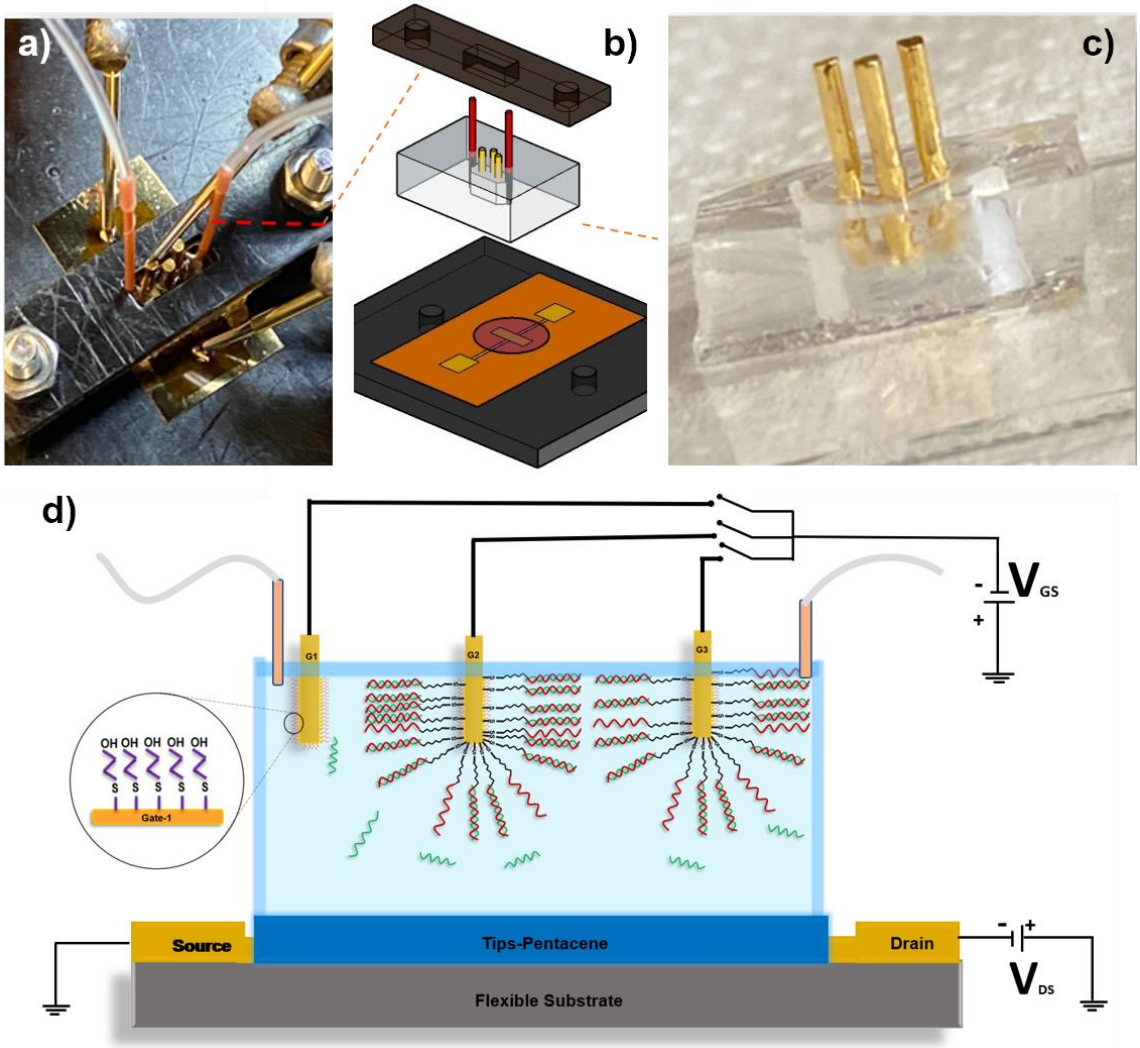

Figure 5.13 a)Top view of the multi-gate (G1,G2,G3) EGOFET model and potentials applied for Source, Drain and Gate (G1) electrodes b) Assembly of the microfluidic device on top of interdigitated S and D electodes c) PDMS microfluidic cell with inlet and outlet tubes, integrated together with 3 Au wires d)

Schematic drawing illustrating the architecture of the multi-gate EGOFET device featuring the PDMS microfluidic device sealed on top of the Source and Drain interdigitated electrodes covered with TIPS-pentacene.

After assembly the device was electrically characterized and the data obtained was processed with Origin Pro 2018 software. Output current (I_{DS}) of the device was obtained by applying various Gate- Source voltages starting from -0.1V to -0.8V (cf. Figure 5.14 a) and a fixed Drain-Source voltage, with the operating mode in linear regime (V_{DS}= -0.2V).

The transfer curve of the three clean gold wire electrodes were measured by making sure that the gate electrodes (G1,G2 and G3) are immersed inside the microfluidics device with the same height (equal surface area immersed into electrolyte equal to 11mm^2).

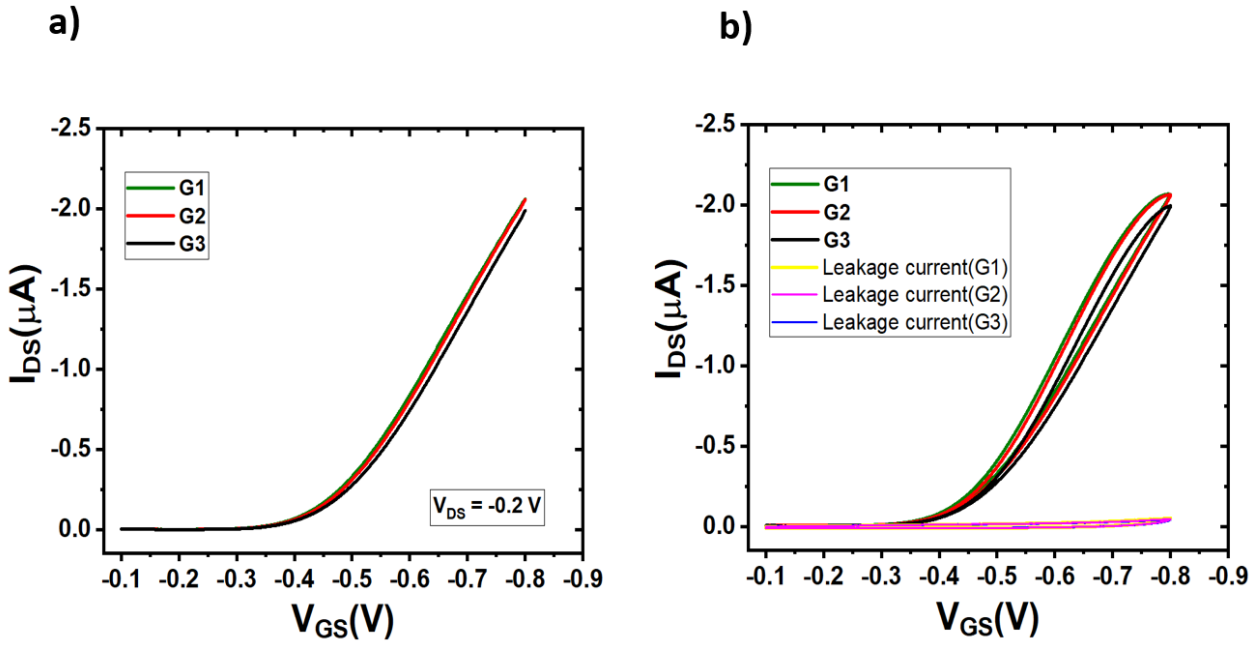

Figure 5.14: a) *Transfer characteristics featuring 3 clean gate electrode (G1,G2 and G3) when measured in linear regime using Tris-EDTA-NaCl buffer (pH.7.4) b)Representing hysteresis and leakage (I_{GS}) current obtained for(G1,G2 and G3), which is around 20-25nA.*

Table 2: Extracted EGOFET parameters featuring transconductance and threshold voltage values of G1,G2 and G3

GATES (clean Au)	**G_m(µS)**	**Standard deviation**	**Threshold voltage (V)**	**Standard deviation**
G1	6.20E-6	8.29E-9	-0.46	3.09E-4
G2	6.35E-6	5.82E-9	-0.47	2.03E-4
G3	6.30E-6	4.81E-9	-0.48	1.62E-4

All the transfer curves for each gate are averaged after sweeping 25 cycles of gate potential to each gate electrode, in order to obtain stable form of I_{DS}(µA). The value of the Gate-Source current has been monitored to ensure no short-circuit was developing and the extent of residual leakage current (less than 30 nA) (cf. Figure 5.14 b). From Table 2, it is possible to appreciate that the variability in the response with the gates was minimum, with standard deviation of threshold voltage and transconductance three orders of magnitude lower than their average value.

Following initial characterization and understanding of the influence of geometry on multigate EGOFET parameters, the three Au gate electrodes were functionalized in order to adsorb thiolated functional molecules on the surface.

The gate G1 is functionalized only with the blocking agent 2-mercaptoethanol (2-ME) and acts as a reference electrode. Au gates G2 and G3 are functionalized with Probe P1 and P2 (See Materials and Methods) together with the blocking agent 2-ME. G2 and G3 act as sensing electrodes.

5.3.1 Materials and functionalization protocols

The probe P1 consist of miRNA-21-3p, which is a natural sequenced RNA-bioreceptor of the target (T) and the probe P2 consist of sequence with base pairs that are 100% complementary to the target analyte(T).

P1 and P2 were synthetized with Thiol group in order to be covalently bound to the gold surface, 7 adenine base pairs and C6 spacers together with the RNA-bioreceptors (Refer Table 3). Tris-EDTA-NaCl is the immobilization buffer used to functionalize the Probe P1 and P2 on the clean gold electrodes.

Table 3: Synthetized [miRNA-21-5p]and Probe (P1 and P2) sequences

Target analyte [miRNA-21-5p]	**uagcuuaucagacugauguuga**
Probe (P1) (with mismatch)	**Thiol-C6-aaaaaaacaacaccagucgaugggcugu**
Probe (P2) (100% complementary)	**Thiol-C6-aaaaaaaucaacaucagucugauaagcua**

For the functionalization step the two different probes (P1, P2) were used for the same target analyte miRNA-21-5p(T). The blocking agent used for this experiment are 2-Mercaptoethanol (2-ME) with the concentration of 1mM, in order to block the non-specific bindings.

2-ME compound provides covalent binding with the free gold area of the sensing and reference electrodes (cf. Figure 5.13d). 5µM concentration of Probes P1 and P2 was used for the functionalization of the sensing electrodes.

5.3.2 Hybridization inside the microfluidic device

For the hybridization step, the microfluidic compartment was filled with [miRNA-21-5p] solution and the hybridization of the target with the probes (P1, P2) takes place for 40 minutes at 39˚C . The temperature was maintained inside the fluidics by an external thermal bath set and each target concentration was preheated to 39˚C. Once the hybridization process is complete, each gate

electrode was measured by applying the Gate-Source voltages from -0.1V to -0.8V while operating the device in linear regime (V_{DS} = -0.2V). When one gate was being measured, the other two gates were kept floating. In this way all the three gates (G1,G2 and G3) were measured with 25 cycles each, in order to stabilize the response of the device and a stable output current Signal (I_{DS}). After measurement, the target analyte solution inside the fluidics was emptied via the outlet tubing and the solution containing the target at a different concentration was infilled inside the microfluidic compartment. Hence, in this way the experiment was performed for various concentrations starting from 100fM to10pM.

Tris-EDTA-NaCl acts as both the hybridization buffer and as electrolyte of the EGOFET device, being therefore responsible for ionic transport between the gate and semiconductor surface.The initial channel current (I_{DS} in µA) was measured for all the 3 functionalized gates (i.e., the gate G1 with 2-ME, G2 with P1 and 2-ME, G3 with P2 and 2-ME), acting as an output current signal for [0fM] concentration.

The output current (I_{DS}) obtained for G2 and G3 after incubation with target concentration equal to [100 fM] was recorded and reported in (cf. Figure 5.15 a,c) showing an increasing current signal for 100fM target analyte concentration, with respect to it's output current signal obtained for [0fM] measurements(signal P1 and P2 in cf. Figure 5.15 a,c).

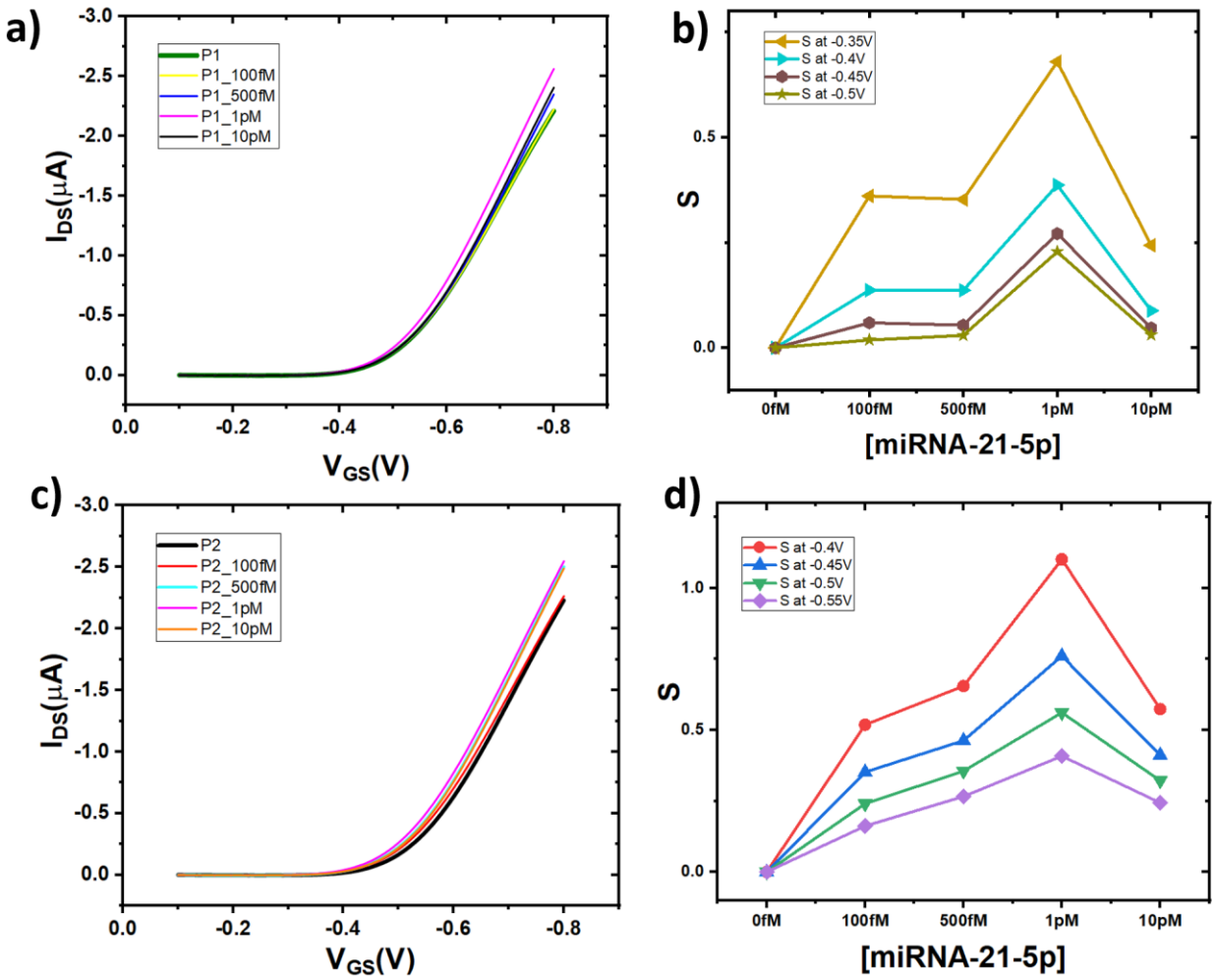

Figure 5.15: a) Transfer curves of EGOFET device for gate (G2) immobilized with Probe (P1) and 2-ME, characterized before (measurement at [0fM] concentration) and after hybridization with solutions containing different concentrations(100fM to 10pM) of the target analyte (T). b) dose curves (S) obtained for gate G2 with various V_{GS} (V) , from -0.35V to -0.5V c) Transfer curves of EGOFET device for gate (G3) immobilized with Probe 100% complementary (P2) and 2-ME, characterized before(measurement at [0fM] concentration) and after hybridization d) dose curves (S) obtained for gate G3 with various V_{GS} (V) , from -0.4V to -0.55V.

The expression to calculate signal plot for each voltage is as follows

$$\langle S \rangle = (I_{sensing} / I_{[0fM]}) - 1$$

In (cf. Figure 5.15 a,c) the increasing output current signals (I_{DS}) for both the gates G2 and G3 is shown. There is a gradual increase in the channel current up to 1pM concentration of the target

analyte, which is more appreciable at gate potential below threshold voltage. At concentration higher than 1 pM the current with respect to the transfer curve recorded at 1 pM. The decrease in current may be an effect of saturation of the probes attached on the gates G2 and G3 with the target for hybridization (cf. Figure 5.15 a,c).

With (cf. Figure 5.15 b) for probe P1, the signal plot shows an increasing trend with increasing concentration and the signal drops at 10pM target concentration. Better signal plots were obtained for V_{GS}=-0.35V, considering the device performance in sub threshold region. Similarly, Gate G3 with probe P2 shows an increasing signal trend until 1pM and the signal drops for 10pM target analyte concentrations. (cf. Figure 5.15 d)

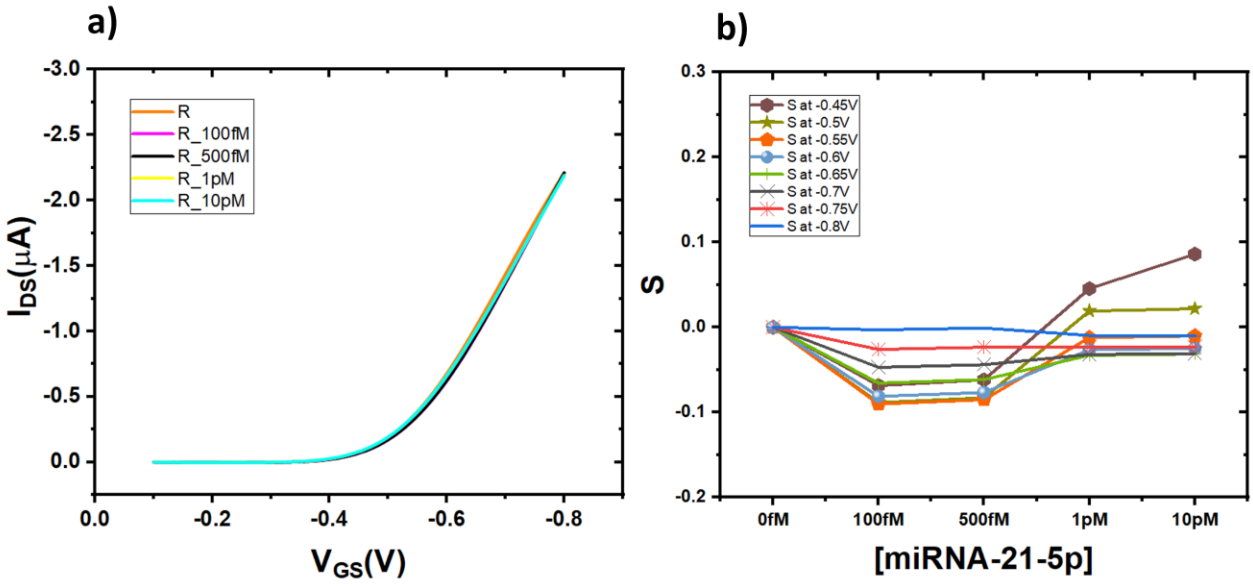

Figure 5.16: a) Transfer curves of EGOFET device for gate (G1) immobilized only with 2-ME, characterized before (measurement at [0fM] concentration) and after hybridization with solutions containing different concentrations(100fM to 10pM) of the target analyte (T) which results in unaltered output current (I_{DS}). b) dose curves (S) obtained for the reference gate G1 with various V_{GS} (V), from -0.45V to -0.8V, shows signal undergoes few shifts at 1pM concentration of (T) at V_{GS} (V)= -0.45V and -0.5V, later remains unchanged.

The current signal for reference G1 shows to be unaltered for 100fM concentration with respect to it's initial [0fM] measurements (cf. Figure 5.16 a). In similar consecutive steps, the fluidics was

filled with higher concentrations (starting from 500fM to 10pM) and I_{DS} in µA was recorded after each incubation step.(cf. Figure 5.16 a,b).

The other figure of merit parameters while performing EGOFET sensing are Transconductance (g_m in µS) and threshold voltage (V_{TH} in V) was analysed for the three gates (G1, G2 and G3). Transconductance behaviour (cf. Figure 5.17 a). increases with respect to increase in concentrations for Gate (G2 and G3). But the g_m (µS) value drops for target concentration at 10pM for gates G2 and G3. Whereas, Gate (G1) was not affected, hence less the changes in transconductance. (cf. Figure 5.17 a).

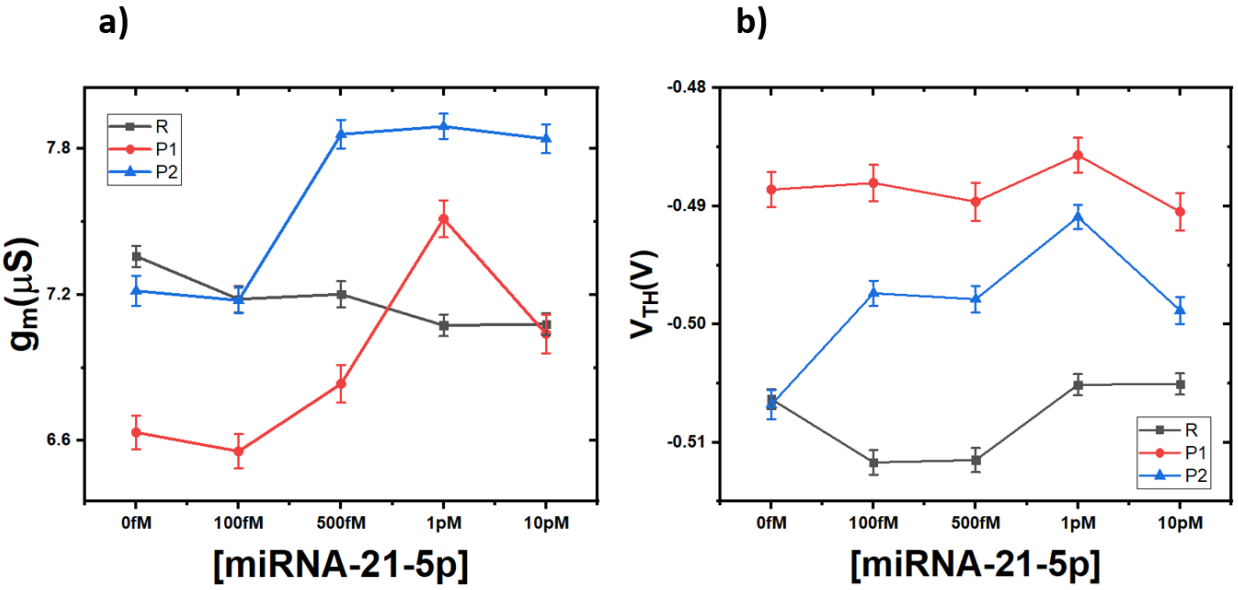

Figure 5.17: a) transconductance (g_m in µS) of gates G1,G2 G3 and b) threshold voltage (V_{TH} in V) respective to the changes upon hybridization with different concentrations of the target analyte (T)

Threshold voltage (V_{TH} in V) is a voltage when the device starts conducting (turning ON) , thus considering it's value as another important figure of merit. V_{TH}(V) analysis was also performed for the three gates (G1, G2 and G3). The V_{TH}(V) values were slightly shifting towards the direct of sub threshold region for the probe (P2). (cf. Figure 5.17 b).

5.3.3 Discussion

The increasing channel current (I_{DS} in µA) trend seen at gates G2 and G3, could be due to the target analyte carrying high negative charges. Also, negative charges are present in the Probes (P1 and P2). In this scenario, there occurs a charge repulsion with a saturation of the probe for concentrations above 1 pM target analyte.

At higher target concentration (>1 pM), the amount of the negative charges is high compared to the total negative charge availability in the probe. So, there occurs a charge repulsion and the output current drops to 20 nA to 25 nA from the signal obtained for 1 pM target concentration. This phenomenon was also verified by making a signal plot for each Gate-Source voltage (V_{GS} in Volts) starting from -0.1 V to -0.8 V, applied to all the three gates.

Since the probe P2 has 100% complementary sequence to that of target analyte RNA sequence, the output signals and the signal plots are comparably better to the probe P1 (sequence with mismatches) in hybridization with [miRNA-21-5p] target.

The change in transconductance reported in (cf. Figure 5.17 a) is the result of the charge carrier modulation in the semiconductor surface. This effect competes with the dynamic response of the electrical double layer at the semiconductor-electrolyte and electrolyte -semiconductor interface after each target-probe bindings, which is depicted by threshold voltage.

In order to further verify the increasing output current (I_{DS}) trend, the experiments were performed with the gates (G2 and G3) incubation in the oven 37˚C for 30 minutes with respect to each concentration of the target analyte separately (cf. Figure 5.18 a,b). After incubation (one concentration in a time, starting from 100 fM) and hybridization process, the gates (G2 and G3) were measured individually by placing it on the 3D printed stage holder with an open microfluidic pool (80 µl volume of Tris-EDTA-NaCl buffer) EGOFET architecture (cf. Figure 5.1 b (insight)). The output channel current (I_{DS}) results in similar increasing behaviour to that of hybridization measurements performed inside the closed microfluidic cell. But with the hybridization step inside the microfluidic compartment is less effective compared to the hybridization process in the oven because the thermal energy needed for the target to move freely and to get binded with the probe decreases with time.

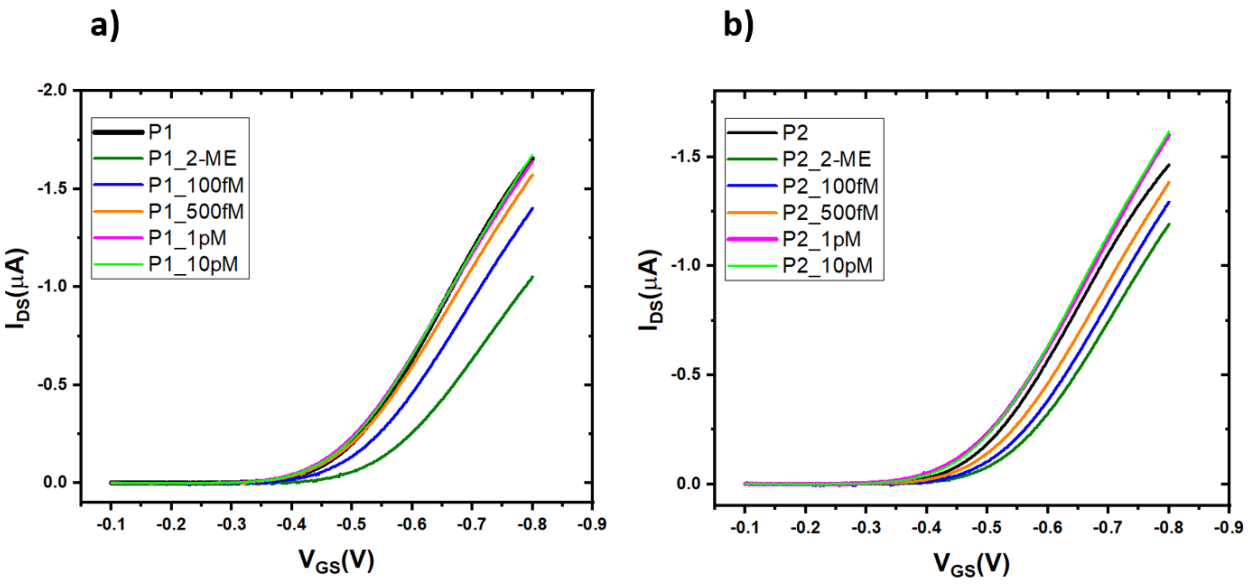

Figure 5.18: a)Transfer curves of EGOFET device for gate (G2) immobilized with probe (P1) and 2-ME, characterized using open pool EFOFET setup,output current shows for before and after hybridization with target analyte (T) b) a)Transfer curves of EGOFET device for gate (G3) immobilized with probe (P2) and 2-ME, characterized using open pool EFOFET setup, showing (I_{DS}) saturation at 1pM concentration of target analyte

Another important consideration is the following: for the hybridization inside the fluidic cell, all the three gates are exposed to only controlled microliter (µl) volume of target analyte concentrations, which could create less chances for all the gates to get equally hybridized. Whereas, a clear increasing output current signal was obtained for the hybridization performed separately from the electrolyte. Besides diffusion, this difference in sensitivity might be esplained because of the volume of target analyte solution was in milliliter range and each gate was exposed separately at controlled temperature of 37˚C inside the oven. Incase of the hybridization inside the fluidics, the temperature could drop down to room temperature with respect to time by hindering the mobility of the target analyte by making it weak to bind with the probe.

5.4 Organic Field Effect Transistor modeling

In the present subchapter I will report on the modelling of EGOFET with finite element software Comsol Multiphysics, designed to predict the response of the EGOFET biosensor.

The dynamics of electrons in semiconductors is often described using the many-body Schroedinger equation. This formidable system should be solved also considering the periodicity of the crystal structure of the solid. In practice, this is not possible and approximations must be made. Solid state physicists have developed several methods to solve the simplified forms, and these methods have been validated by experiments [32].

Because of difficulties to obtain an analytical solution, it is common to make simplifying approximations when solving it. Ultimately, these approximations yield the drift-diffusion equations, here reported for electrons:

$$\mathbf{J_n}(\boldsymbol{r},t) = n\mu_n \nabla E_c + \mu_n k_B T \nabla n + \frac{1}{2} n \mu_n k_B \nabla T \tag{24}$$

in a nondegenerate limit approximation and for a relaxation time dominated by phonon scattering.

It is possible to use finite element modeling to solve equation 24 in simple geometrical model in order to simulate the response of organic electronics device when external environmental conditions affect the charge transport. The set of equations must be completed with Poisson's equation and current continuity equation. In particular, Poisson's equation is expressed in the form:

$$\nabla \cdot (-\epsilon_r \nabla V) = q(p - n + N_d^+ - N_a^-) \tag{25}$$

Including N_d^+ and N_a^- as additional carriers, donors or acceptors, introduced by doping or presence of impurities at the interface between the TIPS-pentacene and the electrolyte.

The current continuity equation, expressed for electron n, takes into account also the recombination rate U_n from all generation mechanism:

$$\frac{\partial n}{\partial t} = \frac{1}{q}(\nabla \cdot \mathbf{J}_n) - U_n \tag{26}$$

Electrolyte and Gate potential modeling.

The electrolyte domain is defined to include also the diffuse double layer modeling. Gouy-Chapman theory describes the ions interacting with a charged surface using the Nernst Planck equation for mass transport of all the ions and the Poisson's equation for the electric field and charge densities. Gouy-Chapman model predicts the spatial extent of the diffuse double layer to be equal to the Debye length for the solution:

$$\lambda_D = \sqrt{\frac{RT\epsilon_r\epsilon_0}{2F^2 c_{bulk}}} \tag{27}$$

Where c_{bulk} is the concentration in the bulk of solution.

With Stern the model was further implemented to detail the structure of the ions interacting with the surface. The plane in close proximity to the surface is called Inner Helmholtz plane and consists of ions attached to the charged electrodes. The outer Helmholtz plane defines the position of ions dissolved in solution, but forming a compact layer, which Stern described as a dielectric with constant permittivity.

The fluxes of the ions are described according to the Nernst-Planck equation:

$$\boldsymbol{J}_i = -D_i c_i - u_{m,i} z_i F c_i \nabla\Psi \tag{28}$$

With D_i the diffusion coefficient, c_i the concentration, u_m, i the mobility, z_i the charge of the ion specie i, Ψ is the electric potential in the electrolyte phase.

The peculiar feature of the present work involves the addition of solute ions in buffer whose equilibria affect the gate potential. The Stern layer is modeled with a simple formula relating the electric potential on each side of the layer. The bulk electrolyte potential is given by a simple formula combining the gate voltage applied on the reference electrode, the work function of the electrode metal, and the equilibrium potential of the reference electrode. The value of the electric potential at the outer surface of the layer between the semiconductor and the electrolyte is solved with a set of equations including the following:

1) the electric potential Ψ_m is the sum of the voltage drop across the Stern layer and the electrolyte potential just outside of the Stern layer,

2) the density of charges on the interface between the semiconductor and electrolyte is set according to reaction equilibria between the ion concentration and the surface,

3) the chemical activity of the ions on the interface semiconductor electrolyte is related to the ion concentration in the bulk electrolyte via the Boltzmann distribution function

The semiconductor and the electrolyte domains are parts of a Multiphysics simulation which appears highly non-linear. For the semiconductor domain, the electric potential Ψ_m is imposed on the interface of the semiconductor to modulate the intensity of the current between source and drain terminals. For the electrolyte domain, the displacement field is calculated from the charge density on the interface according to Gauss distribution. Since there is no space charge accumulated directly in the Stern layer, the displacement field does not change across the Stern layer.

The comparison between the recorded transfer curve for [miRNA-21-5p] detection with the probe P2 (100% complementary, cf. Chapter 5.3) and the output of the model is reported in Fig.5.19 . The I_{DS} vs V_{GS} characteristics obtained with the FEM simulation appears to describe quite well the experimental trend, although some dissimilarities may be relevant. In particular, a slight difference in the transconductance is appreciable in the sublinear region around –0.5 V, and also the start of I_{DS} deviation from linear regime seems to appear at lower Gate potentials with respect to experimental transfer curve. The discrepancies may be due to parameters applied for hole and electron mobilities, which may be different from the real values typical of the fabricated device.

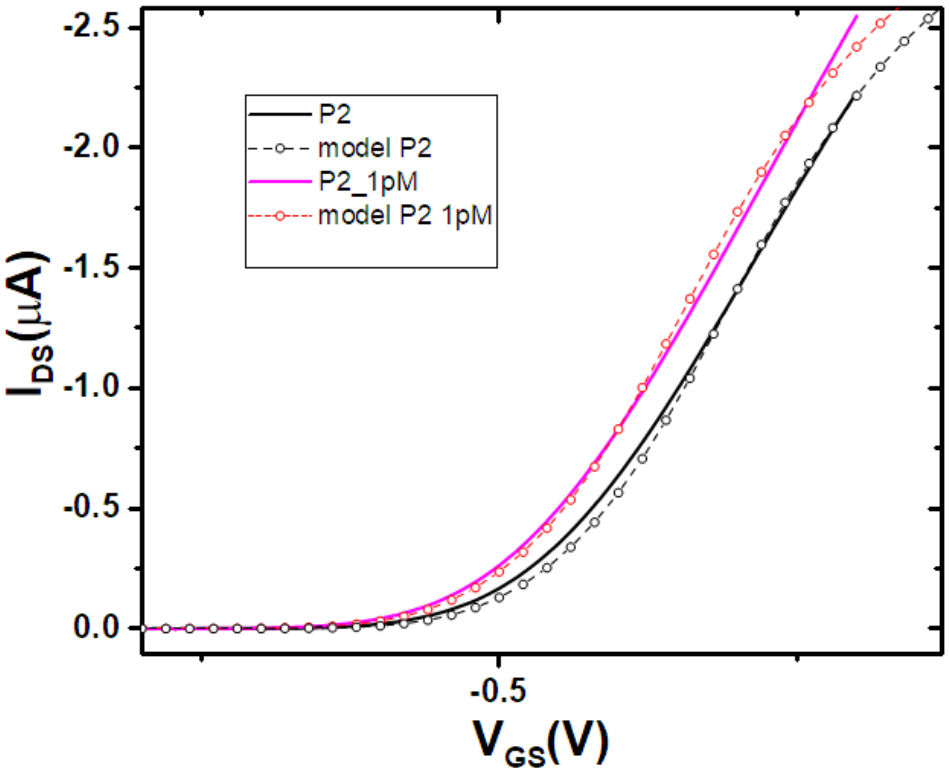

Figure 5.19: Comparison between experimental transfer curves for [miRNA-21-5p] detection with P2 probe and the results of FEM modeling. In black the data referring to the probe P2 before hybridization, and in pink the data referring to the device after hybridization with 1 pM solution of target analyte.

5.5 References

[1] Gambari R, Brognara E, Spandidos DA, et al. Targeting oncomiRNAs and mimicking tumor suppressor miRNAs: New trends in the development of miRNA therapeutic strategies in oncology (Review). International Journal of Oncology Spandidos Publications 2016; 49(1):5–32.

[2] Gasparello J, Allegretti M, Tremante E, et al. Liquid biopsy in mice bearing colorectal carcinoma xenografts: gateways regulating the levels of circulating tumor DNA (ctDNA) and miRNA (ctmiRNA). Journal of Experimental & Clinical Cancer Research 2018; 37(1):124.

[3] Khalil S, Fabbri E, Santangelo A, et al. miRNA array screening reveals cooperative MGMT-regulation between miR-181d-5p and miR-409-3p in glioblastoma. Oncotarget 2016; 7(19):28195–206.

[4] Giuffrida MC, Zanoli LM, D'Agata R, et al. Isothermal circular-strand-displacement polymerization of DNA and microRNA in digital microfluidic devices. Anal Bioanal Chem 2015; 407(6):1533–43.

[5] Feng Y-H, Tsao C-J. Emerging role of microRNA-21 in cancer (Review). Biomedical Reports Spandidos Publications 2016; 5(4):395–402.

[6] Lu TX, Munitz A, Rothenberg ME. MicroRNA-21 Is Up-Regulated in Allergic Airway Inflammation and Regulates IL-12p35 Expression. The Journal of Immunology American Association of Immunologists 2009; 182(8):4994–5002.

[7] Landgraf P, Rusu M, Sheridan R, et al. A Mammalian microRNA Expression Atlas Based on Small RNA Library Sequencing. Cell Elsevier 2007; 129(7):1401–14.

[8] Fang H, Xie J, Zhang M, et al. miRNA-21 promotes proliferation and invasion of triple-negative breast cancer cells through targeting PTEN. Am J Transl Res 2017; 9(3):953–61.

[9] Qu K, Zhang X, Lin T, et al. Circulating miRNA-21-5p as a diagnostic biomarker for pancreatic cancer: evidence from comprehensive miRNA expression profiling analysis and clinical validation. Scientific Reports Nature Publishing Group 2017; 7(1):1692.

[10] Markou A, Zavridou M, Lianidou ES. miRNA-21 as a novel therapeutic target in lung cancer. Lung Cancer (Auckl) 2016; 7:19–27.

[11] Luo G, Luo W, Sun X, et al. MicroRNA‐21 promotes migration and invasion of glioma cells via activation of Sox2 and β‐catenin signaling. Molecular Medicine Reports Spandidos Publications 2017; 15(1):187–93.

[12] Bellassai N, D'Agata R, Jungbluth V, et al. Surface Plasmon Resonance for Biomarker Detection: Advances in Non-invasive Cancer Diagnosis. Front Chem 2019; 7.

[13] Miao X, Wang W, Kang T, et al. Ultrasensitive electrochemical detection of miRNA-21 by using an iridium(III) complex as catalyst. Biosensors and Bioelectronics 2016; 86:454–58.

[14] Cardoso AR, Moreira FTC, Fernandes R, et al. Novel and simple electrochemical biosensor monitoring attomolar levels of miRNA-155 in breast cancer. Biosensors and Bioelectronics 2016; 80:621–30.

[15] Hakimian F, Ghourchian H, Hashemi A sadat, et al. Ultrasensitive optical biosensor for detection of miRNA-155 using positively charged Au nanoparticles. Scientific Reports Nature Publishing Group 2018; 8(1):2943.

[16] Cadoni E, Manicardi A, Madder A. PNA-Based MicroRNA Detection Methodologies. Molecules Multidisciplinary Digital Publishing Institute 2020; 25(6):1296.

[17] D'Agata R, Spoto G. Advanced methods for microRNA biosensing: a problem-solving perspective. Anal Bioanal Chem 2019; 411(19):4425–44.

[18] Majd SM, Salimi A, Ghasemi F. An ultrasensitive detection of miRNA-155 in breast cancer via direct hybridization assay using two-dimensional molybdenum disulfide field-effect transistor biosensor. Biosensors and Bioelectronics 2018; 105:6–13.

[19] Berto M, Casalini S, Di Lauro M, et al. Biorecognition in Organic Field Effect Transistors Biosensors: The Role of the Density of States of the Organic Semiconductor. Anal Chem American Chemical Society 2016; 88(24):12330–38.

[20] Casalini S, Dumitru AC, Leonardi F, et al. Multiscale Sensing of Antibody–Antigen Interactions by Organic Transistors and Single-Molecule Force Spectroscopy. ACS Nano American Chemical Society 2015; 9(5):5051–62.

[21] Lauro MD, Buscemi G, Bianchi M, et al. Photovoltage generation in enzymatic bio-hybrid architectures. 2019[Online] Zenodo 2019.

[22] Macchia E, Manoli K, Di Franco C, et al. Organic Field-Effect Transistor Platform for Label-Free, Single-Molecule Detection of Genomic Biomarkers. ACS Sens American Chemical Society 2020; 5(6):1822–30.

[23] Sensi M, Berto M, Gentile S, et al. Anti-drug antibody detection with label-free electrolyte-gated organic field-effect transistors. Chem Commun The Royal Society of Chemistry 2021; 57(3):367–70.

[24] Aspermair P, Ramach U, Reiner-Rozman C, et al. Dual Monitoring of Surface Reactions in Real Time by Combined Surface-Plasmon Resonance and Field-Effect Transistor Interrogation. J Am Chem Soc American Chemical Society 2020; 142(27):11709–16.

[25] Parkula V, Berto M, Diacci C, et al. Harnessing Selectivity and Sensitivity in Electronic Biosensing: A Novel Lab-on-Chip Multigate Organic Transistor. Anal Chem American Chemical Society 2020;

[26] miRbase.org. miRNA Entry for MI0000077. 2020[Online] 2020 [cited 2020]. Available at: http://www.mirbase.org/cgi-bin/mirna_entry.pl?acc=MI0000077.

[27] Halperin A, Buhot A, Zhulina EB. On the hybridization isotherms of DNA microarrays: the Langmuir model and its extensions. J Phys: Condens Matter 2006; 18(18):S463–90.

[28] Markham NR, Zuker M. DINAMelt web server for nucleic acid melting prediction. Nucleic Acids Res 2005; 33(Web Server issue):W577–81.

[29] SantaLucia J, Hicks D. The Thermodynamics of DNA Structural Motifs. Annual Review of Biophysics and Biomolecular Structure 2004; 33(1):415–40.

[30] Shumaker-Parry JS, Campbell CT. Quantitative methods for spatially resolved adsorption/desorption measurements in real time by surface plasmon resonance microscopy. Anal Chem 2004; 76(4):907–17.

[31] Špringer T, Šípová H, Vaisocherová H, et al. Shielding effect of monovalent and divalent cations on solid-phase DNA hybridization: surface plasmon resonance biosensor study. Nucleic Acids Res 2010; 38(20):7343–51.

[32] COMSOL Multiphysics 3.3a ®. © 1997-2008 COMSOL AB.

LIST OF FIGURES

LIST OF TABLES

LIST OF PUBLICATIONS

- Ricci S, Casalini S, Parkula V, **Selvaraj M**, et al. Label-free immunodetection of α-synuclein by using a microfluidics coplanar electrolyte-gated organic field-effect transistor. Biosensors and Bioelectronics 2020; 167:112433.

- **Selvaraj M**, Greco P, Sensi M, et al. Label free detection of miRNA-21 with electrolyte gated organic field effect transistors (EGOFETs). Biosensors and Bioelectronics 2021; 182:113144.

LIST OF ACTIVITIES DURING PHD

1) Workshop on ‘Brain cancer study’ conducted by AiPBAND project (NT-4), that took place in ‘Regina Elena Institute’ at Rome, Italy|

Date: 24.-28. September 2018

2) Seminar on the title ‘Organic printed electronic and hybrid printed electronic for sensing and actuation’ by Dr. Valerio Beni, Senior scientist (Department of Printed Electronics at RISE-Research Institute of Sweden) and the seminar was held at University of Modena ,Via Campi 103, Modena (IT)

Date: 24 October 2018

2) Workshop on ‘Innovation and entrepreneurship’ and MTC carried out in ‘The Hyve’ at Utrecht, Netherlands

Date : 26.-27. February 2019

3) Subscription and training on the web-based lessons on ‘Clinical research topics’ through the online platform offered by ‘Medical Trials Analysis’, Ferrara (IT)

4) Summer school on research methods and PhD conference on ‘Brain cancer diagnostic study’ at University of Catania,

Date : 30. September – 4. October 2019

5) Workshop on ‘Technology transfer and career development’ organized and performed online by Dr. Nadine Bongaerts, Partner, Science Matters (The Netherlands)

Date: 3. September 2020

6) Workshop on ‘Knowledge Translation in Cancer Study’ performed online by AiPBAND project.

Date: 29.-31. July 2020

7) BioEl 2019 International Winter school on Bioelectronics in Tirol, Austria.

Date: 16.-23. March 2019

8) Workshop on ‘Bioanalytical tools’ and the title is ‘From molecules to devices.’

Location: Parma, Italy. Date: 6. December 2019

9) Online workshop on ‘(Bio) polymers and 2D materials for biosensing and organic (bio) electronics’ conducted by MARIE SKŁODOWSKA-CURIE ACTIONS (MSCA) funded Innovative Training Networks (ITN) project named BORGES (Biosensing with organic electronics)

Date: 22.-25 June 2020

10) Online summer workshop on the title ‘Dressing viruses in tumor’s clothing: cloning-free platforms to trigger tumor-specific immune response’ by Prof. Dr. Vincenzo Cerullo (Faculty of Pharmacy-Helsinki).

Date: 10. July 2020

11) Online summer workshop on the title ‘Discovery of novel antiviral lead compounds: From phenotypic screens to lipid targeting mechanisms’ by Prof. Dr. Mark Brönstrup (Helmholtz Centre for Infection Research, 38124 Braunschweig, Germany)

Date: 17. July 2020

12) Online summer workshop on the title ‘COVID-19: what we know so far?’ by Dr. Laura Pandolfi (Fondazione I.R.C.C.S. Policlinico San Matteo Pavia)

Date: 24. July 2020

13) AIPBAND Network training (NT-8), Online workshop on ‘Knowledge translation in cancer study’

Date: 29.-31. July 2020

14) AIPBAND Network training (NT-8), Online workshop on ‘Public engagement training’ by Science communication

Date: 3. September 2020

15) Online seminar on the title "Organic semiconductor/electrolyte interfaces: some novel concepts for biomedical transducers" by Prof. Tobias Cramer (Dipartimento di Fisica, Università di Bologna)

Date: 9. March 2021

ACKNOWLEDGEMENTS

It gives me immense pleasure to present my PhD thesis. No work, however big or small, has everbeen done without the contributions of others. It would be a great pleasure to write a few words to acknowledge the help of all the people, without whom the successful completion of this thesis would not be possible.

First and foremost, I owe my deepest gratitude to my supervisors **Prof. Dr. Giuseppe Spoto** at University of Catania and **Prof. Dr. Fabio Biscarini** at the University of Modena and Reggio Emilia. Without their persistent support, constant encouragement, and continuous optimism all through my PhD, this work would not be possible. Their expert advice and valuable guidance helped me to expand my domain of knowledge in the biosensing field.

My heartfelt gratitude also goes to my co- supervisor **Dr. Pierpaolo Greco** at University of Modena and Reggio Emilia. He encouraged me in creating an idea from minimal resources to materializing my idea into a valuable thing. He kept me motivated to think innovative and aided me to apply a practical approach in my experiments. Also, he helped me to understand that patience and hard work are the keys to overcome any hurdles in the research world. His constant encouragement and kind mentoring paved a way for empowering my skills and development

I would also like to thank **Dr. Matteo Sensi** at the University of Modena and Reggio Emilia, whose theoretical and practical expertise was my biggest helping hand. Without his insightful comments and valuable experience, this project would not have been a success. His patience and willingness to help is highly appreciated.

My deepest gratitude to **Dr. Xinzhong Li,** the scientific coordinator of MSCA-ITN AiPBAND project at Teesside University, for his versatile support and undiminishable faith during

the whole course of this project work. I would also like to thank all the Early-Stage Researchers (ESRs) from AiPBAND project for their positive vibes and all time cheering up words.

Last but not the least, I would like to thank my father **Mr. P. R. Selvaraj (Late)** and my mother **Mrs. Thangamani Selvaraj (Late)** for their continuous blessing shower from heaven. My parents have been always my inspiration in life, their words helped me to face all the difficult days during my PhD, with positive spirit and never giving up frame of mind. I would like to thank my best friend **Mr. Dominic Hecker** for his constant encouraging words and huge motivation, not only during the PhD work but also in real life. I would like to thank my sister **Ms. Anu Selvaraj** and my husband **Mr. Arunmozhivarman** for providing their invaluable support towards my project work and they constantly checked upon my progression in PhD thesis. They both remain as the pillar of strength in completing my PhD work.